DEPARTAMENTO DE QUÍMICA INORGÁNICA E INGENIERÍA QUÍMICA

Facultad de Ciencias

Instituto Químico para la Energía y el Medioambiente

Programa de doctorado en Química Fina

UNIVERSIDAD Ð CÓRDOBA

ESTUDIO DE HIDRÓXIDOS DOBLES LAMINARES COMO FOTOCATALIZADORES AVANZADOS PARA TAREAS DE DESCONTAMINACIÓN DE GASES NOₓ

STUDY OF LAYERED DOUBLE HYDROXIDES AS ADVANCED PHOTOCATALYSTS FOR NOₓ GASES DECONTAMINATION

Directores:

Dra. Ivana Pavlovic Milicevic

Dr. Luis Sánchez Granados

Memoria de Tesis Doctoral presentada por:

JAVIER FRAGOSO NÚÑEZ

Para aspirar al grado de Doctor por la Universidad de Córdoba

Córdoba, 4 de mayo de 2023

TITULO: *Estudio de Hidróxidos Dobles Laminares como fotocatalizadores avanzados para tareas de descontaminación de gases NOx*

AUTOR: *Javier Fragoso Núñez*

TÍTULO DE LA TESIS:
ESTUDIO DE HIDRÓXIDOS DOBLES LAMINARES COMO FOTOCATALIZADORES AVANZADOS PARA TAREAS DE DESCONTAMINACIÓN DE GASES NO$_X$

DOCTORANDO: Javier Fragoso Núñez

INFORME RAZONADO DE LOS DIRECTORES DE LA TESIS

El trabajo científico que se recoge en la memoria que presenta el graduado en Química D. Javier Fragoso Núñez ha sido realizado bajo nuestra dirección en los laboratorios del departamento de Química Inorgánica e Ingeniería Química.

Este trabajo se desarrolla dentro de la línea de investigación de los grupos FQM-175 y FQM-214, dedicada al estudio de nuevos materiales fotocatalizadores para la eliminación de gases NO$_x$ del entorno urbano. Los resultados obtenidos han dado lugar a la publicación de cinco artículos científicos, cuatro de ellos como primer autor, en revistas internacionales de prestigio y nueve comunicaciones a congresos nacionales e internacionales. Además, como complemento a su formación investigadora, el graduado realizó una estancia de cuatro meses y medio en una institución europea de prestigio: Dipartimento di Chimica, Università degli Studi di Torino (Italia).

En nuestra opinión, la memoria que se presenta reúne los requisitos necesarios para optar al grado de Doctor (doctorado con Mención Internacional) por la Universidad de Córdoba. Por todo ello, se autoriza la presentación de la tesis doctoral.

Córdoba, 4 de mayo de 2023

Firma de los directores

Fdo.: Luis Sánchez Granados   Fdo.: Ivana Pavlovic Milicevic

Índice

Capítulo 1
Introducción

1.1. Contaminación atmosférica

La contaminación del aire es, junto con el cambio climático, una de las mayores amenazas ambientales para la salud humana [1]. De acuerdo con los datos de la Organización Mundial de la Salud (OMS), en el año 2019 prácticamente la totalidad de la población mundial (un 99 %) se encontraba expuesta a niveles de contaminación atmosférica que excedían sus límites de calidad [2].

A pesar de las mejoras en la calidad del aire durante las últimas 3 décadas [3], la exposición a este tipo de contaminación es el tercer mayor factor de riesgo general para la salud humana (Figura 1) a nivel mundial, después de la hipertensión y el tabaquismo [4]. Además, la contaminación atmosférica se ha asociado con tres de las principales causas de muerte en el mundo con porcentajes significativos de mortalidad: accidente cerebrovascular (26 %), cardiopatía isquémica (20.2 %) y cáncer primario de tráquea, bronquios y pulmón (19 %) [4,5].
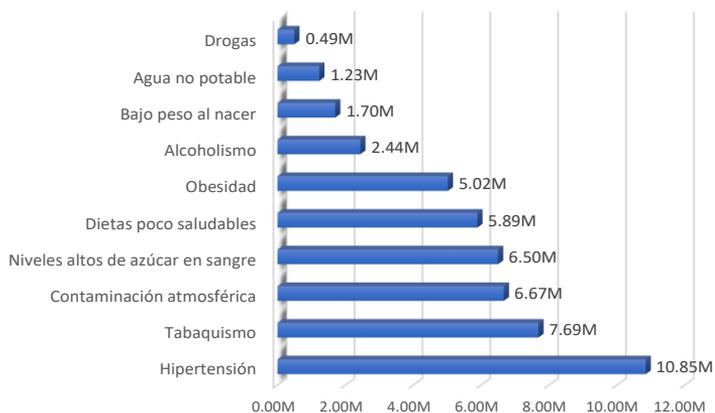
Figura 1. *Número total de muertes en el mundo por factor de riesgo, medidos en todos los grupos de edad y ambos sexos en el año 2019. Adaptada de [6]. Fuente: IHME, Global Burden of Disease-2019.*

En total, la contaminación del aire se vincula con unos siete millones de muertes en todo el mundo, así como con un coste económico elevado. En el año 2013, el Banco Mundial estimó un impacto económico a nivel global de 143.000 millones de dólares estadounidenses en ingresos laborales perdidos y de 3.55 billones de dólares en pérdidas de bienestar por la exposición a PM2.5, uno de los contaminantes atmosféricos más importantes [7].

Además, la contaminación atmosférica también tiene consecuencias sobre el medio ambiente y sobre las actividades humanas, con impactos en el rendimiento de los cultivos, en la biodiversidad, los suelos, lagos y ríos, así como en los materiales e infraestructuras humanas como edificios, puentes e incluso el patrimonio histórico [8-10].

1.1.1. Tipos de contaminantes

La Agencia Europea del Medio Ambiente define la contaminación atmosférica como la presencia de sustancias nocivas en el aire en una concentración que interfiere en la salud y el bienestar humano, o que produce otros efectos ambientales dañinos [11].

Los contaminantes atmosféricos son una mezcla compleja de partículas sólidas, líquidas y gaseosas de distinta procedencia (agentes químicos, físicos o biológicos) [2], que se pueden clasificar atendiendo a criterios como su fuente de emisión o su origen [12].

Atendiendo a su fuente de emisión, los contaminantes atmosféricos se pueden dividir en dos categorías: naturales o antropogénicos.

Los primeros son emitidos directamente por fuentes naturales como, por ejemplo: incendios forestales, erupciones volcánicas, tormentas de polvo, granos de polen, gas radón o agentes biológicos [13]. No obstante, este tipo de contaminantes tienen un ligero efecto sobre la salud y el bienestar, debido a que generalmente estas fuentes de emisión se encuentran alejadas de las grandes poblaciones y suelen ser transitorias [14]. Los segundos son el resultado de las actividades humanas, principalmente del transporte, la producción de energía y las actividades industriales. Este tipo de contaminación ha cobrado mayor importancia desde el comienzo de la industrialización [15].

Según su origen, los contaminantes del aire se pueden dividir en contaminantes primarios y secundarios. Los contaminantes primarios se liberan directamente de una fuente identificable a la atmósfera y son emitidos ya sea por eventos naturales o por actividades humanas. Ejemplos de contaminantes primarios son los óxidos de azufre y nitrógeno, el monóxido de carbono, los hidrocarburos, determinados metales, las partículas y los compuestos orgánicos volátiles (COV). En cambio, los contaminantes secundarios, se forman en la atmósfera por interacción química entre los contaminantes primarios o entre contaminantes primarios y los constituyentes de la atmósfera, mediante procesos de oxidación, oxidación fotoquímica y/o hidrólisis. Entre estos se encuentran, por ejemplo, los ácidos sulfúrico y nítrico que provocan lluvia ácida, ácido carbónico, ozono, etc. Algunos contaminantes del aire son contaminantes primarios y secundarios al mismo tiempo, como el monóxido de nitrógeno y algunas partículas.

El efecto nocivo de estos contaminantes sobre la salud depende sustancialmente de la cantidad y el tiempo de exposición, así como del tipo de contaminante. De entre todos los contaminantes, hay seis que se encuentran ampliamente distribuidos por todo el mundo, y son conocido como "contaminantes de criterio" o "contaminantes básicos" [14] que son: el material particulado, los compuestos orgánicos volátiles (VOC), ozono troposférico, monóxido de carbono, óxidos de azufre, óxidos de nitrógeno y algunos metales como el plomo, el arsénico, el cadmio y el níquel. Para estos contaminantes, se pueden determinar niveles aceptables de exposición y se ha establecido un estándar de calidad del aire [16] por diferentes organismos, como la OMS o la Agencia Europea del medio ambiente (Figura 2).

Figura 2. *Límites recomendados de algunos contaminantes. Fuentes EU Air Quality Directives (2008/50/EC, 2004/107/EC), WHO, 2021 Air quality guidelines: Global udate 2005. Recogida de[17].*

Pollutant	Averaging period	Objective	Concentration	Comments (EU)	IT 1.	IT 2.	IT 3.	IT 4.	AQG level	Comments (WHO)
$PM_{2,5}$	24-hour	Target value	25 µg/m³		75	50	37,5	25	15 µg/m³	99th percentile (i.e. 3–4 exc. Days/year)
$PM_{2,5}$	Annual	Limit value	25 µg/m³		35	25	15	10	5 µg/m³	
$PM_{2,5}$	Annual	Indicative limit value	20 µg/m³							
PM_{10}	24-hour	Limit value	50 µg/m³	Not to be exceeded on more than 35 days/year	150	100	75	50	45 µg/m³	99th percentile (i.e. 3–4 exc. Days/year)
PM_{10}	Annual	Limit value	40 µg/m³		70	50	30	20	15 µg/m³	
O_3	Max. daily 8-hour mean	Target value	120 µg/m³	Not to be exceeded on more than 25 days/year (averaged over 3 years)						
O_3	Max. daily 8-hour mean	Long-term objective	120 µg/m3							
O_3	8-hour	Target value			160	120	–	–	100 µg/m³	99th percentile (i.e. 3–4 exc. Days/year)
O_3	Peak season [a]	Target value			100	70	–	–	60 µg/m³	
NO_2	Hourly	Limit value	200 µg/m³	Not to be exceeded on more than 18 hours/year	200				200 µg/m³	
NO_2	Annual	Limit value	40 µg/m³		40	30	20	–	10 µg/m³	
NO_2	24-hour	Target value			120	50	–	–	25 µg/m³	99th percentile (i.e. 3–4 exc. Days/year)
SO_2	Hourly	Limit value	350 µg/m³	Not to be exceeded on more than 24 hours/year						
SO_2	24-hour	Limit value	125 µg/m³	Not to be exceeded on more than 3 days/year	125	50	–	–	40 µg/m³	99th percentile (i.e. 3–4 exc. Days/year)
CO	Max. daily 8-hour mean	Limit value	10 mg/m³		7	–	–	–	10 mg/m³	
CO	24-hour	Target value							4 mg/m³	99th percentile (i.e. 3–4 exc. Days/year)
C_6H_6	Annual	Limit value	5 µg/m³						1,7 µg/m³	Reference level
BaP	Annual	Target value	1 ng/m³	Measured as content in PM_{10}						
Pb	Annual	Limit value	0,5 µg/m³	Measured as content in PM_{10}					0,5 µg/m³	
As	Annual	Target value	6 ng/m³	Measured as content in PM_{10}					6,6 ng/m³	Reference level
Cd	Annual	Target value	5 ng/m³	Measured as content in PM_{10}					5 ng/m³	
Ni	Annual	Target value	20 ng/m³	Measured as content in PM_{10}					25 ng/m³	Reference level

1.1.2. Contaminación urbana

Las migraciones poblacionales desde las áreas rurales a las urbanas han sido un fenómeno en continuo crecimiento desde la Revolución Industrial en el siglo XVIII [18], alcanzándose el punto de inflexión en el año 2008, cuando la población urbana mundial superó en número a la rural (Figura 3). De acuerdo con datos de la ONU, se prevé que para el año 2050, la población urbana alcance el 70 % de la población mundial [19].
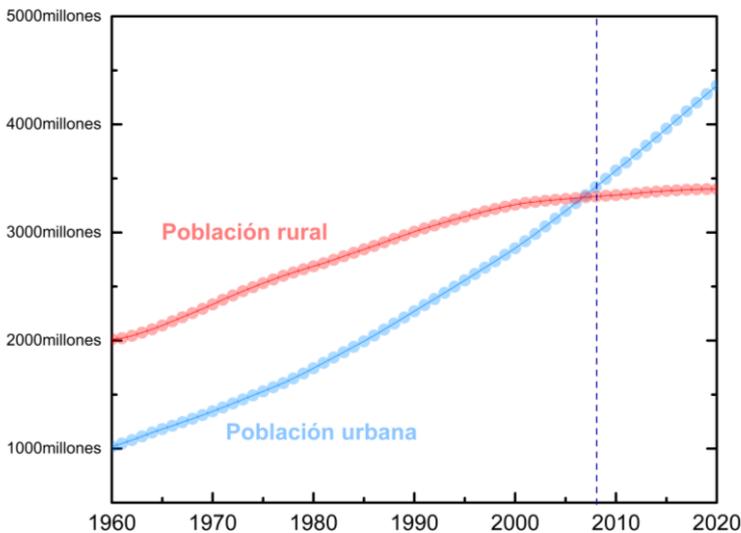
Figura 3. *Evolución del número de personas viviendo en áreas urbanas y rurales a nivel mundial. Adaptada de de Our World in Data [20]. Fuente: Banco Mundial.*

Este rápido movimiento de la población hacia zonas con una mayor industrialización, en las cuales existe un mayor crecimiento económico (más del 80 % del producto interior bruto mundial se genera en las ciudades [21]), ha generado un deterioro considerable en la calidad del aire en las zonas urbanas [22].

En estas zonas, la quema de combustibles fósiles es la mayor fuente de contaminación atmosférica [12], debido principalmente a las emisiones originadas por el tráfico rodado, a las que se suman, en menor proporción, las causadas por las calefacciones, el tráfico marítimo y aéreo, determinadas industrias y centrales energéticas [23].

Las emisiones más importantes de contaminantes a la atmósfera, derivadas de la quema de combustibles fósiles, son las de SO_2, NO_x, CO, partículas y gases de efecto invernadero, como el CO_2. También se emiten otras sustancias en pequeñas cantidades como, por ejemplo, metales pesados, compuestos de haluros o dioxinas, dependiendo de la composición del combustible [24].

En las zonas urbanas, en términos de daño a la salud humana, los contaminantes más dañinos son el material particulado (PM10, PM2.5), el ozono troposférico (O_3) y los óxidos de nitrógeno (NO_x) [25]. De estos tres, resulta interesante el estudio de los gases NO_x, puesto que además de ser un importante contaminante ambiental, también actúan como precursores de otros contaminantes atmosféricos [26].

En este sentido, a través de un conjunto complejo de reacciones, los gases NO_x producen tanto la formación de ozono troposférico como de material particulado en forma de aerosoles orgánicos e inorgánicos. Estos últimos contribuyen a su vez, en la formación de smog [27]. En el caso del ozono troposférico, estas reacciones son de naturaleza cíclica y pueden resultar en una acumulación de NO_x y O_3. Por lo general, hay un lapso de tiempo entre el aumento de la concentración de NO_x (durante las horas punta de la mañana y la tarde) y el aumento de la concentración de O_3 (en las horas de máxima irradiación solar) [27].

Los óxidos de nitrógeno engloban tanto al monóxido de nitrógeno (NO) como al dióxido de nitrógeno (NO_2), siendo este último el que mayores efectos adversos genera tanto para la salud humana (inflamación de las vías aéreas, afecciones de órganos - como el hígado o el bazo - o de sistemas, como el circulatorio o el inmunitario, que propician a su vez infecciones pulmonares e insuficiencias respiratorias [28,29]) como sobre el medio ambiente (acidificación y eutrofización de ecosistemas, afecciones metabólicas, limitación del crecimiento vegetal [30]).

Además, dado que los gases NO_x son precursores de otros contaminantes, se agravan las consecuencias mencionadas sobre la salud y el medio ambiente y conlleva efectos sobre el clima [31]. En lo referente al ozono, una exposición a niveles elevados de este gas origina problemas respiratorios como la irritación de las vías respiratorias, asma, etc. y también puede dañar la vegetación (afectar al crecimiento de cultivos y bosques, reducir la absorción de CO_2 por las plantas, alterar la estructura de los ecosistemas y reducir la biodiversidad) [32]. Respecto al material particulado, son los contaminantes del aire más importantes en términos de peligrosidad para la salud humana [33], ya que pueden alcanzar el torrente sanguíneo y ser transportadas a zonas muy sensibles y agravar patologías que pueden conducir incluso a la muerte prematura [34].

Por tanto, reduciendo los NO_x en la atmósfera, no solo se minimiza los efectos negativos directos asociados a estos, sino que también se reducen los impactos posteriores en la salud asociados a otros contaminantes, como el O_3 troposférico o el material particulado [26].

En septiembre de 2015, 193 países, adoptaron los Objetivos de Desarrollo Sostenible (ODS), conocidos oficialmente como la Agenda 2030 para el Desarrollo Sostenible [35]. La contaminación del aire se reconoce como una preocupación apremiante de sostenibilidad y se menciona explícitamente en dos de sus metas: reducción sustancial de los impactos en la salud de las sustancias peligrosas (ODS3.9) y reducción de los impactos adversos de las ciudades sobre las personas (ODS11.6). Por tanto, resulta de vital importancia encontrar métodos efectivos para reducir la contaminación atmosférica en las ciudades.

1.1.3. Remediación de la contaminación por óxidos de nitrógeno

En los procesos de combustión, las emisiones de gases NO_x pueden deberse a diferentes factores, pudiéndose diferenciar los siguientes tipos de gases NO_x en función de su origen [36]:

1) **NO_x térmico**: que procede de la oxidación a alta temperatura (> 1000 °C) del nitrógeno atmosférico.

2) **NO_x intrínseco**: que se forma por oxidación de los compuestos de nitrógeno presentes en el combustible.

3) **NO_x cinético**: que puede producirse por la reacción entre el nitrógeno atmosférico con radicales libres procedentes de los hidrocarburos mediante combustión a bajas temperaturas (en condiciones ricas en combustible).

Las metodologías que ayudan a mitigar las emisiones y la eliminación de óxidos de nitrógeno se conocen como procesos DeNOx [37]. Se han desarrollado e implementado algunos métodos para controlar las emisiones de NO_x, los cuales se dividen en métodos primarios y secundarios [38].

Los métodos primarios se refieren a la prevención de la formación de gases NO_x, mientras que los métodos secundarios comprenden la reducción de gases NO_x ya formados. Algunos métodos de prevención incluyen la sustitución del combustible común por un combustible con bajo nivel de nitrógeno, el uso de aditivos y el pretratamiento del combustible [39]. Sin embargo, estas técnicas no son suficientes para asegurar las bajas emisiones exigidas por la legislación vigente y, además, no pueden utilizarse en todas las situaciones [40]. Los métodos secundarios incluyen entre otros, los siguientes [41]:

❖ **Reducción catalítica selectiva:** consiste en la reducción de los NO_x, con la ayuda de un catalizador, a nitrógeno molecular y agua. Se pueden emplear diferentes agentes reductores como H_2, hidrocarburos, CO, NH_3 o urea [42].

❖ **Reducción no catalítica selectiva:** también llamado proceso DeNOx termal, se usa para reducir los gases NO_x a altas temperaturas (900– 1000 °C) sin emplear un catalizador. En este proceso, el amoníaco y la urea son los agentes reductores más utilizados. El mecanismo de reacción es bastante más complejo que en el caso anterior, debido a la presencia de radicales libres [43].

❖ **Adsorción:** empleando diferentes adsorbentes como el carbón activado, zeolitas, óxidos metálicos, redes metal orgánicas o el gel de sílice [44].

❖ **Haz de electrones:** este método implica los procesos de humidificación y enfriamiento de los gases de combustión; inyección de amoníaco en la corriente de gases de combustión, bajo la irradiación con un haz de electrones (para formar partículas sólidas); y finalmente, recolección y filtración de subproductos [45].

❖ **Plasma no térmico:** en este método, un gas de combustión fluye a través de un plasma generado en el espacio entre dos electrodos. En el plasma se generan diferentes tipos de radicales (como nitrógeno, oxígeno e hidroxilo) que interaccionan con los gases NO_x produciendo su oxidación o reducción a moléculas inocuas (nitrito/nitrato o a nitrógeno molecular, respectivamente) [40]. El mecanismo de reacción en este proceso se encuentra influenciado por la composición del gas de combustión [46].

❖ **Reducción electroquímica:** consiste en la reducción química de los gases NO_x en una celda de estado sólido basada en un conductor iónico de óxido. Al aplicar el potencial a la celda, se produce la reducción de los gases NO_x a nitrógeno en el cátodo, mientras que en el ánodo se forma oxígeno molecular [47].

En la siguiente tabla se recogen algunas de las ventajas e inconvenientes de los métodos comentados:

Tabla 1. *Resumen de algunas ventajas e inconvenientes de métodos DeNOx postcombustión [41].*

Método	Ventajas	Inconvenientes
Reducción catalítica selectiva (SCR)	Alta eficiencia Bajo coste operativo Instalación relativamente sencilla	Alto coste del catalizador Liberación amoniaco no reaccionado Alto coste de equipo Alta temperatura de funcionamiento
Reducción no catalítica selectiva (SNCR)	Bajo coste de capital y operación Regeneración simple Se pueden emplear con gases con un alto nivel en PM	Baja eficiencia No aplicable con baja concentración de gases NO_x Se requiere alta temperatura de operación
Haz de electrones	No genera residuos Produce subproductos útiles (NH_4NO_3 y NH_4SO_4)	Alto coste de energía Estructura compleja del equipo
Adsorción	No genera residuos líquidos Alta eficiencia de purificación Equipamiento sencillo	Alto coste de inversión Equipamiento grande
Reducción electroquímica	No emplea ningún reductor	En una etapa temprana de desarrollo Todavía muchos mecanismos son desconocidos
Plasma no térmico	Bajo coste del equipo No genera residuos Operación simple Subproductos útiles	Alto consumo de energía Baja eficiencia

No obstante, ninguno de estos métodos es aplicable para eliminar directamente los óxidos de nitrógeno en las zonas urbanas [38]. En este sentido, la fotocatálisis se presenta como una alternativa interesante y prometedora para eliminar dichos contaminantes de las áreas urbanas, debido a que la reacción fotocatalítica de oxidación de los gases NO_x se puede activar *in-situ* mediante irradiación solar y operar a temperatura ambiente y presión atmosférica, utilizando reactivos abundantes como son el agua y oxígeno presentes en la atmósfera [48].

1.2. Fotocatálisis

La palabra fotocatálisis apareció por primera vez en 1911, cuando el científico alemán Alexander Eibner, incorporó este concepto en sus estudios sobre el efecto de la irradiación del ZnO con luz para la degradación de un pigmento, el azul de Prusia [49]. No obstante, la comunidad científica no prestó demasiada atención a la fotocatálisis hasta la década de los 70 del siglo pasado cuando, debido a la "crisis del petróleo" y a los impactos ambientales de las operaciones industriales, los científicos comenzaron a buscar fuentes de energía alternativas y renovables [50]. En este contexto, dos científicos japoneses, Fujishima y Honda, publicaron en 1972, el que posteriormente sería considerado como el primer artículo en este campo [51]. En este estudio, se llevó a cabo por primera vez la electrolisis del agua asistida por luz, empleando para ello como electrodo un material semiconductor, el dióxido de titanio (TiO_2), iluminado con radiación ultravioleta.

Desde entonces, la fotocatálisis heterogénea basada en semiconductores de óxidos metálicos ganó una enorme atención en la

comunidad científica, dando lugar a una amplia variedad de aplicaciones, que incluyen desde la obtención de combustibles (mediante la fotólisis del agua o la reducción de CO_2), células fotovoltaicas y degradación de contaminantes en el agua y en la atmósfera (fotocatálisis ambiental), procesos biocidas y rutas alternativas en síntesis orgánica [52,53].

1.2.1. El proceso fotocatalítico

La fotocatálisis es un fenómeno fotoelectroquímico, que depende esencialmente de la estructura electrónica de los materiales [37]. Desde el punto de vista electrónico, es común clasificar los materiales como conductores, semiconductores y aislantes o dieléctricos, siendo la mayoría de los óxidos metálicos aislantes o semiconductores.

Para entender la estructura electrónica en los sólidos, se puede hacer una extensión simple de la Teoría de Orbitales Moleculares, conocida como Teoría de Bandas, en la cual el sólido se considera como una molécula indefinidamente grande [54]. El punto clave de esta aproximación se encuentra en que la superposición de los orbitales atómicos en los sólidos, da lugar a bandas de niveles de energía separados por brechas de energía, conocidas como bandas prohibidas o "band gaps".

Así, cuando dos átomos se unen para formar una molécula, sus orbitales atómicos se combinan para producir orbitales moleculares enlazantes (baja energía) y antienlazantes (alta energía). Los electrones ocupan los nuevos orbitales de tal manera que la energía del sistema se minimiza, lo que implica que se llenen primero los orbitales de enlace.

Si aumenta el número de átomos que constituyen la molécula, el número de orbitales moleculares crecerá progresivamente. Al mismo tiempo, la diferencia de energía entre niveles discretos del mismo carácter (enlazantes o antienlazantes) disminuirá gradualmente y, de manera similar, la diferencia de energía entre el orbital de enlace de mayor energía y el de antienlace de menor energía disminuirá ligeramente. No obstante, esta diferencia seguirá siendo comparativamente grande.

Si la cantidad de átomos implicados se aproxima al número de Avogadro, como ocurre en los sólidos convencionales, los niveles de energía de los electrones que contribuyen al enlace desarrollarán un continuo virtual de niveles de energía conocido como banda de valencia (BV). De la misma manera, los orbitales antienlazantes más energéticos, se fusionarán para formar una banda continua de estados desocupados llamada banda de conducción (BC) (Figura 4).
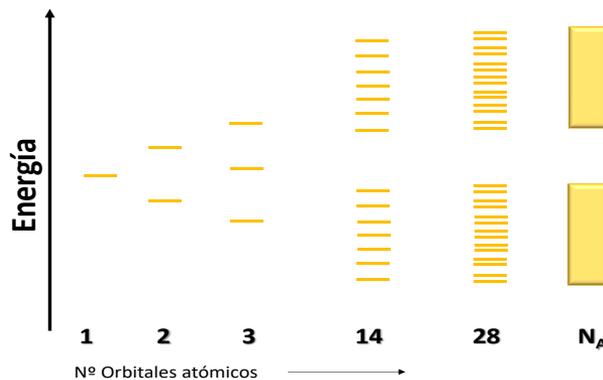
Figura 4. *Diagrama de Orbitales Moleculares en un sólido.*

La conducción electrónica en un sólido ocurre gracias a la libre movilidad de electrones entre la banda de valencia y la de conducción. Así, en los aislantes, los electrones de la BV están separados de la BC por un

band gap grande, por lo que se imposibilita la movilidad electrónica; mientras que, en los conductores como los metales, la BV se superpone con la BC y la movilidad electrónica es espontánea.

Finalmente, en los semiconductores existe un band gap suficientemente pequeño que permite que los electrones de la BV alcancen la BC si se suministra una energía externa adecuada, como por ejemplo calor, luz u otra clase de excitación (Figura 5).
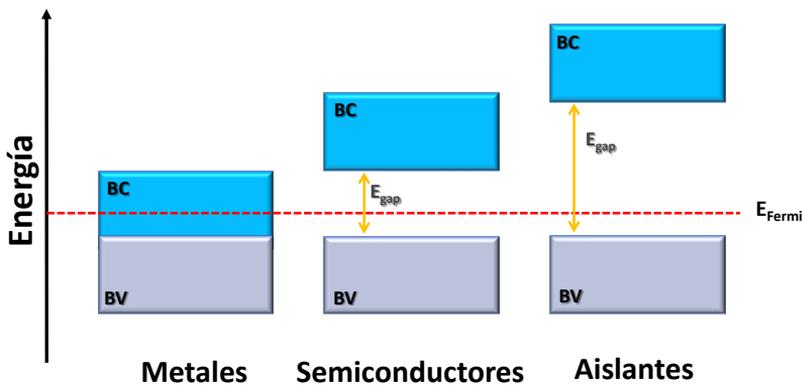
Figura 5. *Comparación de la banda de valencia y de la banda de conducción en materiales metálicos, aislantes y semiconductores.*

En el caso de los semiconductores (denominados semiconductores intrínsecos), para mejorar sus propiedades eléctricas, se pueden añadir pequeñas cantidades de otros elementos en el material (dopantes) que introduzcan nuevos niveles de energía entre la banda de valencia y la banda de conducción del semiconductor original [55]. A este tipo de material se le denomina semiconductor extrínseco y, dependiendo de donde se sitúe la nueva banda de energía, respecto a la banda de valencia o de conducción, se distingue entre semiconductor tipo-n o tipo-p [56] (Figura 6).

En los semiconductores tipo-n, la adición de impurezas donadoras de electrones contribuye a subir los niveles de energía de los electrones en la banda prohibida de los semiconductores. Esto desplaza el nivel de Fermi a un punto intermedio entre los nuevos niveles de los electrones donantes y la banda de conducción. En los semiconductores tipo-p, la adición de impurezas aceptoras de electrones contribuye a bajar los niveles de los huecos en la banda prohibida de los semiconductores, de modo que los electrones pueden ser fácilmente excitados desde la banda de valencia hasta estos niveles, dejando huecos móviles en la banda de valencia. Esto implica un desplazamiento del nivel de Fermi a un punto intermedio entre los niveles aceptores y la banda de valencia.
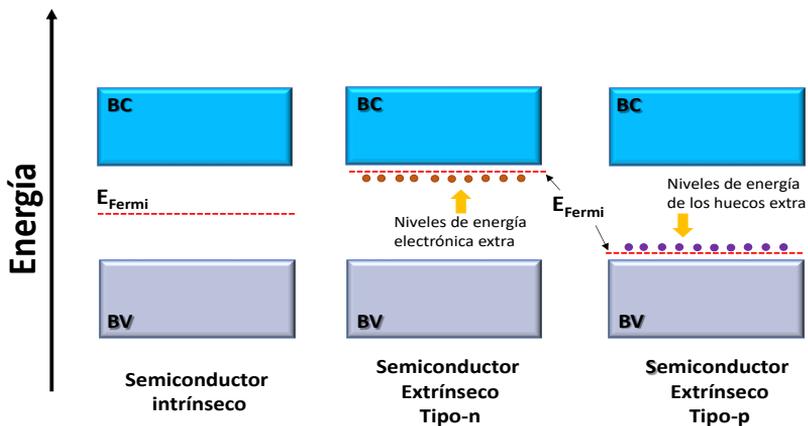
Figura 6. *Diagrama comparativo de los diferentes tipos de semiconductores.*

Según lo anterior, el ampliamente aceptado modelo de fotocatálisis se explica de la siguiente forma: cuando un semiconductor, como el TiO_2, es irradiado con fotones con una energía superior o igual a la de su band gap (E_g), los electrones de la banda de valencia se excitan y alcanzan la banda de conducción (BC), dejando huecos en la banda de valencia (BV) (Figura 7) creándose así el par electrón-hueco (e^-/h^+). El valor de E_g y las

posiciones de los límites de las bandas de valencia y de conducción determinan la propiedad de absorción de luz y la capacidad redox del fotocatalizador, respectivamente [50].

Tras la separación del par electrón-hueco, solo los electrones y los huecos separados que migren a la superficie del material tendrán oportunidad de llevar a cabo reacciones de oxidación o reducción, respectivamente (procesos 1 y 3 en la figura 7).

Durante el proceso de migración, una gran parte de los electrones y huecos se recombinan tanto en la superficie como en el interior, y la energía de los portadores de carga es convertida en energía vibracional de los átomos de la red (fonones) o fotones (procesos 2 y 4 en la Figura 7), lo que reduce la eficiencia del proceso fotocatalítico.
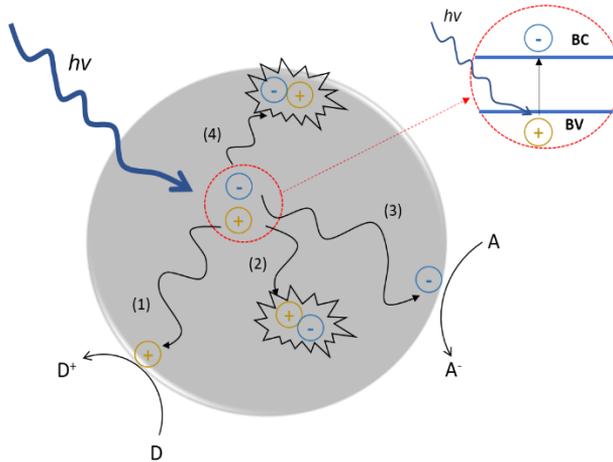
Fig. 7. *Procesos importantes en el fotocatalizador de TiO$_2$: generación del par electrón-hueco, transferencia de carga, recombinación electrón-hueco en el interior y en la superficie y reacciones químicas inducidas por los electrones y los huecos.*

1.2.2. Oxidación fotocatalítica de gases NO$_x$

De forma general, el proceso de oxidación fotoquímica de los gases NO$_x$ (Figura 8) comienza una vez generados los portadores de carga por la incidencia de la radiación sobre el fotocatalizador (ec. 1). Así, una vez en la superficie del fotocatalizador, los electrones y los huecos formados interaccionan con moléculas de agua y oxígeno allí adsorbidas para producir especies reactivas del oxígeno (ROS por sus siglas en inglés), principalmente aniones superóxido y radicales hidroxilo (ec. 2 y 3) [57], siendo dichas especies las que llevan a cabo el proceso de oxidación de los óxidos de nitrógeno. Así, el radical superóxido, debido a su fuerte poder oxidante, es capaz de producir la oxidación completa de NO a NO$_3^-$ (ec. 4) [58]. Simultáneamente, el radical hidroxilo lleva a cabo un proceso oxidativo secuencial: NO → NO$_2^-$ → NO$_2$ → NO$_3^-$ (ec. 5 a 7) [59].
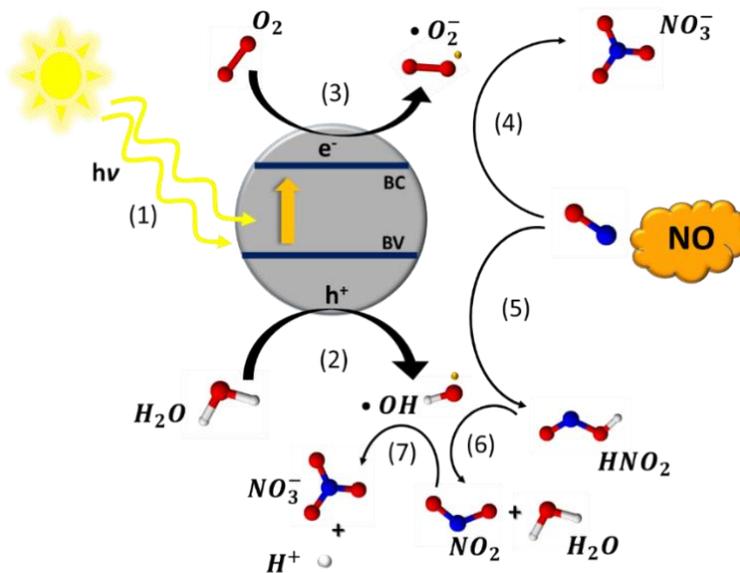
Figura 8. *Mecanismo de oxidación fotocatalítica de NO en una partícula de TiO$_2$. Recogida de [38].*

$$TiO_2 \xrightarrow{h\nu} e_{BC}^- + h_{BV}^+ \qquad (ec.\,1)$$

$$h_{BV}^+ + H_2O \longrightarrow OH^\bullet + H^+ \qquad (ec.\,2)$$

$$e_{BC}^- + O_2 \longrightarrow O_2^{\bullet-} \qquad (ec.\,3)$$

$$NO + O_2^{\bullet-} \longrightarrow NO_3^- \qquad (ec.\,4)$$

$$NO + OH^\bullet \longrightarrow HNO_2 \qquad (ec.\,5)$$

$$HNO_2 + OH^\bullet \longrightarrow NO_2 + H_2O \qquad (ec.\,6)$$

$$NO_2 + OH^\bullet \longrightarrow NO_3^- + H^+ \qquad (ec.\,7)$$
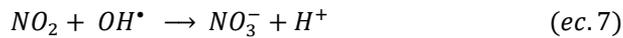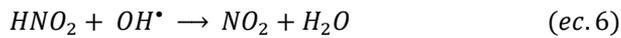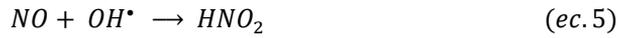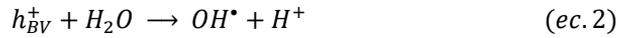
No obstante, hay estudios que demuestran que, en realidad, el proceso fotocatalítico DeNOx en el TiO$_2$ presenta un mecanismo de reacción bastante más complejo [37]. Así, junto con los radicales •OH y •O$_2^-$, también se producen otras especies reactivas, como oxígeno atómico (O), O$^-$ y •HO$_2$, durante la irradiación [60]. Además, también se observaron otros intermediarios de reacción como NO$^+$, N$_2$O N$_2$O$_3$, NO$_2$ y NO$_2^+$ [61]. La Figura 9 muestra un esquema de los diferentes caminos de oxidación fotoquímica de los óxidos de nitrógeno en la superficie del dióxido de titanio.
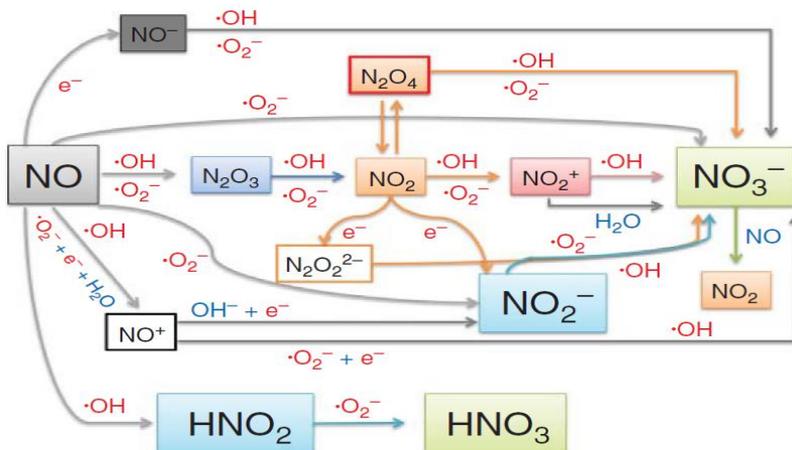
Figura 9. *Diferentes rutas en la oxidación fotocatalítica de los gases NO$_x$ en la superficie del fotocatalizador. Recogida de [37].*

El TiO_2 ha demostrado ser un fotocatalizador muy eficiente en procesos DeNOx. No obstante, presenta una serie de desventajas. El gran valor de su band gap (3.2 eV para la fase anatasa) restringe la utilización de fotones de la región visible del espectro, que es la mayor parte de la irradiación solar que incide en la Tierra (la luz ultravioleta ocupa solo alrededor del 4-5 % del espectro de radiación solar, mientras que la luz visible representa el 43 %) [62]. Además, no es selectivo hacia la oxidación total de los óxidos de nitrógeno, es decir, durante la acción DeNOx se produce gran cantidad de NO_2, como intermedio de reacción, mucho más tóxico que el NO de partida [63]. Por otra parte, su precio resulta ser muy elevado para ciertas aplicaciones, como es el caso de los materiales de construcción fotocatalíticos. Según lo anterior, resulta interesante la búsqueda de nuevos fotocatalizadores DeNOx, que solventen las limitaciones que presenta el TiO_2.

1.2.3. Fotocatalizadores avanzados $DeNO_x$

Las cuestiones comentadas anteriormente están siendo abordadas por la comunidad científica, que ha centrado su atención en el estudio de nuevos semiconductores $DeNO_x$ con propiedades mejoradas, de bajo coste y sostenibles. En este apartado se hace un resumen de los principales sistemas DeNOx alternativos al TiO_2 estudiados, desde las modificaciones llevadas a cabo en el propio TiO_2 hasta otros compuestos químicos.

1.2.3.1. Modificaciones en el TiO_2

Para superar la pobre respuesta a la luz visible del dióxido de titanio, se han implementado diversas estrategias, como la introducción de vacantes de oxígeno [64,65], la sensibilización con tintes (TiO_2-ARS) [66,67], la utilización del efecto de resonancia de plasmones superficiales en metales (nanocristales de TiO_2 anatasa, nanopartículas TiO_2-Au) [68,69], el ajuste del band gap mediante el dopaje con heteroátomos (TiO_2-Fe, TiO_2-N, TiO_2-F) [70,71] o la heterounión con otros fotocatalizadores (g-C_3N_4/TiO_2, g-graphene/TiO_2, WO_3/TiO_2 , PtO_x/TiO_2) [72-75].

1.2.3.2. Fotocatalizadores basados en óxidos de zinc y estaño

Otro tipo de fotocatalizadores avanzados objeto de estudio son los materiales basados en estaño (para la región visible) y los basados en zinc (para la región ultravioleta del espectro). Se han llevado a cabo estudios tanto de sus óxidos binarios por separado (SnO_2 y ZnO) [76,77] como en óxidos multicomponente [78] (especialmente en la estructura espinela Zn_2SnO_4), algunas heterouniones con otros compuestos (SnO_2/TiO_2, SnO_2/Zn_2SnO_4) [79,80] y su deposición sobre otros materiales (ZnO@SiO_2) [81].

Con el diseño apropiado de los fotocatalizadores de SnO_2 o ZnO (tanto de estructura como en composición), se pueden alcanzar eficiencias DeNOx similares o superiores (alrededor del 70 %) a las reportadas normalmente para los compuestos basados en TiO_2 [78,81-83].

1.2.3.3. Óxidos de metales de transición

Los óxidos de metales de transición son fotocatalizadores altamente sostenibles para las acciones DeNOx porque algunos de ellos combinan características interesantes como, por ejemplo, ser materiales abundantes en la tierra, de bajo coste, químicamente estables y muchos de ellos seguros para la salud humana. Se han obtenido resultados interesantes para los fotocatalizadores α-Fe_2O_3, $ZnFe_2O_4$, $ZnWO_4$, $BiVO_4$ o $InVO_4$ [84-88].

Por lo general, presentan valores pequeños de band gap, pudiendo por ello ser activados por la luz visible. Sin embargo, aunque realizan una buena captación de luz, la posición inadecuada de las bandas de energía, o la rápida recombinación e^-/h^+ (que limita la producción de especies reactivas del oxígeno), suele conducir a una baja acción DeNOx.

1.2.3.4. Materiales basados en bismuto

Los materiales a base de bismuto se han estudiado en profundidad como fotocatalizadores DeNOx debido a su capacidad para funcionar solo bajo radiación en el espectro de luz visible [37]. Esta familia de fotocatalizadores incluye principalmente Bi metálico, óxido de bismuto y compuestos de bismuto con fases de Aurivillius (como oxicarbonato de bismuto, oxihalogenuro de bismuto, molibdato de bismuto, volframato, fosfato de bismuto, etc.) (Figura 10) [89].
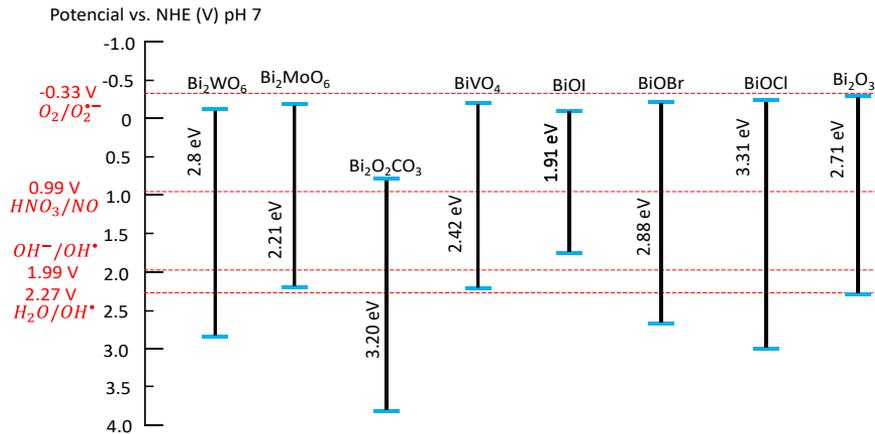
Figura 10. N*iveles de bandas de fotocatalizadores de bismuto. Adaptado de [89].*

Sin embargo, la mayoría de ellos suelen presentar una eficiencia fotocatalítica muy pobre y necesitan acciones adicionales como el uso de nitrógeno atómico como dopante, la deposición de pequeños núcleos de Bi, Fe o Pt, la creación de vacantes de oxígeno, la preparación de soluciones sólidas o la formación de heterouniones, para mejorar su actividad DeNOx.

1.2.3.5. Materiales basados en g-C₃N₄

El nitruro de carbono grafítico, g-C$_3$N$_4$, es un semiconductor típico polimérico, en el que los átomos de carbono y nitrógeno presentan hibridación sp^2 formando un sistema conjugado π altamente deslocalizado. El valor del band gap es de aproximadamente 2.7 eV, lo que le permite absorber luz azul-violeta con una longitud de onda de menos de 475 nm en el espectro solar [90,91].

Los compuestos basados en nitruro de carbono grafítico (g-C$_3$N$_4$) también son materiales interesantes con altas eficiencias DeNOx, ya que facilitan la separación y el transporte de las cargas fotoinducidas (e⁻ y h⁺), prolongando así su vida útil. Sin embargo, el aumento de la fotoactividad

de estos materiales bajo luz visible sigue siendo un objetivo importante a desarrollar [92].

1.3. Hidróxidos dobles laminares

Los hidróxidos dobles laminares (HDL), también conocidos como "compuestos tipo hidrotalcita" son una amplia familia de materiales laminares, naturales y sintéticos, que se conoce desde hace más de 160 años [93,94].

El primer mineral natural perteneciente a esta familia de materiales fue descubierto en Suecia en 1842 y se denominó hidrotalcita, con una fórmula general $Mg_6Al_2(OH)_{16}CO_3 \cdot 4H_2O$. Sin embargo, no fue hasta 100 años más tarde cuando el químico suizo Walter Feitknecht la sintetizó por primera vez en el laboratorio [95,96] y hasta los años 60 del siglo pasado cuando se realizó su determinación estructural mediante difracción de rayos X por Allmann [97] y Tailor [98,99].

Nuestro grupo de investigación ha sido pionero en el empleo de estos materiales como fotocatalizadores DeNOx, obteniendo unos resultados muy satisfactorios [100].

1.3.1. Estructura y composición de los HDL

La estructura de esta familia de compuestos, está basada en la brucita, $Mg(OH)_2$, un mineral que cristaliza con una estructura tipo CdI_2 y que está formado por iones Mg^{2+} octaédricamente coordinados con grupos hidroxilo. Dichas unidades octaédricas $M(OH)_6$ comparten aristas para formar láminas bidimensionales infinitas y de carga neutra, unidas

entre si mediante puentes de hidrógeno. En un hidróxido doble laminar, tiene lugar una sustitución isomórfica del ion Mg^{2+} por un catión trivalente, como por ejemplo el Al^{3+}, generando una carga positiva en la lámina, que es compensada por la intercalación de un anión en el espacio interlaminar (Figura 11).
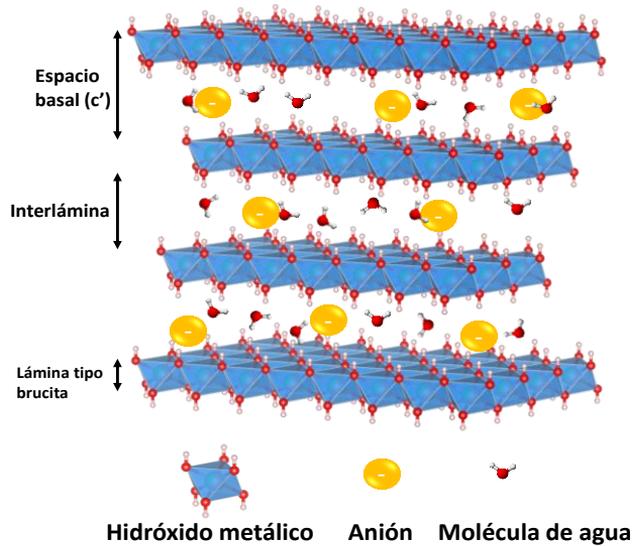
Figura 11. *Representación esquemática de un hidróxido doble laminar.*

La estructura de los HDL puede ser representada por la fórmula química general:

$$[M_{1-x}^{2+}M_x^{3+}(OH)_2]^{x+}\left(A_{x/n}^{n-}\right)^{x-} \cdot mH_2O$$
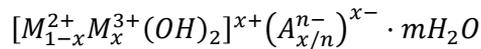
Donde $[M_{1-x}^{2+}M_x^{3+}(OH)_2]^{x+}$ representa la composición de la lámina (siendo M^{2+} y M^{3+} los cationes metálicos divalentes y trivalentes respectivamente y x la relación metálica x= $M^{3+}/(M^{2+}+M^{3+})$), mientras que $\left(A_{x/n}^{n-}\right)^{x-} \cdot mH_2O$ indica la composición de la interlámina, siendo A el

anión con la carga n, y m es el número de moles de agua en el espacio interlaminar. Esta fórmula, a veces es abreviada como $[M^{2+}M^{3+}-A]$ [93].

Los HDL pueden cristalizar en diferentes politipos según la forma en la que se apilan sus láminas. Entre ellos destacan los empaquetamientos que presentan tres láminas hidroxiladas en la celda unidad (con simetría romboédrica y grupo espacial R3m), como en la Figura 11, o bien los que presenta dos láminas en la celda unidad (con simetría hexagonal y grupo espacial P6/mmc). Estos politipos presentan los parámetros de celda a y c = 3c' y a c=2c' respectivamente (donde c' es el espesor de una capa constituida por una lámina tipo brucita y una interlámina) [94].

Atendiendo a su composición, las especies metálicas presentes en las láminas de los HDL pueden variar dentro de un amplio rango, por ejemplo: Mg^{2+}, Co^{2+}, Cu^{2+}, Ni^{2+}, Cd^{2+} o Zn^{2+} para metales divalentes y Al^{3+}, Cr^{3+}, Ga^{3+}, o Fe^{3+} para los trivalentes. No obstante, también existen algunos ejemplos con iones tetravalentes, con composición M(II)-M(IV)-HDL (donde M(IV) puede ser Ti^{4+}, Zr^{4+} o Sn^{4+} [101-103]) y con iones monovalentes M(I). El único caso reportado con cationes monovalentes en la estructura del HDL es el litio, concretamente el HDL LiAl-HDL [101,104].

Respecto a los aniones interlaminares, existe una amplia variedad de especies, que incluyen desde iones inorgánicos simples (haluros, nitratos, carbonatos) [105], hasta aniones orgánicos (tereftalato, acrilato, lactato, etc.) [106,107], compuestos de coordinación [108,109] polioxometalatos [110-112], biomoléculas como nucleósidos monofosfato (AMP, CMP, GMP o ATP) o incluso fragmentos de ADN [113,114].

Prácticamente no hay limitación en cuanto a composición se refiere en los HDL. No obstante, en lo que respecta a los cationes metálicos, cabe señalar que la preferencia de coordinación del metal juega un factor importante [115], ya que los metales se encuentran en entornos octaédricos en la estructura. Además, la relación atómica de los metales, x debe ser 0.2 x <0.4, para obtener fases puras en la mayoría de los HDL [93].

Igualmente, la naturaleza del anión que puede compensar la carga positiva de la lámina tipo brucita es prácticamente ilimitada. El único problema puede estar relacionado con la preparación de una fase pura del HDL o que ésta se encuentre bien cristalizada [94].

1.3.2. Propiedades de los HDL

Los hidróxidos dobles laminares presentan dos propiedades singulares que los hacen muy interesantes para una gran diversidad de aplicaciones que son: la capacidad de intercambiar el anión presente en la interlámina y la capacidad de recuperar su estructura original cuando son sometidos a tratamientos térmicos moderados ("efecto memoria").

❖ **Intercambio aniónico**

Una de las características más importantes de los HDL es que, en la mayoría de los casos, la interacción de los aniones con las láminas de hidróxidos metálicos se produce mediante interacciones electrostáticas relativamente débiles, lo que hace que los HDL sean una clase importante de intercambiadores de iones [93].

$$[M^{2+}M^{3+} - X] + Y \rightarrow [M^{2+}M^{3+} - Y] + X$$
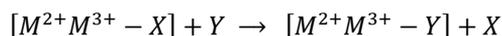
No obstante, la capacidad de intercambio aniónico se ve afectada tanto por la naturaleza de los aniones intercalados inicialmente, como por la densidad de carga de las láminas metálicas (relación M^{2+}/M^{3+}) [116]. Así, a partir de los cálculos de la constante de equilibrio de varias reacciones de intercambio, Miyata proporcionó una secuencia de selectividades iónicas para aniones monovalentes: $OH^- > F^- > Cl^- > Br^- > NO_3^- > I^-$ y divalentes: $CO_3^{2-} > C_{10}H_4N_2O_8S^{2-} > SO_4^{2-}$ para el caso del MgAl-HDL [117]. Para el sistema CuAl-X, Yamaoka et al. [118] determinaron una secuencia de selectividad similar para el caso de aniones monovalentes, mientras que para para el caso de oxoaniones divalentes, propusieron el orden: $HPO_4^{2-}, HAsO_4^{2-} > CrO_4^{2-} > SO_4^{2-} > MoO_4^{2-}$. Además, se observó que las selectividades de los aniones divalentes eran superiores a las de los aniones monovalentes, por tanto, los HDL que contienen cloruro o nitrato se encuentran entre los mejores precursores para las reacciones de intercambio [93].

❖ **Efecto Memoria**

Algunos hidróxidos dobles laminares (hidrotalcita, hidrocalumita, etc.), tras ser sometidos a un tratamiento térmico moderado, tienen la propiedad única de poder recuperar su estructura laminar al rehidratarse en presencia de una disolución acuosa de aniones [93].

Cuando un HDL se calcina a unos 450-500 °C, tiene lugar el colapso de la estructura laminar dando como resultado a la formación de óxidos metálicos mixtos [119].

$$[M_{1-x}^{2+}M_x^{3+}(OH)_2](A_{x/n}^{n-}) \cdot mH_2O \rightarrow [M_{1-x}^{2+}M_x^{3+}O] + (m+1)H_2O + otros$$
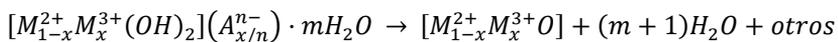
Estos óxidos metálicos pueden volver a la estructura del HDL cuando se rehidratan en una solución que contiene el anión que se desee intercalar. Este proceso de recuperación de su forma original se conoce como "efecto memoria" [120].

$$[M_{1-x}^{2+}M_x^{3+}O] + Y_{x/n}^{n-} + (m+1)H_2O \rightarrow [M_{1-x}^{2+}M_x^{3+}(OH)_2](A_{x/n}^{n-}) \cdot mH_2O$$
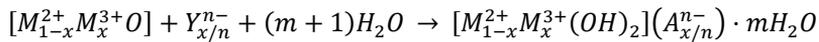
Si el HDL se somete a una temperatura superior a 500 °C, el óxido mixto cambia a una fase espinela, en un proceso irreversible [121].

1.3.3. Métodos de síntesis

Los hidróxidos dobles laminares no están tan extendidos en la naturaleza como las arcillas catiónicas. Sin embargo, una de sus principales ventajas es que se pueden preparar en grandes cantidades de manera reproducible mediante métodos simples y económicos [62,122].

Los principales métodos para preparar estos materiales son: la coprecipitación, el intercambio iónico y la reconstrucción.

❖ **Método de coprecipitación**

Para que ocurra la precipitación simultánea de dos o más cationes, es necesario que el pH sea igual o superior al del hidróxido más soluble que se pretende precipitar [120]. En este sentido, la síntesis de los HDL puede realizarse bajo condiciones de precipitación a baja sobresaturación o a alta sobresaturación [123].

En el caso de la coprecipitación en condiciones de baja sobresaturación, la precipitación se lleva a cabo mediante la adición lenta

de la disolución de sales metálicas di y trivalentes, en la proporción elegida, en un reactor que contiene una disolución acuosa del anión que se desee intercalar. El pH se ajusta a un valor adecuado por agregación lenta al reactor de una disolución de una base, que permite la coprecipitación de las dos sales metálicas. Una de las ventajas de este método es que admite un control más preciso de la relación M^{2+}/M^{3+} en las láminas bruciticas y que el producto que se forma tiene una mayor cristalinidad que los obtenidos bajo condiciones de alta sobresaturación, porque en la primera situación la tasa de crecimiento cristalino es mayor que la tasa de nucleación [124].

En cambio, la coprecipitación en condiciones de alta sobresaturación requiere la adición de la mezcla de sales metálicas M^{2+}/M^{3+} a una disolución alcalina que contenga el anión que se desee intercalar. Este método generalmente da lugar a materiales menos cristalinos debido al alto número de núcleos de cristalización.

❖ **Método del intercambio iónico**

Este método se basa en aprovechar la capacidad de intercambio iónico que presentan los HDL, y se emplea cuando no es posible obtener HDL mediante el método de coprecipitación como, por ejemplo, cuando los aniones involucrados son inestables en solución alcalina, o cuando la reacción directa entre los cationes metálicos y los aniones es más favorable que la formación de HDL [120].

En general, la capacidad de intercambio depende de la carga y del radio tanto del anión interlaminar original como del que se encuentra en la disolución. Este método es especialmente útil para la preparación de

HDL con aniones diferentes al carbonato, ya que este anión tiene mucha afinidad hacia las láminas bructicas y las síntesis se suelen llevar a cabo en una atmósfera inerte para evitar la presencia del CO_2.

❖ **Método de reconstrucción**

Este método se basa en la anteriormente comentada propiedad de "efecto memoria". La facilidad de reconstrucción del HDL va a depender de la naturaleza de los cationes que constituyen las láminas [93]. Este método se suele emplear cuando se desea intercalar aniones de gran tamaño.

❖ **Otros métodos de síntesis**

Otros métodos empleados para la síntesis de HDL son el método sol-gel [125], electrosíntesis [126], método hidrotermal [127] o la síntesis asistida por microondas [128]. El método a elegir dependerá del sistema estudiado y del uso final que se le vaya a dar al material [93].

Debido a las interacciones electrostáticas presentes entre las láminas, los HDL son propensos al apilamiento o agregación [129,130], lo que produce una disminución de su área superficial y por tanto, debilita sus propiedades en diversas aplicaciones. En ese sentido, se han llevado a cabo investigaciones sobre la preparación de HDL con varias morfologías irregulares [131-134] para incrementar el área de superficie específica.

Por otro lado, debido a que la unión entre las láminas es relativamente débil, se han analizado varios métodos de deslaminación para preparar nanoestructuras HDL de baja dimensión (2D) [135-137], entre los que destaca el método AMOST (por sus siglas en inglés "Aqueous

Miscible Organic Solvent Treatment"). En dicho método, el HDL sintetizado mediante coprecipitación, es sometido a un postratamiento con un disolvente orgánico miscible con agua (por ejemplo, acetona o etanol) antes de ser secado, obteniéndose HDL con poco apilamiento de las láminas y baja cristalinidad [138].

1.3.4. Aplicaciones

Una característica atractiva de los HDL es que la gran variedad de posibles cationes a incorporar en la lámina, así como de aniones en la interlámina, permite la síntesis de una muy versátil familia de materiales funcionales con aplicaciones en diferentes campos (Figura 12). En este apartado se muestran algunas de ellas.
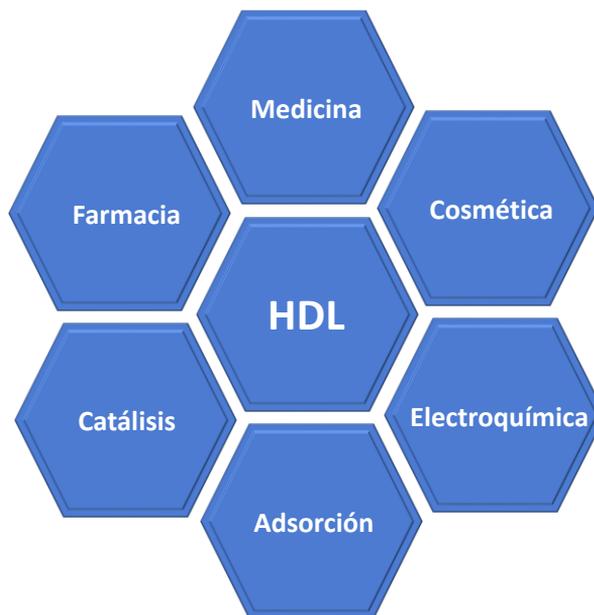
Figura 12. *Algunos de los campos de aplicación de los HDL.*

❖ **Catálisis**

En el ámbito de la catálisis, los HDL y materiales basados en HDL han sido ampliamente utilizados tanto en catálisis heterogénea, como en fotocatálisis y fotoelectrocatálisis [139,140]. Estos compuestos se aplican con frecuencia como catalizadores para la producción de compuestos de Química Fina [141] como, por ejemplo, la esterificación del glicerol con ácido láurico [142]. También se han empleado como electrocatalizadores para reacciones de reducción de oxígeno (ORR) [143,144], la reacción de evolución de oxígeno (OER) [145,146] o la reacción de reducción de nitrógeno (NRR) [147]. Desde el punto de vista fotocatalítico, los HDL se han empleado tanto para la fotodegradación de contaminantes en agua [148,149], como en el proceso de "water splitting" [150] o en la fotorreducción de CO_2 [151,152].

❖ **Adsorción**

Debido tanto a la alta capacidad de intercambio aniónico, como a la propiedad de rehidratación y recuperación de su estructura a partir de su producto calcinado, los HDL pueden alojar materiales muy diversos en su interlámina. Incluso si se modifica la naturaleza de su espaciado interlaminar de hidrofílica a hidrofóbica, intercalando aniones con largas cadenas alquílicas, se pueden adsorber especies moleculares apolares. Además, tras su acción como adsorbente, los HDL se pueden regenerar y reutilizar después de eliminar el contaminante adsorbido por calcinación a 500 °C o por extracción con disolventes orgánicos.

Los HDL se han utilizado como materiales adsorbentes para una amplia gama de contaminantes en el agua [153], desde oxoaniones [154],

ion fosfato [155], metales pesados [156], compuestos radiactivos como el uranio [157,158], hasta contaminantes orgánicos como colorantes [159,160], pesticidas [161,162], herbicidas [163] e incluso productos farmacéuticos y cosméticos [164].

❖ **Medicina, Farmacia y Cosmética**

Los HDL también han encontrado muchas aplicaciones en el campo de la medicina debido a su alta biocompatibilidad (baja toxicidad), capacidad de carga aniónica y estabilidad química [165]. Pueden ser empleados como sistema de liberación lenta tanto para la administración de fármacos y genes [166], como sistemas fotoprotectores en cremas solares [167] o como biosensores de distintas biocompuestos como iones calcio [168] y glucosa [169] entre otros.

❖ **Electroquímica**

Debido a que pueden tener alta actividad redox, los HDL exhiben abundantes sitios electroquímicos activos y rutas eficientes de transporte de carga/masa. Además, junto con su elevada área superficial activa altamente accesible y la buena estabilidad mecánica, los HDL pueden proporcionar una alta capacidad específica teórica y una buena estabilidad del ciclo carga-descarga, lo que es adecuado para su aplicación como materiales de electrodos para supercondensadores [170,171] y baterías [172,173].

1.3.5. Actividad fotocatalítica

En las últimas dos décadas, los HDL se han convertido en un grupo innovador de fotocatalizadores en el campo de la energía y el medio ambiente debido a sus propiedades excepcionales [174] como su bajo coste, fácil escalabilidad de su síntesis y su gran versatilidad estructural, que incluye tanto el tipo de cationes (y su proporción en las láminas) como la naturaleza de los aniones en la interlámina [175]. Esta última propiedad da como resultado a una amplia variedad de combinaciones en cuanto a composición en los HDL, lo que permite diseñar materiales HDL con distintas propiedades físicas y químicas. Concretamente, en el caso de la fotocatálisis, permite diseñar fotocatalizadores con valores de band gap específicos [150]. En la Figura 13, se observan los valores de band gap, así como los límites de la banda de valencia y la banda de conducción para varios HDL.
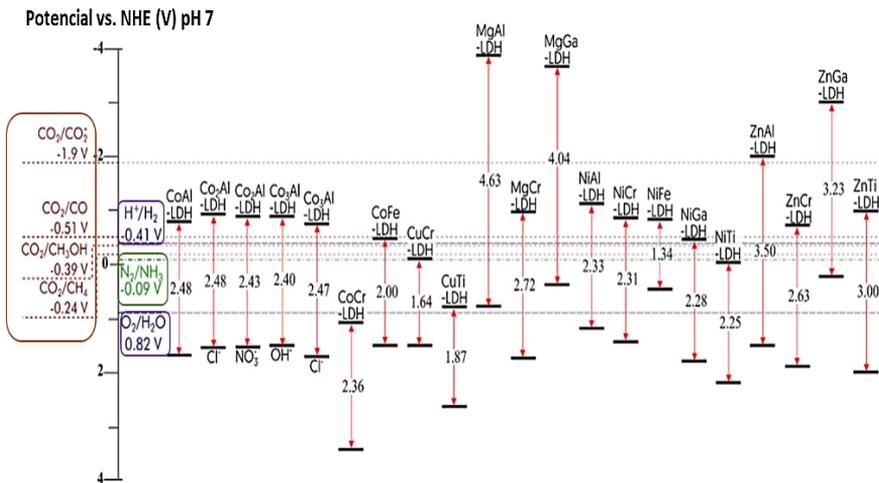
Figura 13. *Posiciones de badas de diferentes HDL con respecto a los potenciales redox de los procesos water splitting, reducción de CO_2 y fijación de nitrógeno. Adaptado de [175].*

Dado que las propiedades fotocatalíticas de los materiales están determinadas por sus propiedades estructurales y electrónicas, es fundamental discutir los factores que influyen en el proceso fotocatalítico de los HDL.

Como se ha comentado anteriormente, la estructura de los HDL se basa en láminas de octaedros MO_6 que comparten aristas [176,177]. El octaedro MO_6 es uno de los factores importantes que afectan la fotofísica y propiedades fotocatalíticas de los HDL. Además, una característica estructural importante de los HDL es que los cationes M^{2+} y M^{3+} se distribuyen de manera uniforme en las láminas de los hidróxidos sin formar clusters [174]. Esta alta dispersión de los metales en la estructura permite que los fotocatalizadores HDL tengan múltiples vías de excitación electrónica (transferencia de carga de metal a metal (M^{2+}-O-M^{3+}), transiciones d–d (en sistemas con metales de transición) y transferencia de carga de ligando a metal a través de O-M^{2+}/M^{3+}) [178] y minimiza la recombinación de electrones y huecos, lo que produce que estos materiales muestren una alta eficiencia fotocatalítica [150,179].

Además, los grupos OH^- superficiales de las láminas de hidróxidos son capaces de reaccionar con los huecos de la banda de valencia para producir radicales hidroxilo (•OH), los cuales tienen un potencial de oxidación muy alto y se consideran un intermediario importante para las reacciones de fotooxidación [180].

1.3.5.1. Estrategias para la mejora de propiedades fotocatalíticas en los HDL

Existen una gran variedad de estrategias para llevar a cabo la mejora de las propiedades fotocatalíticas de los HDL [175]. En este apartado se mostrarán algunas de ellas.

❖ **Composición metálica**

Uno de los métodos más efectivos para potenciar la actividad bajo luz visible de un fotocatalizador es el dopaje con iones metálicos [181,182]. Se ha demostrado que los dos iones metálicos en los HDL y los enlaces M–O los hacen similares a los materiales de TiO_2 dopados [174]. Teniendo en cuenta que los HDL tienen dos o tres iones metálicos diferentes y la proporción entre estos metales puede controlarse, se pueden identificar como un "semiconductor dopado", donde el catión de valencia superior actúa como dopante. Así, los HDL basados en Zn/Cr, Mg/Cr, Zn/Fe, Mg/Fe, Cu/Cr, Co/Cr y Ni/Fe, llevan a estos materiales a exhibir fotoactividad en la región de luz visible, muy importante para el mejor aprovechamiento del espectro solar [183-187].

Por tanto, la introducción de iones metálicos de valencia variable en los HDL binarios facilita el ajuste de los niveles energéticos, lo que a su vez promueve la transferencia de electrones, así como la generación y la estabilización de sitios activos altamente catalíticos, que son sinérgicamente beneficiosos para mejorar el rendimiento fotocatalítico [188].

Nuestro grupo de investigación ha estudiado la influencia del dopado de los HDL, en el proceso de oxidación fotocatalítica de óxidos de

nitrógeno. En un primer estudio sobre el empleo de HDL para procesos DeNOx, se comprobó que el fotocatalizador Zn_3Al-CO_3, presentó valores de eficiencia de conversión de NO del 50 % y de selectividad del 90 % (baja emisión de gas NO_2 durante el proceso DeNOx) [100]. Estos valores aumentaron a 55 – 60 % y 92 %, respectivamente, cuando parte del Al^{3+} fue sustituido en la estructura de HDL por Cr^{3+} o Fe^{3+}. La sustitución parcial del aluminio por los metales de transición también favoreció la actividad fotoquímica va luz visible y mitigó la recombinación e^-/h^+ [189,190] (Figura 14).
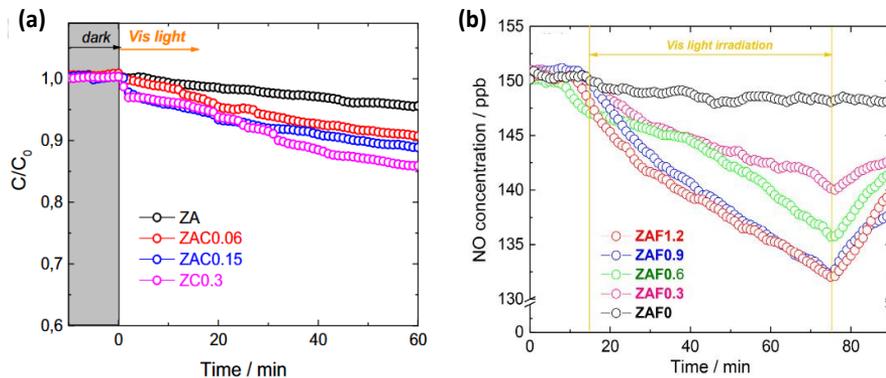
Figura 14. Variación de la concentración de gas NO para fotocatalizadores $Zn_yAl_{1-x}M_x$ irradiados con luz *visible, siendo M (a) Cr^{3+} ó (b) Fe^{3+} recogidas de [189,190]*. Nomenclatura: Z: cinc, A: aluminio, C, cromo y F hierro. El número identifica el grado de sustitución del aluminio por cromo o hierro.

❖ **Anión interlaminar**

Además de la composición de las láminas de hidróxido metálico, los aniones intercalados entre estas también pueden desempeñar un papel importante en la mejora del rendimiento fotocatalítico. En la bibliografía científica existen una gran cantidad de ejemplos de ello:

Xia et al. [191] investigaron la influencia de diferentes aniones interlaminares (F^-, Cl^-, Br^-, I^- y NO_3^-) en el sistema ZnCr-HDL para la degradación fotocatalítica del hexaclorobeneno. Al comparar diferentes aniones intercalados, concluyeron que los HDL intercalados con iones de halógeno exhibieron una mayor actividad catalítica que las muestras intercaladas con nitrato. Atribuyeron la mayor actividad a un área superficial más grande y un band gap más pequeño. No obstante, los cálculos teóricos (DFT – Teoría del Funcional de la Densidad) revelaron que la estabilidad estructural (basada en el efecto electrostático y los enlaces de hidrógeno) era del orden de $HDL-NO_3$ > HDL-F > HDL-Cl > HDL-Br > HDL-I, justo en el orden opuesto de los rendimientos de fotodegradación. Eso indicó que los resultados fotocatalíticos de estos HDL estaban altamente relacionados con la estabilidad de su estructura [192]. También se ha demostrado que muchos de los HDL con polioxometalatos (POM) como aniones interlaminares muestran excelentes actividades fotocatalíticas [193-195].

Varios estudios han afirmado que las propiedades de fotoabsorción de los HDL intercaladas con carbonato son mejores que las de los HDL que contienen otros aniones en la interlámina [196-198]. Esto es debido al efecto sinérgico del carbonato, que da como resultado una mayor actividad fotocatalítica. La presencia de este ion en la interlámina reduce la recombinación electrón-hueco y aumenta significativamente la fotoactividad de los HDL hacia la evolución de hidrógeno [62,198] y también la degradación de tintes [185,186]. Concretamente, para el caso de la oxidación fotocatalítica de los NO_x, el grupo de Fan Dong [199] estudió la respuesta hacia la descontaminación fotoquímica de los gases NO_x con HDL de ZnAl intercalado con diferentes aniones (MoO_4^{2-}, OH^- y

CO$_3^{2-}$) obteniendo los mejores resultados para la muestra que contenía el anión carbonato.

❖ **Heterouniones**

El acoplamiento de los HDL con otros semiconductores puede mejorar el rendimiento fotocatalítico al facilitar la movilidad de los portadores de carga y reducir su recombinación [175]. No obstante, los potenciales de la banda de valencia y la banda de conducción del semiconductor deben ser termodinámicamente favorables con las respectivas bandas del HDL para una transferencia eficiente de portadores de carga fotoinducidos (Figura 15). En este sentido, aunque la formación de semiconductores híbridos con HDL es una estrategia factible, la principal dificultad radica en cómo fabricar una heteroestructura apropiada y efectiva entre un HDL y otro semiconductor. Este es uno de los campos más importantes a explorar, porque la preparación de estructuras bien definidas, composiciones, fases cristalinas, band gaps e interfases afecta la fotoeficiencia de la heteroestructura HDL.
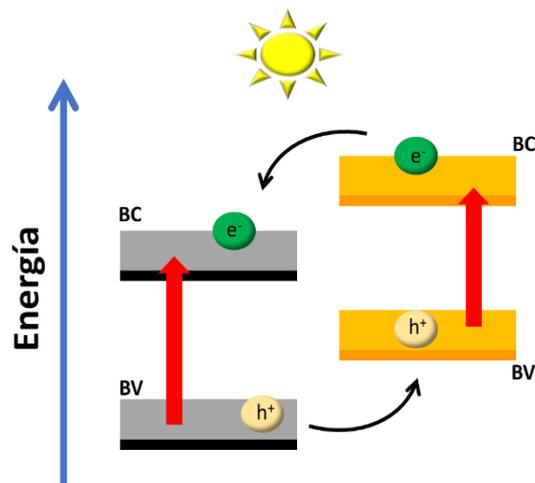
Figura 15. *Esquema de estructura de bandas de dos semiconductores en una heterounión tipo II.*

En la actualidad, se han descrito una gran variedad de heteroestructuras exitosas con diferentes semiconductores (SC/HDL): BiOBr/CoNi-HDL, BiOCl/ZnCr-HDL, Bi_2MoO_6/ZnAl-HDL, g-C_3N_4/NiFe-HDL, Cu_2O/MgAl-HDL, TiO_2/MgAl-HDL, WSe_2/NiFe-HDL, ZnO/ZnMgAl-HDL; ZnS-ZnO/ZnAl-HDL; WO_3–X/Ag/ZnCr-HDL, para las cuales se evaluaron sus actividades fotocatalíticas en aplicaciones limitadas como: descomposición de compuestos orgánicos, oxidación de agua o producción de hidrógeno [200-207].

Por otro lado, una de las estrategias más sencillas para mejorar las propiedades electrónicas del semiconductor es el uso de "puntos cuánticos" (QDs por sus siglas en inglés). Estos nanomateriales han traído la atención de la comunidad científica para el desarrollo de nuevos fotocatalizadores debido a sus características únicas: unas propiedades ópticas especiales dependientes del tamaño y efectos de confinamiento cuántico. Algunos trabajos describen la preparación de heterouniones QDs/HDL, utilizando QDs de C, CdS, CdSe o CdTe y HDLs de fórmula MgAl, NiFe o ZnCr [208-210]. Si bien la preparación de QDs no siempre es una tarea fácil, solo se necesitan cantidades muy escasas de estos para mejorar significativamente la actividad de un semiconductor.

1.4. Materiales fotocatalíticos DeNOx para zonas urbanas

Desde principios de la década de los 2000 es conocido el uso de materiales de construcción, que contienen TiO_2, como fotocatalizadores DeNOx [40]. En la actualidad, la incorporación de TiO_2 fotoactivo en diversos materiales presenta una gran cantidad de aplicaciones

fotocatalíticas en entornos urbanos, como ventanas autolimpiantes [211], baldosas autolimpiantes [212] o revestimientos fotocatalíticos aplicados sobre superficies de edificios [213].

Además, se han producido dos patentes principales propiedad de Mitsubishi Materials Corporation [214] e Italcementi S.p.A [215] para la aplicación del dióxido de titanio en adoquines de hormigón para el mercado europeo e incluso se ha desarrollado una norma ISO (ISO 22197-1 2016) [216] que permite comparar las eficiencias de diferentes superficies recubiertas fotocatalíticas utilizando una metodología precisa para medir la actividad de la muestra descrita en la norma.

En la bibliografía, se pueden encontrar varios estudios que dan valores sobre la eficiencia de una variedad de materiales de construcción fotocatalíticos usando el estándar ISO, principalmente hormigón fotocatalítico [217,218], pero también pinturas fotocatalíticas [219,220] y asfaltos fotocatalíticos [221]. Estos resultados permiten la caracterización de los materiales de construcción fotocatalíticos en laboratorios, bajo condiciones ambientales controladas.

No obstante, en las últimas dos décadas, se han descrito varios estudios de campo relacionados con la aplicación de materiales de construcción fotocatalíticos en áreas urbanas. Hay algunas experiencias sobre aplicaciones a escala real de materiales fotocatalíticos con TiO_2 en diferentes construcciones como el Palacio Italia en la expo de Milán (Italia, 2015), el edificio Santa Lucía en Sevilla (España) la Cité de la Musique en Chambéry (Francia, 2000) y la Iglesia Dives In Misericordia en Roma (Italia, 2003) (Figura 16).
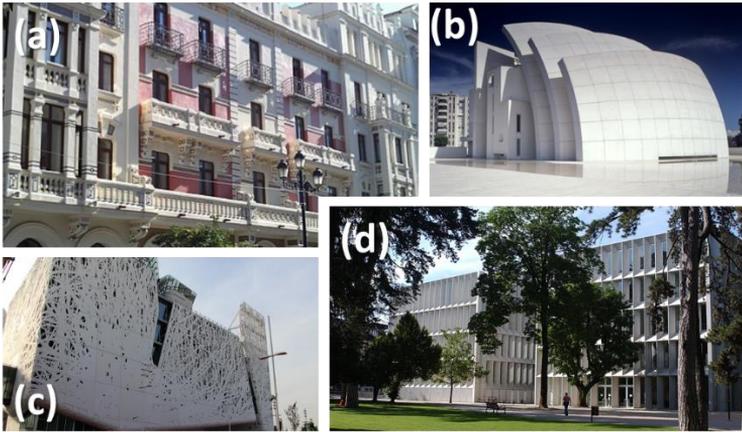
Figura 16. *Fachada del edificio Santa Lucía (a), Iglesia Dives in Misericordia (b), Palacio Italia (c) y Cité de la Musique (d).*

Sin embargo, todas estas aplicaciones reales de construcción encuentran limitaciones que hacen que el uso de este tipo de materiales no esté siendo ampliamente extendido. Por una parte, el aditivo TiO_2 resulta ser muy caro respecto a las materias primas básicas de morteros y hormigones, llegando su adición a multiplicar por cinco el precio de estos materiales de construcción. Por otra parte, si bien el desempeño de estos materiales como fotocatalizadores DeNOx ha sido establecido en laboratorio, la eficiencia de las construcciones mencionadas en la limpieza de la contaminación del aire en condiciones reales no está realmente confirmada [222-224].

Esta falta de información genera muchas incertidumbres a la hora de evaluar y modelar el efecto de los tratamientos fotocatalíticos en las áreas urbanas y deben ser resueltas antes de que el uso de materiales de construcción fotocatalíticos sea una realidad para la eliminación de NOx atmosférico en áreas urbanas.

Por lo mencionado anteriormente, la incorporación de nuevos fotocatalizadores capaces de mejorar la acción DeNOx de los materiales de construcción en condiciones reales de irradiación ambiental (principalmente luz visible), así como abaratar el coste de los mismos, aparece como un reto para su implementación como nueva tecnología de purificación de aire en áreas urbanas altamente contaminadas.

Aunque la mayor parte de la bibliografía sobre materiales de construcción fotocatalíticos se basa en el uso de nanopartículas de TiO_2, algunos estudios recientes han descrito la incorporación de diferentes fotocatalizadores como TiO_2 dopado con hierro o vanadio en morteros base cemento, para mejorar su rendimiento bajo irradiación UV [225], nanopartículas de ZnO en bloques de hormigón [226], g-C_3N_4 en pastas de pastas de cemento [227], pavimento asfáltico [228] y morteros [229] o el BiOBr en materiales de revestimiento cerámico del tipo estuco y pinturas cerámicas [230].

Además, el uso de hidróxidos dobles laminares como aditivos funcionales para morteros de construcción es conocido [231,232]. Por lo tanto, resulta interesante su uso como nuevos aditivos fotocatalíticos de mayor fotoactividad bajo luz visible, una mayor eficiencia de conversión de NO y menor coste, pues pueden producirse por simples métodos de síntesis fácilmente escalables.

1.5. Bibliografía

[1]   World Health Organization, New WHO Global Air Quality Guidelines aim to save millions of lives. https://www.who.int/News/Item/22-09-2021-New-Who-Global-Air-Quality-Guidelines-Aim-to-Save-Millions-of-Lives-from-Air-Pollution, 2021 (accessed 13 March 2023).

[2]   World Health Organization, Air pollution. https://www.who.int/health-topics/air-pollution#tab=tab_1 (accessed 13 March 2023).

[3]   C. Noël, L. Van Landschoot, C. Vanroelen, S. Gadeyne, The Public's Perceptions of Air Pollution. What's in a Name?, Environ. Health Insights. 16 (2022) 11786302221123564. https://doi.org/10.1177/11786302221123563.

[4]   Institute for Health Metrics and Evaluation (IHME), Global Burden of Disease Study 2019 (GBD 2019). https://ghdx.healthdata.org/gbd-2019, (accessed 13 March 2023).

[5]   World Health Organization, The top 10 causes of death. https://www.who.int/news-room/fact-sheets/detail/the-top-10-causes-of-death, 2020 (accessed 15 March 2023).

[6]   Our World in Data, Air Pollution. https://ourworldindata.org/air-pollution, 2021 (accessed 16 March 2023).

[7]   World Bank, Institute for Health Metrics and Evaluation (IHME), The cost of air pollution: strengthening the economic case for action. https://openknowledge.worldbank.org/entities/publication/cf3cfda2-6232-5f57-9979-dacb8aa5a302, 2016 (accessed 17 March 2023).

[8]   F. Chantret, J. Chateau, R. Dellink, O. Durand-Lasserve, E. Lanzi, Can better technologies avoid all air pollution damages to the global economy?, Clim. Change. 163 (2020) 1463–1480. https://doi.org/10.1007/s10584-019-02631-2.

[9]   European Environment Agency, Towards zero pollution in Europe, Publications Office of the European Union, Luxembourg, 2020. ISBN: 978-92-9480-267-5, DOI: 10.2800/40627.

[10]   European Environment Agency, Air quality in Europe 2022. https://www.eea.europa.eu//publications/air-quality-in-europe-2022, 2023 (accessed 21 March 2023).

[11]   European Environment Agency, EEA Glossary. https://www.eea.europa.eu/help/glossary/eea-glossary (accessed 17 March 2023).

[12]   J.A. Bernstein, N. Alexis, C. Barnes, I.L. Bernstein, J. A. Bernstein, A. Nel, D. Peden, D. Diaz-Sanchez, S.M. Tarlo, P.B. Williams, Health effects of air pollution, J. Allergy Clin. Immunol. 114 (2004) 1116–1123. https://doi.org/10.1016/j.jaci.2004.08.030.

[13]   D. Vallero, Air Pollutant Hazards, in: D. Vallero (Ed.), Fundamentals of Air Pollution, 5th Edition, Academic Press, Boston, 2014, pp. 197–214. https://doi.org/10.1016/B978-0-12-401733-7.00007-4.

[14]   A.A. Almetwally, M. Bin-Jumah, A.A. Allam, Ambient air pollution and its influence on human health and welfare: an overview, Environ. Sci. Pollut. Res. 27 (2020) 24815–24830. https://doi.org/10.1007/s11356-020-09042-2.

[15]   World Health Organization, WHO global air quality guidelines: particulate matter (PM2.5 and PM10), ozone, nitrogen dioxide, sulfur dioxide and carbon monoxide. https://apps.who.int/iris/handle/10665/345329, 2021 (accessed 12 March 2023).

[16]   California Air Resources Board, Criteria Air Pollutants. https://ww2.arb.ca.gov/es/our-work/programs/criteria-air-pollutants (accessed 15 March 2023).

[17]   European Environment Agency, Air quality standars. https://www.eea.europa.eu/themes/air/air-quality-concentrations/air-quality-standards, 2021 (accessed 28 March 2023).

[18]   A. Piracha, M.T. Chaudhary, Urban Air Pollution, Urban Heat Island and Human Health: A Review of the Literature, Sustainability. 14 (2022) 9234. https://doi.org/10.3390/su14159234.

[19]   United Nations, Department of Economic and Social Affairs, 68% of the world population projected to live in urban areas by 2050, says UN. https://www.un.org/development/desa/en/news/population/2018-revision-of-world-urbanization-prospects.html, 2019 (accessed 19 March 2023).

[20]   Our World in Data, Number of people living in urban and rural areas, World. https://ourworldindata.org/grapher/urban-and-rural-population (accessed 15 March 2023).

[21]   Banco Mundial, Desarrollo urbano: Panorama general. https://www.bancomundial.org/es/topic/urbandevelopment/overview, 2022 (accessed 17 March 2023).

[22]   Y. Wang, L. Yao, Y. Xu, S. Sun, T. Li, Potential heterogeneity in the relationship between urbanization and air pollution, from the perspective of urban agglomeration, J. Clean Prod. 298 (2021) 126822. https://doi.org/10.1016/j.jclepro.2021.126822.

[23]   Asociación Ibérica de la Fotocatálisis, Libro blanco de la fotocatálisis: Tecnología, Aplicaciones, Medición y FAQ, edición digital, 2020. ISBN:978-84-09-22299-5.

[24]   Gobierno de España, Vicepresidencia Tercera del Gobierno, Ministerio para la Transición Ecológica y el Reto Demográfico, Grandes instalaciones de combustión. https://www.miteco.gob.es/es/calidad-y-evaluacion-ambiental/temas/atmosfera-y-calidad-del-aire/emisiones/act-emis/grandes_instalaciones_combustion.aspx (accessed 20 March 2023).

[25]   European Environment Agency, Air quality in Europe - 2020 report, Luxembourg, 2020, DOI:10.2800/786656.

[26]   S. Shaw, B. Van Heyst, An Evaluation of Risk Ratios on Physical and Mental Health Correlations due to Increases in Ambient Nitrogen Oxide (NO_x) Concentrations, Atmosphere. 13 (2022) 967. https://doi.org/10.3390/atmos13060967.

[27]   C. Muilwijk, P.J.C. Schrijvers, S. Wuerz, S. Kenjereš, Simulations of photochemical smog formation in complex urban areas, Atmos. Environ. 147 (2016) 470–484. https://doi.org/10.1016/j.atmosenv.2016.10.022.

[28]   G.B. Hamra, F. Laden, A.J. Cohen, O. Raaschou-Nielsen, M. Brauer, D. Loomis, Lung Cancer and Exposure to Nitrogen Dioxide and Traffic: A Systematic Review and Meta-Analysis, Environ. Health Perspect. 123 (2015) 1107–1112. https://doi.org/10.1289/ehp.1408882.

[29]   A. Faustini, R. Rapp, F. Forastiere, Nitrogen dioxide and mortality: review and meta-analysis of long-term studies, Eur. Respir. J. 44 (2014) 744-753. https://doi.org/10.1183/09031936.00114713.

[30]   T.H. Panigrahi, S.R. Sahoo, G. Murmu, D. Maity, S. Saha, Current challenges and developments of inorganic/organic materials for the abatement of toxic nitrogen oxides (NOx) – A critical review, Prog. Solid State Chem. 68 (2022) 100380. https://doi.org/10.1016/j.progsolidstchem.2022.100380.

[31]   Gobierno de España, Vicepresidencia Tercera del Gobierno, Ministerio para la Transición Ecológica y el Reto Demográfico, Óxidos de Nitrógeno. https://www.miteco.gob.es/es/calidad-y-evaluacion-ambiental/temas/atmosfera-y-calidad-del-aire/calidad-del-aire/salud/oxidos-nitrogeno.aspx (accessed 18 March 2023).

[32]   Gobierno de España, Vicepresidencia Tercera del Gobierno, Ministerio para la Transición Ecológica y el Reto Demográfico, Ozono. https://www.miteco.gob.es/es/calidad-y-evaluacion-ambiental/temas/atmosfera-y-calidad-del-aire/calidad-del-aire/salud/ozono.aspx (accessed 18 March 2023).

[33]   W. Hill, E.L. Lim, C.E. Weeden, C. Lee, M. Augustine, K. Chen, F.C. Kuan, F. Marongiu, E.J. Evans, D.A. Moore, F.S. Rodrigues, O. Pich, B. Bakker, H. Cha, R. Myers, F. van Maldegem, J. Boumelha, S. Veeriah, A. Rowan, C. Naceur-Lombardelli, T. Karasaki, M. Sivakumar, S. De, D.R. Caswell, A. Nagano, J.R.M. Black, C. Martínez-Ruiz, M.H. Ryu, R.D. Huff, S. Li, M.-J. Favé, A. Magness, A. Suárez-Bonnet, S.L. Priestnall, M. Lüchtenborg, K. Lavelle, J. Pethick, S. Hardy, F.E. McRonald, M.H. Lin, C.I. Troccoli, M. Ghosh, Y.E. Miller, D.T. Merrick, R.L. Keith, M. Al Bakir, C. Bailey, M.S. Hill, L.H. Saal, Y. Chen, A.M. George, C. Abbosh, N. Kanu, S.-H. Lee, N. McGranahan, C.D. Berg, P. Sasieni, R. Houlston, C. Turnbull, S. Lam, P. Awadalla, E. Grönroos, J. Downward, T. Jacks, C. Carlsten, I. Malanchi, A. Hackshaw, K. Litchfield, J.F. Lester, A. Bajaj, A. Nakas, A. Sodha-Ramdeen, K. Ang, M. Tufail, M.F. Chowdhry, M. Scotland, R. Boyles, S. Rathinam, C. Wilson, D. Marrone, S. Dulloo, D.A. Fennell, G. Matharu, J.A. Shaw, J. Riley, L. Primrose, E. Boleti, H. Cheyne, M. Khalil, S. Richardson, T. Cruickshank, G. Price, K.M. Kerr, S. Benafif, K. Gilbert, B. Naidu, A.J. Patel, A. Osman, C. Lacson, G. Langman, H. Shackleford, M. Djearaman, S. Kadiri, G. Middleton, A. Leek, J.D. Hodgkinson, N. Totten, A. Montero, E. Smith, E. Fontaine, F. Granato, H. Doran, J. Novasio, K. Rammohan, L. Joseph, P. Bishop, R. Shah, S. Moss, V. Joshi, P. Crosbie, F. Gomes, K. Brown, M. Carter, A. Chaturvedi, L. Priest, P. Oliveira, C.R. Lindsay, F.H. Blackhall, M.G. Krebs, Y. Summers, A. Clipson, J. Tugwood, A. Kerr, D.G. Rothwell, E. Kilgour, C. Dive, H.J.W.L. Aerts, R.F. Schwarz, T.L. Kaufmann, G.A. Wilson, R. Rosenthal, P. Van Loo, N.J. Birkbak, Z. Szallasi, J. Kisistok, M. Sokac, R. Salgado, M. Diossy, J. Demeulemeester, A. Bunkum, A. Stewart, A.M. Frankell, A. Karamani, A. Toncheva, A. Huebner, B. Chain, B.B. Campbell, C. Castignani, C. Puttick, C. Richard, C.T. Hiley, D.R. Pearce, D. Karagianni, D. Biswas, D. Levi, E. Hoxha, E.L. Cadieux, E. Colliver, E. Nye, F. Gálvez-Cancino, F. Athanasopoulou, F. Gimeno-Valiente, G. Kassiotis, G. Stavrou, G. Mastrokalos, H. Zhai, H.L. Lowe, I.G. Matos, J. Goldman, J.L. Reading, J. Herrero, J.K. Rane, J. Nicod, J.M. Lam, J.A.

Hartley, K.S. Peggs, K.S.S. Enfield, K. Selvaraju, K. Thol, K.W. Ng, K. Dijkstra, K. Grigoriadis, K. Thakkar, L. Ensell, M. Shah, M.V. Duran, M. Litovchenko, M.W. Sunderland, M. Dietzen, M. Leung, M. Escudero, M. Angelova, M. Tanić, O. Chervova, O. Lucas, O. Al-Sawaf, P. Prymas, P. Hobson, P. Pawlik, R.K. Stone, R. Bentham, R.E. Hynds, R. Vendramin, S. Saghafinia, S. López, S. Gamble, S.K.A. Ung, S.A. Quezada, S. Vanloo, S. Zaccaria, S. Hessey, S. Ward, S. Boeing, S. Beck, S.K. Bola, T. Denner, T. Marafioti, T.P. Mourikis, T.B.K. Watkins, V. Spanswick, V. Barbè, W.-T. Lu, W.K. Liu, Y. Wu, Y. Naito, Z. Ramsden, C. Veiga, G. Royle, C.-A. Collins-Fekete, F. Fraioli, P. Ashford, T. Clark, M.D. Forster, S.M. Lee, E. Borg, M. Falzon, D. Papadatos-Pastos, J. Wilson, T. Ahmad, A.J. Procter, A. Ahmed, M.N. Taylor, A. Nair, D. Lawrence, D. Patrini, N. Navani, R.M. Thakrar, S.M. Janes, E.M. Hoogenboom, F. Monk, J.W. Holding, J. Choudhary, K. Bhakhri, M. Scarci, M. Hayward, N. Panagiotopoulos, P. Gorman, R. Khiroya, R.C.M. Stephens, Y.N.S. Wong, S. Bandula, A. Sharp, S. Smith, N. Gower, H.K. Dhanda, K. Chan, C. Pilotti, R. Leslie, A. Grapa, H. Zhang, K. AbdulJabbar, X. Pan, Y. Yuan, D. Chuter, M. MacKenzie, S. Chee, A. Alzetani, J. Cave, L. Scarlett, J. Richards, P. Ingram, S. Austin, E. Lim, P. De Sousa, S. Jordan, A. Rice, H. Raubenheimer, H. Bhayani, L. Ambrose, Tracer. Consortium, Lung adenocarcinoma promotion by air pollutants, Nature. 616 (2023) 159–167. https://doi.org/10.1038/s41586-023-05874-3.

[34]   Gobierno de España, Vicepresidencia Tercera del Gobierno, Ministerio para la Transición Ecológica y el Reto Demográfico, Partículas. https://www.miteco.gob.es/es/calidad-y-evaluacion-ambiental/temas/atmosfera-y-calidad-del-aire/calidad-del-aire/salud/particulas.aspx (accessed 19 March 2023).

[35]   United Nations, Department of Economic and Social Affairs, Sustainable Development, Transforming our world: the 2030 Agenda for Sustainable Development. https://sdgs.un.org/2030agenda (accessed 19 March 2023).

[36]   A. Rao, R.K. Mehra, H. Duan, F. Ma, Comparative study of the NO_x prediction model of HCNG engine, Int. J. Hydrog. Energy. 42 (2017) 22066–22081. https://doi.org/10.1016/j.ijhydene.2017.07.107.

[37]   M. Cruz-Yusta, M. Sánchez, L. Sánchez, Metal oxide nanomaterials for nitrogen oxides removal in urban environments, in: Tailored Functional Oxide Nanomaterials: From Design to Multi-Purpose Applications, Wiley-VCH, 2022: pp. 229–276. ISBN-13: 978-3527347599; https://doi.org/10.1002/9783527826940.ch7.

[38]   J. Balbuena, M. Cruz-Yusta, L. Sánchez, Nanomaterials to Combat NOx Pollution, J. Nanosci. Nanotechnol. 15 (2015) 6373–6385. https://doi.org/10.1166/jnn.2015.10871.

[39]   V.H. Nguyen, B.S. Nguyen, C. W. Huang, T.T. Le, C.C. Nguyen, T.T. Nhi Le, D. Heo, Q.V. Ly, Q.T. Trinh, M. Shokouhimehr, C. Xia, S.S. Lam, D.V.N. Vo, S.Y. Kim, Q.V. Le, Photocatalytic NO_x abatement: Recent advances and emerging trends in the development of photocatalysts, J. Clean. Prod. 270 (2020) 121912. https://doi.org/10.1016/j.jclepro.2020.121912.

[40]   J. Ângelo, L. Andrade, L.M. Madeira, A. Mendes, An overview of photocatalysis phenomena applied to NOx abatement, J. Environ. Manage. 129 (2013) 522–539. https://doi.org/10.1016/j.jenvman.2013.08.006.

[41]   F. Gholami, M. Tomas, Z. Gholami, M. Vakili, Technologies for the nitrogen oxides reduction from flue gas: A review, Sci. Total Environ. 714 (2020) 136712. https://doi.org/10.1016/j.scitotenv.2020.136712.

[42]   X. Wang, X. Du, G. Yang, J. Xue, Y. Chen, L. Zhang, Chemisorption of NO_2 on V-Based SCR Catalysts: A Fundamental Study toward the Mechanism of "Fast SCR" Reaction, J. Phys. Chem C. 123 (2019) 20451–20458. https://doi.org/10.1021/acs.jpcc.9b06910.

[43]   U. Asghar, S. Rafiq, A. Anwar, T. Iqbal, A. Ahmed, F. Jamil, M.S. Khurram, M.M. Akbar, A. Farooq, N.S. Shah, Y.K. Park, Review on the progress in emission control technologies for the abatement of CO_2, SO_x and NO_x from fuel combustion, J. Environ. Chem. Eng. 9 (2021) 106064. https://doi.org/10.1016/j.jece.2021.106064.

[44]   F. Rezaei, A.A. Rownaghi, S. Monjezi, R.P. Lively, C.W. Jones, SO_x/NO_x Removal from Flue Gas Streams by Solid Adsorbents: A Review of Current Challenges and Future Directions,   Energy   Fuels.   29   (2015)   5467–5486. https://doi.org/10.1021/acs.energyfuels.5b01286.

[45]   E. Zwolińska, Y. Sun, A.G. Chmielewski, A. Pawelec, S. Bułka, Removal of high concentrations of NO_x and SO_2 from diesel off-gases using a hybrid electron beam technology,   Energy   Reports.   6   (2020)   952–964. https://doi.org/10.1016/j.egyr.2020.04.008.

[46]   P. Talebizadeh, M. Babaie, R. Brown, H. Rahimzadeh, Z. Ristovski, M. Arai, The role of non-thermal plasma technique in NO_x treatment: A review, Renew. Sust. Energy Rev. 40 (2014) 886–901. https://doi.org/10.1016/j.rser.2014.07.194.

[47]   J. Shao, Q. Cheng, Y. Liu, W. Zhang, Y. Tao, K.K. Hansen, Communication—Perovskite Electrochemical System for Highly Selective NO_x Reduction of Diesel Engine Exhaust,   J.   Electrochem.   Soc.   165   (2018)   H591-H593. https://doi.org/10.1149/2.0261810jes.

[48]   L. Khezami, P. Nguyen-Tri, W.A. Saoud, A. Bouzaza, A. El Jery, D. Duc Nguyen, V.K. Gupta, A.A. Assadi, Recent progress in air treatment with combined photocatalytic/plasma processes: A   review,   J.   Environ.   Manage.   299   (2021)   113588. https://doi.org/10.1016/j.jenvman.2021.113588.

[49]   A. Eibner, Action of light on pigments I, Chem.-Ztg. 35 (1911) 753–755.

[50]   Q. Guo, C. Zhou, Z. Ma, X. Yang, Fundamentals of TiO_2 Photocatalysis: Concepts, Mechanisms,   and   Challenges,   Adv.   Mater.   31   (2019)   1901997. https://doi.org/10.1002/adma.201901997.

[51]   A. Fujishima, K. Honda, Electrochemical Photolysis of Water at a Semiconductor Electrode, Nature. 238 (1972) 37–38. https://doi.org/10.1038/238037a0.

[52]   P. Riente, T. Noël, Application of metal oxide semiconductors in light-driven organic   transformations,   Catal.   Sci.   Technol.   9   (2019)   5186–5232. https://doi.org/10.1039/C9CY01170F.

[53]   E. Giamello, G. Pacchioni, Applied vs fundamental research in heterogeneous photocatalysis: problems and perspectives. An introduction to 'physical principles of photocatalysis,'   J.   Phys.   Condens.   Matter.   32   (2020)   360301. https://doi.org/10.1088/1361-648X/ab926b.

[54]   P. Atkins, J. de Paula, J. Keeler, Atkins' Physical Chemistry, 12th Edition, Oxford University Press, Oxford, 2022.

[55]   G. Rayner-Canham, Descriptive Inorganic Chemistry, 2nd Edition, W.H. Freeman, New York, 1999.

[56]   C.E. Housecroft, A.G. Sharpe, Inorganic Chemistry, 5th Edition, Pearson, New York, 2018.

[57]   A.L. Linsebigler, G. Lu, J.T. Yates, Photocatalysis on TiO$_2$ Surfaces: Principles, Mechanisms, and Selected Results, Chem. Rev. 95 (1995) 735–758. https://doi.org/10.1021/cr00035a013.

[58]   K. Hashimoto, K. Wasada, N. Toukai, H. Kominami, Y. Kera, Photocatalytic oxidation of nitrogen monoxide over titanium(IV) oxide nanocrystals large size areas, J. Photochem. Photobiol. A Chem. 136 (2000) 103–109. https://doi.org/10.1016/S1010-6030(00)00329-4.

[59]   S. Devahasdin, C. Fan, K. Li, D.H. Chen, TiO$_2$ photocatalytic oxidation of nitric oxide: transient behavior and reaction kinetics, J. Photochem. Photobiol. A Chem. 156 (2003) 161–170. https://doi.org/10.1016/S1010-6030(03)00005-4.

[60]   M. Kaneko, I. Okura, Photocatalysis: Science and Technology, Springer Berlin Heidelberg, 2002.

[61]   H. Wang, Y. Sun, G. Jiang, Y. Zhang, H. Huang, Z. Wu, S.C. Lee, F. Dong, Unraveling the Mechanisms of Visible Light Photocatalytic NO Purification on Earth-Abundant Insulator-Based Core–Shell Heterojunctions, Environ. Sci. Technol. 52 (2018) 1479–1487. https://doi.org/10.1021/acs.est.7b05457.

[62]   N. Baliarsingh, L. Mohapatra, K. Parida, Design and development of a visible light harvesting Ni-Zn/Cr-CO$_3^{2-}$ LDH system for hydrogen evolution, J. Mater. Chem. A. 1 (2013) 4236–4243. https://doi.org/10.1039/c2ta00933a.

[63]   R.J. Lewis, Sax's Dangerous Properties of Industrial Materials, 5 Volume Set, 12th Edition, Twelth, Wiley & Sons, New Jersey, 2012.

[64]   Z. Hu, K. Li, X. Wu, N. Wang, X. Li, Q. Li, L. Li, K. Lv, Dramatic promotion of visible-light photoreactivity of TiO$_2$ hollow microspheres towards NO oxidation by introduction of oxygen vacancy, Appl. Catal. B. 256 (2019) 117860. https://doi.org/10.1016/j.apcatb.2019.117860.

[65]   X. Shen, G. Dong, L. Wang, L. Ye, J. Sun, Enhancing Photocatalytic Activity of NO Removal through an In Situ Control of Oxygen Vacancies in Growth of TiO$_2$, Adv. Mater. Interfaces. 6 (2019) 1901032. https://doi.org/10.1002/admi.201901032.

[66]   Z. Wang, X. Lang, Visible light photocatalysis of dye-sensitized TiO$_2$: The selective aerobic oxidation of amines to imines, Appl. Catal. B. 224 (2018) 404–409. https://doi.org/10.1016/j.apcatb.2017.10.002.

[67]   X. Lang, J. Zhao, X. Chen, Visible-Light-Induced Photoredox Catalysis of Dye-Sensitized Titanium Dioxide: Selective Aerobic Oxidation of Organic Sulfides, Angew. Chem. Int. Ed. 55 (2016) 4697–4700. https://doi.org/10.1002/anie.201600405.

[68]   C.J. Dahlman, A. Agrawal, C.M. Staller, J. Adair, D.J. Milliron, Anisotropic Origins of Localized Surface Plasmon Resonance in n-Type Anatase TiO$_2$ Nanocrystals, Chem. Mater. 31 (2019) 502–511. https://doi.org/10.1021/acs.chemmater.8b04519.

[69]   Y. Gao, W. Nie, Q. Zhu, X. Wang, S. Wang, F. Fan, C. Li, The Polarization Effect in Surface-Plasmon-Induced Photocatalysis on Au/TiO$_2$ Nanoparticles, Angew. Chem. Int. Ed. 59 (2020) 18218–18223. https://doi.org/10.1002/anie.202007706.

[70]   S. George, S. Pokhrel, Z. Ji, B.L. Henderson, T. Xia, L. Li, J.I. Zink, A.E. Nel, L. Mädler, Role of Fe Doping in Tuning the Band Gap of TiO$_2$ for the Photo-Oxidation-Induced Cytotoxicity Paradigm, J. Am. Chem. Soc. 133 (2011) 11270–11278. https://doi.org/10.1021/ja202836s.

[71]   A. Biswas, A. Chakraborty, N.R. Jana, Nitrogen and Fluorine Codoped, Colloidal TiO$_2$ Nanoparticle: Tunable Doping, Large Red-Shifted Band Edge, Visible Light Induced Photocatalysis, and Cell Death, ACS Appl. Mater. Interfaces. 10 (2018) 1976–1986. https://doi.org/10.1021/acsami.7b14025.

[72]   T. Giannakopoulou, I. Papailias, N. Todorova, N. Boukos, Y. Liu, J. Yu, C. Trapalis, Tailoring the energy band gap and edges' potentials of g-C$_3$N$_4$/TiO$_2$ composite photocatalysts for NO$_x$ removal, Chem. Eng. J. 310 (2017) 571–580. https://doi.org/10.1016/j.cej.2015.12.102.

[73]   Y. Yang, Y. Li, J. Wang, J. Wu, D. He, Q. An, Graphene-TiO$_2$ mesoporous spheres assembled by anatase and rutile nanowires for efficient NO photooxidation, J. Alloys Compd. 699 (2017) 47–56. https://doi.org/10.1016/j.jallcom.2016.12.204.

[74]   E. Luévano-Hipólito, A. Martínez-de la Cruz, E. López-Cuellar, Q.L. Yu, H.J.H. Brouwers, Synthesis, characterization and photocatalytic activity of WO$_3$/TiO$_2$ for NO removal under UV and visible light irradiation, Mater. Chem. Phys. 148 (2014) 208–213. https://doi.org/10.1016/j.matchemphys.2014.07.034.

[75]   Z. Wu, Z. Sheng, Y. Liu, H. Wang, J. Mo, Deactivation mechanism of PtOx/TiO$_2$ photocatalyst towards the oxidation of NO in gas phase, J. Hazard. Mater. 185 (2011) 1053–1058. https://doi.org/10.1016/j.jhazmat.2010.10.013.

[76]   T.H. Huy, B.D. Phat, C.M. Thi, P. Van Viet, High photocatalytic removal of NO gas over SnO$_2$ nanoparticles under solar light, Environ. Chem. Lett. 17 (2019) 527–531. https://doi.org/10.1007/s10311-018-0801-0.

[77]   T. Long, X. Dong, X. Liu, J. Liu, S. Yin, T. Sato, Synthesis of ZnO crystals with unique morphologies by a low-temperature solvothermal process and their photocatalytic DeNOx properties, Res. Chem. Intermed. 36 (2010) 61–67. https://doi.org/10.1007/s11164-010-0114-9.

[78]   Z. Ai, S. Lee, Y. Huang, W. Ho, L. Zhang, Photocatalytic removal of NO and HCHO over nanocrystalline Zn$_2$SnO$_4$ microcubes for indoor air purification, J. Hazard. Mater. 179 (2010) 141–150. https://doi.org/10.1016/j.jhazmat.2010.02.071.

[79]   T.H. Huy, D.P. Bui, F. Kang, Y.F. Wang, S.H. Liu, C.M. Thi, S.J. You, G.M. Chang, V.V. Pham, SnO$_2$/TiO$_2$ nanotube heterojunction: The first investigation of NO degradation by visible light-driven photocatalysis, Chemosphere. 215 (2019) 323–332. https://doi.org/10.1016/j.chemosphere.2018.10.033.

[80]   Y. Li, X. Wu, W. Ho, K. Lv, Q. Li, M. Li, S.C. Lee, Graphene-induced formation of visible-light-responsive SnO$_2$-Zn$_2$SnO$_4$ Z-scheme photocatalyst with surface vacancy for the enhanced photoreactivity towards NO and acetone oxidation, Chem. Eng. J. 336 (2018) 200–210. https://doi.org/10.1016/j.cej.2017.11.045.

[81]   A. Pastor, J. Balbuena, M. Cruz-Yusta, I. Pavlovic, L. Sánchez, ZnO on rice husk: A sustainable photocatalyst for urban air purification, Chem. Eng. J. 368 (2019) 659–667. https://doi.org/10.1016/j.cej.2019.03.012.

[82]   D.P. Bui, M.T. Nguyen, H.H. Tran, S.J. You, Y.F. Wang, P. Van Viet, Green synthesis of Ag@SnO_2 nanocomposites for enhancing photocatalysis of nitrogen monoxide removal under solar light irradiation, Catal. Commun. 136 (2020) 105902. https://doi.org/10.1016/j.catcom.2019.105902.

[83]   N. Todorova, T. Giannakopoulou, K. Pomoni, J. Yu, T. Vaimakis, C. Trapalis, Photocatalytic NO_x oxidation over modified ZnO/TiO_2 thin films, Catal. Today. 252 (2015) 41–46. https://doi.org/10.1016/j.cattod.2014.11.008.

[84]   R. Sugrañez, J. Balbuena, M. Cruz-Yusta, F. Martín, J. Morales, L. Sánchez, Efficient behaviour of hematite towards the photocatalytic degradation of NO_x gases, Appl. Catal. B. 165 (2015) 529–536. https://doi.org/10.1016/j.apcatb.2014.10.025.

[85]   Y. Huang, Y. Liang, Y. Rao, D. Zhu, J. Cao, Z. Shen, W. Ho, S.C. Lee, Environment-Friendly Carbon Quantum Dots/$ZnFe_2O_4$ Photocatalysts: Characterization, Biocompatibility, and Mechanisms for NO Removal, Environ. Sci. Technol. 51 (2017) 2924–2933. https://doi.org/10.1021/acs.est.6b04460.

[86]   Y. Huang, Y. Gao, Q. Zhang, J. Cao, R. Huang, W. Ho, S.C. Lee, Hierarchical porous $ZnWO_4$ microspheres synthesized by ultrasonic spray pyrolysis: Characterization, mechanistic and photocatalytic NO_x removal studies, Appl. Catal. A Gen. 515 (2016) 170–178. https://doi.org/10.1016/j.apcata.2016.02.007.

[87]   Z. Ai, S. Lee, Morphology-dependent photocatalytic removal of NO by hierarchical $BiVO_4$ microboats and microspheres under visible light, Appl. Surf. Sci. 280 (2013) 354–359. https://doi.org/10.1016/j.apsusc.2013.04.160.

[88]   J. Hu, D. Chen, N. Li, Q. Xu, H. Li, J. He, J. Lu, Fabrication of graphitic-C_3N_4 quantum dots/graphene-$InVO_4$ aerogel hybrids with enhanced photocatalytic NO removal under visible-light irradiation, Appl. Catal. B. 236 (2018) 45–52. https://doi.org/10.1016/j.apcatb.2018.04.080.

[89]   N. Li, C. Wang, K. Zhang, H. Lv, M. Yuan, D.W. Bahnemann, Progress and prospects of photocatalytic conversion of low-concentration NO_x, Chinese J. Catal. 43 (2022) 2363–2387. https://doi.org/10.1016/S1872-2067(22)64139-1.

[90]   F. Dong, Z. Zhao, Y. Sun, Y. Zhang, S. Yan, Z. Wu, An Advanced Semimetal–Organic Bi Spheres–g-C_3N_4 Nanohybrid with SPR-Enhanced Visible-Light Photocatalytic Performance for NO Purification, Environ. Sci. Technol. 49 (2015) 12432–12440. https://doi.org/10.1021/acs.est.5b03758.

[91]   L. Xiong, P. Yao, S. Liu, S. Li, J. Deng, Y. Jiao, Y. Chen, J. Wang, Soot oxidation over CeO_2-ZrO_2 based catalysts: The influence of external surface and low-temperature reducibility, Mol. Catal. 467 (2019) 16–23. https://doi.org/10.1016/j.mcat.2019.01.022.

[92]   A. Nikokavoura, C. Trapalis, Graphene and g-C_3N_4 based photocatalysts for NO_x removal: A review, Appl. Surf. Sci. 430 (2018) 18–52. https://doi.org/10.1016/j.apsusc.2017.08.192.

[93]   V. Rives, Layered double hydroxides: Present and Future, Nova Science Publishers, New York, 2001.

[94]   F. Cavani, F. Trifirò, A. Vaccari, Hydrotalcite-type anionic clays: Preparation, properties and applications., Catal. Today. 11 (1991) 173–301. https://doi.org/10.1016/0920-5861(91)80068-K.

[95]   W. Feitknecht, M. Gerber, Zur Kenntnis der Doppelhydroxyde und basischen Doppelsalze III. Über Magnesium-Aluminiumdoppelhydroxyd, Helv. Chim. Acta. 25 (1942) 131–137. https://doi.org/10.1002/hlca.19420250115.

[96]   W. Feitknecht, Über die Bildung von Doppelhydroxyden zwischen zwei- und dreiwertigen Metallen, Helv. Chim. Acta. 25 (1942) 555–569. https://doi.org/10.1002/hlca.19420250314.

[97]   R. Allmann, The crystal structure of pyroaurite, Acta Cryst. 24 (1968) 972–977. https://doi.org/10.1107/S0567740868003511.

[98]   L. Ingram, H.F.W. Taylor, The crystal structures of sjögrenite and pyroaurite, Mineral. Mag. 36 (1967) 465–479. https://doi.org/10.1180/minmag.1967.036.280.01.

[99]   H.F.W. Taylor, Segregation and cation-ordering in sjögrenite and pyroaurite, Mineral. Mag. 37 (1969) 338–342. https://doi.org/10.1180/minmag.1969.037.287.04.

[100]   F. Rodriguez-Rivas, A. Pastor, C. Barriga, M. Cruz-Yusta, L. Sanchez, I. Pavlovic, Zn-Al layered double hydroxides as efficient photocatalysts for NOx abatement, Chem. Eng. J. 346 (2018) 151–158. https://doi.org/10.1016/j.cej.2018.04.022.

[101]   M.P. Paranthaman, L. Li, J. Luo, T. Hoke, H. Ucar, B.A. Moyer, S. Harrison, Recovery of Lithium from Geothermal Brine with Lithium–Aluminum Layered Double Hydroxide Chloride Sorbents, Environ. Sci. Technol. 51 (2017) 13481–13486. https://doi.org/10.1021/acs.est.7b03464.

[102]   D. Tichit, N. Das, B. Coq, R. Durand, Preparation of Zr-Containing Layered Double Hydroxides and Characterization of the Acido-Basic Properties of Their Mixed Oxides, Chem. Mater. 14 (2002) 1530–1538. https://doi.org/10.1021/cm011125l.

[103]   E.M. Seftel, E. Popovici, M. Mertens, E.A. Stefaniak, R. Van Grieken, P. Cool, E.F. Vansant, Sn[IV]-containing layered double hydroxides as precursors for nano-sized ZnO/SnO$_2$ photocatalysts, Appl. Catal. B. 84 (2008) 699–705. https://doi.org/10.1016/j.apcatb.2008.06.006.

[104]   J. Zhong, S. Lin, J. Yu, Li^{+} adsorption performance and mechanism using lithium/aluminum layered double hydroxides in low grade brines, Desalination. 505 (2021) 114983. https://doi.org/10.1016/j.desal.2021.114983.

[105]   V.R.L. Constantino, T.J. Pinnavaia, Basic Properties of $Mg^{2+}_{1-x}Al^{3+}_{x}$ Layered Double Hydroxides Intercalated by Carbonate, Hydroxide, Chloride, and Sulfate Anions, Inorg. Chem. 34 (1995) 883–892. https://doi.org/10.1021/ic00108a020.

[106]   S. P. Newman, W. Jones, Synthesis, characterization and applications of layered double hydroxides containing organic guests, New J. Chem. 22 (1998) 105–115. https://doi.org/10.1039/A708319J.

[107]   M.S. San Román, M.J. Holgado, C. Jaubertie, V. Rives, Synthesis, characterisation and delamination behaviour of lactate-intercalated Mg,Al-hydrotalcite-like compounds, Solid State Sci. 10 (2008) 1333–1341. https://doi.org/10.1016/j.solidstatesciences.2008.01.026.

[108]   S. Bhattacharjee, J.A. Anderson, Comparison of the epoxidation of cyclohexene, dicyclopentadiene and 1,5-cyclooctadiene over LDH hosted Fe and Mn sulfonato-salen complexes, J. Mol. Catal A Chem. 249 (2006) 103–110. https://doi.org/10.1016/j.molcata.2005.12.042.

[109]   M. del Arco, S. Gutiérrez, C. Martín, V. Rives, Intercalation of $[Cr(C_2O_4)_3]^{3-}$ Complex in Mg,Al Layered Double Hydroxides, Inorg. Chem. 42 (2003) 4232–4240. https://doi.org/10.1021/ic034034u.

[110]   D. Carriazo, C. Domingo, C. Martín, V. Rives, Structural and Texture Evolution with Temperature of Layered Double Hydroxides Intercalated with Paramolybdate Anions, Inorg. Chem. 45 (2006) 1243–1251. https://doi.org/10.1021/ic0508674.

[111]   D. Carriazo, C. Martín, V. Rives, Thermal Evolution of a MgAl Hydrotalcite-Like Material Intercalated with Hexaniobate, Eur. J. Inorg. Chem. 22 (2006) 4608–4615. https://doi.org/10.1002/ejic.200600580.

[112]   M. del Arco, D. Carriazo, S. Gutiérrez, C. Martín, V. Rives, Synthesis and Characterization of New Mg_2Al-Paratungstate Layered Double Hydroxides, Inorg. Chem. 43 (2004) 375–384. https://doi.org/10.1021/ic0347790.

[113]   J.H. Choy, S.Y. Kwak, J.S. Park, Y.J. Jeong, Cellular uptake behavior of $[\gamma\text{-}^{32}P]$ labeled ATP–LDH nanohybrids, J. Mater. Chem. 11 (2001) 1671–1674. https://doi.org/10.1039/B008680K.

[114]   L. Desigaux, M. B. Belkacem, P. Richard, J. Cellier, P. Léone, L. Cario, F. Leroux, C. Taviot-Guého, B. Pitard, Self-Assembly and Characterization of Layered Double Hydroxide/DNA Hybrids, Nano Lett. 6 (2006) 199–204. https://doi.org/10.1021/nl052020a.

[115]   H. Yan, X.J. Zhao, Y.Q. Zhu, M. Wei, D. G. Evans, X. Duan, The Periodic Table as a Guide to the Construction and Properties of Layered Double Hydroxides, in: D.M.P. Mingos (Ed.), The Periodic Table II: Catalytic, Materials, Biological and Medical Applications, Springer International Publishing, Cham, 2019, pp. 89–120. ISBN: 978-3-030-40010-1, https://doi.org/10.1007/430_2019_47.

[116]   M. Sajid, C. Basheer, Layered double hydroxides: Emerging sorbent materials for analytical extractions, TrAC Trend. Anal. Chem. 75 (2016) 174–182. https://doi.org/10.1016/j.trac.2015.06.010.

[117]   S. Miyata, Anion-Exchange Properties of Hydrotalcite-Like Compounds, Clays Clay Miner. 31 (1983) 305–311. https://doi.org/10.1346/CCMN.1983.0310409.

[118]   T. Yamaoka, M. Abe, M. Tsuji, Synthesis of Cu-Al hydrotalcite like compound and its ion exchange property, Mater. Res. Bull. 24 (1989) 1183–1199. https://doi.org/10.1016/0025-5408(89)90193-1.

[119]   J. Rocha, M. del Arco, V. Rives, M. A. Ulibarri, Reconstruction of layered double hydroxides from calcined precursors: a powder XRD and ^{27}Al MAS NMR study, J. Mater. Chem. 9 (1999) 2499–2503. https://doi.org/10.1039/A903231B.

[120]   G. Mishra, B. Dash, S. Pandey, Layered double hydroxides: A brief review from fundamentals to application as evolving biomaterials, Appl. Clay Sci. 153 (2018) 172–186. https://doi.org/10.1016/j.clay.2017.12.021.

[121]   V. Rives, Comment on "Direct Observation of a Metastable Solid Phase of Mg/Al/CO$_3$-Layered Double Hydroxide by Means of High-Temperature in Situ Powder XRD and DTA/TG"1, Inorg. Chem. 38 (1999) 406–407. https://doi.org/10.1021/ic980739y.

[122]   P. Bobde, R.K. Patel, D. Panchal, A. Sharma, A.K. Sharma, R.S. Dhodapkar, S. Pal, Utilization of layered double hydroxides (LDHs) and their derivatives as photocatalysts for degradation of organic pollutants, Environ. Sci. Pollut. Res. 28 (2021) 59551–59569. https://doi.org/10.1007/s11356-021-16296-x.

[123]   F.L. Theiss, G.A. Ayoko, R.L. Frost, Synthesis of layered double hydroxides containing Mg^{2+}, Zn^{2+}, Ca^{2+} and Al^{3+} layer cations by co-precipitation methods—A review, Appl. Surf. Sci. 383 (2016) 200–213. https://doi.org/10.1016/j.apsusc.2016.04.150.

[124]   J. He, M. Wei, B. Li, Y. Kang, D.G. Evans, X. Duan, Preparation of Layered Double Hydroxides, in: X. Duan, D.G. Evans (Eds.), Layered Double Hydroxides, Springer Berlin Heidelberg, Berlin, Heidelberg, 2006, pp. 89–119. ISBN: 978-3-540-28279-2 ,https://doi.org/10.1007/430_006.

[125]   M.A. Ahmed, A.A. brick, A.A. Mohamed, An efficient adsorption of indigo carmine dye from aqueous solution on mesoporous Mg/Fe layered double hydroxide nanoparticles prepared by controlled sol-gel route, Chemosphere. 174 (2017) 280–288. https://doi.org/10.1016/j.chemosphere.2017.01.147.

[126]   A. Mignani, B. Ballarin, M. Giorgetti, E. Scavetta, D. Tonelli, E. Boanini, V. Prevot, C. Mousty, A. Iadecola, Heterostructure of Au Nanoparticles—NiAl Layered Double Hydroxide: Electrosynthesis, Characterization, and Electrocatalytic Properties, J. Phys. Chem. C. 117 (2013) 16221–16230. https://doi.org/10.1021/jp4033782.

[127]   P. Gholami, L. Dinpazhoh, A. Khataee, A. Hassani, A. Bhatnagar, Facile hydrothermal synthesis of novel Fe-Cu layered double hydroxide/biochar nanocomposite with enhanced sonocatalytic activity for degradation of cefazolin sodium, J. Hazard. Mater. 381 (2020) 120742. https://doi.org/10.1016/j.jhazmat.2019.120742.

[128]   L. Luo, S. Wang, Y. Zhou, W. Yan, H. Gao, L. Luo, J. Deng, G. Du, M. Fan, W. Zhao, Microwave-assisted synthesis of hybrid supercapacitors consisting of Ni, Co-layered double hydroxide shell assembled around wood-derived activated carbon fiber core, Electrochim. Acta. 412 (2022) 140148. https://doi.org/10.1016/j.electacta.2022.140148.

[129]   Y. Chen, C. Jing, X. Zhang, D. Jiang, X. Liu, B. Dong, L. Feng, S. Li, Y. Zhang, Acid-salt treated CoAl layered double hydroxide nanosheets with enhanced adsorption capacity of methyl orange dye, J. Colloid. Interface Sci. 548 (2019) 100–109. https://doi.org/10.1016/j.jcis.2019.03.107.

[130]   S. Tang, Y. Yao, T. Chen, D. Kong, W. Shen, H.K. Lee, Recent advances in the application of layered double hydroxides in analytical chemistry: A review, Anal. Chim. Acta. 1103 (2020) 32–48. https://doi.org/10.1016/j.aca.2019.12.065.

[131]   J. Chen, Q. Sheng, Y. Wang, J. Zheng, Dispersed Nickel Nanoparticles on Flower-like Layered Nickel-Cobalt Double Hydroxides for Non-enzymic Amperometric Sensing of Glucose, Electroanalysis. 28 (2016) 979–984. https://doi.org/10.1002/elan.201500599.

[132] L. Yao, D. Wei, D. Yan, C. Hu, ZnCr Layered Double Hydroxide (LDH) Nanosheets Assisted Formation of Hierarchical Flower-Like CdZnS@LDH Microstructures with Improved Visible-Light-Driven H_2 Production, Chem. Asian J. 10 (2015) 630–636. https://doi.org/10.1002/asia.201403387.

[133] S. Tang, G.H. Chia, H.K. Lee, Magnetic core–shell iron(II,III) oxide@layered double oxide microspheres for removal of 2,5-dihydroxybenzoic acid from aqueous solutions, J. Colloid Interface Sci. 437 (2015) 316–323. https://doi.org/10.1016/j.jcis.2014.09.038.

[134] Y. Li, F. Zhou, L. Gao, G. Duan, Co_3O_4 nanosheet-built hollow spheres containing ultrafine neck-connected grains templated by PS@Co-LDH and their ppb-level gas-sensing performance, Sens. Actuators B Chem. 261 (2018) 553–565. https://doi.org/10.1016/j.snb.2018.01.162.

[135] N. Mao, C.H. Zhou, D.S. Tong, W.H. Yu, C.X. Cynthia Lin, Exfoliation of layered double hydroxide solids into functional nanosheets, Appl. Clay Sci. 144 (2017) 60–78. https://doi.org/10.1016/j.clay.2017.04.021.

[136] J. Yu, Q. Wang, D. O'Hare, L. Sun, Preparation of two dimensional layered double hydroxide nanosheets and their applications, Chem. Soc. Rev. 46 (2017) 5950–5974. https://doi.org/10.1039/C7CS00318H.

[137] K. Cermelj, K. Ruengkajorn, J.C. Buffet, D. O'Hare, Layered double hydroxide nanosheets via solvothermal delamination, J. Energy Chem. 35 (2019) 88–94. https://doi.org/10.1016/j.jechem.2018.11.008.

[138] C. Chen, M. Yang, Q. Wang, J.C. Buffet, D. O'Hare, Synthesis and characterisation of aqueous miscible organic-layered double hydroxides, J. Mater. Chem. A. 2 (2014) 15102–15110. https://doi.org/10.1039/C4TA02277G.

[139] C. Li, M. Wei, D.G. Evans, X. Duan, Layered Double Hydroxide-based Nanomaterials as Highly Efficient Catalysts and Adsorbents, Small. 10 (2014) 4469–4486. https://doi.org/10.1002/smll.201401464.

[140] G. Fan, F. Li, D.G. Evans, X. Duan, Catalytic applications of layered double hydroxides: recent advances and perspectives, Chem. Soc. Rev. 43 (2014) 7040–7066. https://doi.org/10.1039/C4CS00160E.

[141] S.B. Ötvös, I. Pálinkó, F. Fülöp, Catalytic use of layered materials for fine chemical syntheses, Catal. Sci. Technol. 9 (2019) 47–60. https://doi.org/10.1039/C8CY02156B.

[142] F. Hamerski, M.L. Corazza, LDH-catalyzed esterification of lauric acid with glycerol in solvent-free system, Appl. Catal. A Gen. 475 (2014) 242–248. https://doi.org/10.1016/j.apcata.2014.01.040.

[143] M. Zhang, J. Zhang, S. Ran, L. Qiu, W. Sun, Y. Yu, J. Chen, Z. Zhu, A robust bifunctional catalyst for rechargeable Zn-air batteries: Ultrathin NiFe-LDH nanowalls vertically anchored on soybean-derived Fe-N-C matrix, Nano Res. 14 (2021) 1175–1186. https://doi.org/10.1007/s12274-020-3168-z.

[144] S.A. Chala, M.C. Tsai, W.N. Su, K.B. Ibrahim, A.D. Duma, M.H. Yeh, C.Y. Wen, C.H. Yu, T.S. Chan, H. Dai, B.J. Hwang, Site Activity and Population Engineering of NiRu-Layered Double Hydroxide Nanosheets Decorated with Silver Nanoparticles for Oxygen Evolution

and Reduction Reactions, ACS Catal. 9 (2019) 117–129. https://doi.org/10.1021/acscatal.8b03092.

[145]   R. Gao, D. Yan, Fast formation of single-unit-cell-thick and defect-rich layered double hydroxide nanosheets with highly enhanced oxygen evolution reaction for water splitting, Nano Res. 11 (2018) 1883–1894. https://doi.org/10.1007/s12274-017-1806-x.

[146]   Z. Zhao, Q. Shao, J. Xue, B. Huang, Z. Niu, H. Gu, X. Huang, J. Lang, Multiple structural defects in ultrathin NiFe-LDH nanosheets synergistically and remarkably boost water oxidation reaction, Nano Res. 15 (2022) 310–316. https://doi.org/10.1007/s12274-021-3475-z.

[147]   M. Arif, G. Yasin, L. Luo, W. Ye, M.A. Mushtaq, X. Fang, X. Xiang, S. Ji, D. Yan, Hierarchical hollow nanotubes of NiFeV-layered double hydroxides@CoVP heterostructures towards efficient, pH-universal electrocatalytical nitrogen reduction reaction to ammonia, Appl. Catal. B. 265 (2020) 118559. https://doi.org/10.1016/j.apcatb.2019.118559.

[148]   L. Wang, Z. Zhu, F. Wang, Y. Qi, W. Zhang, C. Wang, State-of-the-art and prospects of Zn-containing layered double hydroxides (Zn-LDH)-based materials for photocatalytic water remediation, Chemosphere. 278 (2021) 130367. https://doi.org/10.1016/j.chemosphere.2021.130367.

[149]   G. Zhang, X. Zhang, Y. Meng, G. Pan, Z. Ni, S. Xia, Layered double hydroxides-based photocatalysts and visible-light driven photodegradation of organic pollutants: A review, Chem. Eng. J. 392 (2020) 123684. https://doi.org/10.1016/j.cej.2019.123684.

[150]   H. Boumeriame, E.S. Da Silva, A.S. Cherevan, T. Chafik, J.L. Faria, D. Eder, Layered double hydroxide (LDH)-based materials: A mini-review on strategies to improve the performance for photocatalytic water splitting, J. Energy Chem. 64 (2022) 406–431. https://doi.org/10.1016/j.jechem.2021.04.050.

[151]   C. Ning, Z. Wang, S. Bai, L. Tan, H. Dong, Y. Xu, X. Hao, T. Shen, J. Zhao, P. Zhao, Z. Li, Y. Zhao, Y.F. Song, 650 nm-driven syngas evolution from photocatalytic CO_2 reduction over Co-containing ternary layered double hydroxide nanosheets, Chem. Eng. J. 412 (2021) 128362. https://doi.org/10.1016/j.cej.2020.128362.

[152]   M.P. Jerome, F.A. Alahmad, M.T. Salem, M. Tahir, Layered double hydroxide (LDH) nanomaterials with engineering aspects for photocatalytic CO_2 conversion to energy efficient fuels: Fundamentals, recent advances, and challenges, J. Environ. Chem. Eng. 10 (2022) 108151. https://doi.org/10.1016/j.jece.2022.108151.

[153]   R. Acharya, B. Naik, K.M. Parida, Adsorption of Cr (VI) and Textile Dyes on to Mesoporous Silica, Titanate Nanotubes, and Layered Double Hydroxides, in: S. ul-Islam and B.S. Butola (Eds.), Nanomaterials in the Wet Processing of Textiles, Scrivener Publishing LLC, 2018: pp. 219–260. ISBN: 9781119459842, https://doi.org/10.1002/9781119459804.ch7.

[154]   K.H. Goh, T.T. Lim, Z. Dong, Application of layered double hydroxides for removal of oxyanions: A review, Water Res. 42 (2008) 1343–1368. https://doi.org/10.1016/j.watres.2007.10.043.

[155]   F. Ogata, N. Nagai, M. Kishida, T. Nakamura, N. Kawasaki, Interaction between phosphate ions and Fe-Mg type hydrotalcite for purification of wastewater, J. Environ. Chem. Eng. 7 (2019) 102897. https://doi.org/10.1016/j.jece.2019.102897.

[156]   X. Liang, Y. Zang, Y. Xu, X. Tan, W. Hou, L. Wang, Y. Sun, Sorption of metal cations on layered double hydroxides, Colloids Surf. A Physicochem. Eng. Asp. 433 (2013) 122–131. https://doi.org/10.1016/j.colsurfa.2013.05.006.

[157]   P. Gu, S. Zhang, X. Li, X. Wang, T. Wen, R. Jehan, A. Alsaedi, T. Hayat, X. Wang, Recent advances in layered double hydroxide-based nanomaterials for the removal of radionuclides from aqueous solution, Environ. Pollut. 240 (2018) 493–505. https://doi.org/10.1016/j.envpol.2018.04.136.

[158]   P. Li, P. Chen, Z. Liu, S. Nie, X. Wang, G. Wang, W. Zhang, H. Chen, L. Wang, Highly efficient elimination of uranium from wastewater with facilely synthesized Mg-Fe layered double hydroxides: Optimum preparation conditions and adsorption kinetics, Ann. Nucl. Energy. 140 (2020) 107140. https://doi.org/10.1016/j.anucene.2019.107140.

[159]   Z. Yang, F. Wang, C. Zhang, G. Zeng, X. Tan, Z. Yu, Y. Zhong, H. Wang, F. Cui, Utilization of LDH-based materials as potential adsorbents and photocatalysts for the decontamination of dyes wastewater: a review, RSC Adv. 6 (2016) 79415–79436. https://doi.org/10.1039/C6RA12727D.

[160]   M. Daud, A. Hai, F. Banat, M.B. Wazir, M. Habib, G. Bharath, M.A. Al-Harthi, A review on the recent advances, challenges and future aspect of layered double hydroxides (LDH) – Containing hybrids as promising adsorbents for dyes removal, J. Mol. Liq. 288 (2019) 110989. https://doi.org/10.1016/j.molliq.2019.110989.

[161]   D. Chaara, I. Pavlovic, F. Bruna, M.A. Ulibarri, K. Draoui, C. Barriga, Removal of nitrophenol pesticides from aqueous solutions by layered double hydroxides and their calcined products, Appl. Clay Sci. 50 (2010) 292–298. https://doi.org/10.1016/j.clay.2010.08.002.

[162]   N. Hashim, S.N.M. Sharif, M.Z. Hussein, I.M. Isa, A. Kamari, A. Mohamed, N.M. Ali, S.A. Bakar, M. Mamat, Layered hydroxide anion exchanger and their applications related to pesticides: a brief review, Mater. Res. Innov. 21 (2017) 129–145. https://doi.org/10.1080/14328917.2016.1192717.

[163]   J.S. Calisto, I.S. Pacheco, L.L. Freitas, L.K. Santana, W.S. Fagundes, F.A. Amaral, S.C. Canobre, Adsorption kinetic and thermodynamic studies of the 2, 4 – dichlorophenoxyacetate (2,4-D) by the [Co–Al–Cl] layered double hydroxide, Heliyon. 5 (2019) e02553. https://doi.org/10.1016/j.heliyon.2019.e02553.

[164]   E. Li, L. Liao, G. Lv, Z. Li, C. Yang, Y. Lu, The Interactions Between Three Typical PPCPs and LDH, Front. Chem. 6 (2018). https://doi.org/10.3389/fchem.2018.00016.

[165]   V.K. Ameena Shirin, R. Sankar, A.P. Johnson, H. V Gangadharappa, K. Pramod, Advanced drug delivery applications of layered double hydroxide, J. Control. Release. 330 (2021) 398–426. https://doi.org/10.1016/j.jconrel.2020.12.041.

[166]   F. Cao, Y. Wang, Q. Ping, Z. Liao, Zn–Al–NO_3-layered double hydroxides with intercalated diclofenac for ocular delivery, Int. J. Pharm. 404 (2011) 250–256. https://doi.org/10.1016/j.ijpharm.2010.11.013.

[167]   Y. Li, L. Tang, X. Ma, X. Wang, W. Zhou, D. Bai, Synthesis and characterization of Zn-Ti layered double hydroxide intercalated with cinnamic acid for cosmetic application, J. Phys. Chem. Solids. 107 (2017) 62–67. https://doi.org/10.1016/j.jpcs.2017.02.018.

[168]   M. Darder, M. López-Blanco, P. Aranda, F. Leroux, E. Ruiz-Hitzky, Bio-Nanocomposites Based on Layered Double Hydroxides, Chem. Mater. 17 (2005) 1969–1977. https://doi.org/10.1021/cm0483240.

[169]   S.N. Ding, D. Shan, H.G. Xue, D.B. Zhu, S. Cosnier, Glucose Oxidase Immobilized in Alginate/Layered Double Hydroxides Hybrid Membrane and Its Biosensing Application, Anal. Sci. 25 (2009) 1421–1425. https://doi.org/10.2116/analsci.25.1421.

[170]   Q. Sun, K. Yao, Y. Zhang, MnO_2-directed synthesis of NiFe-LDH@FeOOH nanosheeet arrays for supercapacitor negative electrode, Chin. Chem. Lett. 31 (2020) 2343–2346. https://doi.org/10.1016/j.cclet.2020.03.069.

[171]   H. Gao, Y. Cao, Y. Chen, Z. Liu, M. Guo, S. Ding, J. Tu, J. Qi, Ultrathin NiFe-layered double hydroxide decorated $NiCo_2O_4$ arrays with enhanced performance for supercapacitors, Appl. Surf. Sci. 465 (2019) 929–936. https://doi.org/10.1016/j.apsusc.2018.09.180.

[172]   E. Shangguan, H. Zhang, C. Wu, X. Cai, Z. Wang, M. Wang, L. Li, G. Wang, Q. Li, J. Li, CoAl-layered double hydroxide nanosheets-coated spherical nickel hydroxide cathode materials with enhanced high-rate and cycling performance for alkaline nickel-based secondary batteries, Electrochim. Acta. 330 (2020) 135198. https://doi.org/10.1016/j.electacta.2019.135198.

[173]   J. He, W. Zhou, D. Zhu, J. Li, Z. Liu, Y. Chen, Ultrafast $Co_{0.8}Al_{0.2}$-Layered Double-Hydroxide Nanosheets Cathode for High-Performance Co–Zn Battery, ACS Sustain. Chem. Eng. 8 (2020) 14877–14885. https://doi.org/10.1021/acssuschemeng.0c04530.

[174]   L. Mohapatra, K. Parida, A review on the recent progress, challenges and perspective of layered double hydroxides as promising photocatalysts, J. Mater. Chem. A. 4 (2016) 10744–10766. https://doi.org/10.1039/C6TA01668E.

[175]   S.F. Ng, M.Y.L. Lau, W.J. Ong, Engineering Layered Double Hydroxide–Based Photocatalysts Toward Artificial Photosynthesis: State-of-the-Art Progress and Prospects, Solar RRL. 5 (2021) 2000535. https://doi.org/10.1002/solr.202000535.

[176]   G. Hu, D. O'Hare, Unique Layered Double Hydroxide Morphologies Using Reverse Microemulsion Synthesis, J. Am. Chem. Soc. 127 (2005) 17808–17813. https://doi.org/10.1021/ja0549392.

[177]   A.I. Khan, D. O'Hare, Intercalation chemistry of layered double hydroxides: recent developments and applications, J. Mater. Chem. 12 (2002) 3191–3198. https://doi.org/10.1039/B204076J.

[178]   Z. Wang, P. Fang, P. Kumar, W. Wang, B. Liu, J. Li, Controlled Growth of LDH Films with Enhanced Photocatalytic Activity in a Mixed Wastewater Treatment, Nanomater. 9 (2019). https://doi.org/10.3390/nano9060807.

[179]   X.D. Wang, C.J. Summers, Z.L. Wang, Mesoporous Single-Crystal ZnO Nanowires Epitaxially Sheathed with Zn_2SiO_4, Adv. Mater. 16 (2004) 1215–1218. https://doi.org/10.1002/adma.200306505.

[180]   M.R. Hoffmann, S.T. Martin, W. Choi, D.W. Bahnemannt, Environmental Applications of Semiconductor Photocatalysis, Chem. Rev. 95 (1995) 69–96.

[181]   L.G. Devi, R. Kavitha, A review on non metal ion doped titania for the photocatalytic degradation of organic pollutants under UV/solar light: Role of photogenerated charge carrier dynamics in enhancing the activity, Appl. Catal. B. 140–141 (2013) 559–587. https://doi.org/10.1016/j.apcatb.2013.04.035.

[182]   G. Liu, L. Wang, H.G. Yang, H.M. Cheng, G.Q. Lu, Titania-based photocatalysts—crystal growth, doping and heterostructuring, J. Mater. Chem. 20 (2010) 831–843. https://doi.org/10.1039/B909930A.

[183]   Y. Cui, J. Ma, M. Wu, J. Wu, J. Zhang, Y. Xu, Q. Liu, G. Qian, Facet-dependent topo-heterostructure formed by BiOCl and ZnCr-LDH and its enhanced visible-light photocatalytic activity, Sep. Purif. Technol. 254 (2021) 117635. https://doi.org/10.1016/j.seppur.2020.117635.

[184]   C. Gomes Silva, Y. Bouizi, V. Fornés, H. Garcia, Layered Double Hydroxides as Highly Efficient Photocatalysts for Visible Light Oxygen Generation from Water, J. Am. Chem. Soc. 131 (2009) 13833–13839. https://doi.org/10.1021/ja905467v.

[185]   L. Mohapatra, K.M. Parida, Zn–Cr layered double hydroxide: Visible light responsive photocatalyst for photocatalytic degradation of organic pollutants, Sep. Purif. Technol. 91 (2012) 73–80. https://doi.org/10.1016/j.seppur.2011.10.028.

[186]   K.M. Parida, L. Mohapatra, Carbonate intercalated Zn/Fe layered double hydroxide: A novel photocatalyst for the enhanced photo degradation of azo dyes, Chem. Eng. J. 179 (2012) 131–139. https://doi.org/10.1016/j.cej.2011.10.070.

[187]   L. Mohapatra, K. Parida, M. Satpathy, Molybdate/Tungstate Intercalated Oxo-Bridged Zn/Y LDH for Solar Light Induced Photodegradation of Organic Pollutants, J. Phys. Chem. C. 116 (2012) 13063–13070. https://doi.org/10.1021/jp300066g.

[188]   C. Ning, S. Bai, J. Wang, Z. Li, Z. Han, Y. Zhao, D. O'Hare, Y.F. Song, Review of photo- and electro-catalytic multi-metallic layered double hydroxides, Coord. Chem. Rev. 480 (2023) 215008. https://doi.org/10.1016/j.ccr.2022.215008.

[189]   F. Rodriguez-Rivas, A. Pastor, G. de Miguel, M. Cruz-Yusta, I. Pavlovic, L. Sánchez, Cr^{3+} substituted Zn-Al layered double hydroxides as UV-Vis light photocatalysts for NO gas removal from the urban environment, Sci. Total Environ. 706 (2020) 136009. https://doi.org/10.1016/j.scitotenv.2019.136009.

[190]   A. Pastor, F. Rodriguez-Rivas, G. de Miguel, M. Cruz-Yusta, F. Martin, I. Pavlovic, L. Sánchez, Effects of Fe^{3+} substitution on Zn-Al layered double hydroxides for enhanced NO photochemical abatement, Chem. Eng. J. 387 (2020) 124110. https://doi.org/10.1016/j.cej.2020.124110.

[191]   S. Xia, M. Qian, X. Zhou, Y. Meng, J. Xue, Z. Ni, Theoretical and experimental investigation into the photocatalytic degradation of hexachlorobenzene by ZnCr layered double hydroxides with different anions, Mol. Catal. 435 (2017) 118–127. https://doi.org/10.1016/j.mcat.2017.03.024.

[192]   Z. Yang, C. Zhang, G. Zeng, X. Tan, H. Wang, D. Huang, K. Yang, J. Wei, C. Ma, K. Nie, Design and engineering of layered double hydroxide based catalysts for water

depollution by advanced oxidation processes: a review, J. Mater. Chem. A. 8 (2020) 4141–4173. https://doi.org/10.1039/C9TA13522G.

[193]   M. Xu, B. Bi, B. Xu, Z. Sun, L. Xu, Polyoxometalate-intercalated ZnAlFe-layered double hydroxides for adsorbing removal and photocatalytic degradation of cationic dye, Appl. Clay Sci. 157 (2018) 86–91. https://doi.org/10.1016/j.clay.2018.02.023.

[194]   Y. Guo, D. Li, C. Hu, Y. Wang, E. Wang, Y. Zhou, S. Feng, Photocatalytic degradation of aqueous organocholorine pesticide on the layered double hydroxide pillared by Paratungstate A ion, $Mg_{12}Al_6(OH)_{36}(W_7O_{24})\cdot4H_2O$, Appl. Catal. B. 30 (2001) 337–349. https://doi.org/10.1016/S0926-3373(00)00246-0.

[195]   J. Das, K.M. Parida, Heteropoly acid intercalated Zn/Al HTlc as efficient catalyst for esterification of acetic acid using n-butanol, J. Mol. Catal. A Chem. 264 (2007) 248–254. https://doi.org/10.1016/j.molcata.2006.09.033.

[196]   S. Kim, J. Fahel, P. Durand, E. André, C. Carteret, Ternary Layered Double Hydroxides (LDHs) Based on Co-, Cu-Substituted ZnAl for the Design of Efficient Photocatalysts, Eur. J. Inorg. Chem. 2017 (2017) 669–678. https://doi.org/10.1002/ejic.201601213.

[197]   N. Baliarsingh, K.M. Parida, G.C. Pradhan, Effects of Co, Ni, Cu, and Zn on Photophysical and Photocatalytic Properties of Carbonate Intercalated M^{II}/Cr LDHs for Enhanced Photodegradation of Methyl Orange, Ind. Eng. Chem. Res. 53 (2014) 3834–3841. https://doi.org/10.1021/ie403769b.

[198]   K. Parida, L. Mohapatra, Recent progress in the development of carbonate-intercalated Zn/Cr LDH as a novel photocatalyst for hydrogen evolution aimed at the utilization of solar light, Dalton Trans. 41 (2012) 1173–1178. https://doi.org/10.1039/C1DT10957J.

[199]   W. Huo, T. Cao, X. Liu, W. Xu, B. Dong, Y. Zhang, F. Dong, Anion intercalated layered-double-hydroxide structure for efficient photocatalytic NO remove, Green Energy Environ. 4 (2019) 270–277. https://doi.org/10.1016/j.gee.2018.11.001.

[200]   Y. Ao, D. Wang, P. Wang, C. Wang, J. Hou, J. Qian, A BiOBr/Co–Ni layered double hydroxide nanocomposite with excellent adsorption and photocatalytic properties, RSC Adv. 5 (2015) 54613–54621. https://doi.org/10.1039/C5RA05473G.

[201]   Q. Liu, J. Ma, K. Wang, T. Feng, M. Peng, Z. Yao, C. Fan, S. Komarneni, BiOCl and TiO_2 deposited on exfoliated ZnCr-LDH to enhance visible-light photocatalytic decolorization of Rhodamine B, Ceram. Int. 43 (2017) 5751–5758. https://doi.org/10.1016/j.ceramint.2017.01.119.

[202]   H. Li, Q. Deng, J. Liu, W. Hou, N. Du, R. Zhang, X. Tao, Synthesis, characterization and enhanced visible light photocatalytic activity of Bi_2MoO_6/Zn–Al layered double hydroxide hierarchical heterostructures, Catal. Sci. Technol. 4 (2014) 1028–1037. https://doi.org/10.1039/C3CY00940H.

[203]   S. Nayak, L. Mohapatra, K. Parida, Visible light-driven novel g-C_3N_4/NiFe-LDH composite photocatalyst with enhanced photocatalytic activity towards water oxidation and reduction reaction, J. Mater. Chem. A. 3 (2015) 18622–18635. https://doi.org/10.1039/C5TA05002B.

[204]   X. Wu, D. Zhang, F. Jiao, S. Wang, Visible-light-driven photodegradation of Methyl Orange using Cu_2O/ZnAl calcined layered double hydroxides as photocatalysts, Colloids Surf.   A   Physicochem.   Eng.   Asp.   508   (2016)   110–116. https://doi.org/10.1016/j.colsurfa.2016.08.047.

[205]   Š. Paušová, J. Krýsa, J. Jirkovský, G. Mailhot, V. Prevot, Photocatalytic behavior of nanosized TiO_2 immobilized on layered double hydroxides by delamination/restacking process, Environ. Sci. Pollut. Res. 19 (2012) 3709–3718. https://doi.org/10.1007/s11356-012-0780-9.

[206]   X. Xu, H. Chu, Z. Zhang, P. Dong, R. Baines, P.M. Ajayan, J. Shen, M. Ye, Integrated Energy Aerogel of N,S-rGO/WSe_2/NiFe-LDH for Both Energy Conversion and Storage, ACS Appl. Mater. Interfaces. 9 (2017) 32756–32766. https://doi.org/10.1021/acsami.7b09866.

[207]   Y. Zhi, Y. Li, Q. Zhang, H. Wang, ZnO Nanoparticles Immobilized on Flaky Layered Double Hydroxides as Photocatalysts with Enhanced Adsorptivity for Removal of Acid Red G, Langmuir. 26 (2010) 15546–15553. https://doi.org/10.1021/la1019313.

[208]   D. Tang, J. Liu, X. Wu, R. Liu, X. Han, Y. Han, H. Huang, Y. Liu, Z. Kang, Carbon Quantum Dot/NiFe Layered Double-Hydroxide Composite as a Highly Efficient Electrocatalyst for Water Oxidation, ACS Appl. Mater. Interfaces. 6 (2014) 7918–7925. https://doi.org/10.1021/am501256x.

[209]   B.R. Venugopal, N. Ravishankar, C.R. Perrey, C. Shivakumara, M. Rajamathi, Layered Double Hydroxide–CdSe Quantum Dot Composites through Colloidal Processing: Effect of Host Matrix–Nanoparticle Interaction on Optical Behavior, J. Phys. Chem. B. 110 (2006) 772–776. https://doi.org/10.1021/jp054774j.

[210]   M. Zhang, Q. Yao, C. Lu, Z. Li, W. Wang, Layered Double Hydroxide–Carbon Dot Composite: High-Performance Adsorbent for Removal of Anionic Organic Dye, ACS Appl. Mater. Interfaces. 6 (2014) 20225–20233. https://doi.org/10.1021/am505765e.

[211]   B. K. Babu, S. Ghosh, S. Chakrabortty, Recent developments in smart window engineering: from antibacterial activity to self-cleaning behavior, in: G.K. Dalapati, M. Sharma (Eds.), Energy Saving Coating Materials, Elsevier, 2020: pp. 227–263. https://doi.org/10.1016/B978-0-12-822103-7.00010-8.

[212]   A.L. da Silva, M. Dondi, M. Raimondo, D. Hotza, Photocatalytic ceramic tiles: Challenges and technological solutions, J. Eur. Ceram. Soc. 38 (2018) 1002–1017. https://doi.org/10.1016/j.jeurceramsoc.2017.11.039.

[213]   N.T. Padmanabhan, H. John, Titanium dioxide based self-cleaning smart surfaces: A   short   review,   J.   Environ.   Chem.   Eng.   8   (2020)   104211. https://doi.org/10.1016/j.jece.2020.104211.

[214]   M. Yoshihiko, T. Hideo, O. Hiroshi, K. Murata (2003). NO_x-Cleaning Paving Block. EP 0 786 283 B1, 20. European Patent Office. https://patentimages .storage.googleapis.com/c9/9d/f3/07ec7dba0b561f/EP0786283B1.pdf. (accessed 2 April 2023).

[215]   C. Luigi, C. Pepe (1997). Paving Tile Comprising an Hydraulic Binder and Photocatalyst Particles. EP 1 600 430 A1, 21. https://patentimages.storage .googleapis.com/a0/76/35/41ae4be6d197b0/EP1600430A1.pdf. (accessed 2 April 2023).

[216]   ISO. (2016). ISO 22197-1:2016 Fine ceramics (advanced ceramics, advanced technical ceramics) - Test method for air-purification performance of semiconducting photocatalytic materials - Part 1: Removal of Nitric oxide. https://www .iso.org/standard/65416.html.

[217]   M.M. Ballari, Q.L. Yu, H.J.H. Brouwers, Experimental study of the NO and NO_2 degradation by photocatalytically active concrete, Catal. Today. 161 (2011) 175–180. https://doi.org/10.1016/j.cattod.2010.09.028.

[218]   R. Zouzelka, J. Rathousky, Photocatalytic abatement of NOx pollutants in the air using commercial functional coating with porous morphology, Appl. Catal. B. 217 (2017) 466–476. https://doi.org/10.1016/j.apcatb.2017.06.009.

[219]   C. Águia, J. Ângelo, L.M. Madeira, A. Mendes, Photo-oxidation of NO using an exterior paint – Screening of various commercial titania in powder pressed and paint films, J.   Environ.   Manage.   92   (2011)   1724–1732. https://doi.org/10.1016/j.jenvman.2011.02.010.

[220]   J. Ângelo, L. Andrade, A. Mendes, Highly active photocatalytic paint for NO_x abatement under real-outdoor conditions, Appl. Catal. A Gen. 484 (2014) 17–25. https://doi.org/10.1016/j.apcata.2014.07.005.

[221]   D. Wang, Z. Leng, M. Hüben, M. Oeser, B. Steinauer, Photocatalytic pavements with epoxy-bonded TiO_2-containing spreading material, Constr. Build. Mater. 107 (2016) 44–51. https://doi.org/10.1016/j.conbuildmat.2015.12.164.

[222]   A. Folli, M. Strøm, T.P. Madsen, T. Henriksen, J. Lang, J. Emenius, T. Klevebrant, Å. Nilsson, Field study of air purifying paving elements containing TiO_2, Atmos. Environ. 107 (2015) 44–51. https://doi.org/10.1016/j.atmosenv.2015.02.025.

[223]   King's College London, B. Barratt, Environmental Research Group, Statistical analysis of monitoring results from the City of London's NO_x-reducing paint study. https://www.londonair.org.uk/london/reports/CoL_de-nox_paint_statistical_report.pdf, 2007 (accessed 27 March 2023).

[224]   King's College London, A. Tremper and D. Green, Artworks D-NO_x Paint Trial Report. https://www.southwark.gov.uk/assets/attach/2407/Artworks_PainTrial_Report_final.pdf , 2016 (accessed 28 March 2023).

[225]   M. Pérez-Nicolás, I. Navarro-Blasco, J.M. Fernández, J.I. Alvarez, Atmospheric NO_x removal: Study of cement mortars with iron- and vanadium-doped TiO_2 as visible light–sensitive   photocatalysts,   Constr.   Build.   Mater.   149   (2017)   257–271. https://doi.org/10.1016/j.conbuildmat.2017.05.132.

[226]   B.O. Bica, J.V.S. de Melo, Concrete blocks nano-modified with zinc oxide (ZnO) for photocatalytic paving: Performance comparison with titanium dioxide (TiO_2), Constr. Build. Mater. 252 (2020) 119120. https://doi.org/10.1016/j.conbuildmat.2020.119120.

[227]   Y. Yang, T. Ji, W. Su, B. Yang, Y. Zhang, Z. Yang, Photocatalytic NO_x abatement and self-cleaning performance of cementitious composites with g-C_3N_4 nanosheets under visible   light,   Constr.   Build.   Mater.   225   (2019)   120–131. https://doi.org/10.1016/j.conbuildmat.2019.07.189.

[228]   Y. Yang, T. Ji, W. Su, Y. Kang, Y. Wu, Y. Zhang, Enhanced washing resistance of photocatalytic exposed aggregate cementitious materials based on g-C$_3$N$_4$ nanosheets-recycled asphalt pavement aggregate composites, Constr. Build. Mater. 228 (2019) 116748. https://doi.org/10.1016/j.conbuildmat.2019.116748.

[229]   Y. Yang, T. Ji, Z. Yang, Y. Zhang, W. Su, R. Wu, Z. Wu, Efficiency and durability of g-C$_3$N$_4$-based coatings applied on mortar under peeling and washing trials, Constr. Build. Mater. 234 (2020) 117438. https://doi.org/10.1016/j.conbuildmat.2019.117438.

[230]   J.M. Montoya-Zamora, A. Martínez-de la Cruz, E. López-Cuéllar, F.A. Pérez González, BiOBr photocatalyst with high activity for NO$_x$ elimination, Adv. Powder Technol. 31 (2020) 3618–3627. https://doi.org/10.1016/j.apt.2020.07.009.

[231]   Z.M. Mir, A. Bastos, D. Höche, M.L. Zheludkevich, Recent Advances on the Application of Layered Double Hydroxides in Concrete—A Review, Materials. 13 (2020). https://doi.org/10.3390/ma13061426.

[232]   Y. Wu, P. Duan, C. Yan, Role of layered double hydroxides in setting, hydration degree, microstructure and compressive strength of cement paste, Appl. Clay Sci. 158 (2018) 123–131. https://doi.org/10.1016/j.clay.2018.03.024.

Capítulo 2
Hipótesis y
Objetivos

La contaminación atmosférica es uno de los grandes retos a los que nuestra sociedad se enfrenta actualmente. En las zonas urbanas, donde habitan más del 50 % de la población mundial, la quema de combustibles fósiles es la principal fuente de contaminación atmosférica. Entre los diferentes contaminantes atmosféricos, resulta interesante estudiar la eliminación de los óxidos de nitrógeno (NO_x) dado que estos gases, además de ser nocivos, también son precursores de otros contaminantes como el ozono troposférico o el material particulado.

A pesar de que existen múltiples métodos para eliminar los óxidos de nitrógeno (procesos DeNOx) ninguno de ellos resulta factible para su aplicación *in-situ* en el entorno urbano. En este sentido, la fotocatálisis se presenta como una tecnología de remediación medioambiental alternativa e interesante para su uso directo en las ciudades.

El dióxido de titanio, TiO_2, es el fotocatalizador más ampliamente utilizado y presenta una gran eficiencia en el proceso DeNOx. No obstante, a pesar de su alta eficiencia, existen algunas desventajas asociadas al uso de este fotocatalizador como son: un menor aprovechamiento de la radiación solar (solo es activo con luz ultravioleta), una baja selectividad hacia la oxidación completa de los gases NO_x (se libera el gas tóxico NO_2 como subproducto durante la reacción) y un coste elevado en comparación con las materias primas que constituyen los productos fotocatalíticos (vg. materiales de construcción, pinturas, etc.).

Recientemente, los hidróxidos dobles laminares (HDL) han surgido como interesantes materiales fotocatalíticos alternativos al TiO_2 para su empleo en procesos DeNOx. Sin embargo, en la bibliografía científica

apenas se encuentran algunos ejemplos de sistemas HDL estudiados en dicha aplicación. Por tanto, resulta novedoso y de gran interés su estudio.

Dada la gran versatilidad que presenta la estructura de estos materiales, los HDL pueden ser diseñados *ex profeso* para mejorar sus propiedades ópticas (mejor absorción de la radiación solar) y electrónicas (mejor disponibilidad de transportadores de carga) y con ello su actividad fotocatalítica. Por otra parte, es bien conocido que la eficiencia fotocatalítica de un material puede ser claramente mejorada mediante el diseño de adecuadas heterouniones electrónicas entre semiconductores, entre ellos los HDL.

Los materiales de construcción son los productos fotocatalíticos a implementar en las ciudades. Se conocen estudios que indican que los HDL se pueden utilizar como aditivos en materiales de construcción sin alterar sustancialmente las propiedades intrínsecas de los mismos. El estudio de materiales de construcción fotocatalíticos basados en aditivos HDL es un campo inexplorado al inicio de esta tesis doctoral.

Por todo esto, el análisis de los antecedentes presentados permite formular las siguientes **hipótesis de partida,** sobre las que se fundamenta esta tesis doctoral:

Hipótesis 1: *Se pueden preparar hidróxidos dobles laminares que, mediante el diseño adecuado de su composición y morfología, actúen como nuevos fotocatalizadores altamente eficientes: mayor interacción con las moléculas reactantes, activación bajo luz UV-Vis o sólo luz Visible, mayor eficiencia fotónica y mejorada selectividad del proceso fotocatalítico.*

Hipótesis 2: *Es posible incorporar hidróxidos dobles laminares como aditivos en materiales de construcción que, en sustitución del TiO$_2$, sirvan para la preparación de productos fotocatalíticos eficientes y de menor coste.*

Atendiendo a las hipótesis planteadas, se define como **objetivo general** de la presente tesis doctoral *"estudiar composiciones y morfologías de sistemas 2D y 3D basados en hidróxidos dobles laminares que permitan su utilización como nuevos fotocatalizadores eficientes para la eliminación fotoquímica oxidativa de gases NO$_x$"*.

Para alcanzar dicho objetivo, se han planteado una serie de **objetivos específicos**:

1) **Estudiar la influencia de la composición de la lámina metálica de hidroxilo del HDL en su actividad fotocatalítica DeNOx.**

Esta investigación se aborda en el artículo científico titulado: **"**Insight into the role of copper in the promoted photocatalytic removal of NO using Zn$_{2-x}$Cu$_x$Cr-CO$_3$ layered double hydroxide" **(Sección 3.1).**

2) **Estudiar la influencia de los aniones presentes en la interlámina del HDL en su actividad fotocatalítica DeNOx.**

Esta investigación se aborda en el artículo científico titulado: "Use of LDH-chromate adsorption co-product as an air purification photocatalyst" **(Sección 3.2).**

3) **Estudiar la preparación de heterouniones electrónicas adecuadas, basadas en el sistema HDL, para la mejora del proceso fotocatalítico DeNOx.**

Esta investigación se aborda en el artículo científico titulado: "Graphene quantum dots/NiTi layered double hydroxide heterojunction as a highly efficient De-NOx photocatalyst with long persistent post-illumination action" **(Sección 3.3).**

4) **Estudiar la actividad DeNOx de un mortero de construcción que incluye un aditivo fotocatalítico HDL.**

Este estudio se lleva a cabo en el apartado titulado: "Implementing the use of layered double hydroxides as photocatalytic additive for DeNOx building mortars: ZnCr-CO$_3$ a case of study" (**Sección 3.4).**

Chapter 2
Hypotheses and Objectives

Air pollution is one of the greatest challenges facing our society today. In urban areas, where more than 50% of the world's population lives, the burning of fossil fuels is the main source of air pollution. Among the different atmospheric pollutants, it is interesting to study the elimination of nitrogen oxides (NO_x) since these gases, apart from being harmful, are also precursors of other pollutants such as tropospheric ozone or particulate matter.

Despite the existence of multiple methods to remove nitrogen oxides (DeNOx processes), none of them are feasible for in-situ application in the urban environment. In this sense, photocatalysis is presented as an interesting alternative environmental remediation technology for direct use in cities.

Titanium dioxide, TiO_2, is the most widely used photocatalyst and it presents a high efficiency in the DeNOx process. However, despite its high efficiency, there are some disadvantages associated with the use of this photocatalyst such as: a low exploitation of solar radiation (it is only active with ultraviolet light), a low selectivity towards the complete oxidation of NO_x gases (toxic NO_2 gas is released as a by-product during the reaction) and a high cost compared to the raw materials that constitute the photocatalytic products (e.g. building materials, paints, etc.).

Recently, layered double hydroxides (LDHs) have emerged as interesting alternative photocatalytic materials to TiO_2 for use in DeNOx processes. However, in the scientific literature there are only a few examples of HDL systems studied in this application. Therefore, their study is novel and of great interest.

Due to the great versatility of the structure of these materials, LDHs can be specifically designed to improve their optical (better absorption of solar radiation) and electronic (better availability of charge carriers) properties and thus their photocatalytic activity. Moreover, it is well known that the photocatalytic efficiency of a material can be clearly improved by designing suitable electronic heterojunctions between semiconductors, including HDLs.

Building materials are the photocatalytic products to be implemented in cities. There are studies that indicate that LDHs can be used as additives in building materials without substantially altering their intrinsic properties. The study of photocatalytic building materials based on LDH additives is an unexplored field at the beginning of this doctoral thesis.

For all these reasons, the analysis of the precedents presented in the previous chapter allows us to formulate the following **starting hypotheses**, on which this doctoral thesis is based:

> **Hypothesis 1:** *It is possible to prepare layered double hydroxides that, through the appropriate design of their composition and morphology, act as new highly efficient photocatalysts: higher interaction with reactant molecules, activation under UV-Vis or Visible light only, higher photonic efficiency and improved selectivity of the photocatalytic process.*

> **Hypothesis 2:** *It is possible to incorporate layered double hydroxides as additives in building materials that, in substitution of TiO₂, serve for the preparation of efficient and lower cost photocatalytic products.*

According to the hypotheses proposed, the **general objective** of this doctoral thesis is defined as *"study of the compositions and morphologies of 2D and 3D systems based on layered double hydroxides that allow their use as new efficient photocatalysts for the oxidative photochemical removal of NO$_x$ gases"*.

In order to achieve this objective, a set of **specific objectives** have been established:

1) **To study the influence of the hydroxyl metal layer composition of LDH on its DeNOx photocatalytic activity.**

This research is addressed in the scientific paper entitled: "Insight into the role of copper in the promoted photocatalytic removal of NO using Zn$_{2-x}$Cu$_x$Cr-CO$_3$ layered double hydroxide" **(Section 3.1)**.

2) **To study the influence of the anions present in the interlayer of the LDH on its DeNOx photocatalytic activity.**

This research is discussed in the scientific paper entitled: "Use of LDH-chromate adsorption co-product as an air purification photocatalyst" **(Section 3.2)**.

3) **To study the preparation of suitable electronic heterojunctions, based on the LDH system, for the improvement of the DeNOx photocatalytic process.**

This research is reported in the scientific paper entitled: "Graphene quantum dots/NiTi layered double hydroxide heterojunction as a highly efficient De-NOx photocatalyst with long persistent post-illumination action" **(Section 3.3)**.

4) **To study the DeNOx activity of a building mortar including an LDH photocatalytic additive.**

This study is carried out in the section entitled: "Implementing the use of layered double hydroxides as photocatalytic additive for DeNOx building mortars: ZnCr-CO_3 a case of study" **(section 3.4)**.

Chapter 3
Results and Discussion

3.1. Insight into the role of copper in the promoted photocatalytic removal of NO using Zn$_{2-x}$Cu$_x$Cr-CO$_3$ layered double hydroxide
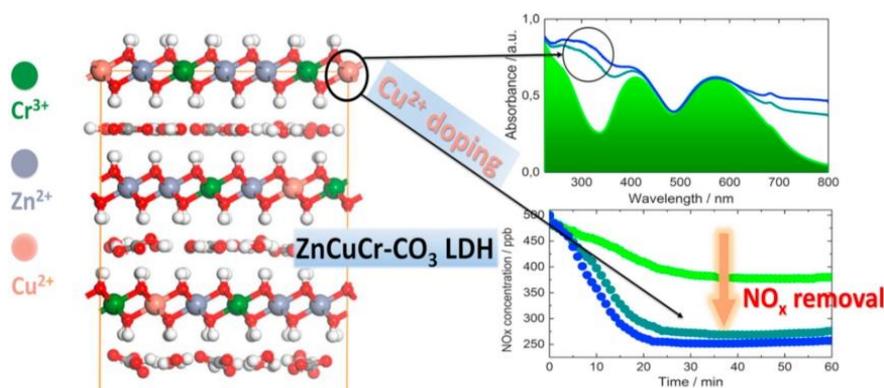
ABSTRACT

In this work the ability of Zn$_{2-x}$Cu$_x$Cr-CO$_3$ layered double hydroxides (LDHs) as highly efficient DeNOx photocatalysts was studied. LDHs with x = 0, 0.2 and 0.4 were prepared using a coprecipitation method. The samples were characterized by different techniques such as XRD, XPS, FT-IR, ICP-MS, TG, SBET, SEM and Diffuse reflectance (DR). The increased amount of copper ions in the LDH layers gave rise to slight changes in the structure and morphology and an important variation of the optical properties of the LDHs. The prepared ZnCuCr-CO$_3$ photocatalysts exhibited favourable conversion efficiency (51%) and an extraordinary selectivity (97%) for the photochemical NO abatement. The photochemical mechanism was elucidated from DOS, EPR, Femtosecond transient absorption and *in-situ* DRIFTS studies. The results suggested that the presence of Cu^{2+} ions in the LDH framework introduced new states in the valence band states, thus favouring the production and mobility of e$^-$/h$^+$ charge carriers and a greater production of •O$_2^-$ and •OH.

J. Fragoso[1], M.A. Oliva[1], L. Camacho[2], M. Cruz-Yusta[1], G. de Miguel[2], F. martín[3], A. Pastor[1], I. Pavlovic[1,*], L. Sánchez[1,*]

[1]Departamento de Química Inorgánica e Ingeniería Química, Instituto Universitario de Nanoquímica IUNAN, Universidad de Córdoba, Campus de Rabanales, E-14014, Córdoba, Spain.

[2]Departamento de Química Física y Termodinámica Aplicada, Instituto Universitario de Nanoquímica IUNAN, Universidad de Córdoba, Campus de Rabanales, E-14014, Córdoba, Spain.

[3]Departamento de Ingeniería Química, Facultad de Ciencias, Universidad de Málaga, Campus de Teatinos, E-29071, Málaga, Spain

HIGHLIGHTS

- $Zn_{2-x}Cu_xCr$ LDHs are effective UV-Vis light DeNOx photocatalysts.

- The Zn^{2+} by Cu^{2+} ion replacement increases the surface area and light absorption.

- The Cu centres create new states in the valence band.

- The production of ROS species is favoured in doped samples.

3.1.1. Introduction

NOx gases (NO_x = NO + NO_2) are one of the priority pollutants in urban environments [1,2]. There is a great interest for their remediation, since they produce highly toxic effects on human health and are related with thousands of early deaths [3,4]. From the early 2000s the use of photocatalysis has been successfully proved to remove NO_x gases (DeNOx action) by using TiO_2 based materials [5]. However, some disadvantages are associated with the use of titania. Due to its large energy band gap (3.2 eV; λ < 387 nm) it can only capture solar energy efficiently in the ultraviolet region of sunlight. Additionally, photocatalytic titania is expensive as a raw material for large-scale applications in urban infrastructures. On the other hand, titania exhibits a low DeNOx selectivity, *i.e.*, considerable emissions of NO_2 occur during the PCO process [6]. These emissions should be avoided because the NO_2 is more toxic than NO [7]. Additionally, the inhalation of TiO_2 nanoparticles has recently been proposed as a cause of cancer [8]. Therefore, there are scientific efforts on the study of new semiconductors such as modified titania [9,10] or alternative compounds [11-19], in order to find low cost, sustainable and enhanced DeNOx photocatalysts.

Layered double hydroxides (LDHs) have been proposed recently as efficient photocatalysts in environmental remediation processes [20-22]. The LDH formula is represented as $[M^{2+}_{1-x}M^{3+}_x(OH)_2]^{x+}(A^{n-}_{x/n})\cdot mH_2O$, where M^{2+} and M^{3+} are divalent and trivalent metal cations and A is the anion placed in the LDH interlayer [23]. The identity of the metals and anions, the M^{2+}/M^{3+} ratio or the co-existence of multiple metals in the same framework have an influence on their electrical properties, and therefore on the absorption of light. The MO_6 octahedron in the layer is one of the

key factors affecting the photocatalytic properties of LDHs. Through placing different metals at diverse ratios in the MO_6 octahedron, the energy band structure of the LDH is modified and should provide a better electron transfer, a lessened electron/hole recombination and improve sunlight harvesting [24,25]. These reasons support the widespread use of these compounds as photocatalysts [26-30].

Our research group has recently successfully proposed the use of LDH compounds as new low-cost DeNOx photocatalysts (*vgr.* LDH benchmark product is about 25 times cheaper than photocatalytic TiO_2), with successful results [2,31,32]. Because of the importance of the M-O octahedron connectivity in the LDH framework and its relationship with the energy band structure and charge transfer pathways, we explore for the first time in this work a ternary LDH constituted only of transition metals as DeNOx photocatalyst. For this purpose, we have based the study on the $ZnCr-CO_3$ LDH system, which has proved to be an efficient visible light photocatalyst [26,27]. The ternary system is obtained by doping with copper ion, a dopant successfully studied in ZnAl and ZnGa LDH photocatalysts [33,34]. Thus, by formulating a $Zn_{2-x}Cu_xCr-CO_3$ LDH the full range of visible light is harvested (due to the presence of both Cu^{2+} and Cr^{3+}) and the low M^{2+}/M^{3+} ratio (2:1) favors the contact between the octahedron of different metals enhancing the charge transfer pathways.

The samples will be fully characterized and the changes observed in their structural, morphological and optical properties commented on with relation to the enhanced DeNOx photocatalytic behaviour. In addition, the photochemical oxidation mechanism will be explained based on the results obtained by using EPR, femtosecond transient absorption and *in-situ* DRIFTS techniques and the estimated theoretical energy band

structure, all of them highlighting the role of Cu^{2+} ion in the promoted photo-activity.

3.1.2. Experimental

3.1.1.1. Synthesis of LDHs

ZnCr and ZnCuCr LDHs were obtained by the co-precipitation method, with M^{2+}/M^{3+} = 2 and $Cu^{2+}/(Cu^{2+}+ Zn^{2+})$= 0, 0.1 and 0.2. A 1.5 M solution of $Zn(NO_3)_2\cdot 6H_2O$, $Cu(NO_3)_2\cdot 3H_2O$ and $Cr(NO_3)_3\cdot 9H_2O$ with the appropriate metal ratio was added dropwise into 100 mL of 1M Na_2CO_3 solution under stirring at room temperature and pH = 10.0 ± 0.2. The resulting suspension was centrifuged and washed with distilled water (until there was no presence of nitrate impurities) and dried at 60 °C.

3.1.1.2. LDH characterization

X-ray diffraction (XRD) patterns of the samples were recorded by a Bruker D8 Discover diffractometer. Thermogravimetric analysis (TGA) was performed on a TGA/DSC 1 Star System Mettler Toledo equipment in oxygen atmosphere (flow: 100 mL·min^{-1}; heating rate: 5 °C·min^{-1}). Elemental chemical analyses were measured by induced coupled plasma mass spectroscopy (ICP-MS) on a PerkinElmer Nexion-X instrument. The Fourier transform infrared spectrum (FT-IR) was recorded with PerkinElmer Frontier MIR using ATR. The scanning electron microscopy (SEM) morphological images were performed on a Jeol JSM 7800F microscope. Pore microstructure and textural properties were studied by N_2 adsorption-desorption isotherms on a Micromeritics ASAP 2020 apparatus. UV-Vis spectra were measured employing a Cary 5000

spectrophotometer. XPS was carried out with a Versaprobe II equipment from PHI provided with a focused monochromatic X-ray source (Al-Kα 1486.6 eV) with scanning and imaging capabilities.

Periodic Density of Functional Theory (DFT) calculations were carried out in order to build up the ZnCr and ZnCuCr LDHs and to calculate the density of states (DOS) plots of both structures.

3.1.1.3. Evaluation of the photocatalytic activity

The photocatalytic activity was investigated by examining the removal ratio of NO at ppb levels (500 ppb) in a continuous-flow reactor illuminated using a sunlight irradiation box.

In order to know about the participation of radical and chemical species in the photocatalytic process, the corresponding electron paramagnetic resonance (EPR) spectra, Femtosecond transient absorption measurements [35] and *in-situ* diffuse reflectance infrared Fourier transform spectroscopy (DRIFTS) measurements were performed.

3.1.3. Results and Discussion

3.1.3.1. Characterization of LDH materials

The preparation of the ZnCr and ZnCuCr LDH samples was carried out following the previously reported experimental procedure [2]. Following this procedure, all LDHs precipitated as very poor crystallized samples which, in any case is typical for LDH frameworks containing Cr^{3+} ions [32], as suggested by the broad and the low intensity diffraction peaks observed in Fig. 1a. The basal spacing (d_{003}) around 7.69 Å obtained for the

$Zn_{2-x}Cu_xCr$ samples is in accordance with the presence of carbonate in the interlayer space [36].

Even though the crystallinity was poor, it was observed that the d_{003} reflection appeared slightly broader and shifted towards higher two-tetha angles in the case of the copper containing samples (Supporting Information; Fig. S1). The broadening is probably associated with a decrease in the size of the particles while the shifting of d_{003} reflections in the ZnCuCr-LDH samples could be due to the differences in the hydration state [34]. Notwithstanding, slightly lower c values (Table 1), observed for Cu-bearing LDH samples, could be related to the incompatibility of copper to fit well in a regular octahedral network of LDH (Jan-Teller effect). In ZnCuCr-LDH samples, a disordered cation distribution could take place, thus provoking stacking faults and a flattering of the brucite-like layers along the c-axis.
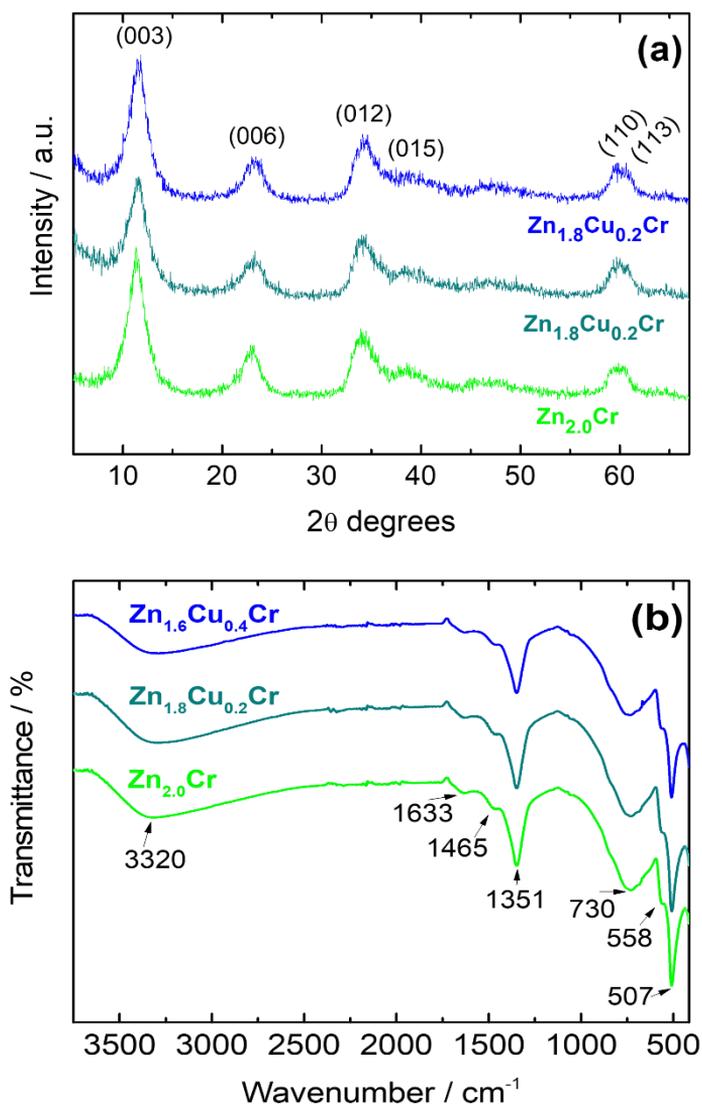
Figure 1. *(a) XRD patterns and (b) IR spectra obtained from the ZnCr-LDH and ZnCuCr-LDH samples.*

The chemical analysis (Table 1) confirmed that the M^{2+}/M^{3+} molar ratio in all the LDH samples was close to that in the starting solutions, *i.e.* $M^{2+}/M^{3+} = 2$. The corresponding thermogravimetric patterns (Fig. S2) served to calculate the amount of water molecules per formula. The

carbonate content was that assumed necessary to compensate the excess of positive charge originated by the presence of Cr^{3+} in a brucite type structure. On the other hand, XPS studies indicated the presence of Zn^{2+}, Cr^{3+} and Cu^{2+} species (Fig. S3).

Table 1. *Physicochemical characterization for the LDH samples.*

Sample	Atomic ratio		Proposed Formula	Lattice parameters	
	Cu^{2+}/M^{2+}	M^{2+}/M^{3+}		a (Å)	c (Å)
Zn_2Cr	--	2.13	$[Zn_{0.68}Cr_{0.32}(OH)_2](CO_3)_{0.16} \cdot 0.37H_2O$	3.09	23.39
$Zn_{1.8}Cu_{0.2}Cr$	0.10	2.20	$[Zn_{0.62}Cu_{0.070}Cr_{0.31}(OH)_2](CO_3)_{0.155}$ $\cdot 0.58H_2O$	3.08	23.09
$Zn_{1.6}Cu_{0.4}Cr$	0.20	2.23	$[Zn_{0.55}Cu_{0.14}Cr_{0.31}(OH)_2](CO_3)_{0.155}$ $\cdot 0.60H_2O$	3.08	22.97

Fig. 1b shows FT-IR spectra for the ZnCr and ZnCuCr LDHs. The bands observed are those expected for pure LDH phases. The presence of O−H bonds is revealed by the broad band located at 3320 cm^{-1} and the H_2O bending vibration occurs at 1633 cm^{-1}, while bands observed at 1465 and 1351 cm^{-1} (the strongest band) correspond to the split asymmetric stretching mode of carbonate interlayer anions. Moreover, and as a result of this lowering symmetry of the interlayer carbonate, the IR inactive v_1 vibration is activated, as a very weak almost imperceptible band at ~1050 cm^{-1} [23]. Concerning the basal layer, the HO−M−OH vibrational bending mode appears at 730 cm^{-1} and those for M−O at 558 and 507 cm^{-1}, which slightly shifts towards higher wavenumbers as Zn^{2+} is substituted by Cu^{2+} [34]. The clear absence of a characteristic sharp nitrate peak at around 1380 cm^{-1} [37], permit us to conclude that the samples were well washed and free of eventual nitrate impurities from the metal precursors.

As mentioned above, and in according to the synthetic procedure, all samples were collected as poor crystallized compounds, Fig. 2. The SEM images of the Zn_2Cr sample show agglomerates of unshaped nanoparticles coexisting with a honeycomb nanometric lamellar macrostructure. Although the formation of lamellar structures is characteristic of LDH compounds, this is restricted on these samples because of the acidic character Cr^{3+} [32]. In samples containing copper, this lamellar macrostructure is minor and practically evanished with an increase of the amount of copper, as in the case of the $Zn_{1.6}Cu_{0.4}Cr$ sample. Additionally, composition and microstructure were corroborated by TEM/HRTEM observations, Fig. S4.

The pore microstructure of each sample was analyzed from the corresponding N_2 adsorption-desorption isotherms, Fig. S5. The specific surface area values measured by BET method were 94, 100 and 140 $m^2 \cdot g^{-1}$ for Zn_2Cr, $Zn_{1.8}Cu_{0.2}Cr$ and $Zn_{1.6}Cu_{0.4}Cr$ samples, respectively. These increased values observed when the copper content increased in the LDH are concordant with the decrease of the crystallinity shown in XRD patterns (Fig. 1) and SEM images (Fig. 2).

The presence of Cu^{2+} in the LDH framework allows for improved harvesting of the UV-Vis light, and doped samples showed new absorption bands at 300 and 785 nm which were not observed for the Zn_2Cr sample, Fig. S6.
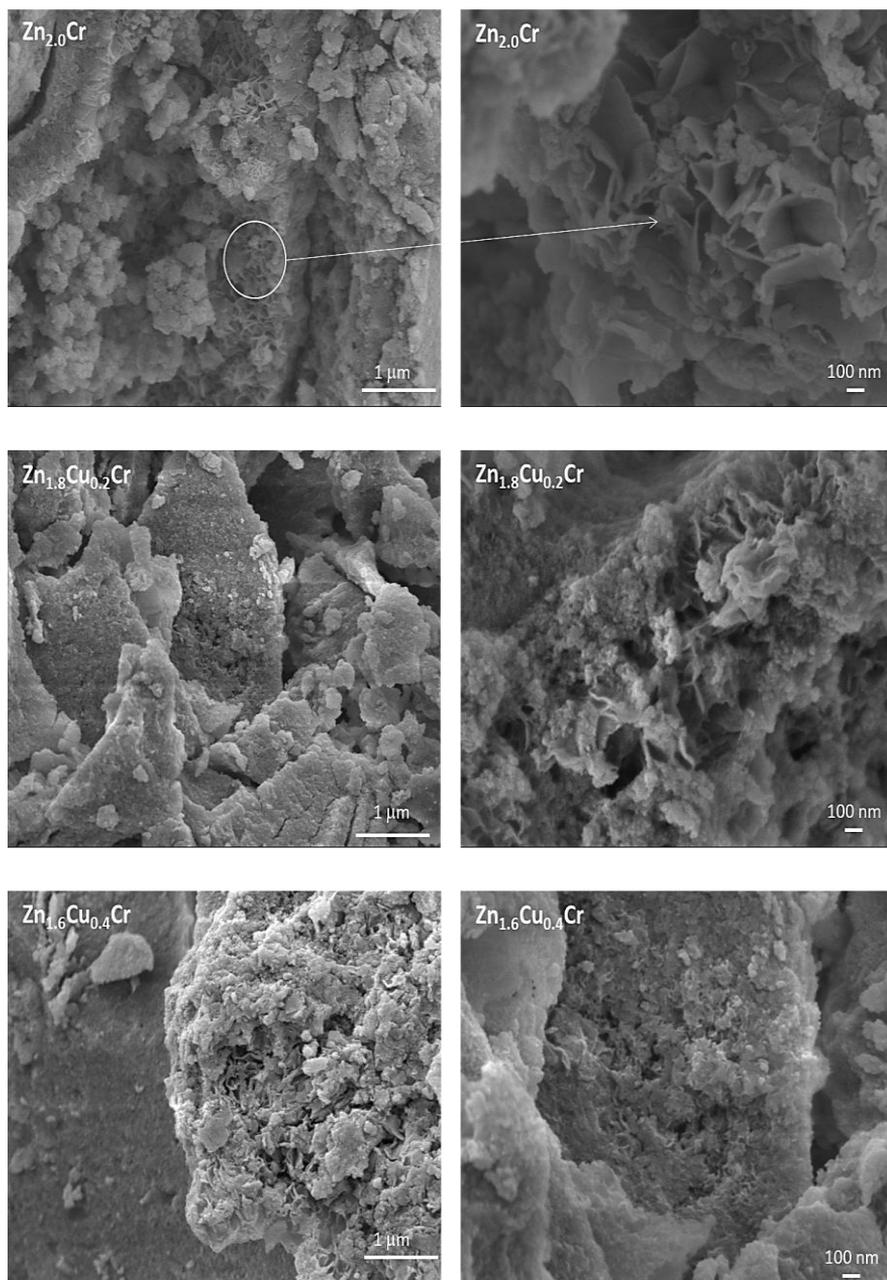
Figure 2. *SEM images of the ZnCr-LDH and ZnCuCr-LDH samples.*

3.1.3.2. Photocatalytic DeNOx tests

The photocatalytic activity of the samples studied was evaluated considering their potential to eliminate nitrogen oxides from air through a photochemical oxidation process (PCO), following the experimental procedure described in SI.

In Fig. 3a, the variation on the NO, NO_2 and NO_x concentration measured during a standard test for the Zn_2Cr photocatalyst is represented. During the first 15 minutes the NO concentration measured is nearly constant, therefore there is no substantial interaction between the inlet NO gas and the catalyst or chamber. When the light is on, a fast decay of the NO concentration is observed indicating that NO is being transformed by a light activated chemical process. In fact, once the light is off the NO concentration returns to the initial values. The following summarized sequential steps are assumed for the DeNOx test: NO → HNO_2 → NO_2 → NO_3^-.

This oxidative mechanism accounts for the presence of high reactive oxygen species (ROS). Once the LDH photocatalyst is irradiated with the appropriate light, the photon energy is briefly transferred to the electron (e^-) in the valence band (VB), which jumps to the conduction band (CB), leaving a hole (h^+) in VB. When both mobile charges reach the surface of the catalyst particles, then water and oxygen adsorbed molecules suffer redox reactions producing •OH and •O_2^- radicals (ROS species), which initiate and participate in the oxidation of nitrogen oxide gases [6].

In the case of the sequential reaction being completely selective, all the NO would be oxidized to nitrate. However, the production of intermediates like NO_2 gas are frequently detected [11]. This intermediate

must be avoided because it is highly more toxic compared to NO_2 [38]. In the case of our samples, serving as a representative of the concentration profiles of Fig. 3a, the release of NO_2 is negligible and reduced to a few ppb (3-5 ppb). Therefore, the DeNOx selectivity exhibited by these LDHs is outstanding with values > 97 %. It is worth mentioning that such high selectivity values are difficult to attain only being reported for some DeNOx advanced photocatalysts [9,15,31,39-41].

Finally, the whole removal of nitrogen gases from the air is considered following the NO_x concentration profile (Fig. 3a), taking into account the sum of NO and NO_2 concentrations. When this NO_x profile is compared from the three samples (Fig. 3b), it is observed that the slope of the initial concentration decay is higher as the copper content increases in the LDH sample, indicating that the photocatalytic activity is favoured in the copper-based systems. In fact, the initial rate constants for NO_x degradation are higher in these samples (Fig. S7).

Once the steady state is reached after the first 20 minutes of sunlight irradiation, the efficiency in the NO_x removal is also higher for samples containing copper, the values being estimated at 27 %, 45 % and 51 % for Zn_2Cr, $Zn_{1.8}Cu_{0.2}Cr$ and $Zn_{1.6}Cu_{0.4}Cr$ samples, respectively. There is a clear correlation between the increase in the DeNOx efficiency and the amount of Cu in the LDH formulation.
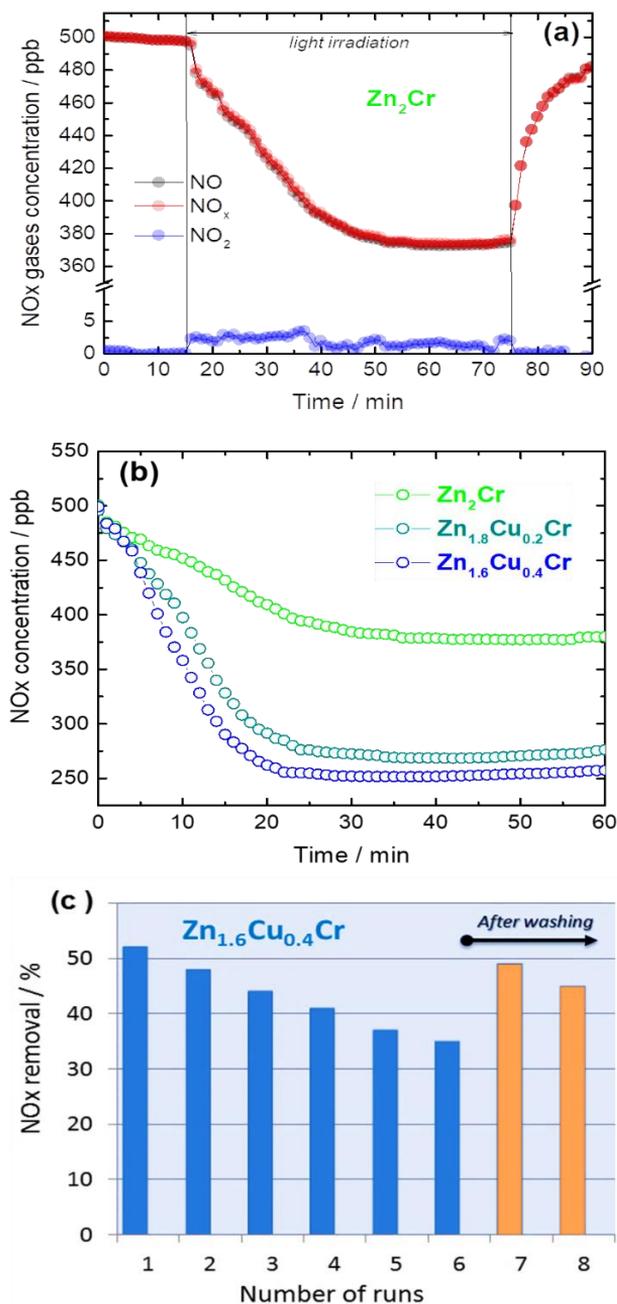
Figure 3. *(a) NO, NO$_2$ and NO$_x$ gases concentration evolution during the photodegradation of gaseous NO under UV-Vis light irradiation on the Zn$_2$Cr sample. (b) Photo-oxidative removal of NO$_x$ gas concentration measured under UV-Vis light irradiation on ZnCr-LDH and ZnCuCr-LDH catalyst. (c) NO removal efficiency calculated for each run of the reusability for the Zn$_{1.6}$Cu$_{0.4}$Cr sample.*

Conversely, considering that Zn_2Cr and $Zn_{1.8}Cu_{0.2}Cr$ samples possess similar specific surface areas, the presence of copper as a doping element in the ZnCr-LDH framework seems to be of key importance in explaining the enhanced photocatalytic activity observed. In fact the $Zn_{1.8}Cu_{0.2}Cr$ LDH DeNOx photocatalyst, with comparison to LDH photocatalysts previously studied by our research group [2,31,32], surpass in ≈ 40 % the efficiency of NO removal showed by LDHs with similar M^{2+}/M^{3+} ratio (2:1) and exhibits the highest selectivity values (S > 97 %), evidencing the advantage to prepare a ternary LDH constituted only of transition metals. Regarding the reusability of the photocatalyst, several successive run tests were performed on the $Zn_{1.6}Cu_{0.4}Cr$ sample (Fig. 3c). For each test, the sample was irradiated for 1 h. The NO_x efficiency slowly decays during the first 6 tests which is due to the accumulation of nitrite/nitrate species on the particle surface of the photocatalyst as will be proved here further on. These species are highly soluble and are eliminated when the sample is collected and washed with Milli-Q water after the sixth run. In fact, in the following runs, number 7 and 8, the photocatalytic performance is recovered, which proves the reusability of ZnCuCr-LDH as a DeNOx photocatalyst.

Moreover, the photocatalytic activity under visible light was examined once the DeNOx test was carried out under $\lambda > 400$ nm light. In Fig. S8, it can be observed that the NO abatement is enhanced in the copper containing samples, which should be associated with better visible light harvesting.

3.1.3.3. Photocatalytic mechanism

The following experiments were performed in order to know the photocatalytic mechanism expected for the copper doped LDH photocatalyst. As was previously commented, the NOx gases were removed following a PCO process assisted by the reactive oxygen species (ROS). In order to shed light on the reactive species involved when ZnCr and ZnCuCr LDHs were used as photocatalysts, EPR measurements were performed using DMPO as the spin-trapping agent under sunlight excitation, Figs. 4a and 4b. In the absence of light irradiation, no signal was detected for the photocatalyst suspension (blank). In all the samples, the characteristic signal of DMPO-•OH adduct appears as a quartet of peaks featuring a 1:2:2:1 intensity ratio, Fig. 4a. In the case of the DMPO-•O_2^- signal, a sextet of peaks is observed for the three samples, Fig. 4b, in similitude to those previously registered for Zn based LDH compounds [14,31,32,42]. The intensity of both signals increases with the Cu content, which is remarkable in the case of the •O_2^- signal. Therefore, the Cu^{2+} doping clearly enhances the ability to generate active radicals. These results confirm that ROS radical species, mainly •O_2^-, are involved in the NO photochemical oxidation accounted for ZnCuCr-LDH photocatalysts.
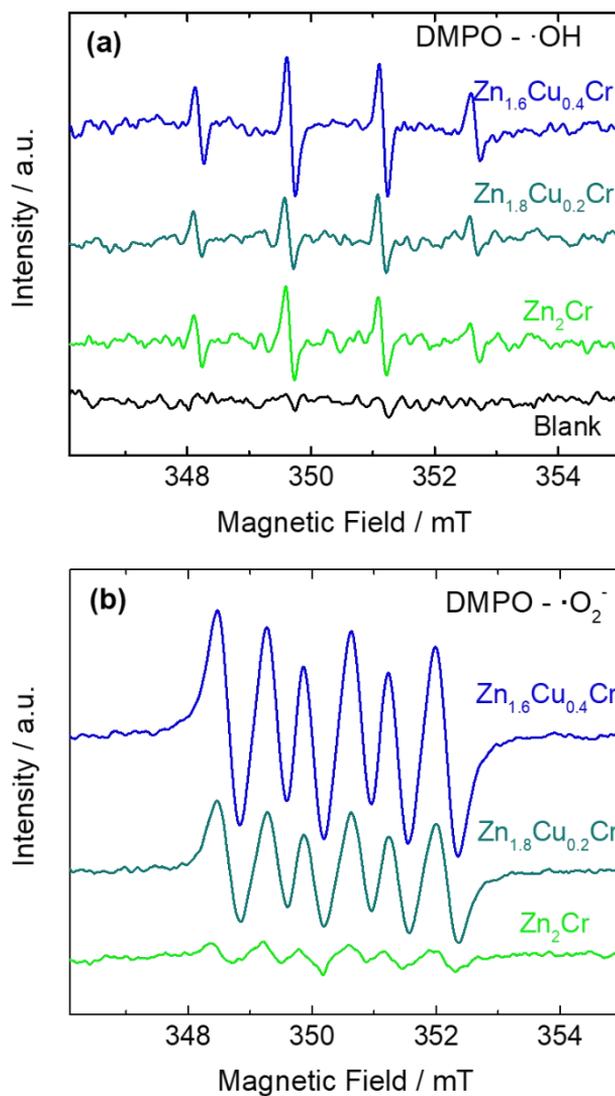
Figure 4. *DMPO spin-trapping EPR spectra of the ZnCr-LDH and ZnCuCr-LDH samples under UV-Vis light irradiation for 15 min in (a) aqueous solution for •OH and (b) methanol solution for •O_2^-.*

Theoretical calculations in order to investigate the atomic nature of the valence and conduction bands were performed for the ZnCr and ZnCuCr LDHs.

Fig. 5 displays the $Zn_{36}Cr_{18}(OH)_{108}(CO_3)_9(H_2O)_{27}$ and $Zn_{29}Cu_7Cr_{18}(OH)_{108}(CO_3)_9(H_2O)_{27}$ supercells exhibiting the layered structure of these materials and the sequential incorporation of Cu to the parent ZnCr LDH.
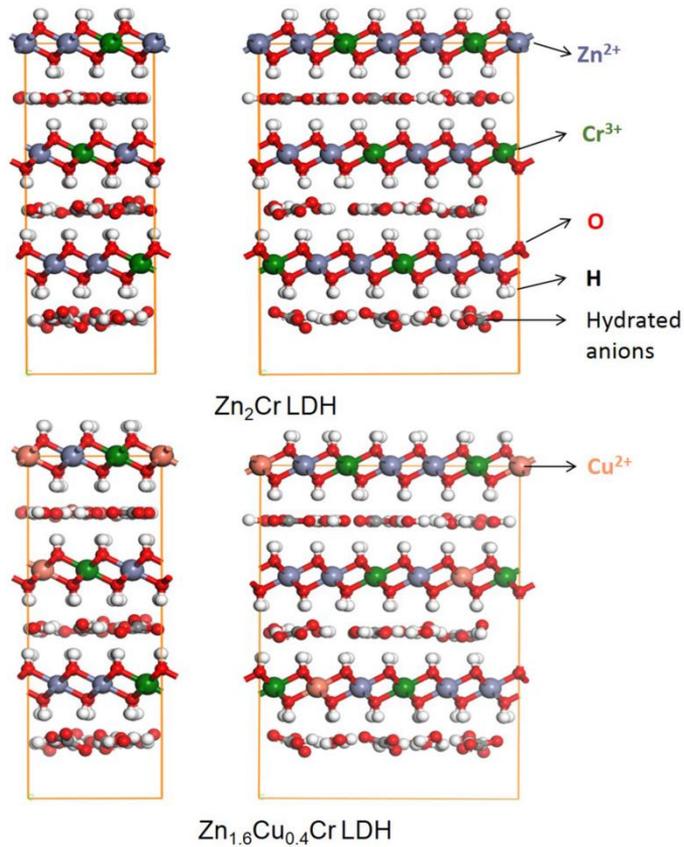
Figure 5. *Schematic representation of the structure of, $Zn_{36}Cr_{18}(OH)_{108}(CO_3)_9(H_2O)_{27}$ and $Zn_{27}Cu_9Cr_{18}(OH)_{108}(CO_3)_9(H_2O)_{27}$ LDHs supercells, side and front view of the layer.*

The density of states (DOS) diagrams calculated for the undoped and doped theoretical LDH structures highlight the role of copper ions. The DOS diagrams are calculated for both structures obtaining alpha and beta plots due to the presence of unpaired electrons in the Cr and Cu atoms.

Fig. S9 depicts the total and partial (for each metal atom) DOS plots for Zn_2Cr LDH in the alpha and beta states. The total DOS diagram displays a band gap of about 1 eV, slightly lower compared to the 1.5 eV, experimentally measured in the absorption measurements. The *d* orbitals are mostly responsible for both valence and conduction bands with a small contribution of the *p* orbitals in the alpha states. However, the most remarkable feature is revealed in the partial DOS plots, where only the *d* orbitals of the Cr atoms are responsible for the valence and conduction bands with the *d* orbitals of the Zn atoms deeply buried at low energies in the valence band. These results agree favourably with those previously reported in the literature [43].

Regarding the $Zn_{1.6}Cu_{0.4}Cr$ LDH, Fig. 6, the DOS plots display similar behavior to that of Zn_2Cr LDH with the *d* orbitals contributing mostly to the valence and conduction bands. However, the partial DOS diagrams show that the *d* orbitals from the Cu atoms contribute significantly to the valence band without participating in the conduction band. Thus, the new electronic states due to Cu orbitals in the valence band of the ZnCuCr LDHs may involve the appearance of novel absorption bands, as has been experimentally observed with the appearance of new peaks at 300 nm and 785 nm in the absorption measurements. The photoexcitation of the Cu-based states in the valence band of the ZnCuCr LDHs involves the formation of energetic holes that might participate in the photocatalytic reactions, unlike the situation of the ZnCr LDHs, which favours the formation of ROS species as inferred from the EPR measurements (Fig. 4).
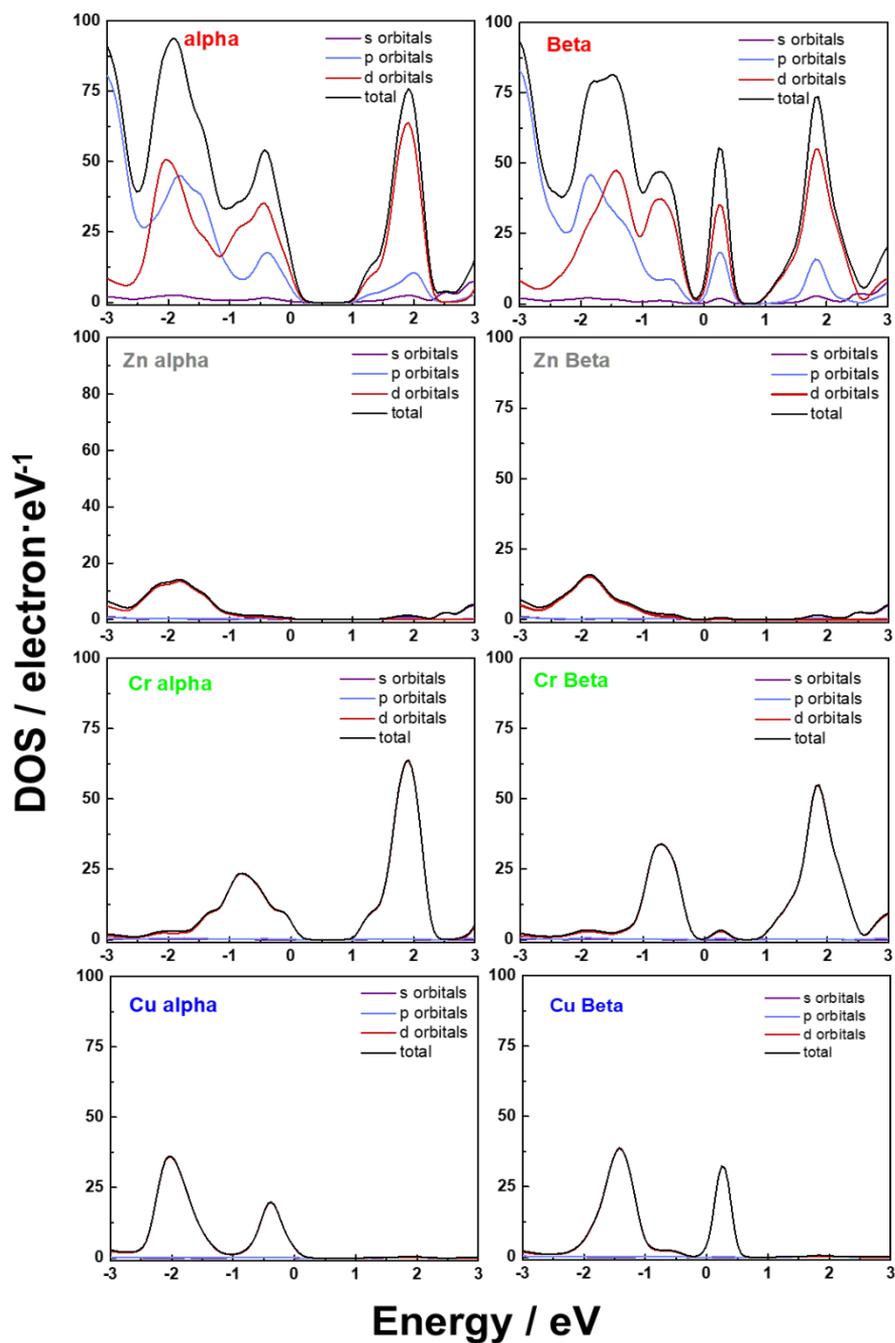
Figure 6. *Calculated total density of states (DOS) and projected density of states (PDOS) of the Zn, Cu and Cr atoms in the alpha and beta states of the $Zn_{1.6}Cu_{0.4}Cr$ photocatalyst.*

To investigate the formation of new electronic states in the ZnCuCr LDHs, femtosecond transient absorption measurements were performed in both photocatalysts. Fig. S10 displays the transient spectra of the Zn_2Cr (A) and $Zn_{1.6}Cu_{0.4}Cr$ (B) LDHs after excitation at 300 nm. The broad positive signal with a maximum value around 480 nm is assigned to the photoinduced absorption (PIA) of the excited electrons in the conduction band. Both LDHs photocatalysts exhibit similar PIA signals which proves the formation of excited electrons with the same energy. Fig. S10 (C and D) depicts the time profiles at 480 nm with the best bi-exponential fits for both photocatalysts and with the signal not recovering completely after 4 ns. The deactivation kinetics for the excited state in both LDHs is developed in the same time range with time constant of 27 ns and 1170 ns for Zn_2Cr LDH and 73 ns and 2125 ns for $Zn_{1.6}Cu_{0.4}Cr$ LDH. Thus, the recombination kinetics of the electrons in the $Zn_{1.6}Cu_{0.4}Cr$ LDH was slightly slower, which might enhance the photocatalytic activity of this compound. Moreover, the superior performance of the ZnCuCr LDHs might also be attributed to an enhanced sunlight harvesting ability or the formation of energetic holes.

Subsequently, *in-situ* DRIFTS measurements were carried out during the dynamic monitoring of the detailed mechanism involved in the photocatalytic removal of NO.

Firstly, the samples were subjected to pretreatment and NO adsorption processes. The background spectrum was recorded before NO flow passed through the reaction chamber. Fig. 7a shows the spectra obtained in each sample, once the background had been subtracted, after 10 min of NO flow in dark conditions.
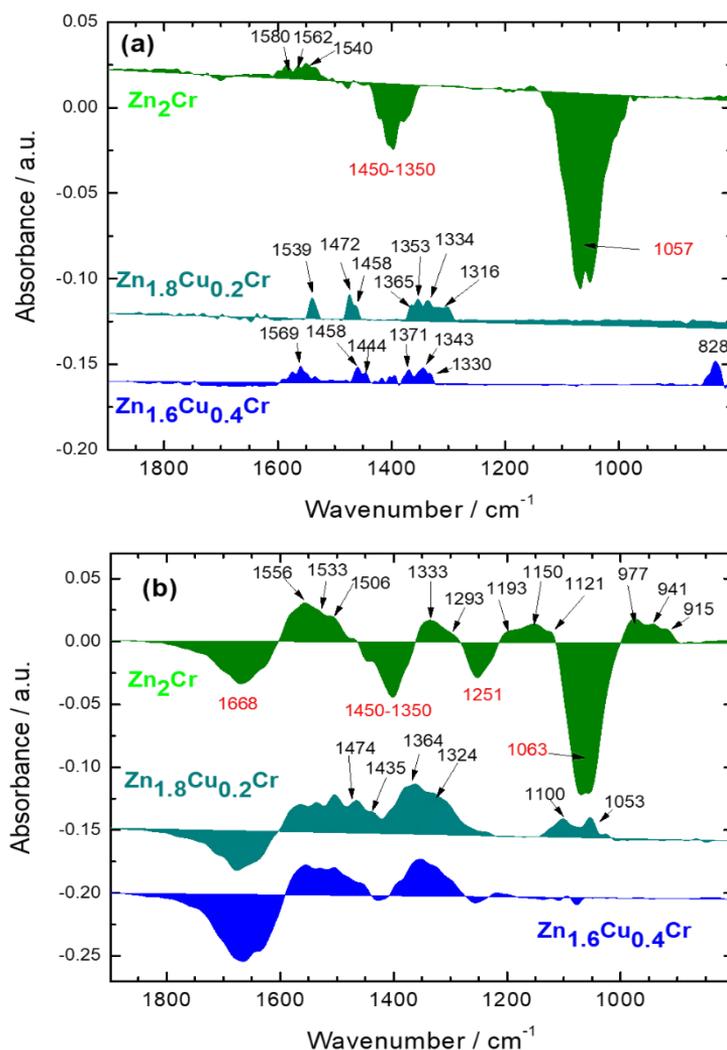
Figure 7. *In-situ DRIFTS spectra of NO adsorption (a) and oxidization processes under UV light illumination (b) over ZnCr-LDH and ZnCuCr-LDH samples.*

Apart the new increased signals corresponding to the apparition of nitrogen oxide species, retrorse peaks were detected in the Zn_2Cr sample indicating that some pristine IR bands were decreasing. These are the peaks located at 1400-1350 and 1057 cm^{-1} mentioned above (Fig. 1b). This

means that some slight perturbation occurred in the interlayer space under the NO flow. In fact, this is also reflected in the 3000 cm^{-1} region of the spectra (Fig. S11), where bands assigned to the interactions of hydrogen bonds between hydroxyl groups, anions and water molecules, are registered [44]. However, the structure of the doped samples seems to be preserved during the NO flow. This difference could be associated with a somewhat different position/symmetry of CO_3^{2-} in the LDH interlayers since ZnCr and ZnCuCr LDHs exhibited different "c" crystallographic parameters.

Regarding the newly appeared bands assigned to nitrogen oxides species, differences were found between non-doped and Cu-doped samples, Fig. 7a. Table S1 lists the assignment of the observed bands. In the case of ZnCuCr-LDH samples, the NO molecules adsorbed in the surface are disproportionate in the presence of the hydroxyl LDH groups, as NO$^-$ (1353 cm^{-1}) and NO$_2^-$ (828, 1330-1343, 1472 cm^{-1}) species appeared [45]. The rest of the bands are associated with the presence of NO$_2$, nitrite and nitrates species.

The main transformations are considered as follows:

$$2\,NO + OH^- \rightarrow HNO_2 + NO^- \qquad\qquad (1)$$
$$NO + HNO_2 + OH^- \rightarrow NO^- + NO_2 + H_2O \quad (2)$$
$$NO^- + NO_2 \rightarrow NO_2^- + NO \qquad\qquad (3)$$
$$NO^- + 2NO_2 \rightarrow NO_3^- + 2NO \qquad\qquad (4)$$
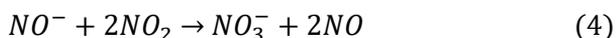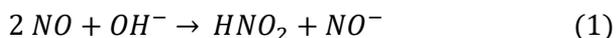
The above process is more difficult to elucidate in the case of the Zn$_2$Cr sample. Thus, the presence of a retrorse peak in the 1350-1440 cm^{-1} range could mask the presence of some bands corresponding to NO$^-$, NO$_2^-$ and NO$_2$ species.

On the other hand, there is some uncertainty in identifying the bands which appeared in the 1500-1600 as nitrate species. In fact, the presence of bicarbonate ion in LDHs has been identified at 1500-1550 cm^{-1} which is formed when a proton is transferred from the hydroxide sheet to the interlayer carbonate ion upon dehydration [46,47]. This matches with the findings associated with the retrorse peaks. In summary, the NO adsorption is favored in the copper doped samples, in accordance with the reported favorable absorption energy for the NO → Cu^{2+} binding [48].

Following the preliminary NO adsorption step, the oxidization process of NO under UV light irradiation was continuously monitored (Fig. S12). Fig. 7b shows the final products obtained on the surface of the photocatalysts after 1 h of light irradiation. The new retrorse peak at 1668 cm^{-1} indicates that constituent water molecules play a role in the photocatalytic process, Equation (6). This signal is higher in the $Zn_{1.6}Cu_{0.4}Cr$ sample, in accordance with its higher ability to produce •OH radicals, as inferred from the EPR measurements. No signals corresponding to NO_2 were observed in agreement with the high selectivity exhibited by these samples. This indicates that NO_2, if formed, is quickly oxidized to nitrate.

In comparison with other DeNO$_X$ photocatalysts, the studied LDHs exhibit two characteristics facilitating this process: i) Zn based photocatalysts exhibit high sensitivity to NO_2 adsorption, remaining the gaseous molecules on surface for ulterior redox process [15,31]; ii) the participation of structural water molecules (OH$^-$ groups) in the photocatalytic process enriches the formation of ROS species [49].

Table S1 shows the multiple signals assigned to the following nitrogen oxide species: NO^-, NOH, NO_2^-, NO_3^- . These signals of oxidized species increase in intensity with the increasing of illumination time, showing a tendency to form nitrites and nitrates as final products (Fig. S12), corroborating the passivation of the photocatalyst´s surface observed during the reusability test (Fig. 3c). The NO^- and NOH bands, in relation to the disproportionation of the NO adsorbed molecule [12], are significantly present in the Zn_2Cr photocatalyst, showing the lower ability of this photocatalyst to promote photo-activated processes, as was observed from EPR studies.

Considering the results obtained, in line with previous reports on DeNOx photocatalysts [50,51], the primary NO oxidation reaction mechanism can be described as follows:
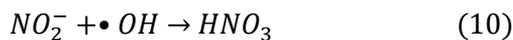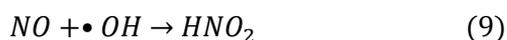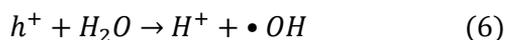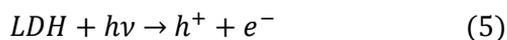
$$LDH + h\nu \rightarrow h^+ + e^- \qquad (5)$$
$$h^+ + H_2O \rightarrow H^+ + \bullet\, OH \qquad (6)$$
$$e^- + O_2 \rightarrow \bullet\, O_2^- \qquad (7)$$
$$NO + \bullet\, O_2^- \rightarrow NO_2^- \qquad (8)$$
$$NO + \bullet\, OH \rightarrow HNO_2 \qquad (9)$$
$$NO_2^- + \bullet\, OH \rightarrow HNO_3 \qquad (10)$$
$$HNO_2 + \bullet\, O_2^- \rightarrow HNO_3^- \qquad (11)$$

The in-situ DRIFTS spectra evidence the higher efficiency of doped samples in promoting NO photochemical oxidation, the nitrites and nitrates species being the final species obtained.

3.1.4. Conclusions

Zn$_{2-x}$Cu$_x$Cr-CO$_3$ LHDs (x = 0.2 and 0.4) photocatalysts were able to activate the photochemical oxidation of NO molecules under UV-Vis and Vis light irradiation. All samples showed an outstanding selectivity towards the NO photochemical process with values of S > 97 %. Reusability was positively tested in the best of the photocatalysts.

The role of copper ions was highly significant in the promotion of the photochemical activity. Firstly, the presence of Cu^{2+} in the LDH framework allows for improved harvesting of the UV-Vis light. The DOS study reveals that increased amount of mobile e$^-$/h$^+$ charge carriers should be produced in ZnCuCr photocatalysts when they are light irradiated which is in agreement with the results obtained from the EPR studies, allows the formation of larger amounts of •OH and •O$_2^-$ radical species.

On the other hand, the femtosecond transient absorption showed a slightly retarded electron-hole recombination. The *in-situ* DRIFTS spectra evidence the higher efficiency of doped samples in promoting NO photochemical oxidation.

3.1.5. Acknowledgements

3.1.6. References

[1]   European Environment Agency, European Union emission inventory report 1990-2015 under the UNECE Convention on Long-range Transboundary Air Pollution (LRTAP), Luxembourg, 2017. https://doi.org/10.2800/478321.

[2]   F. Rodriguez-Rivas, A. Pastor, C. Barriga, M. Cruz-Yusta, L. Sánchez, I. Pavlovic, Zn-Al layered double hydroxides as efficient photocatalysts for NOx abatement, Chem. Eng. J. 346 (2018) 151–158. https://doi.org/10.1016/j.cej.2018.04.022.

[3]   International Institute for Applied Systems Analysis, 5000 deaths annually from dieselgate in Europe https://iiasa.ac.at/web/home/about/news/170918-diesel-nox.html, 2017 (accessed 16 March 2020).

[4]   B. Chen, C. Hong, H. Kan, Exposures and health outcomes from outdoor air pollutants in China, Toxicology. 198 (2004) 291–300. https://doi.org/10.1016/j.tox.2004.02.005.

[5]   J. Ângelo, L. Andrade, L.M. Madeira, A. Mendes, An overview of photocatalysis phenomena applied to NOx abatement, J. Environ. Manage. 129 (2013) 522–539. https://doi.org/10.1016/j.jenvman.2013.08.006.

[6]   J. Balbuena, M. Cruz-Yusta, L. Sánchez, Nanomaterials to Combat NOx Pollution, J. Nanosci. Nanotechnol. 15 (2015) 6373–6385. https://doi.org/10.1166/jnn.2015.10871.

[7]   R.J. Lewis, Sax's Dangerous Properties of Industrial Materials, 5 Volume Set, 12th Edition, Twelth, Wiley & Sons, New Jersey, 2012.

[8]   European Chemicals Agency, Annex 2- Comments and response to comments on CLH PROPOSAL on Titanium dioxide. https://echa.europa.eu/documents/10162/cff283ec-9df1-2198-de07-6541bb3b108b, 2017 (accessed 25 September 2020).

[9]   J. Balbuena, J. M. Calatayud, M. Cruz-Yusta, P. Pardo, F. Martín, J. Alarcón, L. Sánchez, Mesocrystalline anatase nanoparticles synthesized using a simple hydrothermal approach with enhanced light harvesting for gas-phase reaction, Dalton Trans. 47 (2018) 6590–6597. https://doi.org/10.1039/c8dt00721g.

[10]   J.H. Kim, J.H. Han, Y.C. Jung, Y.A. Kim, Mussel adhesive protein-coated titanium oxide nanoparticles for effective NO removal from versatile substrates, Chem. Eng. J. 378 (2019) 122164. https://doi.org/10.1016/j.cej.2019.122164.

[11]   J. Balbuena, M. Cruz-Yusta, A. Pastor, L. Sánchez, α-Fe$_2$O$_3$/SiO$_2$ composites for the enhanced photocatalytic NO oxidation, J. Alloys Compd. 735 (2018) 1553–1561. https://doi.org/10.1016/j.jallcom.2017.11.259.

[12]   P. Chen, H. Liu, Y. Sun, J. Li, W. Cui, L. Wang, W. Zhang, X. Yuan, Z. Wang, Y. Zhang, F. Dong, Bi metal prevents the deactivation of oxygen vacancies in Bi$_2$O$_2$CO$_3$ for stable and efficient photocatalytic NO abatement, Appl. Catal. B. 264 (2020) 118545. https://doi.org/10.1016/j.apcatb.2019.118545.

[13]   J. Hu, D. Chen, N. Li, Q. Xu, H. Li, J. He, J. Lu, Fabrication of graphitic-C_3N_4 quantum dots/graphene-InVO$_4$ aerogel hybrids with enhanced photocatalytic NO removal under visible-light irradiation, Appl. Catal. B. 236 (2018) 45–52. https://doi.org/10.1016/j.apcatb.2018.04.080.

[14]   Y. Huang, D. Zhu, Q. Zhang, Y. Zhang, J. Cao, Z. Shen, W. Ho, S.C. Lee, Synthesis of a $Bi_2O_2CO_3$/$ZnFe_2O_4$ heterojunction with enhanced photocatalytic activity for visible light irradiation-induced NO removal, Appl. Catal. B. 234 (2018) 70–78. https://doi.org/10.1016/j.apcatb.2018.04.039.

[15]   A. Pastor, J. Balbuena, M. Cruz-Yusta, I. Pavlovic, L. Sánchez, ZnO on rice husk: A sustainable photocatalyst for urban air purification, Chem. Eng. J. 368 (2019) 659–667. https://doi.org/10.1016/j.cej.2019.03.012.

[16]   T. Shen, X. Shi, J. Guo, J. Li, S. Yuan, Photocatalytic removal of NO by light-driven Mn_3O_4/BiOCl heterojunction photocatalyst: Optimization and mechanism, Chem. Eng. J. 408 (2021) 128014. https://doi.org/10.1016/j.cej.2020.128014.

[17]   H. Wang, R. Zhao, H. Hu, X. Fan, D. Zhang, D. Wang, 0D/2D Heterojunctions of Ti_3C_2 MXene QDs/SiC as an Efficient and Robust Photocatalyst for Boosting the Visible Photocatalytic NO Pollutant Removal Ability, ACS Appl. Mater. Interfaces. 12 (2020) 40176–40185. https://doi.org/10.1021/acsami.0c01013.

[18]   H. Wu, C. Yuan, R. Chen, J. Wang, F. Dong, J. Li, Y. Sun, Mechanisms of Interfacial Charge Transfer and Photocatalytic NO Oxidation on BiOBr/SnO_2 p–n Heterojunctions, ACS Appl. Mater. Interfaces. 12 (2020) 43741–43749. https://doi.org/10.1021/acsami.0c12628.

[19]   S. Xiao, D. Pan, R. Liang, W. Dai, Q. Zhang, G. Zhang, C. Su, H. Li, W. Chen, Bimetal MOF derived mesocrystal $ZnCo_2O_4$ on rGO with high performance in visible-light photocatalytic NO oxidization, Appl. Catal. B. 236 (2018) 304–313. https://doi.org/10.1016/j.apcatb.2018.05.033.

[20]   G. Fan, F. Li, D.G. Evans, X. Duan, Catalytic applications of layered double hydroxides: recent advances and perspectives, Chem. Soc. Rev. 43 (2014) 7040–7066. https://doi.org/10.1039/C4CS00160E.

[21]   L. Mohapatra, K. Parida, A review on the recent progress, challenges and perspective of layered double hydroxides as promising photocatalysts, J. Mater. Chem. A. 4 (2016) 10744–10766. https://doi.org/10.1039/C6TA01668E.

[22]   X. Xiang, F. Li, Z. Huang, Recent Advances in Layered Double Hydroxide-Based Materials as Versatile Photocatalysts, Rev. Adv. Sci. Eng. 3 (2014) 158–171. https://doi.org/10.1166/rase.2014.1060.

[23]   F. Cavani, F. Trifirò, A. Vaccari, Hydrotalcite-type anionic clays: Preparation, properties and applications., Catal. Today. 11 (1991) 173–301. https://doi.org/10.1016/0920-5861(91)80068-K.

[24]   J. Tang, Z. Zou, J. Ye, Efficient Photocatalytic Decomposition of Organic Contaminants over $CaBi_2O_4$ under Visible-Light Irradiation, Angew. Chem. Int. Ed. 43 (2004) 4463–4466. https://doi.org/10.1002/anie.200353594.

[25]   X.D. Wang, C.J. Summers, Z.L. Wang, Mesoporous Single-Crystal ZnO Nanowires Epitaxially Sheathed with Zn_2SiO_4, Adv. Mater. 16 (2004) 1215–1218. https://doi.org/10.1002/adma.200306505.

[26]   C. Gomes Silva, Y. Bouizi, V. Fornés, H. García, Layered Double Hydroxides as Highly Efficient Photocatalysts for Visible Light Oxygen Generation from Water, J. Am. Chem. Soc. 131 (2009) 13833–13839. https://doi.org/10.1021/ja905467v.

[27]   K. Parida, L. Mohapatra, Recent progress in the development of carbonate-intercalated Zn/Cr LDH as a novel photocatalyst for hydrogen evolution aimed at the utilization of solar light, Dalton Trans. 41 (2012) 1173–1178. https://doi.org/10.1039/C1DT10957J.

[28]   M. Shao, J. Han, M. Wei, D.G. Evans, X. Duan, The synthesis of hierarchical Zn-Ti layered double hydroxide for efficient visible-light photocatalysis, Chem. Eng. J. 168 (2011) 519–524. https://doi.org/10.1016/j.cej.2011.01.016.

[29]   C. Wang, B. Ma, S. Xu, D. Li, S. He, Y. Zhao, J. Han, M. Wei, D.G. Evans, X. Duan, Visible-light-driven overall water splitting with a largely-enhanced efficiency over a Cu_2O@ZnCr-layered double hydroxide photocatalyst, Nano Energy. 32 (2017) 463–469. https://doi.org/10.1016/j.nanoen.2017.01.010.

[30]   Z. Yang, J. Wei, G. Zeng, H. Zhang, X. Tan, C. Ma, X. Li, Z. Li, C. Zhang, A review on strategies to LDH-based materials to improve adsorption capacity and photoreduction efficiency for CO_2, Coord. Chem. Rev. 386 (2019) 154–182. https://doi.org/10.1016/j.ccr.2019.01.018.

[31]   A. Pastor, F. Rodriguez-Rivas, G. de Miguel, M. Cruz-Yusta, F. Martin, I. Pavlovic, L. Sánchez, Effects of Fe^{3+} substitution on Zn-Al layered double hydroxides for enhanced NO photochemical abatement, Chem. Eng. J. 387 (2020) 124110. https://doi.org/10.1016/j.cej.2020.124110.

[32]   F. Rodriguez-Rivas, A. Pastor, G. de Miguel, M. Cruz-Yusta, I. Pavlovic, L. Sánchez, Cr^{3+} substituted Zn-Al layered double hydroxides as UV-Vis light photocatalysts for NO gas removal from the urban environment, Sci. Total Environ. 706 (2020) 136009. https://doi.org/10.1016/j.scitotenv.2019.136009.

[33]   N. Ahmed, Y. Shibata, T. Taniguchi, Y. Izumi, Photocatalytic conversion of carbon dioxide into methanol using zinc-copper-M(III) (M = aluminum, gallium) layered double hydroxides, J. Catal. 279 (2011) 123–135. https://doi.org/10.1016/j.jcat.2011.01.004.

[34]   S. Kim, J. Fahel, P. Durand, E. André, C. Carteret, Ternary Layered Double Hydroxides (LDHs) Based on Co-, Cu- Substituted ZnAl for the Design of Efficient Photocatalysts, Eur. J. Inorg. Chem. (2017) 669–678. https://doi.org/10.1002/ejic.201601213.

[35]   S.Y. Kim, Y.J. Cho, A.R. Lee, H. Son, W.S. Han, D.W. Cho, S.O. Kang, Influence of π-conjugation structural changes on intramolecular charge transfer and photoinduced electron transfer in donor-π -acceptor dyads, Phys. Chem. Chem. Phys. 19 (2017) 426–435. https://doi.org/10.1039/c6cp06566j.

[36]   N. Baliarsingh, L. Mohapatra, K. Parida, Design and development of a visible light harvesting Ni-Zn/Cr-CO$_3{}^{2-}$ LDH system for hydrogen evolution, J. Mater. Chem. A. 1 (2013) 4236–4243. https://doi.org/10.1039/c2ta00933a.

[37]   M.R. Pérez, I. Crespo, M.A. Ulibarri, C. Barriga, V. Rives, J.M. Fernández, Influence of divalent metal on the decomposition products of hydrotalcite-like ternary systems M^{II}-Al-Cr (M^{II} = Zn, Cd), Mater. Chem. Phys. 132 (2012) 375–386. https://doi.org/10.1016/j.matchemphys.2011.11.040.

[38]   J.Z. Bloh, A. Folli, D.E. Macphee, Photocatalytic NO$_x$ abatement: why the selectivity matters, RSC Adv. 4 (2014) 45726–45734. https://doi.org/10.1039/c4ra07916g.

[39]   M.B. Leinen, D. Dede, M.U. Khan, M. Çaglayan, Y. Koçak, H.V. Demir, E. Ozensoy, CdTe Quantum Dot-Functionalized P25 Titania Composite with Enhanced Photocatalytic NO$_2$ Storage Selectivity under UV and Vis Irradiation, ACS Appl. Mater. Interfaces. 11 (2019) 865–879. https://doi.org/10.1021/acsami.8b18036.

[40]   H. Shang, M. Li, H. Li, S. Huang, C. Mao, Z. Ai, L. Zhang, Oxygen Vacancies Promoted the Selective Photocatalytic Removal of NO with Blue TiO$_2$ via Simultaneous Molecular Oxygen Activation and Photogenerated Hole Annihilation, Environ. Sci. Technol. 53 (2019) 6444–6453. https://doi.org/10.1021/acs.est.8b07322.

[41]   B. Tan, X. Zhang, Y. Li, H. Chen, X. Ye, Y. Wang, J. Ye, Anatase TiO$_2$ Mesocrystals: Green Synthesis, In Situ Conversion to Porous Single Crystals, and Self-Doping Ti^{3+} for Enhanced Visible Light Driven Photocatalytic Removal of NO, Chem. Eur. J. 23 (2017) 5478–5487. https://doi.org/10.1002/chem.201605294.

[42]   Q. Yang, S. Wang, F. Chen, K. Luo, J. Sun, C. Gong, F. Yao, X. Wang, J. Wu, X. Li, D. Wang, G. Zeng, Enhanced visible-light-driven photocatalytic removal of refractory pollutants by Zn/Fe mixed metal oxide derived from layered double hydroxide, Catal. Commun. 99 (2017) 15–19. https://doi.org/10.1016/j.catcom.2017.05.010.

[43]   S.M. Xu, H. Yan, M. Wei, Band Structure Engineering of Transition-Metal-Based Layered Double Hydroxides toward Photocatalytic Oxygen Evolution from Water: A Theoretical–Experimental Combination Study, J. Phys. Chem. C. 121 (2017) 2683–2695. https://doi.org/10.1021/acs.jpcc.6b10159.

[44]   V. Rives, Layered Double Hydroxides: Present and Future, Nova Science Publishers, New York, 2001.

[45]   J. Liao, W. Cui, J. Li, J. Sheng, H. Wang, X. Dong, P. Chen, G. Jiang, Z. Wang, F. Dong, Nitrogen defect structure and NO+ intermediate promoted photocatalytic NO removal on H$_2$ treated g-C$_3$N$_4$, Chem. Eng. J. 379 (2020) 122282. https://doi.org/10.1016/j.cej.2019.122282.

[46]   C. Barriga, F. Kooli, V. Rives, M.A. Ulibarri, Layered Hidroxycarbonates with the Hydrotalcite Structure Containing Zn, Al, and Fe, in: M.L. Occelli, H. Kessler (Eds.), Synthesis of Porous Materials: Zeolites: Clays, and Nanostructures, Marcel Dekker, New York, 1996: pp. 661–674. https://books.google.es/books?id=nPG2wAEACAAJ.

[47]   O. Clause, M. Gazzano, F. Trifiro, A. Vaccari, L. Zatorski, Preparation and thermal reactivity of nickel/chromium and nickel/aluminum hydrotalcite-type precursors, Appl. Catal. 73 (1991) 217–236. https://doi.org/10.1016/0166-9834(91)85138-L.

[48]   M.R. Mullen, P.K. Dutta, Building Selectivity for NO Sensing in a NOx Mixture with Sonochemically Prepared CuO Structures, Chemosensors. 4 (2016) 1. https://doi.org/10.3390/chemosensors4010001.

[49]   X. Lv, J. Zhang, X. Dong, J. Pan, W. Zhang, W. Wang, G. Jiang, F. Dong, Layered double hydroxide nanosheets as efficient photocatalysts for NO removal: Band structure engineering and surface hydroxyl ions activation, Appl. Catal. B. 277 (2020) 119200. https://doi.org/10.1016/j.apcatb.2020.119200.

[50]   W. Huo, W. Xu, T. Cao, Z. Guo, X. Liu, G. Ge, N. Li, T. Lan, H.C. Yao, Y. Zhang, F. Dong, Carbonate doped Bi_2MoO_6 hierarchical nanostructure with enhanced transformation of active radicals for efficient photocatalytic removal of NO, J. Colloid Interface Sci. 557 (2019) 816–824. https://doi.org/10.1016/j.jcis.2019.09.089.

[51]   W. Huo, W. Xu, T. Cao, X. Liu, Y. Zhang, F. Dong, Carbonate-intercalated defective bismuth tungstate for efficiently photocatalytic NO removal and promotion mechanism study, Appl. Catal. B. 254 (2019) 206–213. https://doi.org/10.1016/j.apcatb.2019.04.099.

Appendix I: Supporting Information

Experimental

Synthesis of LDHs

All the reagents employed in this study were analytical grade and used without further purification: $Zn(NO_3)_2 \cdot 6H_2O$, $Cr(NO_3)_2 \cdot 9H_2O$ and $Cu(NO_3)_2 \cdot 3H_2O$ (purchased from Panreac AppliChem).

LDH characterization

-   X-ray diffraction (XRD) patterns of the samples were recorded by a Bruker D8 Discover diffractometer, using Cu Kα radiation (λ = 1.5405 Å) with a 2θ step size = 0.02˚ and a step counting = 0.65 s. Unit cell parameters were calculated using full pattern matching as implemented in TOPAS 4.2 software.

-   The specific surface area of each sample was calculated by applying the Brunauer-Emmet-Teller (BET). Before the measurements, the samples were degassed under vacuum (90 °C for 380 min).

-   UV-Vis spectra were measured employing a Cary 5000 spectrophotometer, equipped with an integrating sphere and using $BaSO_4$ as the reference standard. All the spectra were recorded from 200 to 800 nm at a rate of 30 $nm \cdot min^{-1}$ and a step of 0.5 nm.

-   Photoelectronic XPS signal was recorded at a take-off angle of 45° from an analysis area of 100 μm in diameter. Binding energies were corrected against those for C 1s peak of adventitious carbon fixed at 284.8 eV.

First-Principles Density of Functional Theory Calculation

- The functional LDA+CA-PZ, pseudopotential OTFG Ultrasoft and the Koelling-Harmon relativistic treatment have been used to optimize the atomic positions of the CO_3^{2-} and H_2O interlayer molecules. The total and partial density of states (DOS) plots were calculated using the functional GGA+PW91.

- The crystal structure of both photocatalysts was built up based on the crystallographic data of the archetypal hydrotalcite $Mg_2Al(OH)_6(CO_3)_{1/2}(H_2O)_{3/2}$ [1] together with the lattice parameters obtained from our experimental X-ray diffraction measurements. Later, the further replacement of the Mg and Al atoms by Zn, Cr and Cu atoms was performed in the crystal structure with a final optimization of the relative atomic positions of the interlayer molecules, CO_3^{2-} and H_2O, through the functional LDA+CA-PZ, pseudopotencial OTFG Ultrasoft and the Koelling-Harmon relativistic treatment.

Evaluation of the photocatalytic activity

- The photocatalytic activity was investigated by examining the removal ratio of NO at ppb levels (500 ppb) in a continuous-flow reactor illuminated using a sunlight irradiation box. (Solarbox 3000e RH; Xe lamp with irradiances of 25 and 580 $W \cdot m^{-2}$ for UV and visible light respectively). The reactor contained the LDH photocatalyst, 500 mg of sample powder supported in a 5x5 cm sample holder. 500 ppb NO simulated polluted atmosphere flowed through the reactor (0.3 $L \cdot min^{-1}$) with a relative humidity 50 ± 10 %. After adsorption-

desorption equilibrium was achieved (15 min), the lamp was switched on for 60 min. The concentration of NO was continuously detected by a NO_X chemiluminescence analyser (Environnement-AC32M).

- Each DeNOx test was repeated three times in order to calculate the average concentration values. Thus, standard deviations of ± 0.3 ppb for NO concentration and ± 1.0 ppb for NO_2 and NO_X were calculated. The photocatalytic activity indexes to study were the following:

$$NO\ conversion\ (\%) = \frac{[NO]_{in} - [NO]_{out}}{[NO]_{in}} \times 100 \tag{1}$$

$$NO_2\ released\ (\%) = \frac{[NO_2]_{out}}{[NO]_{in}} \times 100 \tag{2}$$

$$NO_x\ conversion\ (\%) = \frac{[NO_x]_{in} - [NO_x]_{out}}{[NO_x]_{in}} \times 100 \tag{3}$$

- EPR spectra were recorded at room temperature in a Bruker-EMXmicro spectrometer. 5,5-Dimethyl-1-pyrroline N-oxide (DMPO, Sigma-Aldrich) was used as the spin-trap. The LDH powder was dispersed in a 45 mM DMPO solution (water or methanol for detecting •OH or •O_2^-, respectively) and irradiated for 15 min with artificial sunlight.

- Femtosecond transient absorption measurements were performed using a broadband pump–probe transient absorption spectrometer (HELIOS, Ultrafast Systems). The pump light was generated using a regenerative Ti: Sapphire amplifier (Spitfire Ace, Spectra Physics, 1 kHz) that provides ultra-short pulses of high power at 800 nm. This system requires a seed laser to provide the input pulses and a pump laser to energize the amplifier. The regenerative amplifier is seeded

using a Ti: Sapphire femtosecond laser (MaiTai SP, Spectra Physics, 80 MHz) and pumped by a diode-pumped Q-switched laser of Nd: YLF (Empower 45, Spectra Physics, 1 kHz). The amplified radiation (800 nm, 100 fs, 5 W) is divided into two beams. The first one is used to pump a tunable optical parametric amplifier (TOPAS prime, Spectra Physics) in the range 290-1600 nm that generates the excitation of the sample and the second one is employed to generate white light for the absorption of the sample. In the Helios spectrometer, the UV-VIS white light continuum generated by focusing the fundamental light from the amplifier on a thin CaF_2 crystal after the controlled optical delay (3.3 ns), was used as a probe beam, directed to the sample and detected with a CMOS sensor. The pump pulse was chopped by a mechanical chopper synchronized to one-half of the laser repetition rate, resulting in a pair of the spectra, with and without the pump, from which the absorption change induced by the pump pulse was estimated.

- DRIFTS measurements were performed with a FTIR spectrometer (PerkinElmer FRONTIER) equipped with a Harrick reaction chamber. The sample was placed in the reaction chamber, treated at a room temperature under high purity Ar flow for 10 minutes to remove environmental impurities and then scanned to produce a baseline. Subsequently, in the dark, a mixture of 50 mL·min^{-1} NO (100 ppm) and 50 mL·min^{-1} O_2 was pumped into the chamber, the sample being subjected to adsorption reactions for 15 min and a new scan was obtained. Afterwards, light was turned on for 60 min. The spectrum evolving along with the photocatalytic reaction was recorded every 5 minutes.
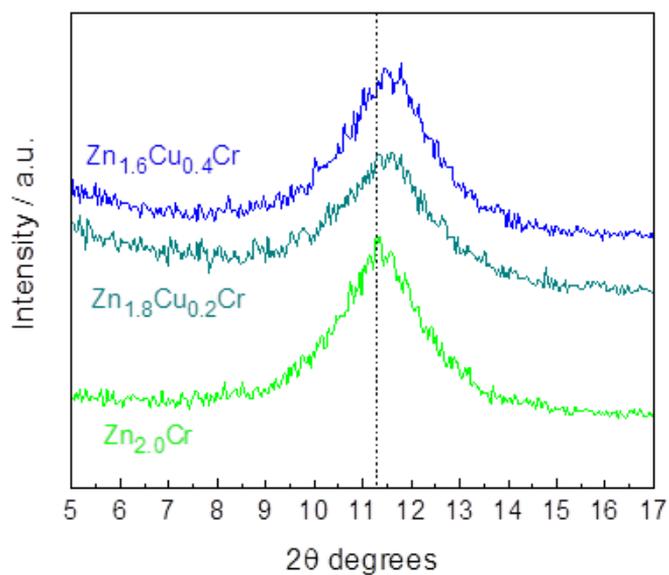
Figure S1. *XRD patterns of the ZnCr-LDH and ZnCuCr-LDH samples.*
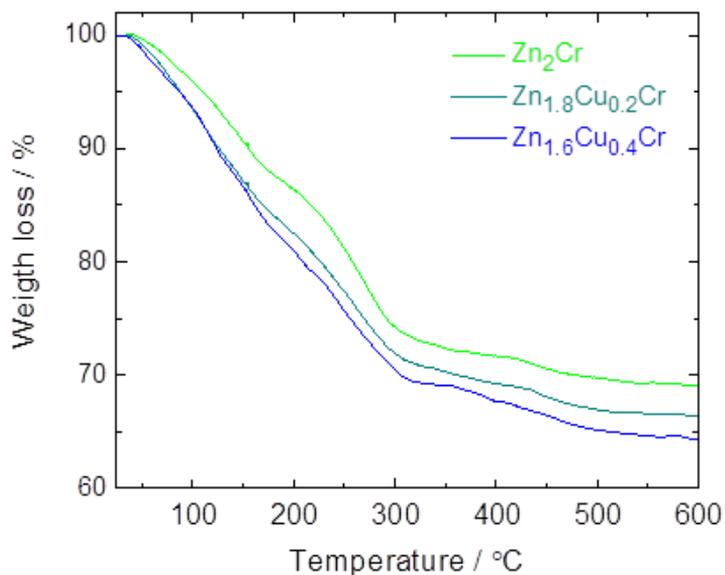
Figure S2. *Thermogravimetric patterns of the ZnCr-LDH and ZnCuCr-LDH samples.*
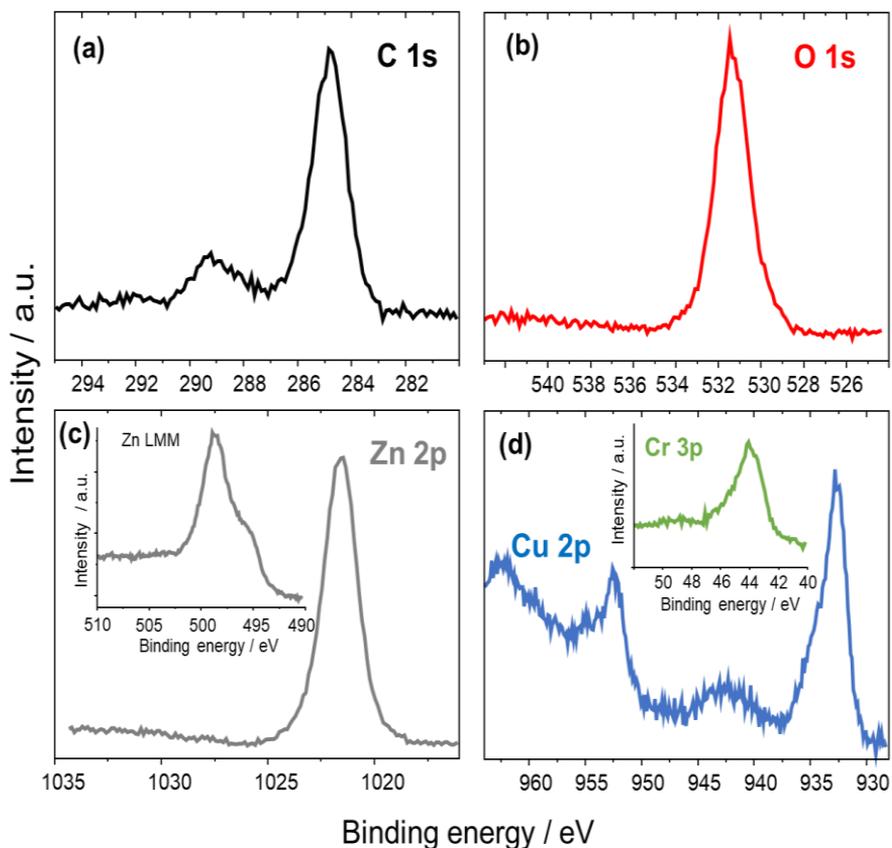
Figure S3. *XPS spectra obtained from the ZnCr-LDH and ZnCuCr-LDH samples surface: C 1s, O 1s, Zn 2p, Zn LMM, Cr 3p and Cu 2p regions.*

Figure S3 shows the C 1s, O 1s, Zn 2p, Cr 3p and Cu 2p XPS regions for ZnCr and ZnCuCr LDH samples. The adventitious C 1s at binding energy of 284.8 eV was used to correct the spectra of charge effects, Fig. S3a. In all the samples, the presence of carbonate (interlayer anion) is shown by the C 1s peak at 289 eV [2]. The O 1s signal (Fig. S3b) was fitted at 531.5 eV using a fixed FWHM of 1.8 eV, which agrees with the majority presence of hydroxides, while the contribution of carbonates is hidden by the hydroxides.

The O 1s peak is shown at 531 eV (Fig. S3b) as expected for Zn^{2+}, Cr^{3+} and Cu^{2+} hydroxides, whereas it would be expected at around 530 eV for the corresponding oxides [2-4].

The identification of chemical oxidation products of zinc by means of the Zn $2p_{3/2}$ peak (Fig. S3c) is not easy due to the small differences in their binding energies. ZnO and $Zn(OH)_2$ can be easily distinguished by the difference in the expected kinetic energies in the Zn LMM Auger region. Figure S3c inset shows the Zn LMM Auger spectra with the main peak at 987.5 eV kinetic energy (499 eV binding energy) confirming the existence of $Zn(OH)_2$.

The Cr $2p_{3/2}$ peak at 577.2 eV has been reported as Cr^{3+} [3], however the Cr 2p signal overlaps strongly with Zn Auger peaks. Because of this, the Cr 3p signal at 44.1 eV was used to identify Cr^{3+} as hydroxide, Fig. S3d inset [2,4]. The Cr 3p spectrum shows a main peak followed by multiplet and charge-transfer effects [5]. As shown in Fig. S3d, the Cu 2p XPS region shows the satellite features corresponding to Cu^{2+} as CuO which is very similar to the $Cu(OH)_2$ [6].
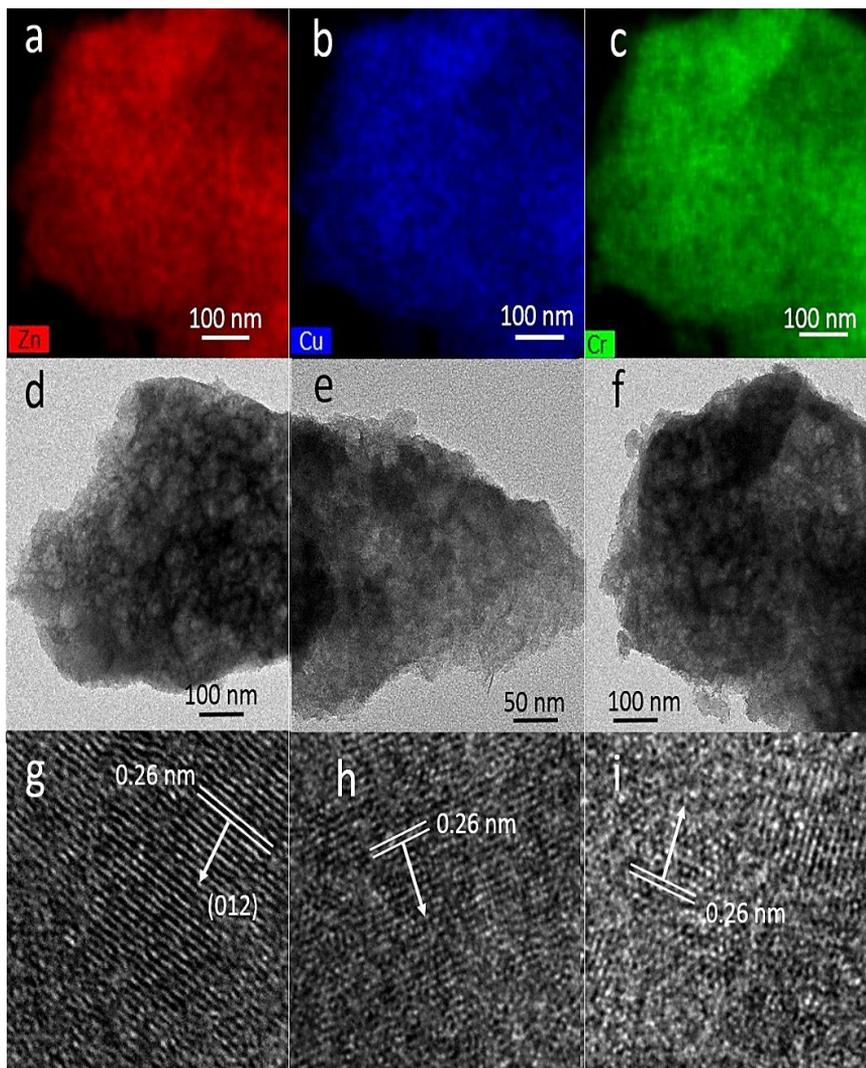
Figure S4. *(a-c) EDS mapping images of Zn, Cu, Cr elements of $Zn_{1.6}Cu_{0.4}Cr$ sample. TEM (d-f) and HRTEM (g-i) images of the Zn_2Cr, $Zn_{1.8}Cu_{0.2}Cr$ and $Zn_{1.6}Cu_{0.4}Cr$ samples, respectively.*

The EDS Mapping shows that Zn, Cu and Cr elements are well distributed in the region. The morphology observed in TEM micrographs is consistent with the SEM results. The lattice fringes interplanar spacing of 0.26 nm (Figs S4. g - i) corresponding to the (012) lattice plane of LDHs.
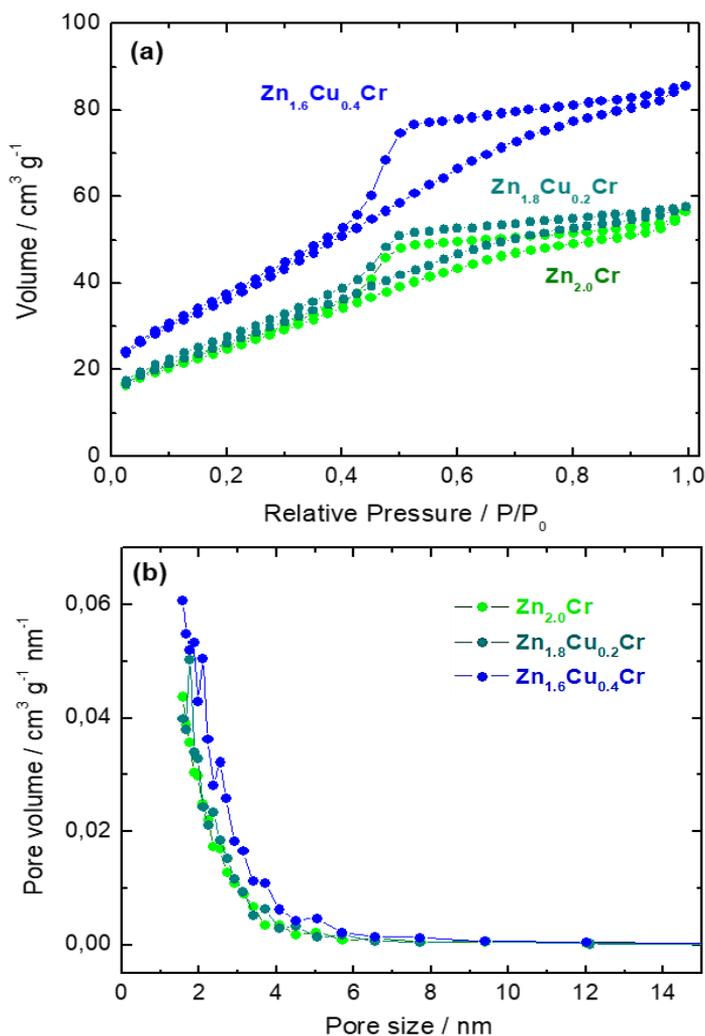
Figure S5. *(a) N$_2$ adsorption-desorption isotherms and (b) pore size distribution of the ZnCr-LDH and ZnCuCr-LDH samples.*

N$_2$ adsorption-desorption isotherms. A type II isotherm shape was observed in the three samples, Fig. S5a, which is characteristic of microporous solids exhibiting relatively small external surfaces. A remarkable type H2 hysteresis loop was observed, being associated with pores with narrow mouths (*vg.* ink-bottle pores). The pore size distribution shows the majority presence of micropores, the size of mesopores being limited to the 2.0 – 6.0 nm.
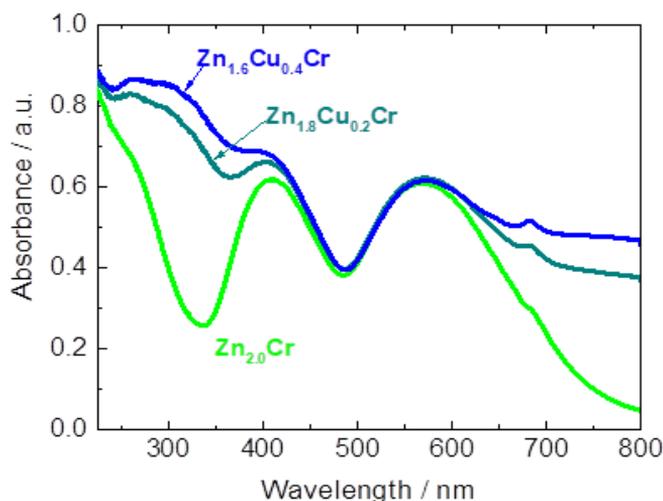
Figure S6. *The UV–Vis absorption spectra of the ZnCr-LDH and ZnCuCr-LDH samples.*

Figure S6 shows the light absorption spectra in the studied samples. All of them exhibit the characteristic features of Zn-Cr LDHs consisting in a most intense absorption band below 250 nm and a doublet of wide and intense bands appearing at 410 and 570 nm. The first band is characteristic of zinc-based LDHs [7]. Those bands in the visible light region correspond to spin allowed electron transitions from the ground state $^4A_{2g}(F)$ to $^4T_{1g}(F)$ and $^4T_{2g}(F)$ excited states, respectively, for Cr^{3+} in octahedral symmetry [8,9]. The small band at 682 nm is associated with the spin-forbidden $^4A_{2g}{}^2E_g$ transition [10]. The spectrum evidence clearly changes once the LDH is doped with Cu^{2+} ions showing the apparition of two new bands. The high intense band at 300 nm is associated with charge transfer processes, while the lower intensity band at 785 nm corresponds to $^2E_g \rightarrow {}^2T_{2g}$ electron transition of octahedral copper [11]. This band is broad, because of the octahedral distortion due to the Jahn-Teller effect and extended to the near-infrared region. The comparison of spectra suggests that copper doped Zn-Cr LDHs would be able to perform a full harvesting of sunlight when used as potential photocatalysts.
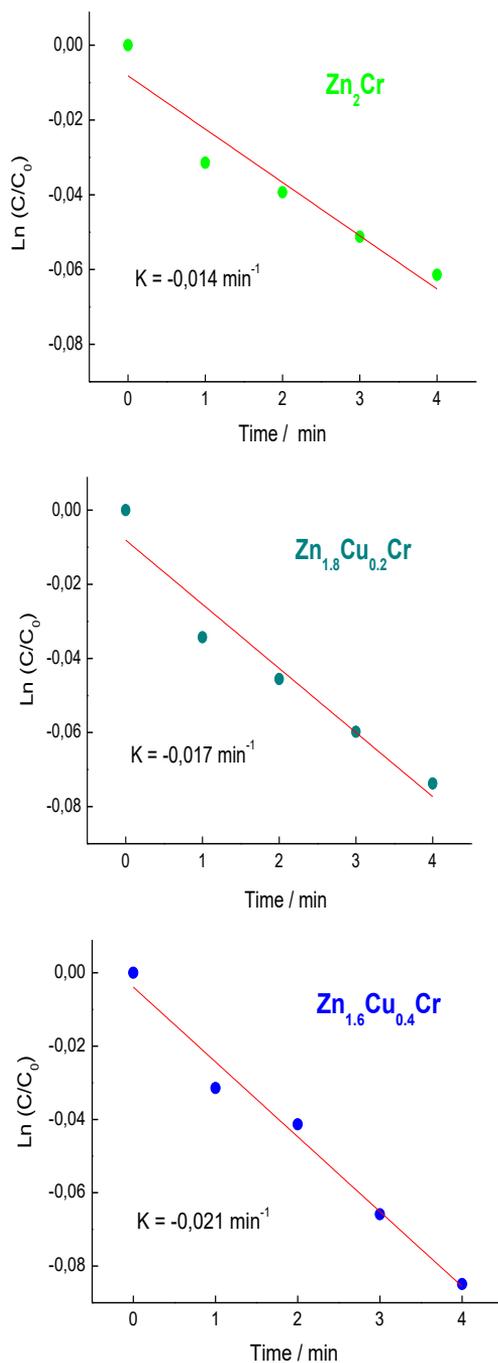
Figure S7. *Variation of the NO concentration: dependence of ln(C/C₀) with irradiation time in the presence of different Zn₂₋ₓCuₓCr samples.*
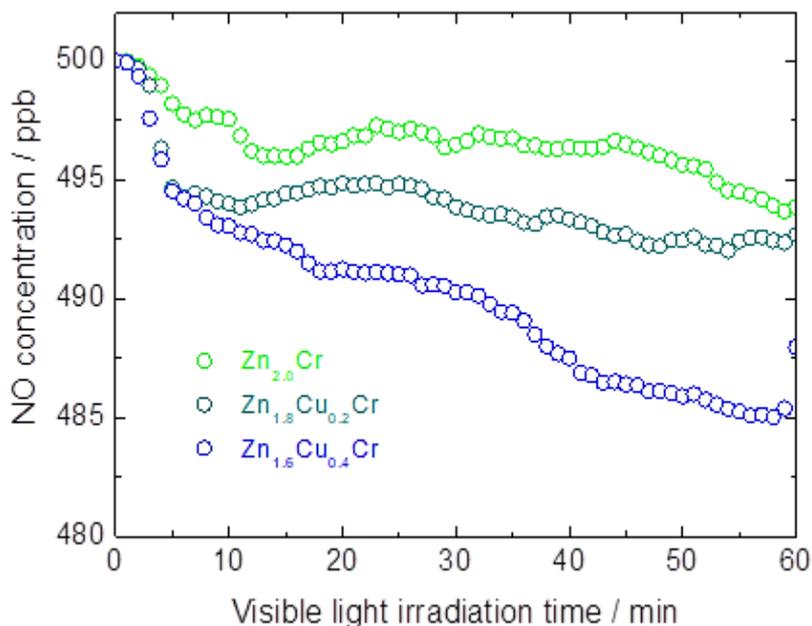
Figure S8. *NO gas concentration evolution during the photo-degradation process under Vis light irradiation on ZnCr-LDH and ZnCuCr-LDH catalysts.*

As is previously known [12], the presence of chromium in the LDH framework allows photocatalytic DeNOx activity under visible light. In this figure S8, it can be observed that the NO abatement is enhanced in the copper containing samples, which should be associated with better visible light harvesting. Thus, ZnCuCr-LDH samples showed an improved visible light absorption in the 380-430 and 620-800 nm ranges (Fig. S6). The increased NO abatement is not of the same magnitude as that observed when the catalyst was irradiated with sunlight (Fig. 3b). Therefore, the highest NO removal efficiency found would be associated with a UV light activated mechanism and the potential role of the copper ions in this mechanism.
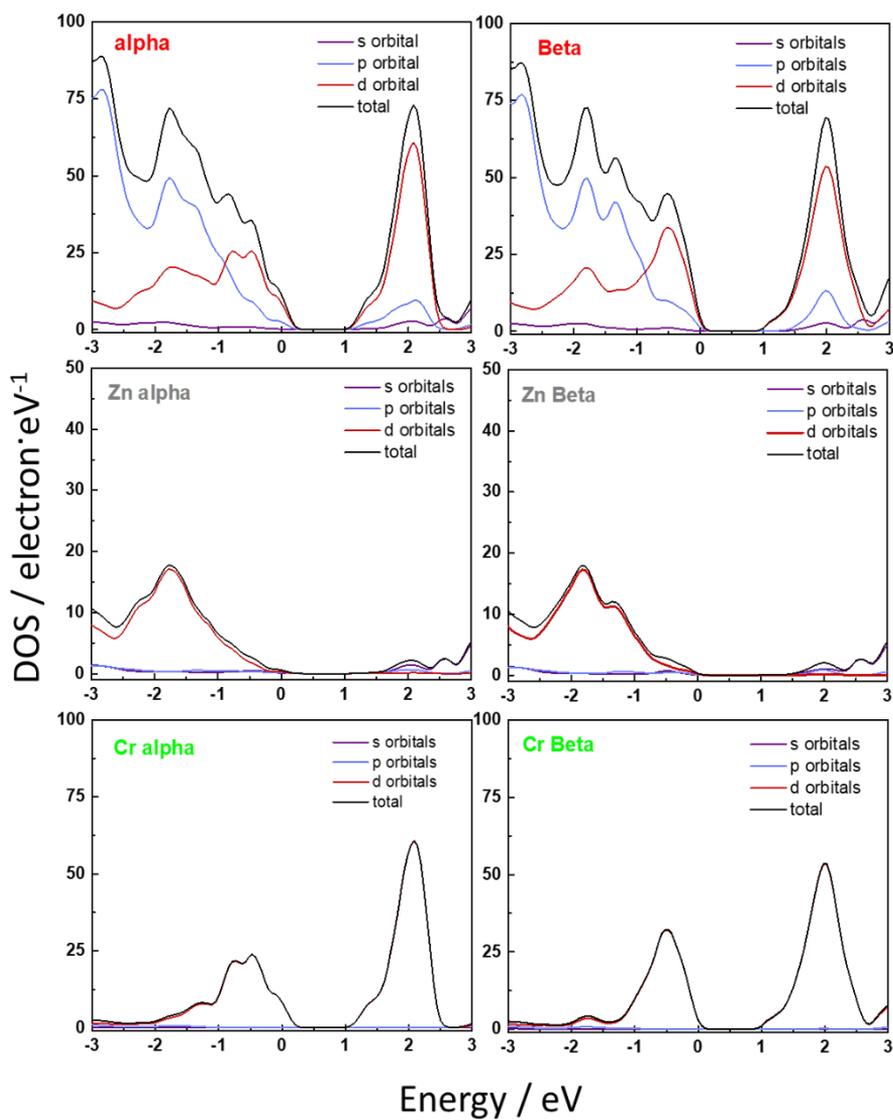
Figure S9. *Calculated total density of states (DOS) and projected density of states (PDOS) of the Zn and Cr atoms in the alpha and beta states of the Zn$_2$Cr-LDH photocatalyst.*
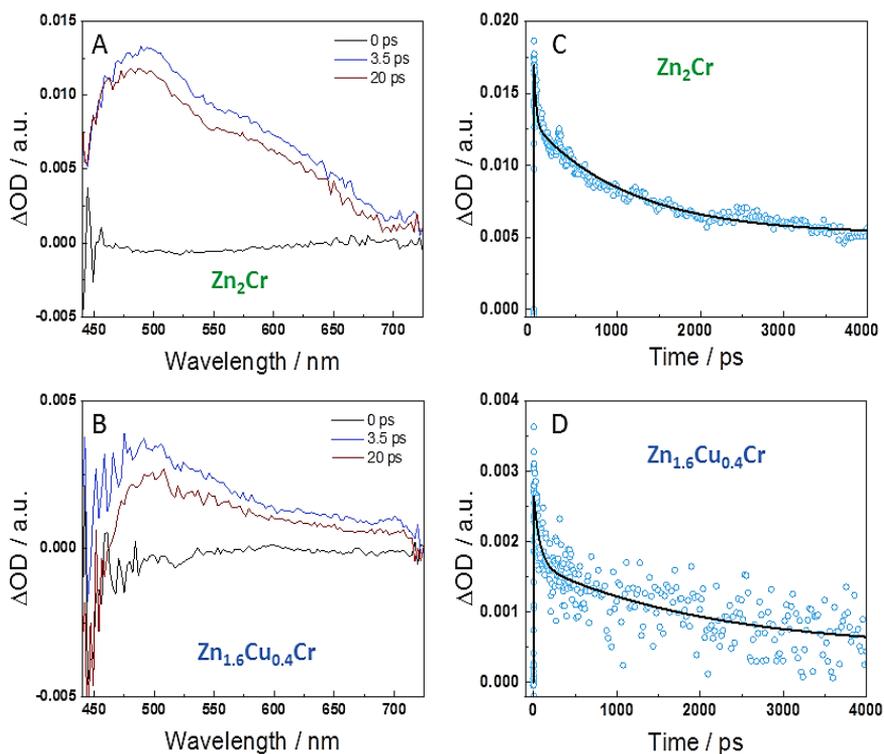
Figure S10. *Transient absorption spectra at different delay times (A and B) and decay times at λ_{probe} = 480 nm (C and D) of the ZnCr-LDH (A and C) and ZnCuCr-LDH (B and D) samples. λ_{exc} = 300 nm.*
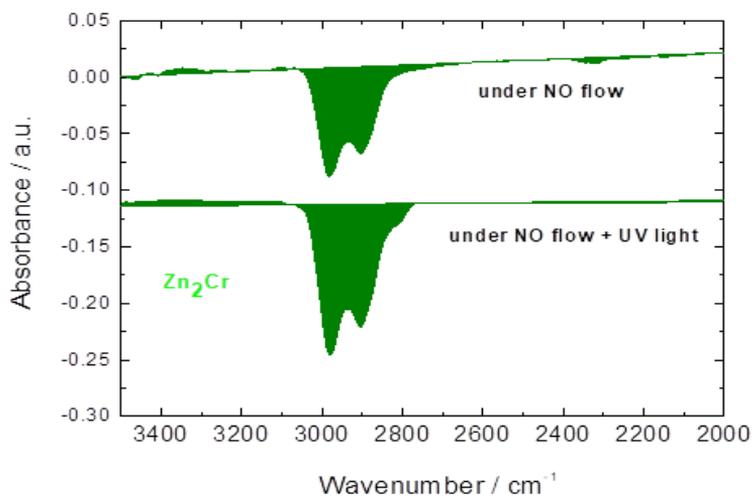

Figure S11. *In-situ DRIFTS spectra of NO adsorption and photo-oxidization process over the Zn_2Cr sample.*

Adsorption process			Photocatalytic process		
position / cm^{-1}	Assignment	Ref.	position / cm^{-1}	Assignment	Ref.
828	NO$_2^-$	[13]	915, 941, 977	monodentate NO$_3^-$	[13]
			1053, 1303	Bidentate v (NO$_3^-$)	[14]
			1100	NOH	[15]
			1121, 1150, 1193	NO$^-$	[14,16]
1293	NO$_2^-$	[17]	1293	NO$_2^-$	[17]
1316	bridge nitrate v (NO$_3^-$)	[14]	1324	bridge nitrate v (NO$_3^-$)	[14]
1330, 1334, 1343	bridge nitrite v (NO$_2^-$)	[14,18]	1333	bridge nitrite v (NO$_2^-$)	[14,18]
1365	Monodentate v (NO$_2^-$)	[18]	1364	Monodentate v (NO$_2^-$)	[18]
1371, 1458	NO$_2$	[13]			
1444	NO$_2$	[18]			
1472	chelated NO$_2^-$	[17]	1435, 1474	chelated NO$_2^-$	[17]
			1506	monodentate NO$_3^-$	[18,19]
1539 - 1580	bidentate nitrate	[15,17,19]	1533, 1556	bidentate nitrate	[15,17,19]

Table S1. Assignment of the in-situ DRIFTS bands observed during the adsorption and photocatalytic oxidation processes of NO over Zn$_{2-x}$Cu$_x$Cr samples.
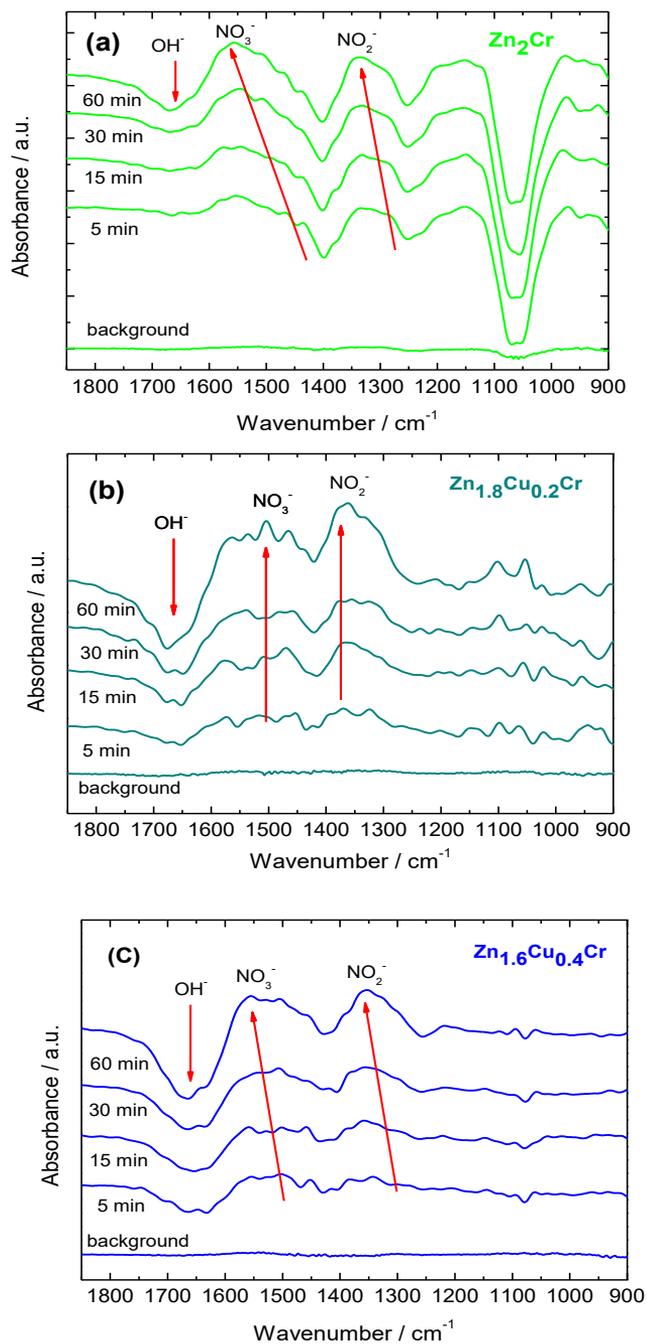
Figure S12. *In-situ DRIFTS spectra of NO photo-oxidization process under UV light illumination over the ZnCr-LDH and ZnCuCr-LDH samples.*

References

[1]   D.G. Evans, R.C.T. Slade, Structural aspects of layered double hydroxides, in: X. Duan and D.G. Evans (Ed.), Layer Double Hydroxide, Springer-Verlag Berlin, Heidelberger, 2006: pp. 1–87. https://doi.org/10.1007/430_005.

[2]   J.F. Moulder, W.F. Stickle, P.E. Sobol, K.D. Bomben, Handbook of X-ray photo-electron spectroscopy, PerkinElmer Corp., Eden Prairie, Minnesota, 1992.

[3]   M.C. Biesinger, C. Brown, J.R. Mycroft, R.D. Davidson, N.S. McIntyre, X-ray photoelectron spectroscopy studies of chromium compounds, Surf. Interface Anal. 36 (2004) 1550–1563. https://doi.org/10.1002/sia.1983.

[4]   M.C. Biesinger, L.W.M. Lau, A.R. Gerson, R.S.C. Smart, Resolving surface chemical states in XPS analysis of first row transition metals, oxides and hydroxides: Sc, Ti, V, Cu and Zn, Appl. Surf. Sci. 257 (2010) 887–898. https://doi.org/10.1016/j.apsusc.2010.07.086.

[5]   T. Uozumi, K. Okada, A. Kotani, R. Zimmermann, P. Steiner, S. Hüfner, Y. Tezuka, S. Shin, Theoretical and experimental studies on the electronic structure of M_2O_3 (M=Ti, V, Cr, Mn, Fe) compounds by systematic analysis of high-energy spectroscopy, J. Electron Spectros. Relat. Phenomena. 83 (1997) 9–20. https://doi.org/10.1016/S0368-2048(96)03063-0.

[6]   M.C. Biesinger, Advanced analysis of copper X-ray photoelectron spectra, Surf. Interface Anal. 49 (2017) 1325–1334. https://doi.org/10.1002/sia.6239.

[7]   A.A.A. Ahmed, Z.A. Talib, M.Z. bin Hussein, A. Zakaria, Zn-Al layered double hydroxide prepared at different molar ratios: Preparation, characterization, optical and dielectric properties, J. Solid State Chem. 191 (2012) 271–278. https://doi.org/10.1016/j.jssc.2012.03.013.

[8]   Y. Zhao, S. Zhang, B. Li, H. Yan, S. He, L. Tian, W. Shi, J. Ma, M. Wei, D.G. Evans, X. Duan, A Family of Visible-Light Responsive Photocatalysts Obtained by Dispersing CrO_6 Octahedra into a Hydrotalcite Matrix, Chem. Eur. J. 17 (2011) 13175–13181. https://doi.org/10.1002/chem.201101874.

[9]   S.L. Reddy, T. Endo, G.S. Reddy, Electronic (Absorption) Spectra of 3d Transition Metal Complexes, in: M.A. Farrukh (Ed.), Advanced Aspects of Spectroscopy, InTech, Rijeka, 2012: pp. 3–48. https://doi.org/10.5772/2757.

[10]   N. Gutmann, B. Muller, Insertion of the dinuclear dihydroxo-bridged Cr(III) aquo complex into the layered double hydroxides of hydrotalcite-type, J. Solid State Chem. 122 (1996) 214–220. https://doi.org/10.1006/jssc.1996.0104.

[11]   V. Rives, S. Kannan, Layered double hydroxides with the hydrotalcite-type structure containing Cu^{2+}, Ni^{2+} and Al^{3+}, J. Mater. Chem. 10 (2000) 489–495. https://doi.org/10.1039/a908534c.

[12]   F. Rodriguez-Rivas, A. Pastor, G. de Miguel, M. Cruz-Yusta, I. Pavlovic, L. Sánchez, Cr^{3+} substituted Zn-Al layered double hydroxides as UV-Vis light photocatalysts for NO gas removal from the urban environment, Sci. Total Environ. 706 (2020) 136009. https://doi.org/10.1016/j.scitotenv.2019.136009.

[13] W. Zhang, X. Dong, Y. Liang, Y. Sun, F. Dong, Ag/AgCl nanoparticles assembled on BiOCl/Bi$_{12}$O$_{17}$Cl$_2$ nanosheets: Enhanced plasmonic visible light photocatalysis and *in situ* DRIFTS investigation, Appl. Surf. Sci. 455 (2018) 236–243. https://doi.org/10.1016/j.apsusc.2018.05.171.

[14] W. Huo, W. Xu, T. Cao, X. Liu, Y. Zhang, F. Dong, Carbonate-intercalated defective bismuth tungstate for efficiently photocatalytic NO removal and promotion mechanism study, Appl. Catal. B Environ. 254 (2019) 206–213. https://doi.org/:10.1016/j.apcatb.2019.04.099.

[15] P. Chen, H. Liu, Y. Sun, J. Li, W. Cui, L. Wang, W. Zhang, X. Yuan, Z. Wang, Y. Zhang, F. Dong, Bi metal prevents the deactivation of oxygen vacancies in Bi$_2$O$_2$CO$_3$ for stable and efficient photocatalytic NO abatement, Appl. Catal. B Environ. 264 (2020). https://doi.org/10.1016/j.apcatb.2019.118545.

[16] J. Liao, W. Cui, J. Li, J. Sheng, H. Wang, X. Dong, P. Chen, G. Jiang, Z. Wang, F. Dong, Nitrogen defect structure and NO+ intermediate promoted photocatalytic NO removal on H$_2$ treated g-C$_3$N$_4$, Chem. Eng. J. 379 (2020) 122282. https://doi.org/10.1016/j.cej.2019.122282.

[17] X. Li, W. Zhang, W. Cui, J. Li, Y. Sun, G. Jiang, H. Huang, Y. Zhang, F. Dong, Reactant activation and photocatalysis mechanisms on Bi-metal@Bi$_2$GeO$_5$ with oxygen vacancies: A combined experimental and theoretical investigation, Chem. Eng. J. 370 (2019) 1366–1375. https://doi.org/10.1016/j.cej.2019.04.003.

[18] W. Huo, W. Xu, T. Cao, Z. Guo, X. Liu, G. Ge, N. Li, T. Lan, H.C. Yao, Y. Zhang, F. Dong, Carbonate doped Bi$_2$MoO$_6$ hierarchical nanostructure with enhanced transformation of active radicals for efficient photocatalytic removal of NO, J. Colloid Interface Sci. 557 (2019) 816–824. https://doi.org/10.1016/j.jcis.2019.09.089.

[19] W. Huo, T. Cao, W. Xu, Z. Guo, X. Liu, H.C. Yao, Y. Zhang, F. Dong, Facile construction of Bi$_2$Mo$_3$O$_{12}$@Bi$_2$O$_2$CO$_3$ heterojunctions for enhanced photocatalytic efficiency toward NO removal and study of the conversion process, Chinese J. Catal. 41 (2020) 268–275. https://doi.org/10.1016/S1872-2067(19)63460-1.

3.2.   Use of LDH-chromate adsorption co-product as an air purification photocatalyst
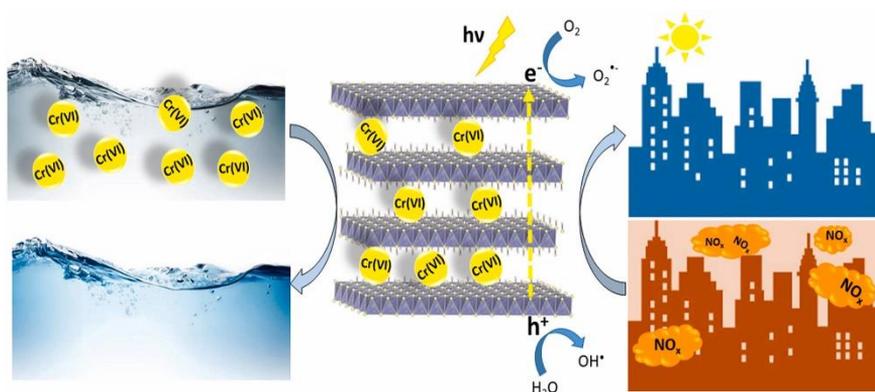
ABSTRACT

This work deals with the use of layered double hydroxides for a double environmental remediation. The residue obtained in the use of these materials as a chromate sorbent in water, was subsequently studied as a photocatalyst for the removal of NOx gases. With this aim, MgAl–CO_3 layered double hydroxides were synthesized by the coprecipitation method with a divalent/trivalent metal ratio of 3. After its calcination at 500 °C, the mixed oxide was obtained and MgAl–CrO_4 were synthesized by the reconstruction method. A complete chemical, morphological and photochemical study of the samples was carried out with techniques such as XRD, FT-IR, TGA, XRF, PL, DRIFTS and UV–Vis spectroscopy. Results showed that LDH materials presented no significant changes in their structure after their use as a sorbent. Photocatalytic tests of the samples showed a very good NO removal efficiency, as well as a high selectivity (low NO_2 emissions) through complete oxidation of these oxides to nitrate. The incorporation of chromate into the LDH structure improved the absorption of light in the visible region of the spectra, producing an improvement of 20% in the NO elimination compared with the LDH without chromate.

A. Nehdi[1], N. Frini-Srasra[1,2], G. de Miguel[3], I. Pavlovic[4], L. Sánchez[4,*], J. Fragoso[4,*]

[1]Laboratoire des Matériaux Composites et Minéraux Argileux, Centre National de Recherche en Sciences des Matériaux CNRSM, Technopôle Borj Cedria, BP 73, 8027, Soliman, Tunisia.

[2]Faculty of Sciences of Tunis (FST), Manar University, Tunisia.

[3]Departamento de Química Física y Termodinámica Aplicada, Instituto Universitario de Nanoquímica IUNAN, Universidad de Córdoba, Campus de Rabanales, E-14014, Córdoba, Spain.

[4]Departamento de Química Inorgánica, Instituto Universitario de Nanoquímica IUNAN, Universidad de Córdoba, Campus de Rabanales, E-14014, Córdoba, Spain.

HIGHLIGHTS

- LDH is used to remove pollutants from water and air successively.

- LDH-chromate adsorption product is an effective UV-Vis light DeNOx photocatalyst.

- The presence of CrO_4^{2-} anions on LDH enhances its photochemical response.

3.2.1. Introduction

Layered double hydroxides (LDH), also known as hydrotalcite like materials, are an important class of lamellar anionic clays, which have been attracting scientific attention in recent decades. Due to their unique properties and easy and inexpensive synthesis, these materials have been widely studied for many applications in different fields such as catalysis [1,2], pharmacy [3,4], polymer stabilizers [5], flame control [6], electrochemistry [7] photocatalysis [8,9], etc. They have a brucite-like structure where divalent metal ions are partially substituted by trivalent ones, and a positive charge thus generated is balanced by the arrangement of hydrated anions in the interlayer [10,11]. The composition of LDH may be expressed by the general formula $[M^{II}_{1-x}M^{III}_x(OH)_2]^{x+}(A^{n-}_{x/n})\cdot mH_2O$ where M^{II} = Mg, Zn, Ni, etc. M^{III} = Al, Cr, etc., A= CO_3^{2-}, NO_3^-, Cl^- etc., x is the value that determines the layer charge density and the anion exchange capacity, and ranges between 0.2 – 0.4. One of the peculiarities of these compounds is when calcined at 500 °C, they are converted into mixed oxides, which recover the LDH structure in the presence of anions in aqueous solutions ("memory effect").

These versatile materials can be considered as doped semiconductors where the doping agent is the transition metal cation located at the octahedral sites of the brucite sheets. The high LDH photocatalytic activity is due to the easy mobility and separation of electrons and holes created in these materials [12], as well as to the surface OH^- groups which can react with holes in the valence band and produce hydroxyl radicals, a key intermediary in photo-oxidative reactions [13].

We recently reported excellent LDH photocatalytic activity for the degradation of NO$_x$ gases (DeNOx process) [14,15]. These gases (NO$_x$ = NO + NO$_2$), emitted from industrial and traffic sources, are classified as priority air pollutants in urban zones [16]. They participate in the formation of tropospheric ozone which, when inhaled, produce respiratory problems, reduce lung function and in general, many early deaths are associated with NO$_x$ emissions [17]. Titania is the standard photocatalyst used for DeNOx applications, but it is only active under UV light ($\lambda < 387$ nm; 3.2 eV energy band gap) and not under visible light irradiation. Moreover, TiO$_2$ exhibits a low DeNOx selectivity. If we consider NO $\rightarrow$ NO$_2^-$ $\rightarrow$ NO$_2$ $\rightarrow$ NO$_3^-$ as the basic photocatalytic mechanism, a huge emission of NO$_2$, a gas much more toxic than NO, occurs during the process. However, LDH materials, besides high photocatalytic activity, also showed an outstanding selectivity (no NO$_2$ emissions) for the DeNOx process. Thus, LDH could be a highly efficient alternative to TiO$_2$ in the battle for NO$_x$ abatement.

On the other hand, one of the widely studied LDH applications is as adsorbents for water pollutants. Due to the exchangeability of interlayer anions and, the so called memory effect of its calcined product, LDH have attracted great interest for removing many inorganic and organic anions from contaminated waters [18-21]. The chromate ion is a very harmful water pollutant due to its mutagenicity, genotoxicity, bioaccumulation and carcinogenicity. It can reach surface and groundwaters as an effluent of different industries such as chrome plating, fertilizers, batteries, leather, textile, etc [22-24], as well as from filtration from metal mines or inadequate handling of mining supplies [25]. One of the proposed methods for chromate removal from waters is through its adsorption on LDH and its calcined product, and there are many reports claiming its high

adsorption capacity for this pollutant [26-32]. However, the desorption of adsorbed contaminants and the regeneration of adsorbents is the most difficult and expensive part of an adsorption technology, which could elevate the total cost for an adsorption system up to 70 % [33].

The purpose of this study is to assess the reuse of the Mg_3Al-CrO_4 adsorption residue as a desirable good in the field of photocatalysis. Thus, this work deals a double environmental remediation technology: removal of pollutants from water (chromate ion) and from air (NO_x gases) by using a single starting component, calcined MgAl-LDH. In a first step, the MgAl-LDH is used to remove chromate ions from water. Secondly, once the Mg_3Al-CrO_4 was collected and dried, this co-product was reused for the photocatalytic NO_x removal from air. For this last process, an enhanced response is expected due to the presence of interlayer chromate ions, in similarity to that found for the chemistry parent compound molybdate which electronic structure assists to the formation of electron/hole pairs [34]. The structural, morphological and optical properties of LDH chromate adsorbate are fully characterized. The changes observed are commented on with relation to their ability to perform photocatalytic DeNOx processes. The chromate containing sample shows a high photochemical activity, the oxidation mechanism being explained in the light of the results obtained by using EPR, PL and DRIFTS techniques.

3.2.2. Methods and materials

3.2.2.1. Synthesis of the photocatalyst

The preparation of $Mg_3Al-CrO_4$ proceeded in two steps: firstly, a Mg_3Al-CO_3 LDH ("MgAl" sample) was prepared by the co-precipitation method at a constant pH = 10, at room temperature [35]. Then, 0.75 mol of $Mg(NO_3)_2.6H_2O$ and 0.25 mol of $Al(NO_3)_3.9H_2O$ mixed solution (250 mL) were added dropwise to 500 mL of magnetically stirred solution containing 1.7 mol of NaOH and 0.5 mol of Na_2CO_3. The suspension thus obtained was aged for 24 h at room temperature. Then, it was centrifuged and washed several times with distilled water to eliminate the presence of nitrates, and dried. The resulting product was then thermally treated in a furnace at 500 °C for 6 h. After that, 2 g of thus obtained Mg-Al mixed oxide (named MgAl/500) was added to a 100 mL of 0.05 M K_2CrO_4 solution and stirred during 24 h to obtain reconstructed $Mg_3Al-CrO_4$ LDH (named MgAl-Cr). Then, it was centrifuged, washed several times and dried for 24h at 90 °C.

3.2.2.2. Characterization of the samples

X-ray diffraction powder (XRD) patterns were obtained using a Bruker D8 Discover instrument, with Cu Kα radiation (λ = 1.5406 Å). Infrared spectra (IR) analyses were carried out on transmission mode in a FT-MIR PerkinElmer FRONTIER with a resolution of 4 cm^{-1}. Chemical analyses were determined by X-ray fluorescence (XRF) on an ZSX Primus IV Rigaku. The water content of LDH was calculated from the thermogravimetric (TG) analysis which was obtained by using a Mettler Toledo apparatus in air atmosphere (flow: 100 mL·min^{-1}) at a heating rate of 5 °C·min^{-1}. Nitrogen adsorption–desorption isotherms were recorded in

an ASAP 2020 apparatus (Micromeritics). Prior to the sorption measurements, samples were degassed at 100 °C under vacuum for 4 h. The morphological characterizations were done by scanning electron microscopy (SEM) using a Jeol JSM 7800F microscope. Diffuse reflectance UV-Vis (DRS) spectra of the samples were recorded from 200 to 800 nm employing a Cary 5000 spectrophotometer with PTFE as reference.

3.2.2.3. Photocatalytic activity evaluation

Photocatalytic activity was examined analyzing the removal ratio of NO in a continuous-flow reactor illuminated by a sunlight irradiation box (Solarbox 3000e RH; Xe lamp with irradiances of 25 and 580 $W \cdot m^{-2}$ for UV and visible light respectively). The reactor contained the LDH photocatalyst. 300 mg of sample powder, supported in a 5x5 cm sample holder, was used in each experiment. 500 ppb NO simulated polluted atmosphere flowed through the reactor (0.3 $L \cdot min^{-1}$) with a relative humidity 50 ± 10 %. Firstly, the adsorption-desorption equilibrium between gas and sample was assured for 10 min. Subsequently, the lamp was switched on for 30 min. The concentration of NO was continuously measured by a NO_X chemiluminescence analyzer (Environnement-AC32M).

Electron paramagnetic resonance (EPR) technique assisted in corroborating the radical species involved in the photocatalytic process. The spectra were recorded at room temperature in a Bruker-EMX micro spectrometer. The spin-trap 5,5-dimethyl-1-pyrroline N-oxide (DMPO, Sigma-Aldrich) was used for radical detection. Water or methanol solutions were prepared for detecting •OH or •O_2^- radicals, respectively. The photocatalyst specimen was immersed in a 45 mM DMPO solution and

irradiated for 30 min with sunlight. Photoluminescence (PL) measurements were carried out in a FLS920 Fluorimeter (Edinburgh Instrument Ltd, Livingston, UK). A 450 W Xe lamp was employed as the excitation source in the steady-state measurements and a picosecond pulsed diode laser (l_{exc} = 406 nm and pulse width = 87 ps) was used for the time-resolved measurements. In order to find out about the photochemical DeNOx mechanism, *in-situ* diffuse reflectance infrared Fourier transform spectroscopy (DRIFTS) measurements were performed using a PerkinElmer FRONTIER FT-IR spectrometer equipped with a Harrick reaction chamber. The sample was placed in the reaction chamber, treated at room temperature under high-purity Ar flow for 10 min to remove environmental impurities. Subsequently, in the dark, a mixture of 50 mL·min^{-1} NO (100 ppm) and 50 mL·min^{-1} O_2 was pumped into the chamber, the sample being subjected to adsorption reactions for 25 min. Afterwards, light was turned on for 60 min. The spectra evolving in both periods were sequentially recorded every 5 min.

3.2.3. Results and discussion

3.2.3.1. Characterization of photocatalysts

The MgAl and MgAl-Cr XRD patterns (Fig. 1a) were both identified as hydrotalcite-like compounds indexed in a rhombohedral lattice [10]. MgAl-Cr shows strong (00l) plane reflections, which confirms the rehydration and reconstruction of the mixed oxide MgAl/500 (Fig. S1) into the LDH, after its exposure to an aqueous solution of chromate anions.

The first two peaks at 10-11°/2θ and 22-23°/2θ correspond to the basal reflections (00l), which in the case of MgAl-Cr are shifted to the right indicating a decrease in its interlayer space, compared to those of MgAl from d = 7.87 Å to d= 7.72 Å (Fig. 1a). The shortening of the interlayer distance in these layered structures is related to the grafting of CrO_4^{2-} to the metal hydroxide slab by displacing OH^- molecules [36]. After grafting, the interlayer anions are better attached to the layers and are much more difficult to exchange with other anions [37]. This is very important for the scavenging of toxics as it will prevent the eventual leaching of chromate ions from the hydrotalcite interlayer. On the other hand, a part of the chromate anions could be adsorbed by a surface complexation at the edges of hydrotalcite particles [38]. The patterns were indexed in a rhombohedral lattice with a values [a= $2d_{(110)}$] 3.06 Å and c values 23.61 Å and 23.16 Å [c=$3d_{(003)}$] corresponding to MgAl and MgAl-Cr, respectively. The crystal size was D=90.4 nm for MgAl and 90.2 nm for MgAl-Cr.

The Fourier Transform Infrared (FT-IR) spectra of both samples are shown in Fig. 1b, being characteristic of LDH compounds. In both cases, a broad band observed around 3500 cm^{-1} corresponds to the stretching vibrations of the hydrogen-bonded hydroxyl group of both hydroxide layers and interlayer water molecules, while the band at ~1639 cm^{-1} is attributed to O-H bending vibration of water molecules. The MgAl sample exhibits a strong band at 1360 cm^{-1}, which corresponds to the asymmetric stretching mode of carbonate interlayer anions. However, the presence of a weaker carbonate band (1366 cm^{-1}) is also observed in MgAl-Cr because, despite the precautions taken during the synthesis, some intercalation of carbonate is difficult to avoid, due to its high reactivity and affinity for the hydrotalcite interlayer.

Chromate incorporation in the LDH structure is verified by the appearance of an absorption band at 863 cm^{-1}, which corresponds to the stretching frequency v (Cr–O) [27]. Compared to the free anion, this band is slightly shifted toward lower frequencies (27 cm^{-1}), indicating the lowering of symmetry of the chromate ion in the LDH interlayer [31,39]. Absorptions below 800 cm^{-1} are due to lattice vibrations, involving metal–oxygen stretching modes.
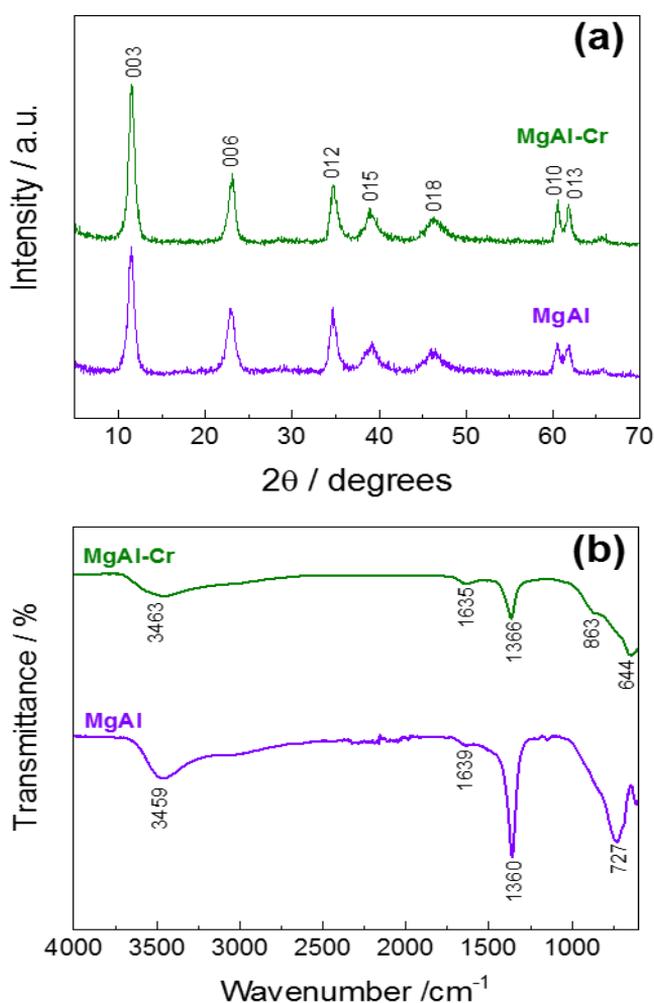

Figure 1. *(a) XRD patterns and (b) IR spectra obtained from the MgAl and MgAl-Cr samples.*

The chemical analysis of the original and modified MgAl-LDH is shown in Table 1. In both cases, the Mg:Al molar ratio is similar to that of the starting solution. Figure S2 shows that the thermal behavior of Mg–Al LDH is characterized by two main steps: up to 250 °C the physisorbed and interlayer water is lost, while at 250–500 °C the simultaneous 143ihydroxylation and decarbonization processes take place and the LDH converts into a MgAl mixed-oxide [11,40] (Fig. S1). The amount of interlayer water, determined by the thermogravimetric curves from the first weight loss, together with the Mg/Al molar ratio obtained by XRF analysis were used to propose the chemical formula of the samples. It is inferred from these results that, based on this synthetic procedure, around 30 % of anions per LDH formula can be retained as chromate.

Table 1. *Physicochemical characterization for the LDH samples.*

	% w/w			M^{2+}/M^{3+}		
LDH	Mg	Al	Cr	Atomic ratio	Proposed formula	S_{BET} /m^2g^{-1}
MgAl	23.5	8.68	-	3	$[Mg_{0.75}Al_{0.25}(OH)_2](CO_3)_{0.125} \cdot 0.62H_2O$	30
MgAl-Cr	22.3	8.54	1.85	2.9	$[Mg_{0.745}Al_{0.255}(OH)_2](CrO_4)_{0.036}(CO_3)_{0.092} \cdot 0.69H_2O$	74

The morphology of the samples was evaluated by SEM observations, Fig. 2. The MgAl sample appears as agglomerates of poor crystallized pseudo-hexagonal nanoparticles (Fig. 2a). The reconstruction of the LDH structure during the inclusion of the chromate anion leads to a better crystallization and growth of the hexagonal particles, but also to the appearance of a high presence of smaller unshaped particles (Fig. 2b). In consequence, the pore microstructure analyzed for the samples was

somewhat different. Figure S3 shows the N$_2$ adsorption-desorption isotherms measured for each sample.

Slight differences were found on the isotherms shape. The presence of a hysteresis loop suggests the presence of mesopores, which were more pronounced in the case of the MgAl sample (from 2 to 40 nm; inset Fig. S3a), fitting to a type IV isotherm. However, a large fraction of macropores was also observed in the case of the MgAl-Cr sample (from 50 to 160 nm; inset Fig. S3b) exhibiting a type II shape [15], that assigned to the adsorption on macro and non-porous materials. The specific surface area values (SSA; BET method) for both samples are given in Table 1. As usually accounts for reconstructed LDHs an increase on SSA is observed [11]. Thus, a significant value of 74 m^2·g^{-1} was measured for the MgAl-Cr sample, being more than double of that exhibited by the MgAl sample, this being of importance for its potential use in heterogeneous photocatalytic processes.
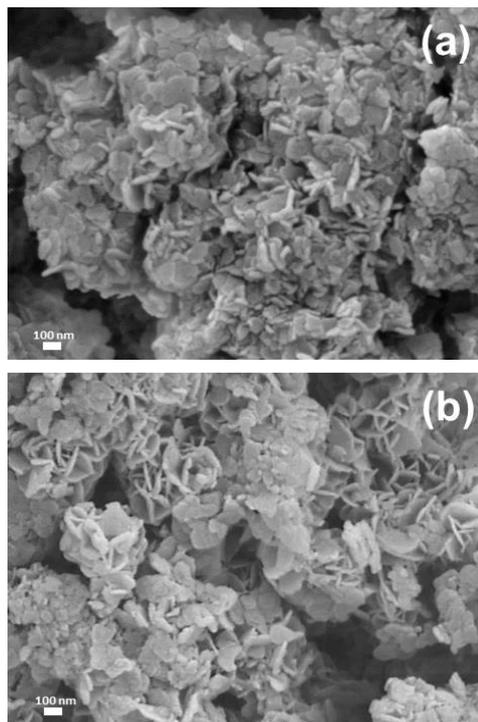
Figure 2. SEM images of the (a) MgAl and (b) MgAl-Cr samples.

Finally, in that concerning the characterization of the samples, the light absorption spectra were recorded, Fig. 3. The spectrum obtained for the MgAl sample is similar to that previously reported for this system [41]. Because of its large band-gap value, $E_g > 5.0$ eV [13,42], an intense peak at 220 nm is observed in the UV light region. Considering the activation of environmental photocatalytic processes by sunlight, the observation of bands at $\lambda > 250$ nm is most interesting. Thus, on this sample, a small absorption band at 305 nm in the UV light region is observed, with a tail extending to the visible region until 430 nm. On the other hand, two intense UV bands are observed at 275 and 370 nm for the chromate intercalated sample, the last showing a shoulder in the visible light region at 445 nm. This spectrum resembles that of chromate (VI) ions in solution and differs from those of samples containing insoluble chromate (VI)

[43,44], which could indicate the presence of CrO_4^{2-} ions grafted to metal hydroxide sheets. In summary, the spectra have shown that the chromate containing LDH sample exhibits a higher ability to harvest sunlight radiation.
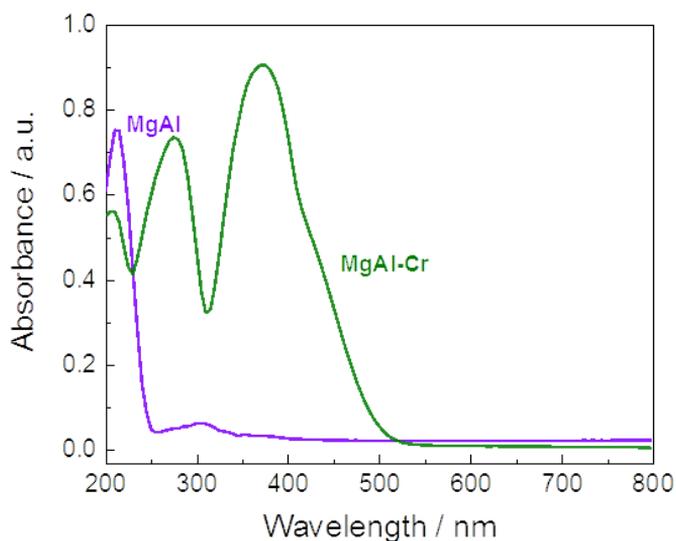
Figure 38. *UV-Vis absorption spectra of the MgAl and MgAl-Cr samples.*

3.2.3.2. Photocatalytic behaviour in DeNOx processes

Once the chromate ion is retained in the LDH structure and the resulting LDH-chromate complex shows a noticeable light absorption ability, it is interesting to test its potential use in environmental remediation processes assisted by photocatalysis. Thus, the efficiency in the photocatalytic NO gas removal from air was studied as an air purification technique. This process consists in promoting the photochemical oxidation (PCO) of nitrogen oxide gases to nitrite/nitrate (NO_2^-/NO_3^-) species, which are removed from air and retained on the surface of the photocatalyst. The successful use of different LDH as DeNOx

photocatalysts has recently been reported [15, 45-47]. Moreover, the MgAl-LDH system has also shown a modest activity in this process [13].

When the LDH photocatalyst is light irradiated, the electron in the valence band (VB) can acquire the necessary energy to jump to the conduction band (CB). Then, pairs of mobile charges (e^- and h^+) are generated and, once they reach the surface of photocatalyst particles, react with the adsorbed water and oxygen molecules. In consequence, reactive oxygen species (ROS), mainly hydroxide ($\bullet OH$) and superoxide radicals ($\bullet O_2^-$) are formed, initiating a fast oxidation of nitrogen oxide gases because of their powerful oxidant character. The evolution of the nitrogen oxide concentration profiles in the presence of the MgAl-LDH samples were recorded with the function of light irradiation time, Fig. 4. During the first 10 min, because there was no light irradiation, the NO concentration in the reaction chamber remained constant to the inlet value. However, a sudden decrease in the NO concentration values occurred once the lamp was switched on, evidencing the participation of a light activated process (Fig. 4a and 4b). For both samples, the PCO process reached a stationary state after 15 min of light irradiation. Following these experiments, the ability of each sample to remove NO gas from air could be related with the decrease in NO concentration values under light irradiation. The modest NO removal efficiency of 40 % for the MgAl sample agrees with its low ability to harvest sunlight ($\lambda > 250$ nm), Fig. 4c. However, a remarkable efficiency of 60 % was measured for the chromate containing sample; a value in line with the best reported for LDH DeNOx photocatalysts [45-47]. This test proves that LDH chromate-sorbents can successfully be reused as air purification photocatalysts. Moreover, no emission of NO_2 gas was displayed during the PCO process

(Fig. 4a and 4b). NO_2 is an expected intermediate in this PCO process [47,48], but it must be avoided since it is much more toxic than NO [49]. Therefore, the MgAl-Cr sample is a highly efficient DeNOx photocatalyst, but also environmentally sustainable because there is no release of NO_2 gas. Finally, this photocatalyst was studied in successive DeNOx runs exhibiting a small loss of NO removal efficiency, Fig. 4d.

The higher photocatalytic efficiency exhibited by MgAl-Cr, in comparison with MgAl, should be associated to their different microstructural and electronic properties. The higher specific surface area exhibited, once the LDH is reconstructed with CrO_4^{2-}, allows many active sites on particle surface to be available for the gaseous reactant molecules, increasing the process efficiency. On the other hand, the harvesting of the sunlight is remarkably done through the incorporation of chromate ions, which should eventually lead to a higher formation of ROS species and better photochemical activity. It is known that the electronic structure of a LDH could be influenced by different factors: the ionic nature and ratio of metal elements, as well as the nature of the interlayer anion [50]. On the other hand, the important role of interlayer anions in the photocatalytic activity of LDHs has also been reported [51]. Therefore, changes in the electronic structure of MgAl-LDH are expected after the incorporation of CrO_4^{2-} ions. Because of its similarity to the molecular electronic structure, the participation of chromate on the LDH electronic structure should be considered like that reported for molybdate intercalated LDH [34]. Following the predicted molecular orbital energy level diagrams for tetrahedral oxyanions of transition elements, the non-bonding HOMO orbital of chromate is a fully filled oxygen 2p orbital, while the LUMO is the molecular orbital contributing Cr (3d orbital). Thus, ligand

to metal charge transfer from HOMO to LUMO should take place under light irradiation forming additional e$^-$ and h$^+$ pairs, which favour a major production of ROS species.
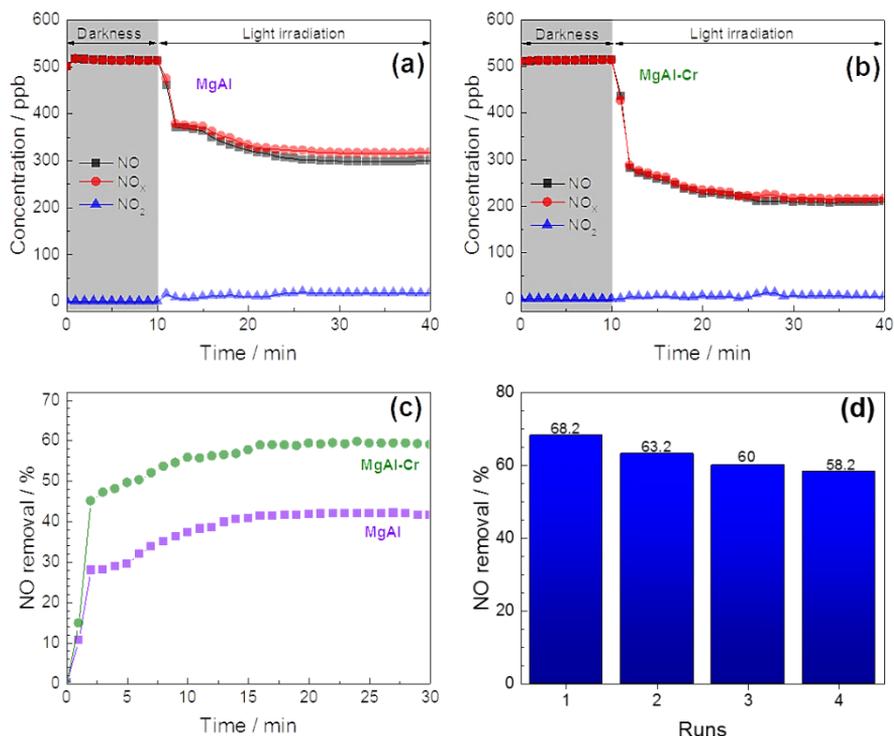

Figure 4. *NO, NO$_2$ and NO$_x$ gases concentration evolution during the photo-degradation of gaseous NO under UV-Vis light irradiation on the (a) MgAl and (b) MgAl-Cr samples. (c) NO removal efficiency for both LDH samples. (d) No removal efficiency calculated for each run of the reusability tests for the MgAl-Cr sample.*

The EPR experiments are in line with the assumed electronic structure. Figure 5 shows the EPR signal obtained using MgAl-LDH as photocatalysts and DMPO as the spin-trapping agent under sunlight excitation, in aqueous and methanol solutions (Fig. 5a and 5b, respectively). No signal was obtained for the photocatalyst suspension (blank) in darkness. An identical signal for the DMPO-•OH adduct was registered for both examples, indicating a similar ability to produce electron holes. However, in the case of the DMPO-•O$_2^-$ signal huge

differences were found, this signal being negligible for MgAl samples but very intense for MgAl-Cr. Therefore, the production of excited electrons seems to be favored by the presence of chromate ions, probably assisted by the injection of additional electrons from the HOMO → LUMO transition. In line with the results obtained from DeNOx tests, the clear production of superoxide radicals with the MgAl-Cr photocatalyst turns in a key factor enhancing the photochemical oxidation of NO gas.

An efficient charge separation and transfer of the photogenerated electron-holes is essential for the enhanced photocatalytic activity. To reveal the effect of chromate in the separation of electron-hole pairs, PL spectroscopy is employed to clarify the ability of the recombination of photogenerated species. Figure S4 exhibits a PL band centred around 405 nm in the MgAl sample (λ_{exc} = 315 nm) while a red-shifted PL peak is detected around 560 nm for the MgAl-Cr sample (λ_{exc} = 400 nm). The MgAl-Cr sample was also excited at 315 nm but no PL was detected which indicates a different deactivation mechanism in both materials. The shift in the PL position is clear evidence of the presence of the chromate species in the MgAl-Cr sample. Thus, the addition of the chromate species modifies the energy of the electronic bands opening a radiative mechanism at lower energy. In addition, Figure 5 displays the PL decay of both samples where mono- or bi-exponential functions were used to fit the experimental data. Time constant of 0.67 and 3.05 ns were obtained for the MgAl sample (Fig. 5c) in agreement with previous reports, while a longer time constant of 1341 ns was obtained for the MgAl-Cr sample (Fig. 5d). The extended time for the excited electron-hole pairs in the MgAl-Cr sample forecasts a larger reaction with O_2 to generate the superoxide species, $\bullet O_2^-$, as previously observed in the EPR measurements.
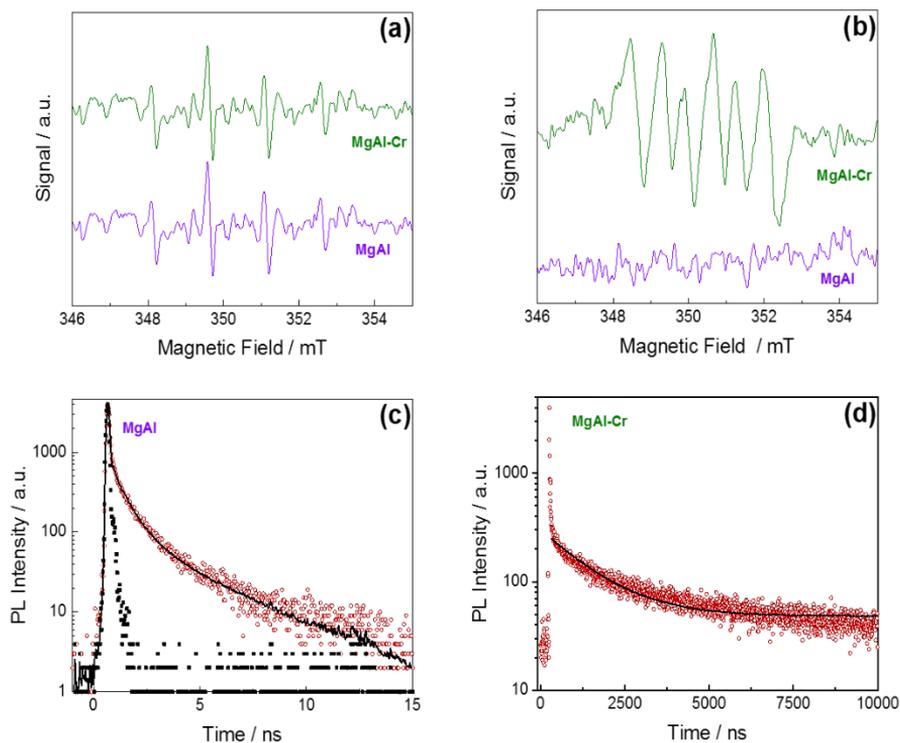
Figure 59. *DMPO spin-trapping EPR spectra of the MgAl and MgAl-Cr samples under UV-Vis light irradiation for 15 min in (a) aqueous solution for •OH and (b) methanol solution for •O$_2^-$. Decay times of the (c) MgAl and (d) MgAl-Cr samples.*

Finally, with the aim of discerning the photocatalytic removal mechanism of NO taking place on the sample surface, *in-situ* DRIFTS measurements were performed. Firstly, the NO adsorption processes in the absence of light irradiation were analyzed. Figure 6, shows sequential spectra obtained in dark conditions under NO flow for the MgAl-Cr sample, once the background (spectrum obtained before NO flow) had been subtracted. During the first 5 minutes, signals corresponding to nitrogen oxide species were registered. The appearance of NO$^-$ (1126 cm^{-1}) and NO$_2^-$ species (830, 1355, 1424 and 1490 cm^{-1}) [52-55] is a consequence of the NO disproportionation in the presence of the hydroxyl LDH groups [54]; therefore the adsorption of NO occurs on this photocatalyst. These species

were ultimately oxidized to nitrates (933, 961, 998 and 1019 cm^{-1}) [55]. After 25 minutes, as higher amounts of NO came into contact with the surface, they also suffered oxidation to N_2O_4, signal at 908 cm^{-1} [56]. Subsequently, the sample was light irradiated and then a sequential disappearance of lower oxidation nitrogen oxides species was observed, being photochemically oxidized to nitrate (961, 998 and 1019 cm^{-1}). The latter was the most abundant specie on the surface, the monodentate nitrate being gradually transformed with time into more stable bridged linkage (1227 cm^{-1}) [56]. Moreover, during the irradiation period signals of NO_2 or N_2O_4 were not observed, in line with the high DeNOx selectivity shown by this photocatalyst.
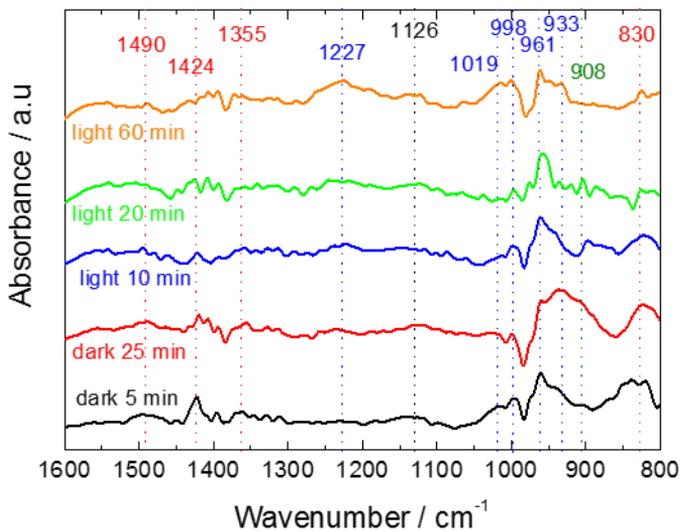
Figure 6. *DRIFTS spectra of MgAl-Cr, NO adsorption in darkness and NO oxidation processes under light illumination.*

3.2.4. Conclusions

Mixed oxide obtained by calcination of MgAl LDH is proved as an efficient sorbent to capture chromate ions from aqueous solutions. Compared to the pristine MgAl-CO$_3$ LDH, the reconstructed LDH containing chromate exhibits a modified morphology, different micropore structure and higher specific surface. Moreover, the presence of CrO$_4^{2-}$ anions enhances the ability of the LDH sample to absorb UV and Visible light. These characteristics promote the use of MgAl-Cr as a promising photocatalyst. In fact, good efficiency for NO removal is measured, which is oxidized towards nitrate on the photocatalyst surface under light irradiation. Interestingly, MgAl-Cr performs as an ecofriendly photocatalyst as no emissions of toxic NO$_2$ are accounted for during the PCO process. EPR and PL results highlight the role of chromate in the enhanced photoactivity, facilitating the production of photoexcited electrons and retarding the electron-hole recombination. The obtained results point out that LDH co-products obtained from water depollution tasks are valuable for additional environmental processes, the air purification through photocatalysis in this case, opening an interesting field of study in environmental chemical engineering.

3.2.5. Acknowledgments

3.2.6. References

[1]   J.E. Olszówka, R. Karcz, B.D. Napruszewska, A. Michalik-Zym, D. Duraczyńska, J. Kryściak-Czerwenka, A. Niecikowska, K. Bahranowski, E.M. Serwicka, Effect of Mg-Al hydrotalcite crystallinity on catalytic Baeyer-Villiger oxidation of cyclohexanone with H_2O_2/acetonitrile, Catal. Commun. 107 (2018) 48–52. https://doi.org/10.1016/j.catcom.2018.01.014.

[2]   W. Zhou, S. Zhai, J. Pan, A. Cui, J. Qian, M. He, Z. Xu, Q. Chen, Bifunctional NiGa Layered Double Hydroxide for the Aerobic Oxidation/Condensation Tandem Reaction between Aromatic Alcohols and Active Methylene Compounds, Asian J. Org. Chem. 6 (2017) 1536–1541. https://doi.org/10.1002/ajoc.201700352.

[3]   R. Acharya, A.M. Alsharabasy, S. Saha, S.H. Rahaman, A. Bhattacharjee, S. Halder, M. Chakraborty, J. Chakraborty, Intercalation of shRNA-plasmid in Mg-Al layered double hydroxide nanoparticles and its cellular internalization for possible treatment of neurodegenerative diseases, J. Drug. Deliv. Sci. Technol. 52 (2019) 500–508. https://doi.org/10.1016/j.jddst.2019.05.008.

[4]   H.J. Kim, J.Y. Lee, T.H. Kim, G.H. Gwak, J.H. Park, J.M. Oh, Radioisotope and anticancer agent incorporated layered double hydroxide for tumor targeting theranostic nanomedicine, Appl. Clay Sci. 186 (2020) 105454. https://doi.org/10.1016/j.clay.2020.105454.

[5]   C. Taviot-Guého, V. Prévot, C. Forano, G. Renaudin, C. Mousty, F. Leroux, Tailoring Hybrid Layered Double Hydroxides for the Development of Innovative Applications, Adv. Funct. Mater. 28 (2018) 1703868. https://doi.org/10.1002/adfm.201703868.

[6]   L. Jin, H.Y. Zeng, J.Z. Du, S. Xu, Intercalation of organic and inorganic anions into layered double hydroxides for polymer flame retardancy, Appl. Clay Sci. 187 (2020) 105481. https://doi.org/10.1016/j.clay.2020.105481.

[7]   M.A. González, R. Trócoli, I. Pavlovic, C. Barriga, F. la Mantia, Layered double hydroxides as a suitable substrate to improve the efficiency of Zn anode in neutral pH Zn-ion batteries, Electrochem. Commun. 68 (2016) 1–4. https://doi.org/10.1016/j.elecom.2016.04.006.

[8]   A. Mantilla, F. Tzompantzi, J.L. Fernández, J.A.I. Díaz-Góngora, G. Mendoza, R. Gómez, Photodegradation of 2,4-dichlorophenoxyacetic acid using ZnAlFe layered double hydroxides as photocatalysts, Catal. Today. 148 (2010) 119–123. https://doi.org/10.1016/j.cattod.2009.02.036.

[9]   K. Parida, M. Satpathy, L. Mohapatra, Incorporation of Fe^{3+} into Mg/Al layered double hydroxide framework: Effects on textural properties and photocatalytic activity for H_2 generation, J. Mater. Chem. 22 (2012) 7350–7357. https://doi.org/10.1039/c2jm15658j.

[10]   F. Cavani, F. Trifirò, A. Vaccari, Hydrotalcite-type anionic clays: Preparation, properties and applications., Catal. Today. 11 (1991) 173–301. https://doi.org/10.1016/0920-5861(91)80068-K.

[11]   V. Rives, Layered Double Hydroxides: Present and Future, Nova Science Publishers, New York, 2001.

[12]   K. Parida, L. Mohapatra, Recent progress in the development of carbonate-intercalated Zn/Cr LDH as a novel photocatalyst for hydrogen evolution aimed at the utilization of solar light, Dalton Trans. 41 (2012) 1173–1178. https://doi.org/10.1039/C1DT10957J.

[13]   X. Lv, J. Zhang, X. Dong, J. Pan, W. Zhang, W. Wang, G. Jiang, F. Dong, Layered double hydroxide nanosheets as efficient photocatalysts for NO removal: Band structure engineering and surface hydroxyl ions activation, Appl. Catal. B. 277 (2020) 119200. https://doi.org/10.1016/j.apcatb.2020.119200.

[14]   W. Huo, T. Cao, X. Liu, W. Xu, B. Dong, Y. Zhang, F. Dong, Anion intercalated layered-double-hydroxide structure for efficient photocatalytic NO remove, Green Energy Environ. 4 (2019) 270–277. https://doi.org/10.1016/j.gee.2018.11.001.

[15]   F. Rodriguez-Rivas, A. Pastor, C. Barriga, M. Cruz-Yusta, L. Sánchez, I. Pavlovic, Zn-Al layered double hydroxides as efficient photocatalysts for NOx abatement, Chem. Eng. J. 346 (2018) 151–158. https://doi.org/10.1016/j.cej.2018.04.022.

[16]   European Environment Agency, Air quality in Europe-2019 report, Luxembourg, 2019. https://doi.org/10.2800/822355.

[17]   B. Chen, C. Hong, H. Kan, Exposures and health outcomes from outdoor air pollutants in China, Toxicology. 198 (2004) 291–300. https://doi.org/10.1016/j.tox.2004.02.005.

[18]   D. Chaara, F. Bruna, K. Draoui, M.A. Ulibarri, C. Barriga, I. Pavlovic, Study of key parameters affecting adsorption of the herbicide Linuron on organohydrotalcites, Appl. Clay Sci. 58 (2012) 34–38. https://doi.org/10.1016/j.clay.2012.01.008.

[19]   R. Otero, J.M. Fernández, M.A. González, I. Pavlovic, M.A. Ulibarri, Pesticides adsorption – desorption on Mg – Al mixed oxides. Kinetic modelling, competing factors and recyclability, Chem. Eng. J. 221 (2013) 214–221. https://doi.org/10.1016/j.cej.2013.02.007.

[20]   S. Paikaray, M.J. Hendry, J. Essilfie-Dughan, Controls on arsenate, molybdate, and selenate uptake by hydrotalcite-like layered double hydroxides, 345 (2013) 130–138. https://doi.org/10.1016/j.chemgeo.2013.02.015.

[21]   I. Pavlovic, M.A. González, F. Rodríguez-Rivas, M.A. Ulibarri, C. Barriga, Caprylate intercalated layered double hydroxide as adsorbent of the linuron, 2,4-DB and metamitron pesticides from aqueous solution, Appl. Clay Sci. 80–81 (2013) 76–84. https://doi.org/10.1016/j.clay.2013.06.008.

[22]   Y. Fei, C. Liu, Chapter 12 - Detoxification and Resource Recovery of Chromium-Containing Wastes, in: M.N. Prasad, K. Shih (Eds.), Environmental Materials and Waste, Academic Press, 2016: pp. 265–284. https://doi.org/10.1016/B978-0-12-803837-6.00012-3.

[23]   E. Kaprara, N. Kazakis, K. Simeonidis, S. Coles, A.I. Zouboulis, P. Samaras, M. Mitrakas, Occurrence of Cr(VI) in drinking water of Greece and relation to the

geological background, J. Hazard. Mater. 281 (2015) 2–11. https://doi.org/10.1016/j.jhazmat.2014.06.084.

[24]   N. Koleli, A. Demir, Chapter 11 - Chromite, in: M.N. Prasad, K. Shih (Eds.), Environmental Materials and Waste, Academic Press, 2016: pp. 245–263. https://doi.org/10.1016/B978-0-12-803837-6.00011-1.

[25]   K.E. Ukhurebor, U.O. Aigbe, R.B. Onyancha, W. Nwankwo, O.A. Osibote, H.K. Paumo, O.M. Ama, C.O. Adetunji, I.U. Siloko, Effect of hexavalent chromium on the environment and removal techniques: A review., J. Environ. Manage. 280 (2021) 111809. https://doi.org/10.1016/j.jenvman.2020.111809.

[26]   H.P. Chao, Y.C. Wang, H.N. Tran, Removal of hexavalent chromium from groundwater by Mg/Al-layered double hydroxides using characteristics of in-situ synthesis, Environ. Pollut. 243 (2018) 620–629. https://doi.org/10.1016/j.envpol.2018.08.033.

[27]   M. del Arco, D. Carriazo, C. Martín, A.M. Pérez Grueso, V. Rives, Characterization of chromate-intercalated layered double hydroxides, Mater. Sci. Forum 514-516 (2006) pp. 1541–1545. https://doi.org/10.4028/www.scientific.net/MSF.514-516.1541

[28]   L.C. Hsu, Y.M. Tzou, P.N. Chiang, W.M. Fu, M.K. Wang, H. Yi, Y.T. Liu, Adsorption mechanisms of chromate and phosphate on hydrotalcite: A combination of macroscopic and spectroscopic studies, Environ. Pollut. 247 (2019) 180–187. https://doi.org/10.1016/j.envpol.2019.01.012.

[29]   N.K. Lazaridis, T.A. Pandi, K.A. Matis, Chromium(VI) Removal from Aqueous Solutions by Mg−Al−CO$_3$ Hydrotalcite: Sorption−Desorption Kinetic and Equilibrium Studies, Ind. Eng. Chem. Res. 43 (2004) 2209–2215. https://doi.org/10.1021/ie030735n.

[30]   Y. Lu, B. Jiang, L. Fang, F. Ling, J. Gao, F. Wu, X. Zhang, High performance NiFe layered double hydroxide for methyl orange dye and Cr(VI) adsorption, Chemosphere. 152 (2016) 415–422. https://doi.org/10.1016/j.chemosphere.2016.03.015.

[31]   S.V. Prasanna, R.A.P. Rao, P.V. Kamath, Layered double hydroxides as potential chromate scavengers, 304 (2006) 292–299. https://doi.org/10.1016/j.jcis.2006.08.064.

[32]   H.N. Tran, D.T. Nguyen, G.T. Le, F. Tomul, E.C. Lima, S.H. Woo, A.K. Sarmah, H.Q. Nguyen, P.T. Nguyen, D.D. Nguyen, T.V. Nguyen, S. Vigneswaran, D.V.N. Vo, H.P. Chao, Adsorption mechanism of hexavalent chromium onto layered double hydroxides-based adsorbents: A systematic in-depth review, J. Hazard. Mater. 373 (2019) 258–270. https://doi.org/10.1016/j.jhazmat.2019.03.018.

[33]   K.H. Goh, T.T. Lim, Z. Dong, Application of layered double hydroxides for removal of oxyanions: A review, Water Res. 42 (2008) 1343–1368. https://doi.org/10.1016/j.watres.2007.10.043.

[34]   L. Mohapatra, K. Parida, M. Satpathy, Molybdate/Tungstate Intercalated Oxo-Bridged Zn/Y LDH for Solar Light Induced Photodegradation of Organic Pollutants, J. Phys. Chem. C. 116 (2012) 13063–13070. https://doi.org/10.1021/jp300066g.

[35] N.A. Comelli, M.L. Ruiz, N.A. Merino, I.D. Lick, E. Rodríguez-Castellón, A. Jiménez-López, M.I. Ponzi, Preparation and characterisation of calcined Mg/Al hydrotalcites impregnated with alkaline nitrate and their activities in the combustion of particulate matter, Appl. Clay Sci. 80–81 (2013) 426–432. https://doi.org/10.1016/j.clay.2013.05.013.

[36] M. del Arco, D. Carriazo, S. Gutiérrez, C. Martín, V. Rives, Synthesis and Characterization of New Mg_2Al-Paratungstate Layered Double Hydroxides, Inorg. Chem. 43 (2004) 375–384. https://doi.org/10.1021/ic0347790.

[37] U. Costantino, M. Casciola, L. Massinelli, M. Nocchetti, R. Vivani, Intercalation and grafting of hydrogen phosphates and phosphonates into synthetic hydrotalcites and a.c.-conductivity of the compounds thereby obtained, Solid State Ion. 97 (1997) 203–212. https://doi.org/10.1016/S0167-2738(97)00043-X.

[38] M. Jobbágy, A.E. Regazzoni, Complexation at the edges of hydrotalcite: the cases of arsenate and chromate, J. Colloid. Interface Sci. 393 (2013) 314–318. https://doi.org/10.1016/j.jcis.2012.10.069.

[39] F. Malherbe, L. Bigey, C. Forano, A. de Roy, J.P. Besse, Structural aspects and thermal properties of takovite-like layered double hydroxides pillared with chromium oxo-anions, J. Chem. Soc., Dalton Trans. (1999) 3831–3839. https://doi.org/10.1039/A903766G.

[40] R.L. Frost, A.W. Musumeci, T. Bostrom, M.O. Adebajo, M.L. Weier, W. Martens, Thermal decomposition of hydrotalcite with chromate, molybdate or sulphate in the interlayer, Thermochim Acta. 429 (2005) 179–187. https://doi.org/10.1016/j.tca.2005.03.014.

[41] G. Gao, Z. Zhu, J. Zheng, Z. Liu, Q. Wang, Y. Yan, Ultrathin magnetic Mg-Al LDH photocatalyst for enhanced CO_2 reduction: Fabrication and mechanism, J. Colloid. Interface Sci. 555 (2019) 1–10. https://doi.org/10.1016/j.jcis.2019.07.025.

[42] A. Mantilla, G. Jácome-Acatitla, G. Morales-Mendoza, F. Tzompantzi, R. Gómez, Photoassisted Degradation of 4-Chlorophenol and p-Cresol Using MgAl Hydrotalcites, Ind. Eng. Chem. Res. 50 (2011) 2762–2767. https://doi.org/10.1021/ie1006883.

[43] J. Kuncewicz, P. Ząbek, G. Stochel, Z. Stasicka, W. Macyk, Visible light driven photocatalysis in chromate(VI)/TiO_2 systems—Improving stability of the photocatalyst, Catal. Today. 161 (2011) 78–83. https://doi.org/10.1016/j.cattod.2010.10.075.

[44] T.R. Zheng, L.L. Qian, M. Li, Z.X. Wang, K. Li, Y.Q. Zhang, B.L. Li, B. Wu, A bifunctional cationic metal–organic framework based on unprecedented nonanuclear copper(II) cluster for high dichromate and chromate trapping and highly efficient photocatalytic degradation of organic dyes under visible light irradiation, Dalton Trans. 47 (2018) 9103–9113. https://doi.org/10.1039/C8DT01685B.

[45] J. Fragoso, M.A. Oliva, L. Camacho, M. Cruz-Yusta, G. de Miguel, F. Martin, A. Pastor, I. Pavlovic, L. Sánchez, Insight into the role of copper in the promoted photocatalytic removal of NO using $Zn_{2-x}Cu_xCr$-CO_3 layered double hydroxide, Chemosphere. 275 (2021) 130030. https://doi.org/10.1016/j.chemosphere.2021.130030.

[46]   A. Pastor, F. Rodriguez-Rivas, G. de Miguel, M. Cruz-Yusta, F. Martin, I. Pavlovic, L. Sánchez, Effects of Fe^{3+} substitution on Zn-Al layered double hydroxides for enhanced NO photochemical abatement, Chem. Eng. J. 387 (2020) 124110. https://doi.org/10.1016/j.cej.2020.124110.

[47]   F. Rodriguez-Rivas, A. Pastor, G. de Miguel, M. Cruz-Yusta, I. Pavlovic, L. Sánchez, Cr^{3+} substituted Zn-Al layered double hydroxides as UV-Vis light photocatalysts for NO gas removal from the urban environment, Sci. Total Environ. 706 (2020) 136009. https://doi.org/10.1016/j.scitotenv.2019.136009.

[48]   J. Balbuena, M. Cruz-Yusta, L. Sánchez, Nanomaterials to Combat NOx Pollution, J. Nanosci. Nanotechnol. 15 (2015) 6373–6385. https://doi.org/10.1166/jnn.2015.10871.

[49]   R.J. Lewis, Sax's Dangerous Properties of Industrial Materials, 5 Volume Set, 12th Edition, Twelth, Wiley & Sons, New Jersey, 2012.

[50]   M.J. Wu, J.Z. Wu, J. Zhang, H. Chen, J.Z. Zhou, G.R. Qian, Z.P. Xu, Z. Du, Q.L. Rao, A review on fabricating heterostructures from layered double hydroxides for enhanced photocatalytic activities, Catal. Sci. Technol. 8 (2018) 1207–1228. https://doi.org/10.1039/C7CY02314F.

[51]   L. Mohapatra, K. Parida, A review on the recent progress, challenges and perspective of layered double hydroxides as promising photocatalysts, J. Mater. Chem. A Mater. 4 (2016) 10744–10766. https://doi.org/10.1039/C6TA01668E.

[52]   W. Huo, W. Xu, T. Cao, X. Liu, Y. Zhang, F. Dong, Carbonate-intercalated defective bismuth tungstate for efficiently photocatalytic NO removal and promotion mechanism study, Appl. Catal. B. 254 (2019) 206–213. https://doi.org/10.1016/j.apcatb.2019.04.099.

[53]   X. Li, W. Zhang, W. Cui, J. Li, Y. Sun, G. Jiang, H. Huang, Y. Zhang, F. Dong, Reactant activation and photocatalysis mechanisms on Bi-metal@Bi_2GeO_5 with oxygen vacancies: A combined experimental and theoretical investigation, Chem. Eng. J. 370 (2019) 1366–1375. https://doi.org/10.1016/j.cej.2019.04.003.

[54]   J. Liao, W. Cui, J. Li, J. Sheng, H. Wang, X. Dong, P. Chen, G. Jiang, Z. Wang, F. Dong, Nitrogen defect structure and NO+ intermediate promoted photocatalytic NO removal on H_2 treated g-C_3N_4, Chem. Eng. J. 379 (2020) 122282. https://doi.org/10.1016/j.cej.2019.122282.

[55]   W. Zhang, X. Dong, Y. Liang, Y. Sun, F. Dong, Ag/AgCl nanoparticles assembled on BiOCl/$Bi_{12}O_{17}Cl_2$ nanosheets: Enhanced plasmonic visible light photocatalysis and *in situ* DRIFTS investigation, Appl. Surf. Sci. 455 (2018) 236–243. https://doi.org/10.1016/j.apsusc.2018.05.171.

[56]   P. Chen, H. Liu, Y. Sun, J. Li, W. Cui, L. Wang, W. Zhang, X. Yuan, Z. Wang, Y. Zhang, F. Dong, Bi metal prevents the deactivation of oxygen vacancies in $Bi_2O_2CO_3$ for stable and efficient photocatalytic NO abatement, Appl. Catal. B. 264 (2020). https://doi.org/10.1016/j.apcatb.2019.118545.

## Appendix II: Supporting Information
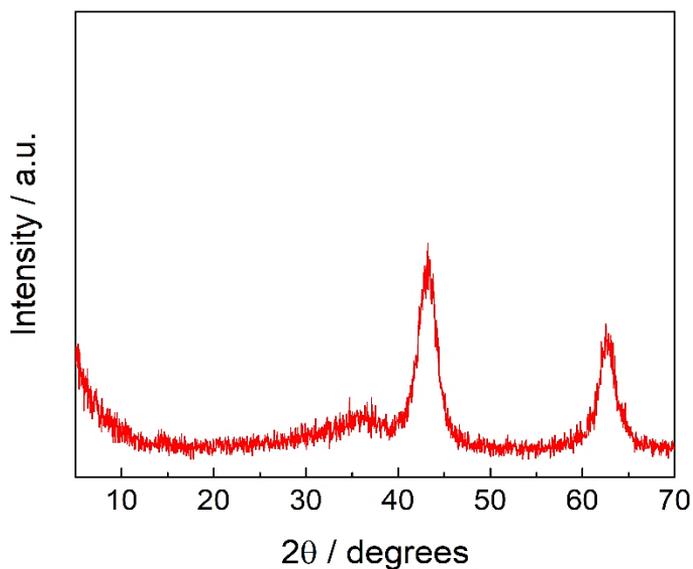
**Figure S1.** *XRD pattern of the MgAl/500 sample.*
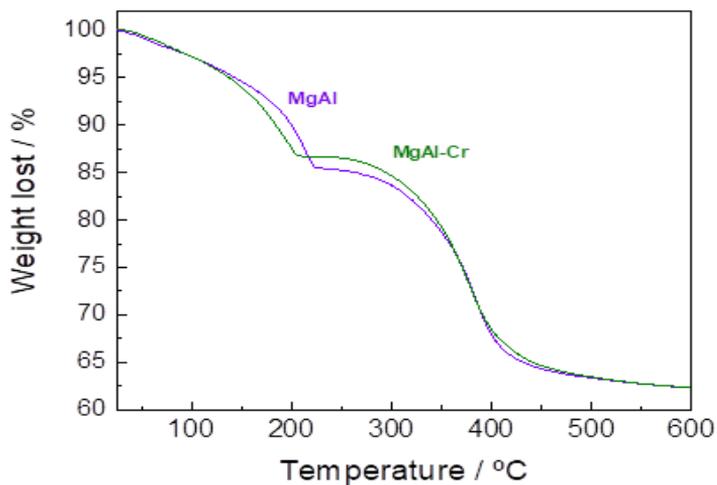
Figure S2. *Thermogravimetric patterns of the MgAl and MgAl-Cr samples.*
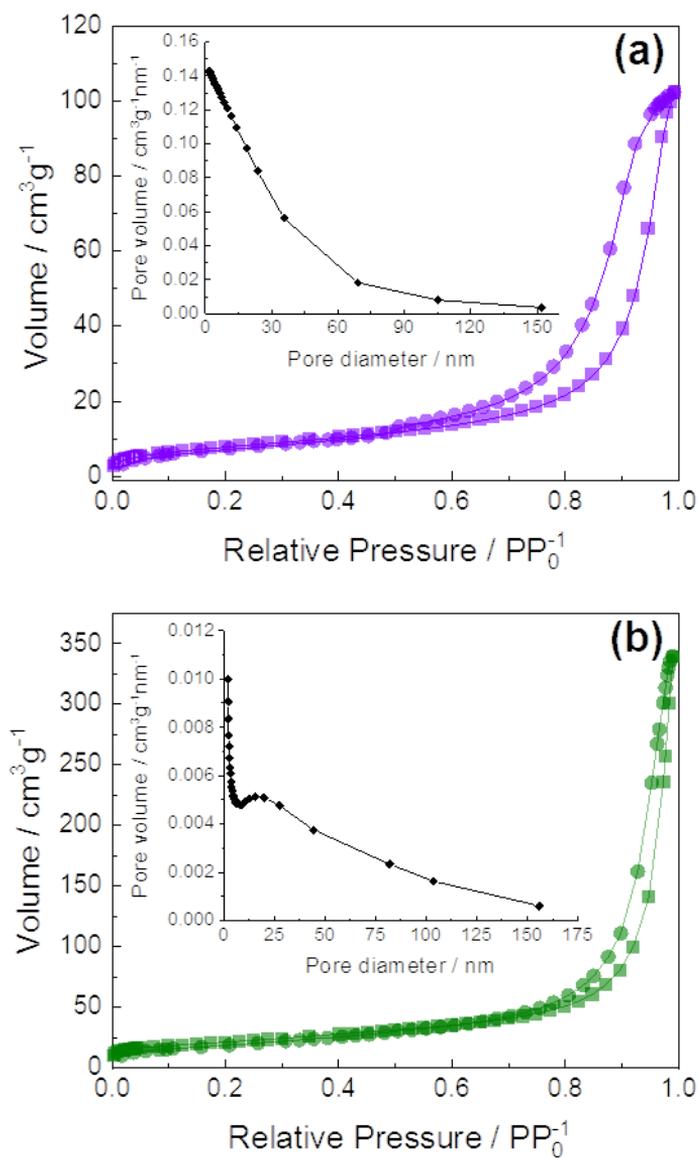
**Figure S3.** *N$_2$ adsorption-desorption isotherms and pore size distribution of the (a) MgAl and (b) MgAl-Cr samples.*
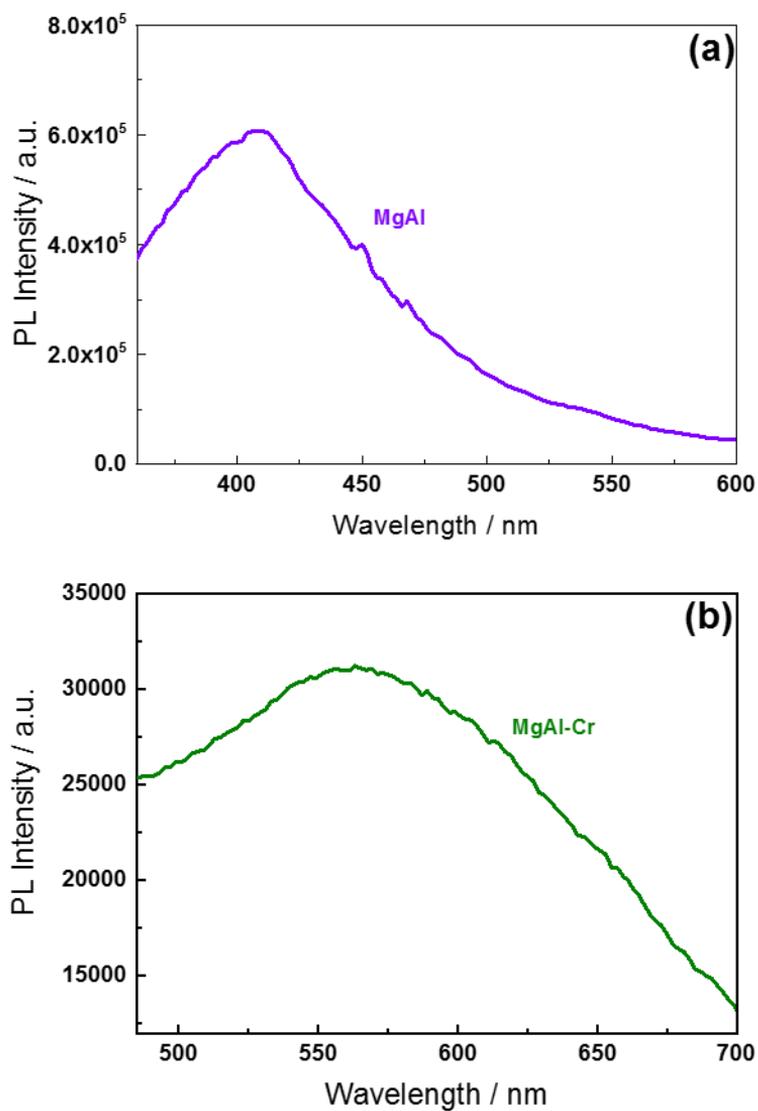
Figure S4. *Photoluminescence spectra of the (a) MgAl (λ_{exc} = 315) and (b) MgAl-Cr (λ_{exc} = 400) samples.*

3.3. Graphene quantum dots/NiTi layered double hydroxide heterojunction as a highly efficient DeNOx photocatalyst with long persistent post-illumination action
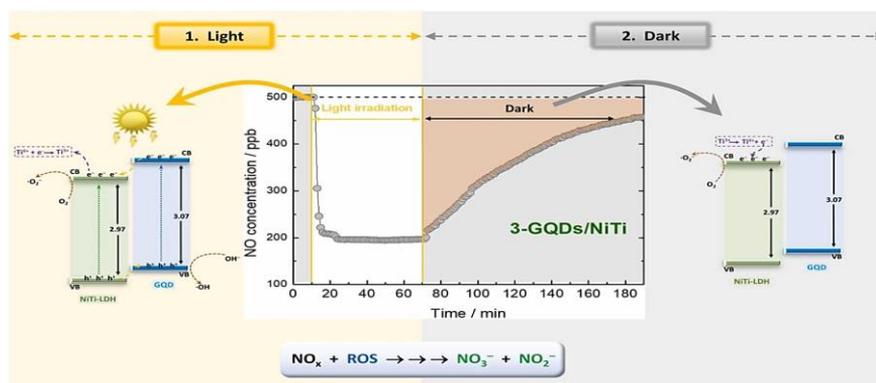
ABSTRACT

Persistent photocatalysis is an attractive process to broaden the spectrum of environmental applications. Herein, blue luminescent graphene quantum dots (GQD) are incorporated into NiTi-based layered double hydroxide nanosheets (NiTi-LDH) by a facile impregnation method. The enhanced performance of GQD/NiTi-LDH leads to excellent NO photo-removal activity (61 %) and insignificant NO_2 release (< 0.6 %), beating the standard TiO_2 P25 (48 % and 14.2 %, respectively). Interestingly, after the end of light irradiation period, GQD/NiTi-LDH maintained a NO removal efficiency higher than 20 % for up to 75 min regardless of the previous irradiation time. This De-NOx post photocatalytic process is the most effective reported at present. The dark/light mechanism is explained by the electron storage capacity of NiTi-LDH under light excitation, which is assisted by the electron migration from GQD to NiTi-LDH. Once the light is shut off, electrons are released and take part in the superoxide radical generation.

J. Fragoso[1], A. Pastor[1,*], M. Cruz-Yusta[1], F. Martin[2], G. de Miguel[3,] I. Pavlovic[1], M. Sánchez[1], L. Sánchez[1,*].

[1]Departamento de Química Inorgánica, Instituto Químico para la Energía y Medioambiente IQUEMA, Universidad de Córdoba, Campus de Rabanales, E-14014, Córdoba, Spain.

[2]Departamento de Ingeniería Química, Facultad de Ciencias, Universidad de Málaga, Campus de Teatinos, E-29071, Málaga, Spain.

[3]Departamento de Química Física y Termodinámica Aplicada, Instituto Químico para la Energía y Medioambiente IQUEMA, Universidad de Córdoba, Campus de rabanales, E-14014, Córdoba, Spain.

HIGHLIGHTS

- GQD/NiTi beats standard TiO_2 P25 (NO_x removal: 61 vs 48; emitted NO_2 0.6 bs 14.2%).

- GQD/NiTi photocatalysts show outstanding selectivity to nitrate/nitrite (>98%).

- GQD charge injection promotes electron storage capacity in NiTi-LDH.

- GQD/NiTi shows exceptional post-photocatalytic effect.

- Post-photocatalysis is independent of the irradiation time and lasts up to 75 min.

3.3.1. Introduction

The photocatalytic processes and related materials have been deeply studied as adequate environmental air remediation tools promoting the pollutant removal from the urban atmosphere [1]. The environmental photocatalytic air purification proceeds only under continuous external light irradiation source, this being the sunlight. Once light irradiation is absent, after sunset or because of the presence of clouds, the pollutant removal finishes immediately.

Due to the high levels of atmospheric pollutants in geographical areas with large population, it is desirable that the removal of pollutants continue after sunset. This action is highly interesting for the removal of the NO_x gases (De-NOx action) from the urban atmosphere.

Nitrogen oxides, NO_x ($NO_x = NO + NO_2$), cause serious environmental problems and negative effects on human health [2]. The emission and accumulation of these gases in the urban atmosphere frequently exceed the limits recommended by international health institutions, this being a major concern for society [3]. Over the last two decades, high attention has been paid to the development of advanced photocatalysts, with successful results in terms of NO_x removal and De-NOx selectivity under both UV and Visible light irradiation [4-6]. A typical curve of variations in NO_x emissions for highly populated cities is shown in Figure S1. It is observed that a main peak of NO_x pollution occurs between 5 and 12 h. During this period, the photocatalytic process is useful for removing the pollutant gas.

Of importance, the NO_x concentration levels increase after the sunset, from 19 to 24 h. During this period the nitrogen oxide gases cannot be photocatalytically removed because of the absence of light irradiation. Therefore, it is highly interesting to develop new systems that allow the De-NOx process to be maintained once light irradiation is off, an action scarcely explored in this research field. To our knowledge, only few works from T. Sato´s research group have paid attention to the post-catalytical NO_x removal in dark conditions [7-10].

Persistent Photo Catalysis (PPC) is a recent field of study aiming to sustain the photocatalytic processes once the light is off. In this sense, the development of post-photocatalytic reactions in the dark is assisted by two main processes: persistent luminescence and photo-assisted chemical reactions [11-13].

In the first case, materials with persistent luminescence (MPL) are mixed with photocatalytic materials (PCM) to prepare MPL@PCM composites. Basis on the storage capacity of the MPLs when they are illuminated for a short time, once the light is off, their correlated persistent luminescence is used by the PCM as a light source to sustain a self-induced photocatalytic activity in dark conditions. MPLs are mainly prepared by using rare earth elements as dopants, also being relevant the use of transition metal dopants (*vg.* $Sr_2SiO_4:Eu^{2+}$ [14], $CaAl_2O_4:Ce^{3+}$ [15], $Ca_6BaP_4O_{17}:Eu^{2+}$ [16], $CaAl_2Si_2O_8:Eu^{2+}$, Dy^{3+} [17], $Ca_4(PO_4)_2O:Eu^{2+},Y^{3+}$ [18], $MgAl_2Si_2O_8:Mn^{4+}$ [19], $ZnGa_2O_4:Cr^{3+}$ [20], $Zn_2GeO_4:Mn^{2+}$ [21]).

In the second case, the existence of an electron storage material (ESM) is required to allow the photocatalytic process to proceed under dark conditions. Basically, when the light source is on, the ESM is involved

in the storage of electrons through the formation of an intermediate compound. In the absence of light this process is reverted, and electrons are released, sustaining the catalytic activity. Typical ESM materials are: TiO_2/WO_3 [22,23], $TiO_2/Ni(OH)_2$ [24], TiO_2/Cu_2O [25], Au-TiO_2/WO_3 [26], TiON/PdO [27], g-C_3N_4/CNTs/Gr [28], between others [12].

From the above, it is interesting to use PPC to enlarge the amount per day of NO_x removed in the urban atmosphere. Sato´s group proposed the use of MPL@PCM composites using $CaAl_2O_4$:(Eu,Nd) as MPL together with different photocatalytic materials such as $TiO_{2-x}N_y$, (Ta,N)-codoped TiO_2/Fe_2O_3, $SrTiO_3/Fe_2O_3$ or Cr-doped $SrTiO_3$ [7-10]. Once the light was off, post-photocatalytic De-NOx reactions during 100 – 180 min were observed for these materials. However, the NO_x removal efficiency was as low as 8 – 10 % and only a substantial abatement of NO_x gases was accounted for during the first 15 mins in the dark. Since they are usually lower cost and easier to prepare than MPL materials, to enhance the post-photocatalytic De-NOx process in terms of efficiency and lifetime, we have studied the use of ESM materials.

In this work, we have successfully implemented the preparation of graphene quantum dots/layered double hydroxides as the first LDH-based heterojunction with a successful post-photocatalytic De-NOx response. Ni_3Ti-CO_3 layered double hydroxide (LDH) was selected because of its outstanding De-NOx ability (high NO conversion, outstanding selectivity and stable photocatalytic activity in running tests) [29]. In addition, it is known that some TiO_2-based heterojunctions lead to persistent photocatalysis. Specifically, the TiO_2/Cu_2O system has been demonstrated to photochemically works under dark conditions thanks to the prior accumulation of electrons in TiO_2 by Ti^{4+} partial reduction. This charge

accumulation into TiO_2 comes from the electron injection from the Cu_2O phase under light conditions. Subsequently, the stored electrons are further released in the dark to promote photochemical reactions [25,30,31]. Similarly, the high dispersion of TiO_6 octahedra in NiTi-LDH and its pseudocapacitor properties might lead to these compounds acting as ESM [32,33]. On the other hand, the study of quantum dots (QDs) as a new type of light responsive 0D material with extraordinary applications in photocatalysis has flourished in the last decade [34-37]. Thus, the benefits of the use of carbon (CQDs) or graphene quantum dots (GQDs) in photocatalytic heterojunctions, specifically, enhanced photocatalytic activities (higher De-NOx efficiency) [38-42] and the potential luminescence light harvesting [43,44] were recently reported.

From the above premises, herein we propose the GQDs/Ni₃Ti-LDH compounds as new and efficient persistent De-NOx photocatalysts. We have prepared Ni_3Ti-CO_3 LDHs nanosheets by the Aqueous Miscible Organic Solvent Treatment (AMOST) [45], which were subsequently mixed with blue luminescent GQDs to form a 0D/2D heterojunction. A multi-technique characterization enabled light to be shed on the physicochemical properties and the photocatalytic performance of the samples. We found that GQDs/Ni₃Ti compounds exhibit good photocatalytic NO_x removal under UV and/or Visible light, and with a considerable persistence of the catalytic reaction in the dark. The persistent photocatalytic mechanism was explained on the basis of the results obtained by using EPR and DRIFTS techniques. The appealing post-photocatalytic De-NOx performance of the obtained materials opens the door to exploring LDHs compounds as new materials for persistent photocatalytic processes.

3.3.2. Experimental

3.3.2.1. Materials

Ni(NO$_3$)$_2$·6H$_2$O, titanium isopropoxide (abbreviated as Ti(O^{i}Pr$_4$), Na$_2$CO$_3$, NaOH, HCl, K$_2$Cr$_2$O$_7$, p-benzoquinone (PBQ), Nafion^{TM} 117 solution and 5,5-dimethyl-1-pyrroline-N-oxide (DMPO) were purchased from Sigma-Aldrich. Ethanol (EtOH; 99.8%) and methanol (99.9%) were purchased from PanReac AppliChem. Demineralised water was used in all the experiments. Blue luminescent graphene quantum dots (1 mg·mL^{-1} in H$_2$O; abbreviated as GQDs) were purchased from Sigma-Aldrich, for which a complete characterization is provided in Figs. S2. The measured Quantum Yield of the GQDs was 87%.

3.3.2.2. Preparation of Ni$_3$Ti-CO$_3$ LDH nanosheets and GQDs/Ni$_3$Ti-LDH photocatalysts

The synthesis of Ni$_3$Ti-CO$_3$ LDH compound, labelled as NiTi-LDH, was carried out by the coprecipitation method following by the AMOST, as described in our previous work [29] and detailed in Supplementary Information (SI). The impregnation method was used to prepare photocatalysts containing GQDs with 1 wt% and 3 wt% of GQDs. For the first one, 0.3 g of NiTi-LDH nanosheets were placed in a glass petri dish (Ø = 40 mm) and 3 mL of GQD aqueous dispersion and 2 mL water were added. The slurry was stirred using a magnetic bar and heated to 50 °C to evaporate the solvent. Subsequently, 5 mL of EtOH were added while stirring and the solvent was allowed to evaporate at room temperature, the sample being collected and labelled as 1-GQDs/NiTi. To prepare the photocatalyst with 3 wt% of GQDs, 3-GQDs/NiTi sample, a similar

procedure was carried out, but 9 mL of GQDs aqueous dispersion and 9 mL of EtOH were now used.

3.3.2.3. Characterization and photocatalytic experiments

The structural, morphological, chemical identity and physical properties of the compounds were characterised by using different techniques: X-ray diffraction (XRD), X-ray photoelectron spectroscopy (XPS), infrared spectroscopy (IR), high-resolution transmission electron microscopy (HRTEM); thermogravimetric analysis (TGA), nitrogen adsorption–desorption isotherms study, ultraviolet-visible spectroscopy (UV-Vis), ultraviolet-visible diffuse reflectance spectroscopy (UV-vis DRS), steady-state photoluminescence (PL), time-resolved photoluminescence (TRPL), electron paramagnetic resonance (EPR), *in-situ* diffuse reflectance infrared Fourier transform spectra (DRIFTS), ultraviolet photoelectron spectroscopy (UPS) and electrochemical measurements (Mott-Schottky). Additional detailed information about these studies is provided in "Supplementary Information" (SI).

The ISO 22197-1 method was used to carried out the NO gas abatement photocatalytic experiments. This is a method used to characterise the air purification measurement. The ability of the photocatalysts to induce NO photo-oxidation was assessed in a laminar flow reactor containing a 50×50 mm quartz sample holder with 300 mg of the powdered sample. The reactor was placed inside a solar simulator (Solarbox 3000e RH with Xe lamp; 36 and 250 $W \cdot m^{-2}$ irradiances for UV and visible light, respectively). Experiments were also carried out under visible light irradiation by using a LED ($\lambda = 420$ nm; irradiance = 510 $W \cdot m^{-2}$). De-NOx experiments were performed using NO gas (500 ppb; air balanced)

as a reactant (flow rate gas = 0.37 L·min^{-1}). The relative humidity was controlled to 50 ± 5% by passing the air flow through a gas-washing bottle filled with demineralised water. Adsorption−desorption equilibrium for the photocatalysts was achieved after passing the air/NO flow in the dark for 10 minutes, before the irradiation period started. A photocatalytic blank test (empty sample holder) was carried out in order to discard NO photolysis. A chemiluminescence analyser (Environment AC32M) measured the concentration of NO, NO_x and NO_2 gases from the reactor outlet. Tests were repeated three times and the average concentration values were calculated. The obtained standard deviations were ∼ 0.3 ppb for NO concentration and ∼ 1.0 ppb for NO_2 and NO_x concentrations. The photocatalytic performance of the samples was studied regarding the NO, NO_x and selectivity (S) indexes:

$$NO\ conversion\ (\%) = \frac{[NO]_{in} - [NO]_{out}}{[NO]_{in}} \times 100 \qquad (1)$$

$$NO_x\ conversion\ (\%) = \frac{[NO_x]_{in} - [NO_x]_{out}}{[NO_x]_{in}} \times 100 \qquad (2)$$

$$Selectivity;\ S\ (\%) = \frac{([NO_x]_{in} - [NO_x]_{out})/[NO_x]_{in}}{([NO]_{in} - [NO]_{out})/[NO]_{in}} \times 100 \qquad (3)$$

where $[NO]_{in}$, $[NO_x]_{in}$ and $[NO]_{out}$, $[NO_x]_{out}$ is the measured inlet and outlet concentrations, respectively, and $[NO_x]=[NO]+[NO_2]$.

3.3.3. Results and Discussion

3.3.3.1. Composition and structural characterization

The X-ray diffraction (XRD) patterns corresponding to NiTi-LDH and GQDs/NiTi samples are shown in Fig. 1a. These exhibit the characteristic reflections expected for a Ni_3Ti-CO_3 LDH prepared via the Aqueous Miscible Organic Solvent Treatment (AMOST procedure) [29]. The reflections for the (*003*) and (*006*) basal planes are located at 2θ ~ 10.9° and 22°, respectively, while the rest of the peaks at a higher 2θ angle correspond to (*012*), (*015*) and (*110*) planes [46].

The basal spacing d_{003} was calculated to be 8.09 Å, typical for a Ni_3Ti-AMO LDH and consistent with the presence of carbonate as the interlayer anion and the coexistence of ethanol molecules in the LDH gallery. During the AMOST procedure the organic solvent molecules replace the co-intercalated water molecules present in the interlayer galleries and, because the hydrogen bonding between layers is reduced [47], the LDH layer delamination is favoured and consequently layer stacking is reduced [45]. Thus, the basal XRD reflections were broad and low in intensity (Fig. 1a). On the other hand, the addition of GQDs during the AMOST procedure does not alter the LDH structure, as similar patterns were observed for GQDs/NiTi samples. Fig. 1b shows FT-IR spectra obtained for both samples. The intense and lower in frequency bands at 575 and 778 cm^{-1} correspond, respectively, to the M-O and HO-M-OH vibrational bending modes in the basal layer [48]. The vibration mode v_3 of the CO_3^{2-} interlayer anions appears split into two bands at 1360 and 1483 cm^{-1}. The bending vibration of water molecules is observed at 1639 cm^{-1}, while the broad band at 3346 cm^{-1} shows the presence of O-H bonds. Noticeably, the low

intensity signals at 1048, 2880 and 2982 cm⁻¹ reveal the existence of ethanol molecules remaining adsorbed/incorporated in the LDH structure [29].
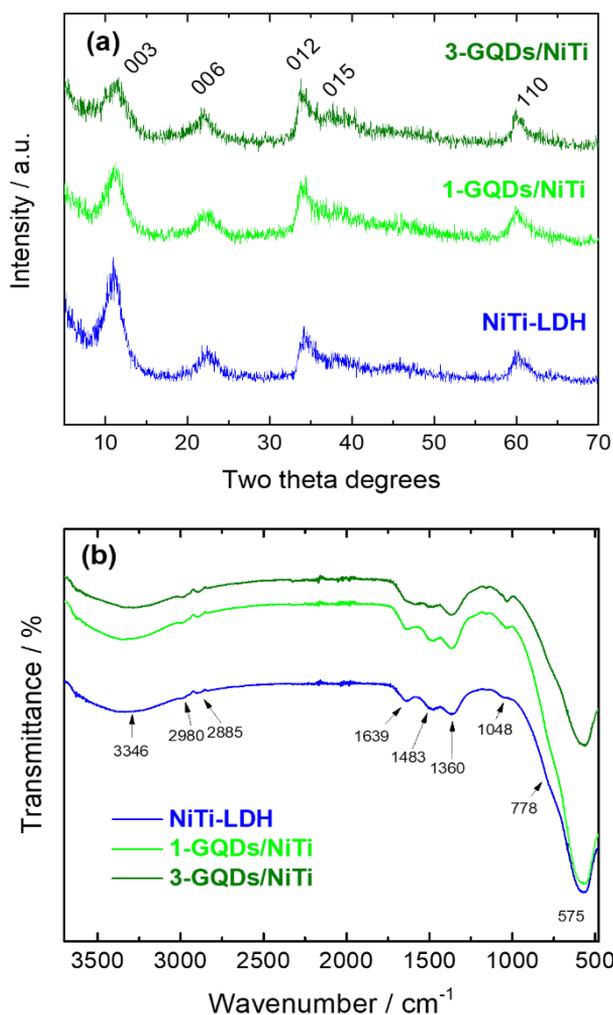

Figure 1. (a) XRD patterns and (b) IR spectra obtained from the NiTi-LDH and GQDs/NiTi samples.

The chemical composition of the LDH sample was elucidated from TGA (Fig. S3a) and ICP-MS analysis. Good agreement was found between the experimental values and the theoretical metal ratios in the initial

solution for a Ni_3Ti-LDH. The content of carbonate anions was assumed as those necessary to balance all the layer positive charge, and that for ethanol and water molecules (Fig. S3b) was calculated following the procedure previously reported for the Ni_3Ti-AMO LDH [29]. Thus, $[Ni_{0.77}Ti_{0.23} (OH)_2](CO_3)_{0.23}$ $0.16 \cdot H_2O$ $0.1 \cdot EtOH$ is proposed as the chemical formula. The presence of graphene quantum dots in samples 1-GQDs/NiTi and 3-GQDs/NiTi was corroborated through photoluminescence experiments (Fig. S4), showing these samples blue fluorescence compared with NiTi-LDH sample under UV light (365 nm).

X-ray photoelectron spectroscopy (XPS) was used to analyse the oxidation states of Ti and Ni on the surface of NiTi-LDH and 3-GQDs/NiTi samples. Figure 2 shows the XPS high resolution region of Ti 2p, Ni 2p, O 1s and C 1s. In order to ensure the correction of the energy shift, gold was used as a reference (Au $4f_{7/2}$ peak at 84.0 eV). The Ti 2p photoelectron peak positions (Fig. 2a) for the NiTi-LDH sample (Ti $2p_{3/2}$ = 458.1 eV; Ti $2p_{1/2}$ = 463.9 eV) correspond to the contributions from Ti^{4+} ions in an octahedral coordination [29,49]. When GQDs are present in the sample, a shift to lower binding energies is observed for (Ti $2p_{3/2}$ = 457.8 eV; Ti $2p_{1/2}$ = 463.5 eV) which indicates the increased electron density on Ti atoms in LDH, suggesting the existence of chemical interactions between GQDs and NiTi. The binding energy for Ni $2p_{3/2}$ corresponds to hydroxide as corroborated by Warner´s diagram [50], Fig. 2b. However, no changes were observed for Ni 2p (Ni $2p_{3/2}$ = 855.2 eV; Fig. 2b) or NiLMM (843.3 eV kinetic energy) peaks recorded for both samples. This should be correlated with the difference in the 3d electron occupancy, Ti possesses empty states which could accept electrons from the HOMO levels of GQDs while Ni has the 3d orbitals almost completely full [51].
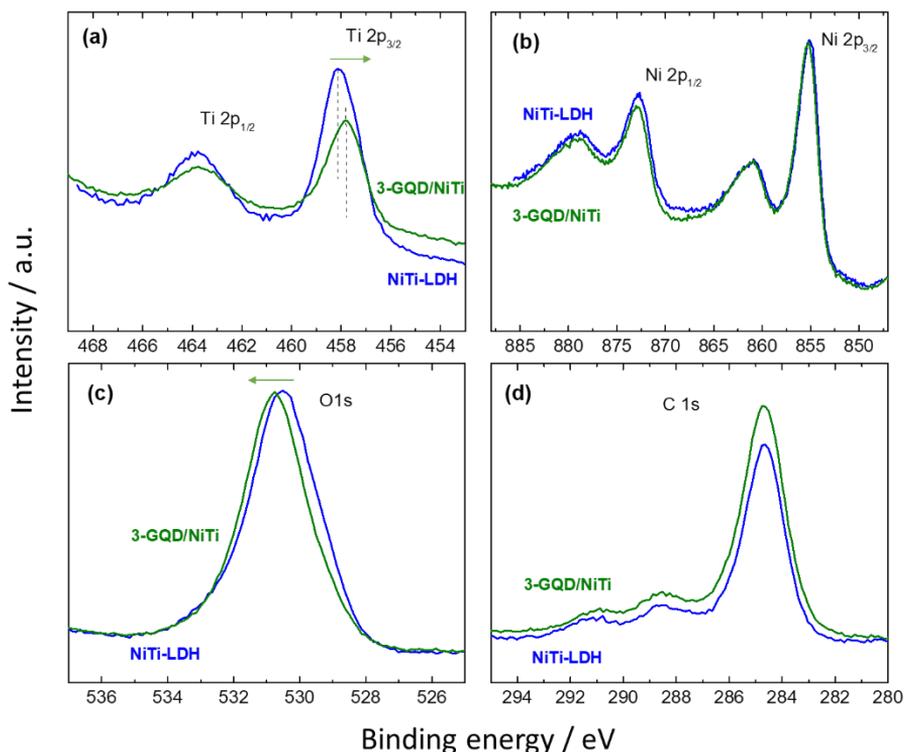
Figure 2. *XPS spectra obtained from the NiTi-LDH and GQDs/NiTi samples surface: (a) Ti 2p, (b) Ni 2p, (c) O 1s and (d) C 1s regions.*

The broad O 1s peak is the result of different contributions: lattice oxygen in metal oxides, hydroxyl groups, carbonate, and adsorbed water. Due to the change in the electron density on Ti atoms in the 3-GQDs/NiTi sample, the O 1s peak shifts to higher binding energy (530.8 eV) compared to the position recorded for the NiTi-LDH sample (530.5 eV), Fig. 2c. This result indicates that changes in electron density on metal atoms modify the spatial charge location in the layer [52]. Finally, the C 1s photoelectron peaks (Fig. 2d) appear at 284.7, 288.5 and 291.1 eV, values corresponding to the adventitious carbon, carbonate and hydrocarbonate groups, respectively. The high intense signal of these adventitious species masks any information about C in GQDs, preventing to know about the changes in their electron density. However, the above XPS results demonstrate the

occurrence of electronic interactions between GQDs and LDH, which should be beneficial for photocatalysis.

3.3.3.2. Morphology. Textural and optical properties

HRTEM study was performed to determine the morphology of the particles, Fig 3. The NiTi-LDH sample appears as a two-dimensional solid (2D) and flower-type particles constituted by corrugated nanosheets, Fig. 3a. The 2D morphology is a consequence of the presence of ethanol molecules in the LDH structure, which displaces the water molecules from the interlayer space and reduces the hydrogen bonding tendency, the metal hydroxide layer exfoliation being promoted [53]. The observed thickness of the nanosheets is 1.5 − 3.0 nm (Fig. 3b), which means that they consist of a few LDH monolayers (Fig. 3c). After being modified with < 5 nm GQDs, the LDH maintains the original 2D morphology (Fig. S5a). In contrast to the pristine sample (Fig. S5b), the HRTEM image of GQDs/NiTi shows how GQDs are embedded in the nanosheets (Fig. S5c). The high-resolution TEM image of GQDs/NiTi reveals the hexagonal lattice with lattice interplanar spacing of 0.30 nm corresponding to the exposed (001) facets of the NiTi-LDH [54], Fig. 3d. In addition, lattice interplanar spacing of 0.21 nm belongs to the graphene quantum dots [41].

The BET surface area of photocatalysts were investigated by N_2 adsorption–desorption isotherms. Fig. 4a shows the isotherm corresponding to the NiTi-LDH sample, of which shape is a characteristic of a type IV isotherm with a H3 hysteresis loop. This pore structure, typical of LDHs, obtained by the AMOST method [29], corresponds to slit-shaped pores appearing from the nano-sheet morphology as observed in TEM images. A high specific surface area value of 410 $m^2 \cdot g^{-1}$ was estimated and

related with the presence of mesoporous and macroporous pores, respectively (Fig. 4b). The preparation of GQDs/NiTi did not alter the pore structure nor the surface areas of the samples (Fig. S6) also exhibiting specific surface area values around 400 $m^2 \cdot g^{-1}$. The mentioned features predict a good photochemical De-NOx response, as the contact with the reactant gas molecules and the photocatalyst´s active sites should be facilitated across the large area exposed.
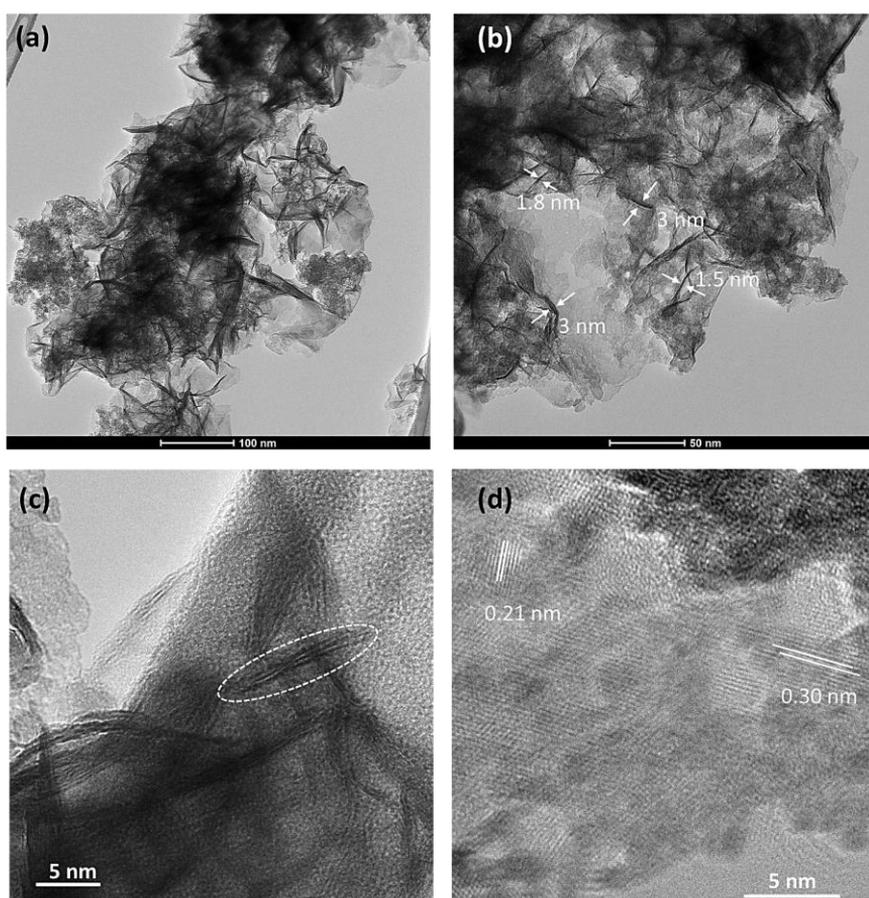

Figure 3. *HRTEM images of (a-c) NiTi-LDH and (d) GQDs/NiTi samples.*
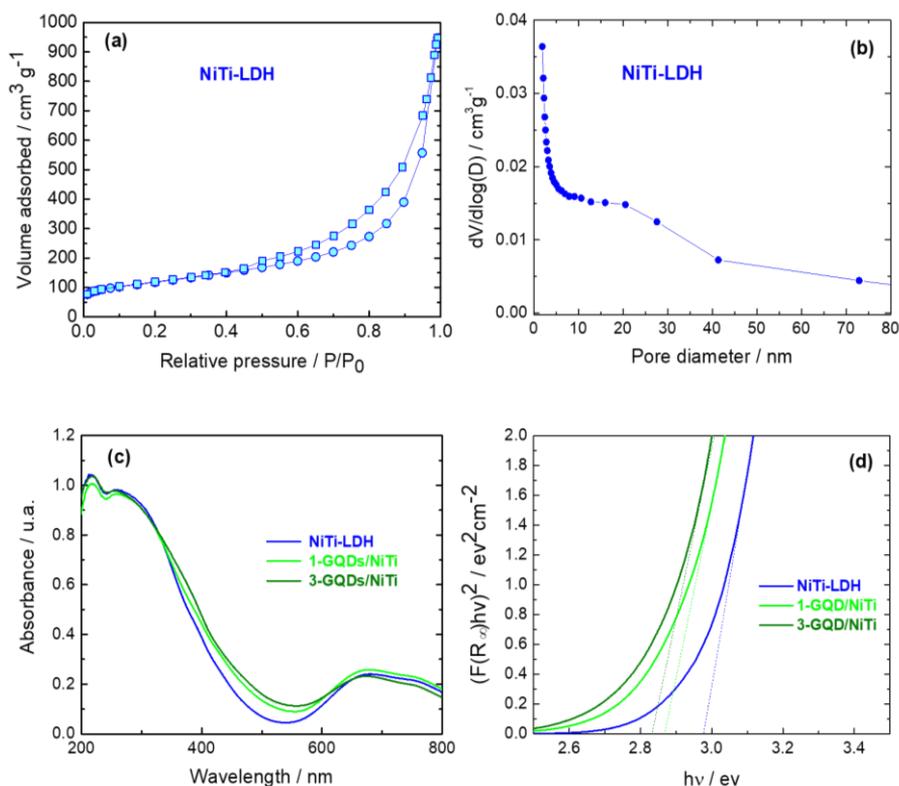
Figure 4. *(a) N$_2$ adsorption-desorption isotherms and (b) pore volume distribution for NiTi-LDH sample. (c) UV-Vis absorption spectra and (b) Kubelka-Munk transformed function plots for NiTi-LDH and GQDs/NiTi samples.*

The light absorption properties of the NiTi-LDH and GQDs/NiTi samples were inferred from their diffuse reflectance UV–Vis absorption spectra. Two sets of bands were observed (Fig. 4c), those with the highest intensity located at the 200 – 400 nm range are pertained to the ligand to-metal charge transfer for Ti(IV) cations in an octahedral environment. On the other hand, low intensity and broad bands in the 580 – 800 nm are ascribed to d-d transitions for the Ni(II) cations located in the layers [33]. An increase in the absorbance of the visible light, mainly in the 380 – 550 nm range, is observed as the GQDs content is increased and associated to their light absorption ability (Fig. S2b). Additionally, the band gap values

were estimated by the Kubelka-Munk method, Fig 4d. In line with those previously reported [41,55] the presence of GQDs decreases the band gap from 2.97 to 2.86 and 2.83 eV, for NiTi-LDH, 1-GQDs/NiTi and 3-GQDs/NiTi, respectively. This decrease should be related with the increased electron density observed for Ti atoms in GQDs/NiTi samples (XPS results in Fig. 2). Accordingly, it is reported that 3d orbitals of Ti have influence in the conduction band minimum value [56]. From above, the sunlight harvesting is enhanced by the presence of GQDs, which may serve to boost the production of electron-hole pairs for photocatalytic reactions.

3.3.3.3. Photocatalytic activity

The ability of the samples to remove nitrogen oxide gases from air by means of a photocatalytic process was evaluated. Figure 5a shows the variation of NO concentration measured during a standard test (500 ppb NO inlet concentration; 1 h UV-Vis light irradiation) for the NiTi-LDH and GQDs/NiTi samples used as photocatalysts. During a first period of 10 minutes in the dark, the inlet gas concentration remained strictly constant, indicating that no physical or chemical interaction between the gas reactant and catalyst or reactor accounts. Subsequently, once the samples are light irradiated (from 10th to 70th minute), a fast decay in the NO concentration measured values is observed. Therefore, a light induced process accounts for the photochemical oxidation (PCO) of NO molecules. As is known, the irradiation of a LDH semiconductor with the appropriate light promotes the transfer of electrons (e$^-$) from the valence band (VB) to the conduction band (CB) with the creation of holes (h$^+$) in the VB. This pair of charges (e$^-$/h$^+$), once they reach the photocatalyst´s surface, initiate redox reactions on water and oxygen adsorbed molecules producing hydroxyl (•OH) and superoxide (•O$_2^-$) radical species, which in term take

part in the oxidation of nitrogen oxide gases. This photochemical process, even though it is quite complex [4-6], could be summarized in the following sequential oxidation steps: $NO \rightarrow NO_2^- \rightarrow NO_2 \rightarrow NO_3^-$.

The presence of GQDs enhances the photochemical De-NOx activity of the LDH, as can be deduced from the NO concentration profiles shown in Fig. 5a. Thus, under light irradiation, the NO removal efficiency increases from 55 % for the NiTi-LDH sample to 61 % for GQDs/NiTi samples. In addition, the decay of NO concentration values in the first few minutes of light irradiation is faster for the samples containing GQDs. In fact, the initial rate constants for NO degradation are higher in these samples (Fig. S7). Moreover, compared to the NiTi-LDH sample, the reached stationary state is completely constant with time during the irradiation period. In line with previous works, these observations are indicative that the addition of GQDs addition seems to enhance the electronic processes and, therefore, the De-NOx performance [41,57].

The NO and NO_X conversion, NO_2 emission and selectivity values (%) measured for the three photocatalysts are shown in Fig 5b. As is usual for LDH De-NOx photocatalysts [48,58-60], the released NO_2 is insignificant for NiTi-LDH (1.2 %) and GQDs/NiTi (< 0.6 %) samples. This is of high importance as the NO_2 intermediate product arising from the photochemical NO oxidation is considered a highly toxic product [61]. In this sense the De-NOx selectivity (S), defined as the amount of NO molecules removed from air as harmless nitrite/nitrate species, reaches outstanding values of 98 % for GQDs/NiTi. For comparison purposes, values corresponding to the TiO_2 P25 benchmark product (used as standard in this research field) were obtained under identical experimental conditions. Because of their high selectivity values, after one

hour of light irradiation, the overall NO_x removal efficiency exhibited by the GQDs/NiTi samples (60 %) clearly surpasses that for TiO_2 P25 (48 %), Fig. 5b. Considering both NO_x and S efficiencies, the De-NOx performance of these photocatalysts are among the best values recently reported for advanced De-NOx photocatalysts, Table S1. Subsequently, the De-NOx experiments were repeated using visible light as the irradiation source (Fig. 5c). Clearly, the presence of GQDs promotes the visible light activity which should be associated with the better light harvesting (Figs. 4c and 4d) and/or an enhanced charge carrier separation in the system. The above results demonstrate that GQDs/NiTi samples can be successfully used for air purification purposes.

Interestingly, once the light is off (70th minute), a different behaviour in the evolution of the NO concentration in the dark was observed for GQDs/NiTi samples. The NiTi-LDH sample exhibits the expected NO concentration values profile, Fig 5d. Thus, in the absence of light irradiation, the photochemical process does not occur, and the NO values return to the initial values. However, the GQDs/NiTi samples showed a significant and prolonged post-photocatalytic NO removal, Figs 5e and 5f. In fact, this process is clearly related to the amount of GQDs. Thus, a NO removal efficiency value in the dark, greater than 20% (which means 100 ppb of NO removed) is sustained for 30 minutes, and 75 minutes in the case of 1-GQDs/NiTi for 3-GQDs/NiTi samples, respectively. Furthermore, the De-NOx behaviour in the dark was not dependent on the light irradiation period, as similar NO removal in the dark was observed after 10, 30 and 60 min of light irradiation, Fig S8.
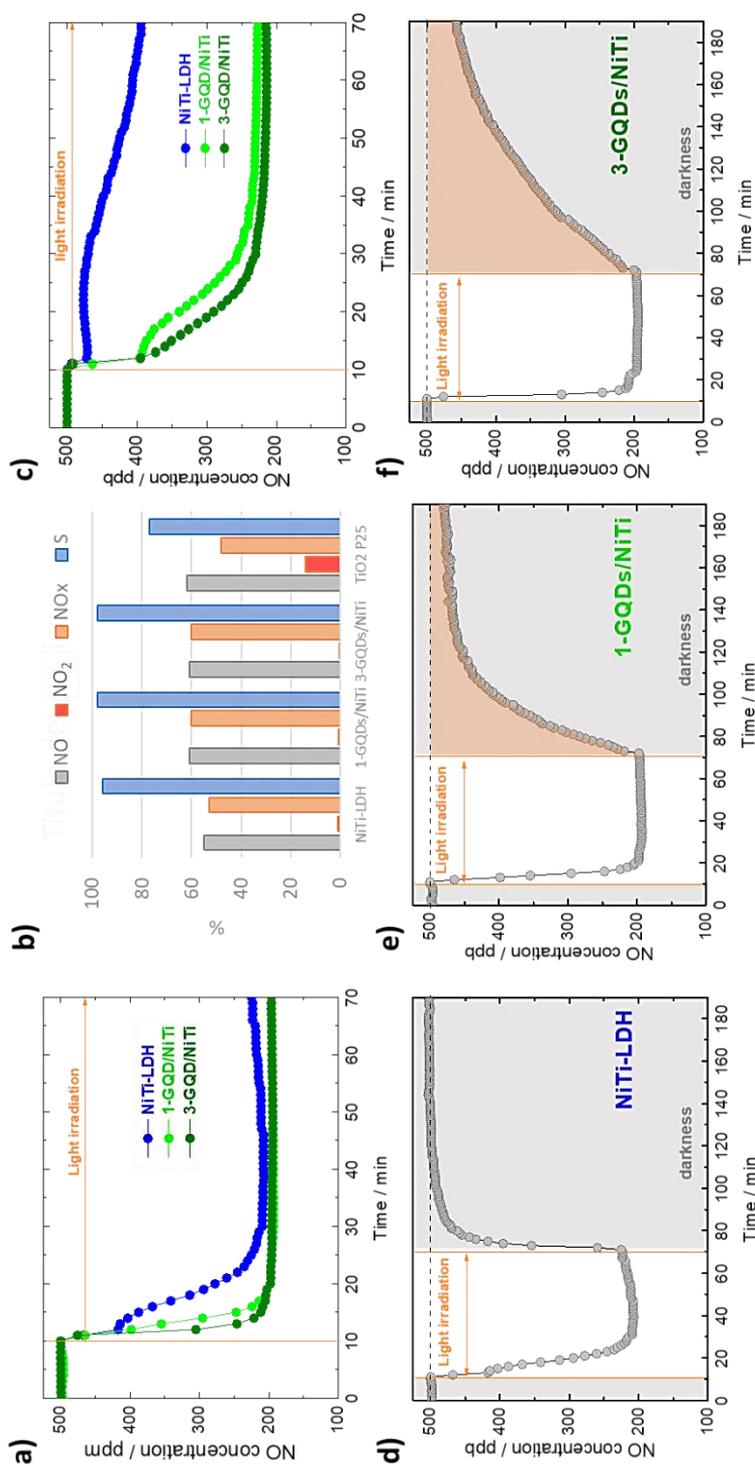
Figure 5. *(a) Gas concentration evolution during the photodegradation of NO under (a) UV-Vis or (c) visible light irradiation on NiTi-LDH and GQDs/NiTi samples. (b) NO conversion, NO_2 emitted, NOx conversion and selectivity values (%) for NiTi-LDH, GQDs/NiTi and TiO_2 P25 samples. (d-f) Gas concentration evolution during the catalytic reaction of NO in light/dark periods on NiTi-LDH and GQDs/NiTi samples.*

On the other hand, the stability of the sample after the catalytic tests was corroborated as no significative chemical nor morphological changes were found (Fig. S9). Compared to previous works, these results are a clear advance in post-photocatalytic De-NOx processes, as significant De-NOx ability (> 20%) was previously reported to persist for only 8-10 minutes in the dark [7-10].

To gain information about the nature of the process observed on GQDs/NiTi samples in the dark period, additional studies were performed. Firstly, the massive adsorption of NO gas molecules on the surface of the photocatalyst was discarded because it was not observed during the first ten minutes of this De-NOx test. No nitrogen oxide adsorption was observed in additional experiments either, when the gas reactant was put in contact with the photocatalyst for a long time in the absence of light irradiation, Fig. S10. Therefore, an induced chemical process must be responsible for the NO removal in the dark period. Moreover, it is reasonable to consider the photoluminescence effect produced by GQDs under light irradiation as a new light activation process which should promote photochemical reactions once the light is off [62]. However, the photoluminescence signal emitted by GQDs persist only a few tens of nanoseconds in the absence of light, Fig. S2d, thus indicating that a long-lasting activity of De-NOx in the dark is not due to the persistent luminescence. In addition, the temperature effect should be considered. In our experimental setup, the light irradiation box is air refrigerated to maintain a constant ambient temperature of 35 °C, but the continuous UV-Vis light fall on the sample increases the temperature to almost 60 °C on its surface, Fig. S11a. This temperature is that expected for a photocatalyst directly exposed to the sunlight, since roofs and walls of buildings −

architectural elements on which De-NOx photocatalysts are applied – reach temperatures in the range of 55-61 °C under sunlight exposition [63]. To ascertain the effect of temperature on NO removal, the De-NOx process was performed in the dark while maintaining the reaction chamber at a constant temperature of 60 °C, Fig. S11b. It was observed that, in comparison to the photocatalytic experiment (Fig. 5), a very low NO removal efficiency of 15% was obtained. However, once the heater is off, the NO abatement does not occur with temperatures lower than 40 °C. Both NiTi-LDH and 3-GQDs/NiTi samples exhibit a very similar behaviour. Figure S11a shows that the temperature of the sample surface decreases to 40 °C in only ten minutes once the light is off, but the NO abatement persists for 110 additional minutes. From these observations, it is concluded that a large persistent post-photocatalytic De-NOx process observed for the 3-GQDs/NiTi sample (Fig. 5f) is not promoted by temperature changes.

To confirm that the De-NOx process in the dark is a light induced process, an additional experiment was performed in which the photocatalyst was only exposed to the reactant NO gas in dark conditions. Previously, the photocatalysts were activated by UV-Vis light (1 h of light irradiation) before being placed in the reaction chamber. The corresponding NO gas concentration profile for NiTi-LDH and 3-GQDs/NiTi samples are shown in Fig. 6. In both cases, the samples were introduced into the reaction chamber after the first 20 min in which the NO flow was stabilized. Subsequently, the disruption of the NO values occurred because the reaction chamber was open to accommodate the sample. In the case of the NiTi-LDH sample, the disrupted inlet NO values were rapidly recovered in only a few minutes, indicating that no De-NOx process

occurs in the dark. However, a significant NO removal (> 20%) was preserved for at least one hour for the 3-GQDs/NiTi sample, confirming its ability to perform persistent photo-catalysis after light irradiation.
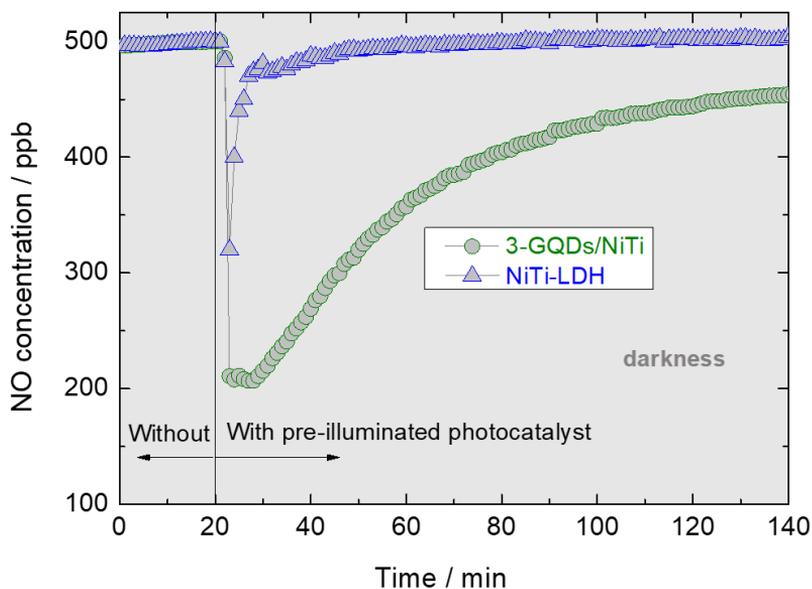
Figure 6. *NO gas concentration evolution in the dark on pre-illuminated NiTi-LDH and 3-GQDs/NiTi samples.*

As a control test, similar experiments were carried out with the standard TiO_2 P25 photocatalyst, with (3 wt.%) and without GQDs (Fig. S12). Once the light was off, no post-photocatalytic process was observed as the NO concentration values were quickly recovered for both samples. Therefore, the observed light-induced De-NOx process is not related to the individual systems (NiTi-LDH or GQDs), but to the actual GQDs/NiTi-LDH heterojunction. Finally, the light/dark catalytic process was repeated in different successive runs, Fig. S13. The same NO removal efficiency was found in both light and dark periods for the six runs indicating that the catalyst is not poisoned, and any chemical reaction accounted during the dark period should be reversible.

3.3.3.4. Photocatalytic mechanism assessment

Several experiments were performed to gain information about the plausible mechanism accounting under light and dark conditions. The ability of NiTi-LDH, under illumination, to produce •OH and •O_2^- radicals was reported in our previous work [29]. These reactive oxygen species (ROS) are responsible for initiating the redox processes. To get an insight into the photo-charge separation efficiency of the photocatalysts, picosecond time-resolved photoluminescence (TRPL) measurements were performed. Fig. 7a shows the time profiles obtained at λ_{exc} = 405 nm with the best bi-exponential fits for the GQDs and also mixed with the NiTi-LDH photocatalyst, leading to deactivation times equal to 10.3 ns (GQDs), 0.6 and 5.4 ns ($\tau_{av.}$ = 2.1 ns) for 1-GQDs/NiTi sample, 0.5 and 5.3 ns ($\tau_{av.}$ = 2.2 ns) for 3-GQDs/NiTi sample. The deactivation kinetics for the excited state in GQDs/NiTi-LDH samples is developed in a shorter time range compared with the GQDs sample.

Furthermore, Fig. 7b compares the PL spectra of the NiTi-LDH, 3-GQDs/NiTi and GQDs samples (λ_{exc} = 350 nm). A large quenching of the GQD emission signal is observed when the GQDs are linked to the LDH structure, indicating a marked transfer of photoexcited electrons from GQDs to LDH. These observations, together with those from XPS measurements (Fig. 2) confirm the formation of an effective electronic heterojunction between GQDs and LDH, which is beneficial for the photocatalytic activity of these samples, as inferred from the De-NOx results (Fig. 5).
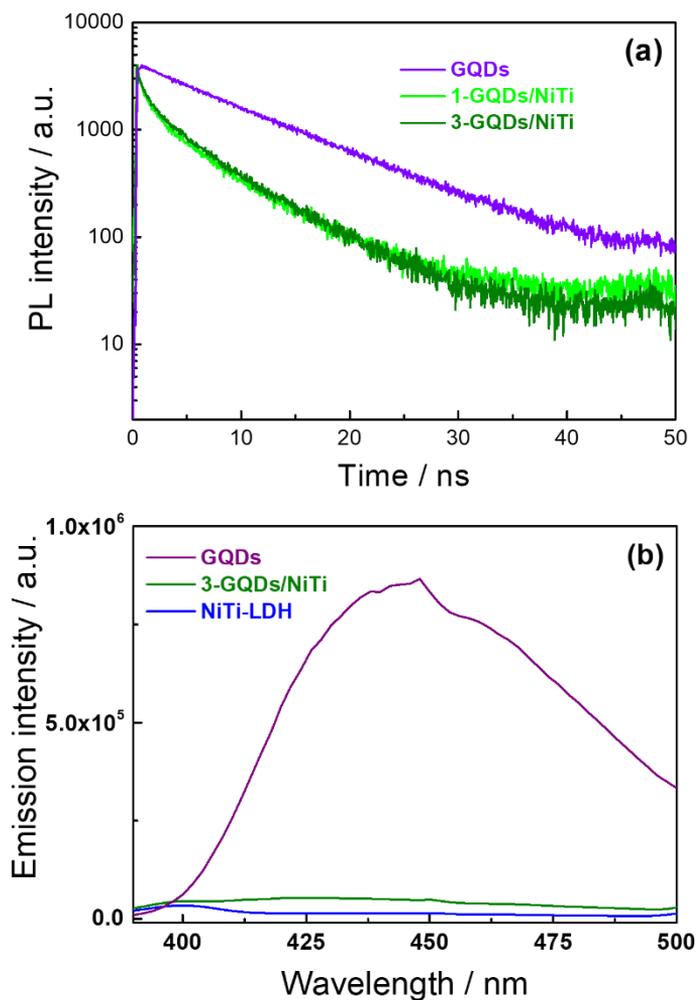
Figure 7. (*a*) *Time decay of the photoluminescence signals for GQDs and GQDs/NiTi samples. (b) PL spectra of GQDs, NiTi-LDH and 3-GQDs/NiTi samples.*

Additionally, *in-situ* DRIFTS technique was used to perform the dynamic monitoring of the detailed mechanism involved in the photocatalytic removal of NO. Firstly, to remove environmental impurities, the samples were subjected to a pre-treatment process flowing the measurement cell with Ar for 10 min, and no IR spectral variations were found. The background spectrum was recorded before the reactant gas mixture (NO + O_2) flowed through the reaction chamber.

Subsequently, and after 10 min of stabilization in the dark, the samples were light irradiated for 30 min. The corresponding spectra obtained, once the background had been subtracted, for samples NiTi-LDH and 3-GQDs/NiTi at different periods of illumination, are shown in Fig. 8.
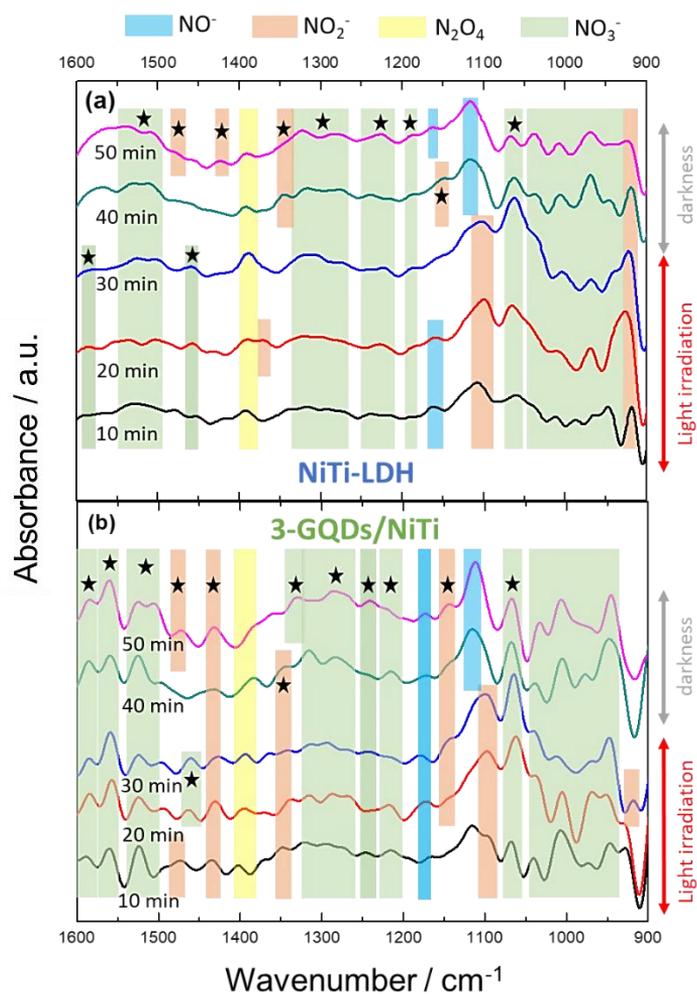
Figure 8. *In-situ DRIFTS spectra obtained while NO and O_2 gases are flowing through the (a) NiTi-LDH and (b) 3-GQDs/NiTi samples under light and dark conditions.*

When light interacts with the samples, photoexcited e^- and h^+ are generated on the surface of the photocatalyst and react with H_2O and O_2 to produce hydroxyl and superoxide radicals. These radicals initiate the photochemical oxidation of NO, as revealed by the IR signals corresponding to nitrite and nitrate species. The detailed band assignment is reported in Table S2, SI.

The low intensity signal at 1392-1397 cm^{-1} shows the appearance of N_2O_4 as an intermediary in the oxidation process. In both samples, the appearance of the NO^- signal corresponds to the NO disproportionation in the presence of the hydroxyl LDH groups [64]. In the case of NiTi-LDH (Fig. 8a), after 10 min of light irradiation, the main signal corresponds to nitrite (1100 cm^{-1}). The transformation of nitrites into nitrates takes place as the irradiation time is prolonged (20 and 30 min). Now, the highest intense signal corresponds to nitrate (1063 cm^{-1}) and the growth of 1534-1507 cm^{-1} and 1322-1277 cm^{-1} signals are observed, all corresponding to bridge/bidentate nitrate species.

Similar features were found in the spectra obtained for 3-GQDs/NiTi sample during the illumination period. In comparison to NiTi-LDH, the nitrate signals increase in intensity and those for bidentate/quelated nitrates (1066, 1461, 1534 and 1584 cm^{-1}) are clearly observed, indicating that monodentate NO_3^- species transformation into the more stable bidentate ones, is favoured. These findings match with the De-NOx efficiency results (Fig 5). Thus, the 3-GQDs/NiTi photocatalyst promotes the complete NO oxidation to nitrate, which is related to a more efficient charge transfer (Fig. 7).

Afterwards when the light was off, interestingly, the evolution of IR signals in the dark was markedly different for NiTi-LDH and 3-GQDs/NiTi samples. In the absence of light, as NO gas interacts with the surface of the NiTi-LDH sample (Fig. 8a), the main signal observed is that corresponding to NO^- (1116 cm^{-1}). In addition, signals of new nitrite species (1347, 1420 and 1476 cm^{-1}) are found together with a decrease in intensity for some of the nitrate signals, mainly those located at 1063 cm^{-1}. These findings indicate that, once the photochemical oxidation process has stopped, the reactions that occur on photocatalyst surface correspond to: i) the NO disproportionation, ii) a renoxification process between NO as NO_3^-. A different evolution of the IR spectra is found for the 3-GQDs/NiTi sample (Fig. 8b). Even though the NO^- signal is again the highest in intensity, the decrease in intensity for the nitrate signal at 1063 cm^{-1} is now attenuated. Of importance, a significant increase in several nitrate signals (944, 1007, 1033, 1211-1327 and 1507 cm^{-1}) is observed. Therefore, the oxidation of NO gas molecules to nitrate species continues after the light is off, thus explaining the persistent post-photocatalytic De-NOx process observed for this sample (Fig. 5f).

In order to confirm the existence of the persistent catalytic process once the light is off, an additional DRIFTS experiment was performed. On this occasion, the 3-GQDs/NiTi sample was previously exposed to light irradiation under Ar atmosphere for one hour. Subsequently, the light was turned off and then the NO was flowed inside the reaction chamber. This means that NO interacts with the surface of the photocatalyst in the dark only when the sample was previously activated by light irradiation. Signals corresponding to nitrite and nitrate species are clearly observed again, Fig. 9, corroborating that NO oxidation occurs in the dark over the pre-

irradiated 3-GQDs/NiTi sample. Now, several intense signals for nitrite species (906, 1341, 1438 and 1487 cm^{-1}) are registered, which indicates that catalytic reaction is less effective in the dark compared to that directly assisted by light. This is in accordance with the De-NOx performance observed for the 3-GQDs/NiTi sample for both light irradiation and dark periods (Fig. 5).
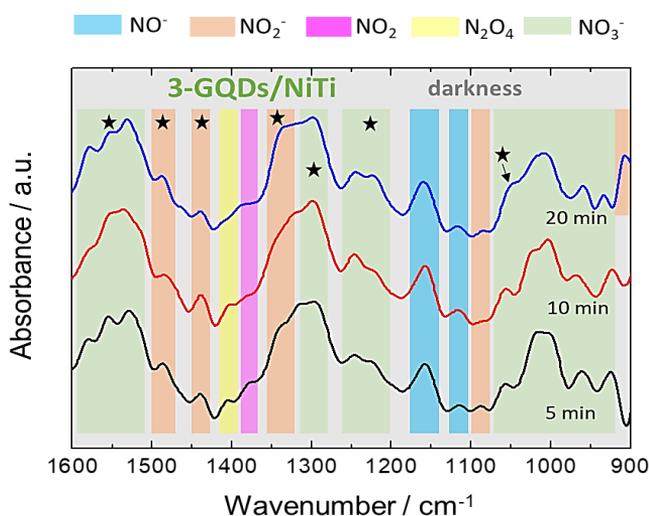

Figure 9. *In-situ DRIFTS spectra obtained in the dark for the pre-illuminated 3-GQDs/NiTi sample.*

To explain the mechanism occurring in the dark, we assume that NiTi-LDH also acts as ESM material when GQDs/NiTi is light irradiated. As previously commented in the Introduction section, this assumption is based on the role played by graphene and Ti^{4+} cations in energy storage systems, as a source and drain of electrons, respectively [25,30,65,66].

The participation of electrons during the dark period was double checked. Firstly, EPR measurements were performed to prove the existence of reactive species which could be involved in the chemical

reaction, using DMPO (5,5-dimethyl-1-pyrroline N-oxide) for radical detection.

Before EPR measurements, the 3-GQDs/NiTi sample was light irradiated for one hour. Subsequently, in the dark, the sample and DMPO were put in close contact and the corresponding EPR signals measured after 10 min. Fig. 10a shows that the DMPO-•OH adduct was not formed, but weak signals attributed to the DMPO-•O_2^- adduct. [48,67] were observed. This confirms that 3-GQDs/NiTi is supplying electrons to the reaction medium.

To corroborate this evidence, scavenger experiments using p-benzoquinone (PBQ) to trap superoxide anion radical species were carried out during De-NOx tests performed with NiTi-LDH and 3-GQDs/NiTi samples, Fig. 10b and 10c. For both photocatalysts, as expected, the presence of PBQ decreases the NO removal activity during the light irradiation period. In the dark period, PBQ only has influence in the NO signal recorded for the 3-GQDs/NiTi sample (Fig. 10c), indicating again that superoxide radicals are present in this period.

Additionally, the use of $K_2Cr_2O_7$ scavenger shows that electrons also participate in the chemical reaction which takes place in the dark when 3-GQDs/NiTi is used as a photocatalyst, Fig. S14. With similarity to that reported for the TiO_2-Cu_2O storage material [25,30], titanium centres should be contemplated as the electron trap. Under light irradiation, Ti^{4+} would be partially reduced to Ti^{3+} due to the deep electron injection from excited GQDs nanoparticles, which explains the persistent post-photocatalytic De-NOx reaction in samples containing GQDs and its intensification when the amount of GQDs is increased.
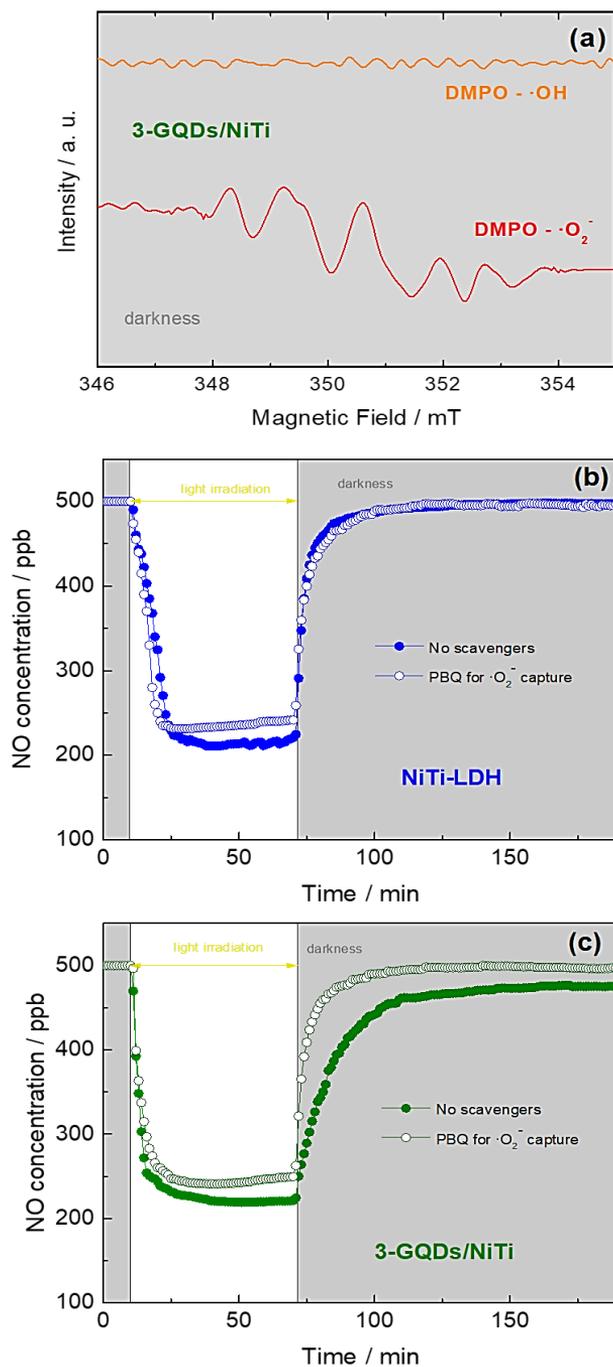
Figure 10. *(a) DMPO spin-trapping EPR spectra obtained in dark conditions for the pre-illuminated 3-GQDs/NiTi sample. Active species trapping experiments for the photocatalytic NO oxidation process over (b) NiTi-LDH and (c) 3-GQDs/NiTi sample.*

Because the Ti(IV) and Ti(III) ionic radius in octahedral coordination are different enough (68 and 79 pm, respectively [68]), the partial reduction of Ti(IV) should induce changes in the M-O-M bonds through the interconnected octahedra constituting the LDH layer. Thus, we studied the far-IR spectra of the 3-GQDs/NiTi sample using the *in-situ* DRIFTS technique. Previously, the IR spectrum of the 3-GQDs/NiTi sample was recorded and used as a background spectrum.

Fig. S15 shows the dynamic monitoring of the IR signal, once the background spectrum is subtracted, at different periods of light illumination and dark. Before the sample was irradiated, the signal measured in dark served as a baseline. Under light irradiation new bands appear, which are associated to changes in the vibration modes of Ti-O-Ti and Ni-O-Ni (460 and 483 cm^{-1} ;[69-72]), δ_{OH} in-plane deformation (521 cm^{-1} ; [71]), Ni-O (535 cm^{-1} ; [72,73]) and Ti-O (560, 588 and 607 cm^{-1} ; [69,70]) bonds. After 60 minutes of light illumination, the lamp was switched off and spectra were recorded in the dark. After 15 minutes in the dark, some M-O bands (535 cm^{-1}) tend to disappear and those corresponding to Ti-O-Ti and Ni-O-Ni bonds are slightly shifted to lower frequencies, indicating that the LDH layer is being rearranged. Finally, the new signals observed during the experiment are vanished after 30 minutes in the dark and, presumably, the pristine chemical identity of the 3-GQDs/NiTi sample is recovered, in accordance with the preserved De-NOx activity observed in the running tests shown in Fig. S13.

The results described above show that pre-illuminated GQDs/NiTi photocatalysts exhibit a catalytic memory thanks to the existence of stored electrons. The ability of Ti^{4+} to be photo-reduced in adequate heterojunctions together with the electron injection [69] assist this

mechanism [25,30,65,74]. Moreover, the participation of electrons and superoxide radicals once the light is off, are both indicative that a simultaneous electron storage mechanism takes place in GQD/NiTi compound. Therefore, the complete De-NOx process for GQDs/NiTi photocatalysts in light/dark conditions should be assumed to occur by a combination of photocatalytic and energy storage mechanisms.

In order to stablish the alignment of the energy bands for GQDs/NiTi photocatalyst, several measurements were performed. The Valence Band XPS spectrum was acquired for the NiTi-LDH, the valence band edge being 3.14 eV *vs* NHE (Fig. S16a). Therefore, by considering the previously obtained band gap value (2.97 eV), the conduction band edge is located at 0.17 eV. Meanwhile, the UPS spectrum of NiTi-LDH (Fig. S16b) allowed to locate the Fermi level at 1.3 eV from the valence band (p-type semiconductor). Furthermore, the GQDs band gap value was calculated to be 3.07 eV (Fig. S17a), whereas its Mott-Schottky plot showed a positive slope, indicating its n-type semiconductive behaviour (Fig. S17b). By extrapolating the linear region of the Mott-Schottky plot, the flat band potential can be estimated, and it can be considered as the conduction band value [36,37]. Considering all these results, the conduction band edge and the valence band edge of the GQDs were located at –0.38 eV and 2.69 eV *vs* NHE, respectively. Consequently, a p-n heterojunction between NiTi-LDH and GQDs is created.

Fig. S18 represents the p-n heterojunction formed between NiTi-LDH and GQDs, a mechanism successfully used in previously reported works [75-78]. The photocatalysis mechanism is initiated once light photons are absorbed on the surface of NiTi-LDH nanosheets resulting in electron excitation to the CB, whereas holes are generated in the

VB (eq 1). Simultaneously, because of the effective heterojunction formed between GQDs and NiTi-LDH, as inferred from the aforementioned XPS and PL results (Figs. 2 and 7), a charge transfer (electrons) from GQDs CB to NiTi-LDH CB is generated under irradiation, leading to an electron enrichment in NiTi-LDH. Similarly, the holes move from NiTi-LDH VB to GQDs VB. Thus, the e⁻/h⁺ recombination is retarded, increasing the photocatalytic De-NOx efficiency of GQDs/NiTi photocatalysts, mainly under Visible light irradiation (Fig 5c). On the photocatalyst surface, the e⁻ and h⁺ promote the formation of ROS species which initiate the oxidation of NO molecules towards nitrite/nitrate species, as was monitored by the DRIFTS technique (Fig. 8). This photo-oxidative De-NOx process involving several steps was previously reported by our group [29] and is now described in SI. Furthermore, in similitude with previous works [25,30], the following energy storage mechanisms should be considered. The occurrence of Ti^{3+} in NiTi LDH should be possible due to the GQD electron injection during the irradiation period (eq 2). Once the light is off, the stored electrons are released again (by $Ti^{3+} \rightarrow Ti^{4+}$ process) to the catalyst surface (eq 3) where they react with oxygen molecules to produce superoxide radicals (eq 4) (Fig. 10), the latter activating the De-NOx oxidative process in the dark.

$$NiTi + h\nu \rightarrow NiTi^{*}(e_{CB}^{-} + h_{VB}^{+}) \qquad (1)$$
$$e_{CB}^{-}(GQD^{*}) + NiTi^{*} \rightarrow NiTi^{4+}Ti^{3+} \qquad (2)$$
$$NiTi^{4+}Ti^{3+} \rightarrow NiTi + e^{-} \qquad (3)$$
$$e^{-} + O_2 \rightarrow \bullet O_2^{-} \qquad (4)$$
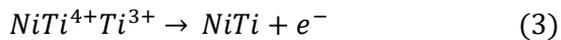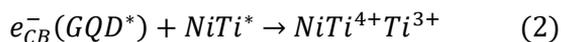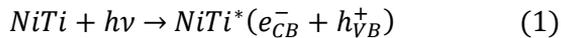
This reversible catalytic mechanism could explain the good reusability of the catalyst in successive runs (Fig. S13).

3.3.4. Conclusions

GQDs/NiTi-LDH heterojunctions were synthesized with different amounts of graphene quantum dots. The incorporation of GQDs to the NiTi-LDH photocatalyst does not alter the morphological, chemical nor microstructural properties. GQDs nanoparticles are placed between NiTi-LDH nanosheets forming an efficient electronic heterojunction. The incorporation of GQDs enhance the light harvesting ability of the photocatalyst as the absorbance of the visible light is increased.

The beneficial effects of GQDs incorporation led to a better De-NOx response of GQDs/NiTi photocatalysts compared to NiTi-LDH, mainly under visible light. GQDs/NiTi photocatalysts are highly selective towards the NO photo-oxidation to nitrite/nitrate species and, therefore, exhibiting higher NO_x gas abatement values than the standard TiO_2 P25 photocatalyst. Once the light is off, a great persistence of the catalytic process is observed in the dark for the GQDs/NiTi compounds. This process is dependent on the GQDs content in the heterojunction, but not on the illumination time nor the temperature reached by the photocatalyst during the light irradiation period. The similar De-NOx efficiency observed for all catalytic run tests performed in the dark is related to a chemical/electron reversible process.

The De-NOx process performed by GQDs/NiTi compounds in light/dark conditions is explained by the simultaneous occurrence of photocatalytic and energy storage mechanisms. Under light irradiation, the creation of charge carriers (e^- and h^+) promote the formation of ROS radical species which initiates the sequential $NO \rightarrow NO_2^- \rightarrow NO_2 \rightarrow NO_3^-$ oxidation process. Thanks to the formation of a p-n heterojunction

between GQDs and NiTi-LDH, the photo-oxidative process is favoured in GQDs/NiTi compounds. Simultaneously, some of the excited electrons occurring during the light irradiation period are trapped and stored by the NiTi-LDH. Once the light is off, the stored electrons are released again, favouring the formation of superoxide radicals which maintain the De-NOx process in the dark. We conclude that LDHs provide a new platform approach to develop new persistent photocatalytic systems with the aim to achieve day/night photocatalysis practical applications.

3.3.5. Acknowledgements

3.3.6. References

[1]   S. Rajendran, T.A.K. Priya, K.S. Khoo, T.K.A. Hoang, H.S. Ng, H.S.H. Munawaroh, C. Karaman, Y. Orooji, P.L. Show, A critical review on various remediation approaches for heavy metal contaminants removal from contaminated soils, Chemosphere. 287 (2022) 132369. https://doi.org/10.1016/j.chemosphere.2021.132369.

[2]   B. Chen, C. Hong, H. Kan, Exposures and health outcomes from outdoor air pollutants in China, Toxicology. 198 (2004) 291–300. https://doi.org/10.1016/j.tox.2004.02.005.

[3]   European Environment Agency, Air quality in Europe-2019 report, Luxembourg, 2019. https://doi.org/10.2800/822355.

[4]   J. Balbuena, M. Cruz-Yusta, L. Sánchez, Nanomaterials to Combat NO_x Pollution, J. Nanosci. Nanotechnol. 15 (2015) 6373–6385. https://doi.org/10.1166/jnn.2015.10871.

[5]   M. Cruz-Yusta, M. Sánchez, L. Sánchez, Metal oxide nanomaterials for nitrogen oxides removal in urban environments, in: C. Maccato, D. Barreca (Eds.), Tailored Functional Oxide Nanomaterials: From Design to Multi-Purpose Applications, Wiley-VCH GmbH, 2022, pp. 229-276. ISBN-13: 978-3527347599; https://doi.org/10.1002/9783527826940.ch7.

[6]   A. Nikokavoura, C. Trapalis, Graphene and g-C_3N_4 based photocatalysts for NO_x removal: A review, Appl. Surf. Sci. 430 (2018) 18–52. https://doi.org/10.1016/j.apsusc.2017.08.192.

[7]   H. Li, S. Yin, T. Sato, Novel luminescent photocatalytic deNO$_x$ activity of $CaAl_2O_4$:(Eu,Nd)/$TiO_{2-x}N_y$ composite, Appl. Catal. B. 106 (2011) 586–591. https://doi.org/10.1016/j.apcatb.2011.06.019.

[8]   H. Li, S. Yin, Y. Wang, T. Sato, Efficient persistent photocatalytic decomposition of nitrogen monoxide over a fluorescence-assisted $CaAl_2O_4$:(Eu, Nd)/(Ta, N)-codoped TiO_2/Fe_2O_3, Appl. Catal. B. 132–133 (2013) 487–492. https://doi.org/10.1016/j.apcatb.2012.12.026.

[9]   H. Li, S. Yin, Y. Wang, T. Sato, Microwave-Assisted Hydrothermal Synthesis of Fe_2O_3-Sensitized $SrTiO_3$ and its Luminescent Photocatalytic deNO$_x$ Activity with $CaAl_2O_4$:(Eu, Nd) Assistance, J. Am. Ceram. Soc. 96 (2013) 1258–1262. https://doi.org/10.1111/jace.12206.

[10]   H. Li, S. Yin, Y. Wang, T. Sekino, S.W. Lee, T. Sato, Roles of Cr^{3+} doping and oxygen vacancies in $SrTiO_3$ photocatalysts with high visible light activity for NO removal, J. Catal. 297 (2013) 65–69. https://doi.org/10.1016/j.jcat.2012.09.019.

[11]   F. Kang, G. Sun, P. Boutinaud, H. Wu, F.X. Ma, J. Lu, J. Gan, H. Bian, F. Gao, S. Xiao, Recent advances and prospects of persistent luminescent materials as inner secondary self-luminous light source for photocatalytic applications, Chem. Eng. J. 403 (2021) 126099. https://doi.org/10.1016/j.cej.2020.126099.

[12]   M. Sakar, C.C. Nguyen, M.H. Vu, T.O. Do, Materials and Mechanisms of Photo-Assisted Chemical Reactions under Light and Dark Conditions: Can Day–Night Photocatalysis Be Achieved?, ChemSusChem. 11 (2018) 809–820. https://doi.org/10.1002/cssc.201702238.

[13]   J.Y.Y. Loh, G. Sharma, N.P. Kherani, G.A. Ozin, Post-Illumination Photoconductivity Enables Extension of Photo-Catalysis after Sunset, Adv. Energy. Mater. 11 (2021) 2101566. https://doi.org/10.1002/aenm.202101566.

[14]   N. Lakshminarasimhan, U.V. Varadaraju, Luminescence and afterglow in Sr_2SiO_4:Eu^{2+}, RE^{3+} [RE=Ce, Nd, Sm and Dy] phosphors—Role of co-dopants in search for afterglow, Mater. Res. Bull. 43 (2008) 2946–2953. https://doi.org/10.1016/j.materresbull.2007.12.005.

[15]   D. Jia, R.S. Meltzer, W.M. Yen, W. Jia, X. Wang, Green phosphorescence of CaAl$_2$O$_4$:Tb^{3+},Ce^{3+} through persistence energy transfer, Appl. Phys. Lett. 80 (2002) 1535–1537. https://doi.org/10.1063/1.1456955.

[16]   H. Guo, Y. Wang, W. Chen, W. Zeng, S. Han, G. Li, Y. Li, Controlling and revealing the trap distributions of Ca$_6$BaP$_4$O$_{17}$:Eu^{2+},R^{3+} (R = Dy, Tb, Ce, Gd, Nd) by codoping different trivalent lanthanides, J. Mater. Chem. C. 3 (2015) 11212–11218. https://doi.org/10.1039/C5TC02283E.

[17]   J. Zhang, B. Chen, J. Sun, X. Li, L. Cheng, H. Zhong, White long-lasting phosphorescence generation in a CaAl$_2$Si$_2$O$_8$.: Eu^{2+}, Mn^{2+}, Dy^{3+} system through persistent energy transfer, J. Phys. D. Appl. Phys. 45 (2012) 325105. https://doi.org/10.1088/0022-3727/45/32/325105.

[18]   W. Chen, Y. Wang, W. Zeng, G. Li, H. Guo, Design, synthesis and characterization of near-infrared long persistent phosphors Ca$_4$(PO$_4$)$_2$O:Eu^{2+},R^{3+} (R = Lu, La, Gd, Ce, Tm, Y), RSC Adv. 6 (2016) 331–337. https://doi.org/10.1039/C5RA19762G.

[19]   E. Uzun, E. Öztürk, N. K. Ozpozan, E. Karacaoglu, Thermoluminescence and photoluminescence properties of Mn^{4+}, Pr$^{3+,4+}$, Nd^{3+} and Eu^{3+} in MgAl$_2$Si$_2$O$_8$, J. Lumin. 173 (2016) 73–81. https://doi.org/10.1016/j.jlumin.2015.12.043.

[20]   V. Castaing, A.D. Sontakke, A.J. Fernández-Carrión, N. Touati, L. Binet, M. Allix, D. Gourier, B. Viana, Persistent Luminescence of ZnGa$_2$O$_4$:Cr^{3+} Transparent Glass Ceramics: Effects of Excitation Wavelength and Excitation Power, Eur. J. Inorg Chem. 2017 (2017) 5114–5120. https://doi.org/10.1002/ejic.201700841.

[21]   Y. Cong, Y. He, B. Dong, Y. Xiao, L. Wang, Long afterglow properties of Zn$_2$GeO$_4$:Mn^{2+}, Cr^{3+} phosphor, Opt. Mater. 42 (2015) 506–510. https://doi.org/10.1016/j.optmat.2015.01.045.

[22]   T. Tatsuma, S. Saitoh, Y. Ohko, A. Fujishima, TiO$_2$–WO$_3$ Photoelectrochemical Anticorrosion System with an Energy Storage Ability, Chem. Mater. 13 (2001) 2838–2842. https://doi.org/10.1021/cm010024k.

[23]   T. Tatsuma, S. Saitoh, P. Ngaotrakanwiwat, Y. Ohko, A. Fujishima, Energy Storage of TiO$_2$–WO$_3$ Photocatalysis Systems in the Gas Phase, Langmuir. 18 (2002) 7777–7779. https://doi.org/10.1021/la026011i.

[24]   Y. Takahashi, T. Tatsuma, Oxidative Energy Storage Ability of a TiO$_2$–Ni(OH)$_2$ Bilayer Photocatalyst, Langmuir. 21 (2005) 12357–12361. https://doi.org/10.1021/la052107b.

[25]   L. Xiong, M. Ouyang, L. Yan, J. Li, M. Qiu, Y. Yu, Visible-light Energy Storage by Ti^{3+} in TiO$_2$/Cu$_2$O Bilayer Film, Chem. Lett. 38 (2009) 1154–1155. https://doi.org/10.1246/cl.2009.1154.

[26]   Y. Takahashi, T. Tatsuma, Visible light-induced photocatalysts with reductive energy storage abilities, Electrochem. Commun. 10 (2008) 1404–1407. https://doi.org/10.1016/j.elecom.2008.07.026.

[27]   Q. Li, Y.W. Li, P. Wu, R. Xie, J.K. Shang, Palladium Oxide Nanoparticles on Nitrogen-Doped Titanium Oxide: Accelerated Photocatalytic Disinfection and Post-

Illumination Catalytic "Memory," Adv.Mater. 20 (2008) 3717–3723. https://doi.org/10.1002/adma.200800685.

[28] Q. Zhang, H. Wang, Z. Li, C. Geng, J. Leng, Metal-Free Photocatalyst with Visible-Light-Driven Post-Illumination Catalytic Memory, ACS Appl. Mater. Interfaces. 9 (2017) 21738–21746. https://doi.org/10.1021/acsami.7b02473.

[29] A. Pastor, C. Chen, G. de Miguel, F. Martin, M. Cruz-Yusta, J.C. Buffet, D. O'Hare, I. Pavlovic, L. Sánchez, Aqueous miscible organic solvent treated NiTi layered double hydroxide De-NO$_x$ photocatalysts, Chem. Eng. J. 429 (2022) 132361. https://doi.org/10.1016/j.cej.2021.132361.

[30] L. Liu, W. Yang, Q. Li, S. Gao, J.K. Shang, Synthesis of Cu$_2$O Nanospheres Decorated with TiO$_2$ Nanoislands, Their Enhanced Photoactivity and Stability under Visible Light Illumination, and Their Post-illumination Catalytic Memory, ACS Appl. Mater. Interfaces. 6 (2014) 5629–5639. https://doi.org/10.1021/am500131b.

[31] J.P. Yasomanee, J. Bandara, Multi-electron storage of photoenergy using Cu$_2$O–TiO$_2$ thin film photocatalyst, Sol. Energy Mater. and Sol. Cells. 92 (2008) 348–352. https://doi.org/10.1016/j.solmat.2007.09.016.

[32] Y. Gu, Z. Lu, Z. Chang, J. Liu, X. Lei, Y. Li, X. Sun, NiTi layered double hydroxide thin films for advanced pseudocapacitor electrodes, J. Mater. Chem. A. 1 (2013) 10655–10661. https://doi.org/10.1039/C3TA10954B.

[33] Y. Zhao, P. Chen, B. Zhang, D.S. Su, S. Zhang, L. Tian, J. Lu, Z. Li, X. Cao, B. Wang, M. Wei, D.G. Evans, X. Duan, Highly Dispersed TiO$_6$ Units in a Layered Double Hydroxide for Water Splitting, Chem. Eur. J. 18 (2012) 11949–11958. https://doi.org/10.1002/chem.201201065.

[34] C. Cheng, Q. Liang, M. Yan, Z. Liu, Q. He, T. Wu, S. Luo, Y. Pan, C. Zhao, Y. Liu, Advances in preparation, mechanism and applications of graphene quantum dots/semiconductor composite photocatalysts: A review, J. Hazard Mater. 424 (2022) 127721. https://doi.org/10.1016/j.jhazmat.2021.127721.

[35] J. Qian, J. Yan, C. Shen, F. Xi, X. Dong, J. Liu, Graphene quantum dots-assisted exfoliation of graphitic carbon nitride to prepare metal-free zero-dimensional/two-dimensional composite photocatalysts, J. Mater. Sci. 53 (2018) 12103–12114. https://doi.org/10.1007/s10853-018-2509-8.

[36] J. Qian, C. Shen, J. Yan, F. Xi, X. Dong, J. Liu, Tailoring the Electronic Properties of Graphene Quantum Dots by P Doping and Their Enhanced Performance in Metal-Free Composite Photocatalyst, J. Physic. Chem. C. 122 (2018) 349–358. https://doi.org/10.1021/acs.jpcc.7b08702.

[37] A. Yuan, H. Lei, F. Xi, J. Liu, L. Qin, Z. Chen, X. Dong, Graphene quantum dots decorated graphitic carbon nitride nanorods for photocatalytic removal of antibiotics, J. Colloid. Interface Sci. 548 (2019) 56–65. https://doi.org/10.1016/j.jcis.2019.04.027.

[38] Y. Huang, Y. Liang, Y. Rao, D. Zhu, J. Cao, Z. Shen, W. Ho, S.C. Lee, Environment-Friendly Carbon Quantum Dots/ZnFe$_2$O$_4$ Photocatalysts: Characterization, Biocompatibility, and Mechanisms for NO Removal, Environ. Sci. Technol. 51 (2017) 2924–2933. https://doi.org/10.1021/acs.est.6b04460.

[39]   X. Li, H. Shi, T. Wang, Y. Zhang, S. Zuo, S. Luo, C. Yao, Photocatalytic removal of NO by Z-scheme mineral based heterojunction intermediated by carbon quantum dots, Appl. Surf. Sci. 456 (2018) 835–844. https://doi.org/10.1016/j.apsusc.2018.06.133.

[40]   Y. Huang, Y. Gao, Q. Zhang, Y. Zhang, J. Cao, W. Ho, S.C. Lee, Biocompatible FeOOH-Carbon quantum dots nanocomposites for gaseous NO_x removal under visible light: Improved charge separation and High selectivity, J. Hazard. Mater. 354 (2018) 54–62. https://doi.org/10.1016/j.jhazmat.2018.04.071.

[41]   Y. Cui, T. Wang, J. Liu, L. Hu, Q. Nie, Z. Tan, H. Yu, Enhanced solar photocatalytic degradation of nitric oxide using graphene quantum dots/bismuth tungstate composite catalysts, Chem. Eng. J. 420 (2021) 129595. https://doi.org/10.1016/j.cej.2021.129595.

[42]   Y. Ou, G. Zhu, F. Rao, J. Gao, J. Chang, X. Xie, W. Zhang, Y. Huang, M. Hojamberdiev, Coral-Shaped $TiO_{2-\delta}$ Decorated with Carbon Quantum Dots and Carbon Nanotubes for NO Removal, ACS Appl. Nano Mater. 4 (2021) 7330–7342. https://doi.org/10.1021/acsanm.1c01306.

[43]   J. Liu, R. Li, B. Yang, Carbon Dots: A New Type of Carbon-Based Nanomaterial with Wide Applications, ACS Cent. Sci. 6 (2020) 2179–2195. https://doi.org/10.1021/acscentsci.0c01306.

[44]   S.K. Pal, Versatile photoluminescence from graphene and its derivatives, Carbon 88 (2015) 86–112. https://doi.org/10.1016/j.carbon.2015.02.035.

[45]   Q. Wang, D. O'Hare, Large-scale synthesis of highly dispersed layered double hydroxide powders containing delaminated single layer nanosheets, Chem. Commun. 49 (2013) 6301–6303. https://doi.org/10.1039/C3CC42918K.

[46]   U. Costantino, F. Marmottini, M. Nocchetti, R. Vivani, New Synthetic Routes to Hydrotalcite-Like Compounds – Characterisation and Properties of the Obtained Materials, Eur. J. Inorg. Chem. 1998 (1998) 1439–1446. https://doi.org/10.1002/(SICI)1099-0682(199810)1998:10<1439::AID-EJIC1439>3.0.CO;2-1.

[47]   C. Chen, M. Yang, Q. Wang, J.C. Buffet, D. O'Hare, Synthesis and characterisation of aqueous miscible organic-layered double hydroxides, J. Mater. Chem. A. 2 (2014) 15102–15110. https://doi.org/10.1039/C4TA02277G.

[48]   J. Fragoso, M.A. Oliva, L. Camacho, M. Cruz-Yusta, G. de Miguel, F. Martin, A. Pastor, I. Pavlovic, L. Sánchez, Insight into the role of copper in the promoted photocatalytic removal of NO using $Zn_{2-x}Cu_xCr-CO_3$ layered double hydroxide, Chemosphere. 275 (2021) 130030. https://doi.org/10.1016/j.chemosphere.2021.130030.

[49]   M.C. Capel-Sánchez, G. Blanco-Brieva, J.M. Campos-Martin, M.P. de Frutos, W. Wen, J.A. Rodriguez, J.L.G. Fierro, Grafting Strategy to Develop Single Site Titanium on an Amorphous Silica Surface, Langmuir. 25 (2009) 7148–7155. https://doi.org/10.1021/la900578u.

[50]   M.C. Biesinger, L.W.M. Lau, A.R. Gerson, R.St.C. Smart, The role of the Auger parameter in XPS studies of nickel metal, halides and oxides, Phys. Chem. Chem. Phys. 14 (2012) 2434–2442. https://doi.org/10.1039/C2CP22419D.

[51] H. Yoon, D. Kim, M. Park, J. Kim, J. Kim, W. Srituravanich, B. Shin, Y. Jung, S. Jeon, Extraordinary Enhancement of UV Absorption in TiO_2 Nanoparticles Enabled by Low-Oxidized Graphene Nanodots, J. Phys. Chem. C. 122 (2018) 12114–12121. https://doi.org/10.1021/acs.jpcc.8b03329.

[52] X. Lv, J. Zhang, X. Dong, J. Pan, W. Zhang, W. Wang, G. Jiang, F. Dong, Layered double hydroxide nanosheets as efficient photocatalysts for NO removal: Band structure engineering and surface hydroxyl ions activation, Appl. Catal. B. 277 (2020) 119200. https://doi.org/10.1016/j.apcatb.2020.119200.

[53] C. Chen, A. Wangriya, J.C. Buffet, D. O'Hare, Tuneable ultra high specific surface area Mg/Al-CO_3 layered double hydroxides, Dalton Trans. 44 (2015) 16392–16398. https://doi.org/10.1039/C5DT02641E.

[54] Y. Zhao, Q. Wang, T. Bian, H. Yu, H. Fan, C. Zhou, L.Z. Wu, C.H. Tung, D. O'Hare, T. Zhang, Ni^{3+} doped monolayer layered double hydroxide nanosheets as efficient electrodes for supercapacitors, Nanoscale. 7 (2015) 7168–7173. https://doi.org/10.1039/C5NR01320H.

[55] A. Qu, H. Xie, X. Xu, Y. Zhang, S. Wen, Y. Cui, High quantum yield graphene quantum dots decorated TiO_2 nanotubes for enhancing photocatalytic activity, Appl. Surf. Sci. 375 (2016) 230–241. https://doi.org/10.1016/j.apsusc.2016.03.077.

[56] Y. Zhao, B. Li, Q. Wang, W. Gao, C.J. Wang, M. Wei, D.G. Evans, X. Duan, D. O'Hare, NiTi-Layered double hydroxides nanosheets as efficient photocatalysts for oxygen evolution from water using visible light, Chem. Sci. 5 (2014) 951–958. https://doi.org/10.1039/C3SC52546E.

[57] Y. Liu, S. Yu, Z. Zhao, F. Dong, X.A. Dong, Y. Zhou, N-Doped $Bi_2O_2CO_3$/Graphene Quantum Dot Composite Photocatalyst: Enhanced Visible-Light Photocatalytic NO Oxidation and In Situ DRIFTS Studies, J. Phys. Chem. C. 121 (2017) 12168–12177. https://doi.org/10.1021/acs.jpcc.7b02285.

[58] A. Pastor, F. Rodriguez-Rivas, G. de Miguel, M. Cruz-Yusta, F. Martin, I. Pavlovic, L. Sánchez, Effects of Fe^{3+} substitution on Zn-Al layered double hydroxides for enhanced NO photochemical abatement, Chem. Eng. J. 387 (2020) 124110. https://doi.org/10.1016/j.cej.2020.124110.

[59] F. Rodriguez-Rivas, A. Pastor, C. Barriga, M. Cruz-Yusta, L. Sánchez, I. Pavlovic, Zn-Al layered double hydroxides as efficient photocatalysts for NO_x abatement, Chem. Eng. J. 346 (2018) 151–158. https://doi.org/10.1016/j.cej.2018.04.022.

[60] F. Rodriguez-Rivas, A. Pastor, G. de Miguel, M. Cruz-Yusta, I. Pavlovic, L. Sánchez, Cr^{3+} substituted Zn-Al layered double hydroxides as UV-Vis light photocatalysts for NO gas removal from the urban environment, Sci. Total Environ. 706 (2020) 136009. https://doi.org/10.1016/j.scitotenv.2019.136009.

[61] J.R. Balmes, M.D. Eisner, 74 - Indoor and Outdoor Air Pollution, in: V.C. Broaddus, R.J. Mason, J.D. Ernst, T.E. King, S.C. Lazarus, J.F. Murray, J.A. Nadel, A.S. Slutsky, M.B. Gotway (Eds.), Murray and Nadel's Textbook of Respiratory Medicine (Sixth Edition), Sixth Edition, W.B. Saunders, Philadelphia, 2016: pp. 1331-1342. https://doi.org/10.1016/B978-1-4557-3383-5.00074-9.

[62]   J. Fan, D. Li, X. Wang, Effect of modified graphene quantum dots on photocatalytic degradation property, Diam. Relat. Mater. 69 (2016) 81–85. https://doi.org/10.1016/j.diamond.2016.07.008.

[63]   K.H. Kwak, J.J. Baik, Diurnal variation of NO_x and ozone exchange between a street canyon and the overlying air, Atmos. Environ. 86 (2014) 120–128. https://doi.org/10.1016/j.atmosenv.2013.12.029.

[64]   J. Liao, W. Cui, J. Li, J. Sheng, H. Wang, X. Dong, P. Chen, G. Jiang, Z. Wang, F. Dong, Nitrogen defect structure and NO+ intermediate promoted photocatalytic NO removal on H_2 treated $g\text{-}C_3N_4$, Chem. Eng. J. 379 (2020) 122282. https://doi.org/10.1016/j.cej.2019.122282.

[65]   K.J. Williams, C.A. Nelson, X. Yan, L.S. Li, X. Zhu, Hot Electron Injection from Graphene Quantum Dots to TiO_2, ACS Nano. 7 (2013) 1388–1394. https://doi.org/10.1021/nn305080c.

[66]   P. Sudhagar, I. Herraiz-Cardona, H. Park, T. Song, S.H. Noh, S. Gimenez, I.M. Sero, F. Fabregat-Santiago, J. Bisquert, C. Terashima, U. Paik, Y.S. Kang, A. Fujishima, T.H. Han, Exploring Graphene Quantum Dots/TiO_2 interface in photoelectrochemical reactions: Solar to fuel conversion, Electrochim. Acta. 187 (2016) 249–255. https://doi.org/10.1016/j.electacta.2015.11.048.

[67]   A. Nehdi, N. Frini-Srasra, G. de Miguel, I. Pavlovic, L. Sánchez, J.Fragoso, Use of LDH-chromate adsorption co-product as an air purification photocatalyst, Chemosphere. 286 (2022) 131812. https://doi.org/10.1016/j.chemosphere.2021.131812.

[68]   N.N. Greenwood, A. Earnshaw, Chemistry of Elements, second ed., Butterworth-Heinemann, Oxford, 1997.

[69]   T. López, E. Ortiz, R. Gómez, M. Picquart, Amorphous sol-gel titania modified with heteropolyacids, J. Solgel Sci. Technol. 37 (2006) 189–193. https://doi.org/10.1007/s10971-005-6627-9.

[70]   A. Larbot, I. Laaziz, J. Marignan, J.F. Quinson, Porous texture of a titanium oxide gel: evolution as a function of medium used, J. Non-Cryst. Solids. 147–148 (1992) 157–161. https://doi.org/10.1016/S0022-3093(05)80610-6.

[71]   P. Oliva, J. Leonardi, J.F. Laurent, C. Delmas, J.J. Braconnier, M. Figlarz, F. Fievet, A. de Guibert, Review of the structure and the electrochemistry of nickel hydroxides and oxy-hydroxides, J. Power Sources. 8 (1982) 229–255. https://doi.org/10.1016/0378-7753(82)80057-8.

[72]   P.C. Yu, G. Nazri, C.M. Lampert, Spectroscopic and electrochemical studies of electrochromic hydrated nickel oxide films, Sol. Energy Materials. 16 (1987) 1–17. https://doi.org/10.1016/0165-1633(87)90003-7.

[73]   A. Claude, V. Vaithianathan, R. Bairava Ganesh, R. Sathyalakshmi, P. Ramasamy, Growth and Characterization of Novel (Ni^{3+}, Mg^{2+}) Bimetallic Crystals of Ammonium Di Hydrogen Phosphate, J. Appl. Sci. 6 (2006) 85–89. https://doi.org/10.3923/jas.2006.85.89.

[74]   R. Long, D. Casanova, W.H. Fang, O.V. Prezhdo, Donor–Acceptor Interaction Determines the Mechanism of Photoinduced Electron Injection from Graphene Quantum Dots into TiO_2: π-Stacking Supersedes Covalent Bonding, J. Am. Chem. Soc. 139 (2017) 2619–2629. https://doi.org/10.1021/jacs.6b09598.

[75]   Z. Guo, H. Wu, M. Li, T. Tang, J. Wen, X. Li, Phosphorus-doped graphene quantum dots loaded on TiO_2 for enhanced photodegradation, Appl. Surf. Sci. 526 (2020) 146724. https://doi.org/10.1016/j.apsusc.2020.146724.

[76]   S. Kumar, A. Dhiman, P. Sudhagar, V. Krishnan, ZnO-graphene quantum dots heterojunctions for natural sunlight-driven photocatalytic environmental remediation, Appl. Surf. Sci. 447 (2018) 802–815. https://doi.org/10.1016/j.apsusc.2018.04.045.

[77]   D. Pan, J. Jiao, Z. Li, Y. Guo, C. Feng, Y. Liu, L. Wang, M. Wu, Efficient Separation of Electron–Hole Pairs in Graphene Quantum Dots by TiO_2 Heterojunctions for Dye Degradation, ACS Sustain. Chem. Eng. 3 (2015) 2405–2413. https://doi.org/10.1021/acssuschemeng.5b00771.

[78]   A. Raghavan, S. Sarkar, L.R. Nagappagari, S. Bojja, S. MuthukondaVenkatakrishnan, S. Ghosh, Decoration of Graphene Quantum Dots on TiO_2 Nanostructures: Photosensitizer and Cocatalyst Role for Enhanced Hydrogen Generation, Ind. Eng. Chem. Res. 59 (2020) 13060–13068. https://doi.org/10.1021/acs.iecr.0c01663.

Appendix III: Supporting Information

Table of contents

Experimental

Materials

Ni_3Ti-CO_3 LDH nanosheets were prepared as follows. Typically, 25 mmol of Ti(O^{i}Pr$_4$) were slowly added dropwise into 100 mmol of concentrated HCl, under N_2 atmosphere. The obtained yellowish solution was subsequently added into a 75 mmol of $Ni(NO_3)_2$ aqueous solution (Ni:Ti atomic ratio = 3:1). This metal source solution was dropped into a Na_2CO_3 aqueous solution (25 mmol), stirring being maintained for 1 h. A pH = 10 value was accurately maintained during the reaction process, for which NaOH 4M was sequentially added from an auto-titrator (725 Dosimat, Methrom). The dispersion was stirred at room temperature for 16 h and finally, filtered and washed with water until pH = 7 was reached. The collected wet LDH product (around 8 g) was then washed with 500 mL of ethanol, filtered again and the obtained wet solid was dispersed in ethanol (300 mL) and stirred at room temperature for 4 h. Finally, the solid was filtered, washed with 200 mL of ethanol and dried in a vacuum oven at 30 °C.

Characterization

X-ray diffraction (XRD) patterns of powdered samples were obtained on a Bruker D8 Discover instrument using Cu Kα radiation (λ=1.5406 Å). From the XRD patterns, the crystalline domain size of the samples was calculated by the Scherrer's equation (DIFFRACT.EVA V3.1 software). In the Scherrer's equation, a K value of 0.9 and 1.84 was taken for the (*003*) and (*110*) planes, respectively. The instrumental broadening was previously measured under the same experimental conditions by using a LaB$_6$ standard (Sigma-Aldrich). Infrared spectra were obtained in a FT-IR PerkinElmer FRONTIER. *In-situ* diffuse reflectance infrared Fourier transform spectra (DRIFTS) were measured using a Harrick reaction chamber.

X-ray photoelectron spectra (XPS) analyses were performed on a Physical Electronics PHI 5700 spectrometer with non-monochromatic Mg Kα radiation (300 W, 15 kV, 1253.6 eV std) and a multichannel detector. All narrow scan spectra have been recorded with a path energy of 29.35 eV and an analysis area of 720 μm.

The Ni and Ti content in the samples was analysed by induced coupled plasma mass spectroscopy (ICP-MS) on a PerkinElmer Nexion X. Thermogravimetric curves were performed by using a Mettler Toledo equipment. High-Resolution Transmission Electron Microscopy (HRTEM) images were obtained with a FEI Talos F200X.

Nitrogen adsorption–desorption isotherms were measured in a ASAP 2020 apparatus surface characterization analyzer (Micromeritics). Isotherms were measured at 77.4 K. Samples were degassed overnight at 90 °C under vacuum prior to analysis. Specific surface areas were

measured by nitrogen adsorption and desorption isotherms using the multipoint Brunauer–Emmett–Teller (BET) method over the relative equilibrium pressure interval $0.05 < P/P_0 < 0.30$. Thermogravimetric curves were measured from 30 to 800 °C (heating rate = 5 °C·min^{-1}; oxygen flow = 50 mL·min^{-1}).

The ultraviolet-visible diffuse reflectance spectra (UV-vis DRS) were measured, from 200 to 800 nm (30 nm·min^{-1}; step = 0.5 nm) using BaSO$_4$ as a reference, on a Varian Cary 5000 spectrophotometer. A FLS920 Fluorimeter (Edinburgh Instrument) was used to measure the steady-state photoluminiscence (PL), time-resolved photoluminescence (TRPL) decays at room temperature (λ_{exc} = 350 nm). The PL Quantum Yield measurements were measured using an integrating sphere coupled to an FLS980 photoluminescence spectrometer. The FLS980 was equipped with double monochromators, a 450 W Xenon lamp and a PMT-R2658P detector. A neutral density filter (Optical Density = 3) was placed in the emission path in order to measure excitation region of the spectrum without detector saturation effects. The excitation wavelength was 350 nm.

Electron paramagnetic resonance (EPR) spectra were recorded on a EMXmicro spectrometer (Bruker) at room temperature. For the detection of •OH, a water dispersion containing 45 mM DMPO and the powdered photocatalyst was used. For the detection of •O$_2^-$, the same conditions were used but using methanol instead of water.

Potassium dichromate (K$_2$Cr$_2$O$_7$) and p-benzoquinone (p-BQ) were used as electron scavenger (e$^-$) and superoxide radical scavenger (•O$_2^-$), respectively. 0.3 g of photocatalyst were dispersed in 22.5 mL ethanol together with the scavenger (5 wt. %). After that, the water was

evaporated and the dried sample was subjected to photocatalytic De-NO$_x$ experiments.

The DRIFT spectroscopy measurements were used to monitor the photochemical De-NO$_x$ process and the intermediates and products formed on the photocatalyst surface. Firstly, the photocatalyst was placed in the reaction chamber and high purity Ar gas was flown through the photocatalyst at room temperature for 10 minutes to remove adsorbed species and then scanned to produce a baseline. Next, under dark conditions, a mixture of 50 mL min $^{-1}$ NO (50 ppm) and 50 mL min^{-1} O$_2$ was injected into the chamber, the sample being subjected to adsorption reactions for 10 minutes. Subsequently, the light was turned on for 30 minutes. The spectrum (accumulation of 12 scans) evolving along with the photocatalytic reaction was obtained every 5 minutes. Finally, the light was turned off and succesive spectra registered for 20 minutes.

A different DRIFTS experiment was performed to check the photocatalytic mechanism in dark conditions. After the cleaning process with Ar, the photocatalyst was irradiated for 30 min. Subsequently, the lamp was shut off, and a mixture of 50 mL·min $^{-1}$ NO (100 ppm) and 50 mL min^{-1} O$_2$ was injected into the chamber for 60 min. The spectra were collected in the dark with the same conditions aforementioned.

The ultraviolet photoelectron spectrometer (UPS) was a Thermo Scientific Multilab 2000 with a He (I) UV source, a photon flux > 1.5× 0^{12} s^{-1} and a 110 mm mean radius hemispherical sector analyzer. UPS measurements were done on the as-prepared samples after 2 min of Ar ions sputtering. The binding energy scale was calibrated using the Fermi level as measured on a polycrystalline gold foil in electrical contact with the samples. The position obtained at the Fermi level was cross-checked

with that deduced from the position of the bulk Au 4 $f_{5/2}$ emission. The estimated uncertainty in the binding energy calibration is ‡ 20 meV.

Electrochemical measurements were done in order to get the Mott-Shottkky plot of the GQDs. The cell consisted of three electrodes: Pt (counter electrode), Ag/AgCl (reference electrode), a working electrode and a 0.2 M Na_2SO_4 electrolyte aqueous solution. The working electrode was prepared by drop-casting ~ 1 mL of a GQD suspension onto a Pt layer, and it was dried at 60 °C in an oven. The suspension was prepared by mixing 1 mL of the raw GQD suspension (1.0 mg·mL^{-1}) with 40 µL of Nafion, the mixture being sonicated for 30 min. After the working electrode was dried, it was placed into the cell for measurement. The Mott–Schottky plots were obtained at a frequency of 1 kHz by using a potentiostat (Metrohm Autolab PGSTAT204).
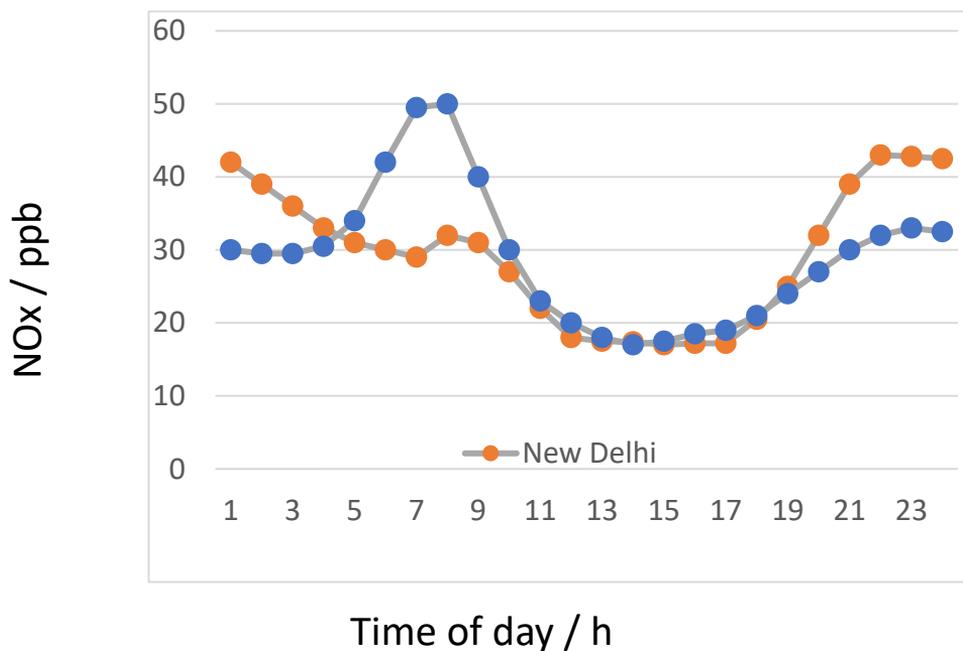

**Figure S1.** *Diurnal profiles of NO$_x$ concentrations at Chicago [1] and New Delhi [2] urban centres.*
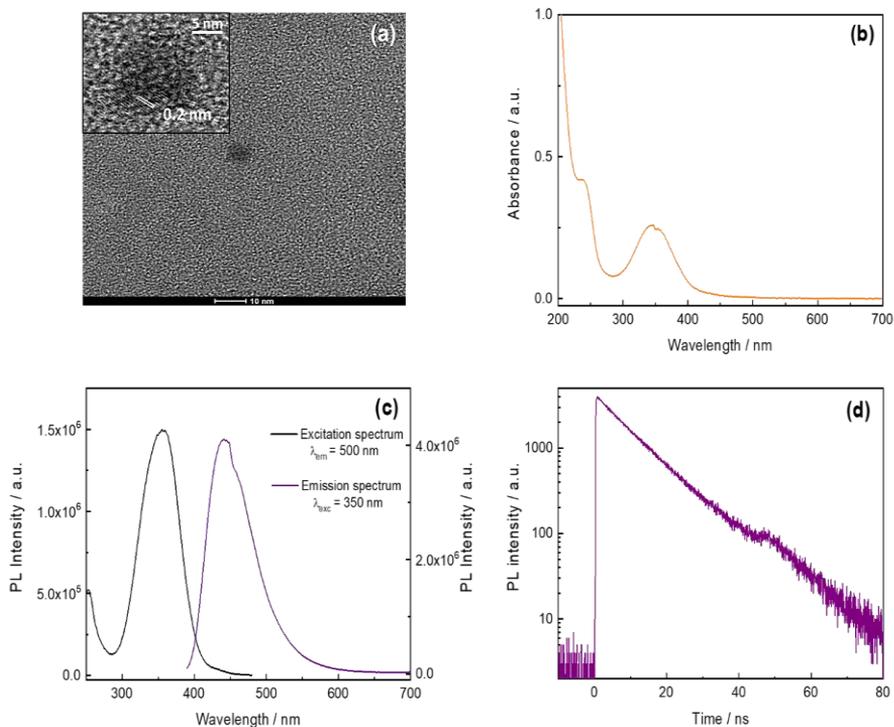
Figure S2. *(a) HR-TEM image, (b) UV-Vis absorption spectrum, (c) excitation and emission spectra and (d) Time-Resolved Photoluminescence for GQDs.*
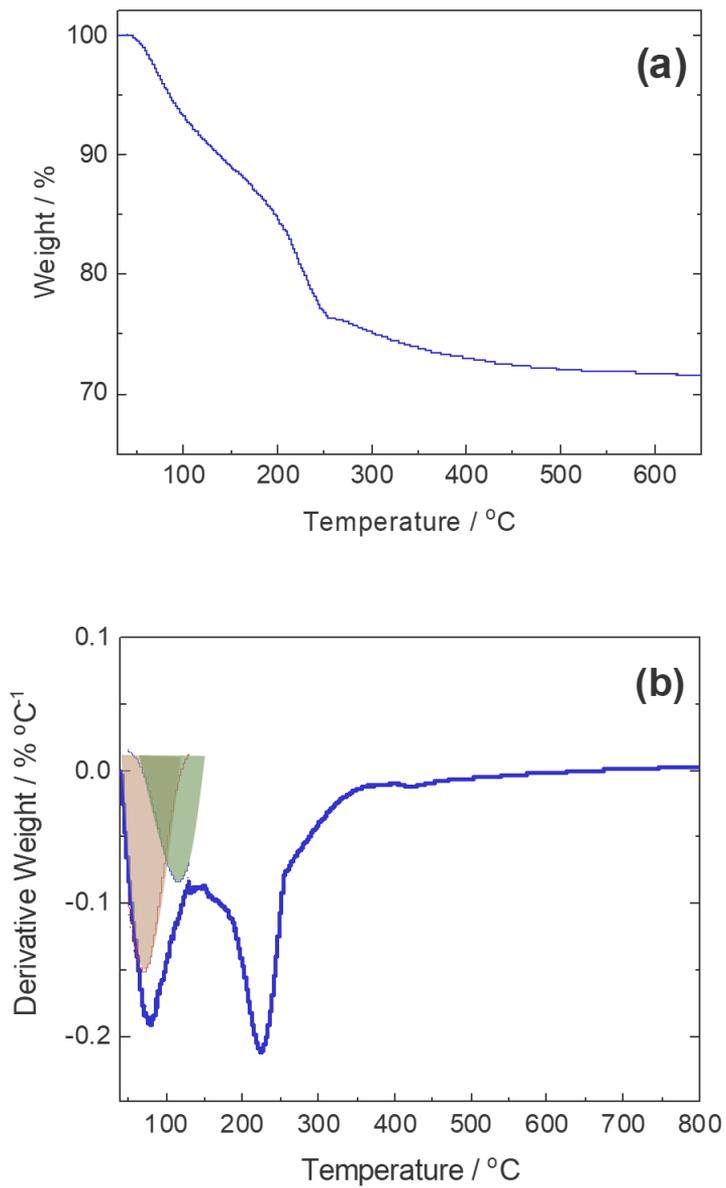
**Figure S3.** *(a) TGA and (b) derivative curve for NiTi-LDH sample.*
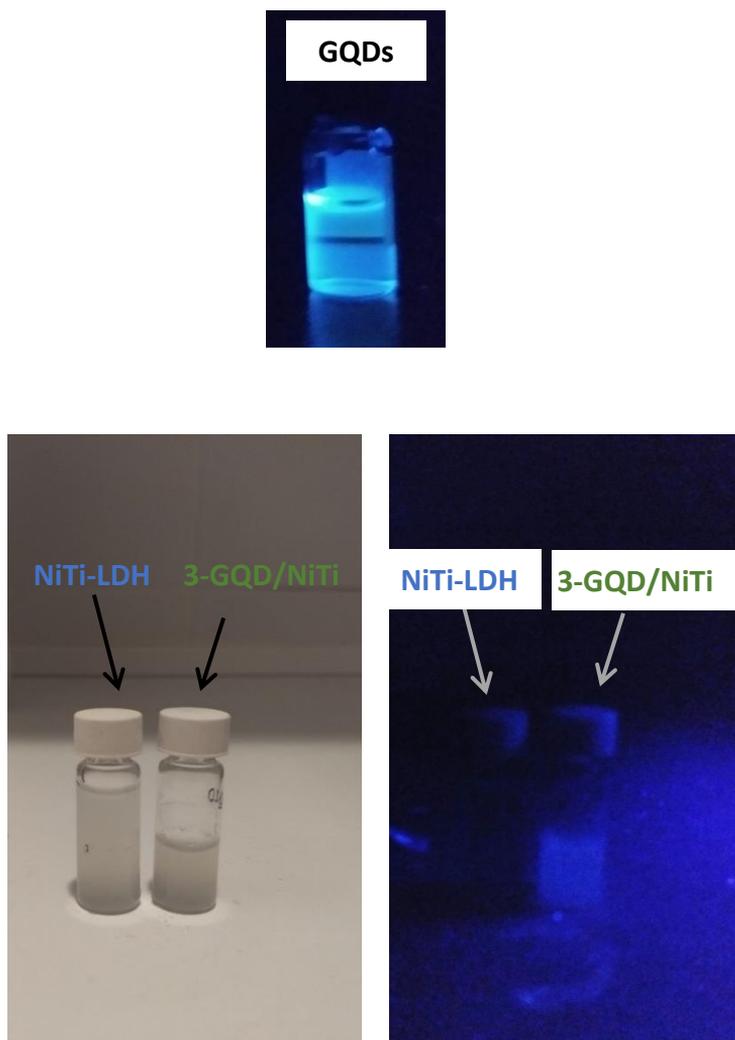
Figure S4. *Images of (up) GQDs and (down) NiTi-LDH and GQDS/NiTi dispersions in light and dark conditions.*
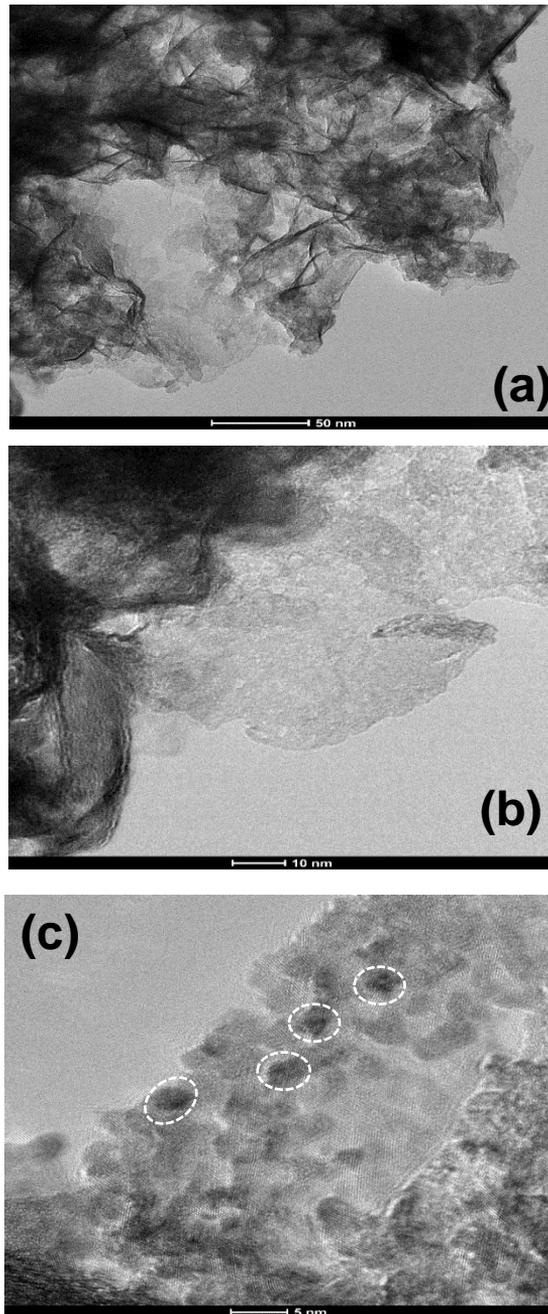
**Figure S5.** *HR-TEM images of (a,c) GQDs/NiTi samples and (b) NiTi-LDH.*
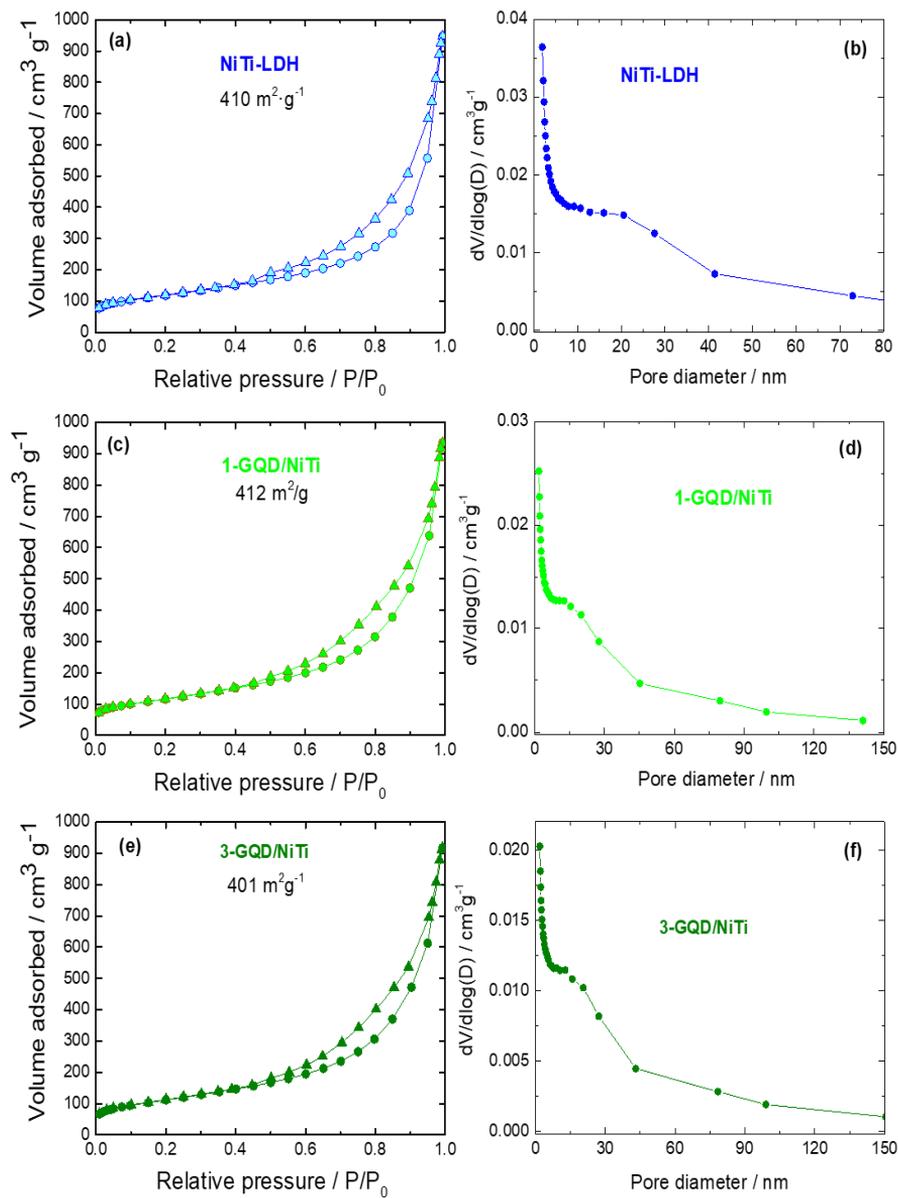
Figure S6. *N$_2$ adsorption-desorption isotherms and pore volume distribution for NiTi-LDH and GQDs/NiTi samples.*
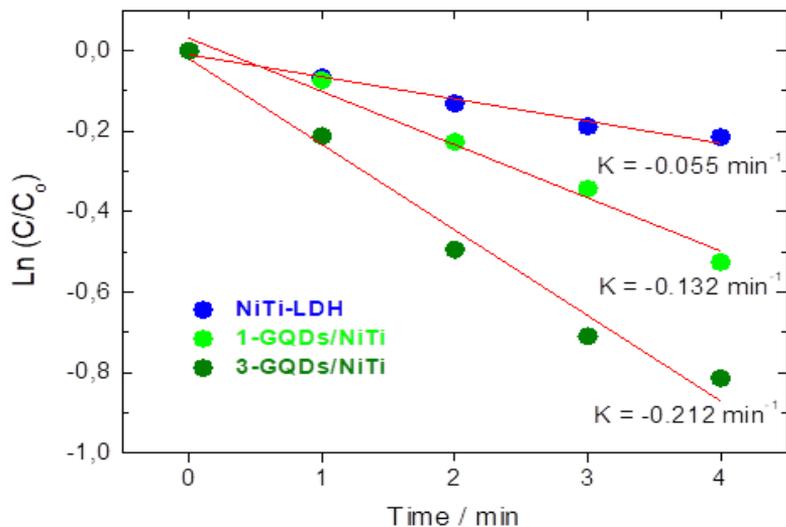
Figure S7. *Variation of the NO concentration: dependence of ln (C/C₀) on irradiation time in the presence of NiTi-LDH and GQDs/NiTi samples.*

Table S1. *NO removed efficiency and Selectivity values observed for different De-NOx photocatalysts.*

Photocatalyst	NO removed / %	Selectivity / %
BiOCl-Ov [3]	70	99
g-C$_3$N$_4$/BiOCl/WO$_{2.92}$ [4]	69	93
GQDs/Bi$_2$WO$_6$ [5]	73	81
MnO$_2$/Bi$_2$WO$_6$ [6]	74	100
TiO$_2$/C$_3$N$_4$ [7]	67	--
ZnO@SiO$_2$ [8]	70	90
Zn$_4$Al$_{0.45}$Fe$_{0.55}$-LDH [9]	59	92
TiO$_2$-δ/CNTs/N-CQDs [10]	60	98
Mesocrystalline TiO$_2$ [11]	59	89
TiO$_2$-P25 (this work)	62	77
GQDs/NiTi-LDH (this work)	61	98
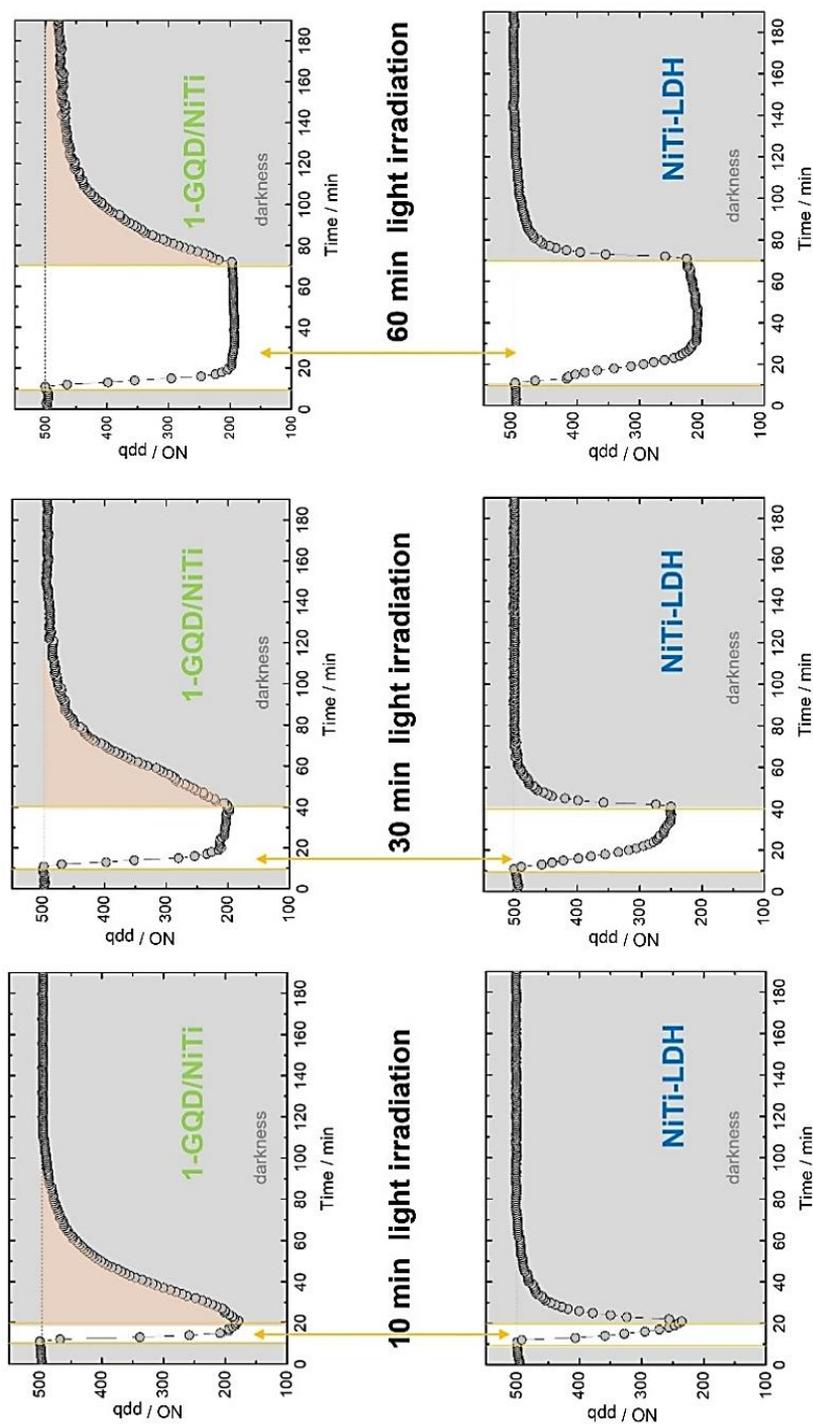
Figure S8. *NO gas concentration evolution during the catalytic reaction of NO in light/dark periods on NiTi-LDH and GQDs/NiTi samples.*
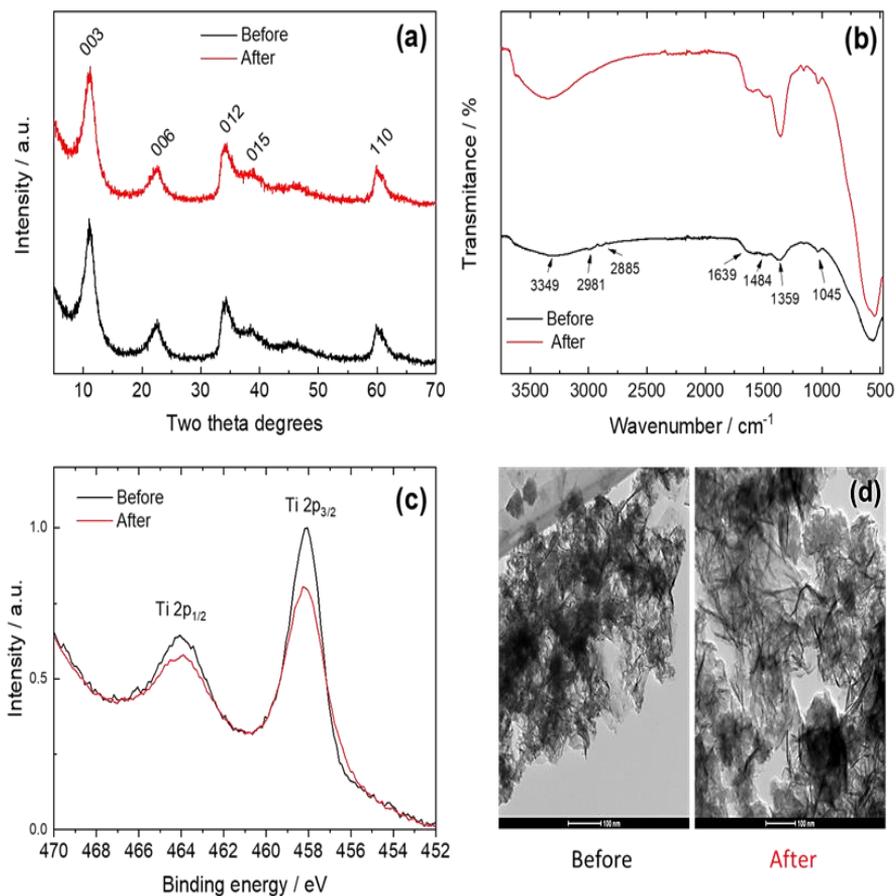
Figure S9. *(a) XRD patterns, (b) IR spectra, (c) Ti 2p XPS spectra and (d) HR-TEM images obtained from 3-GQDs/NiTi before (black line) and after (red line) De-NOx photocatalytic process.*
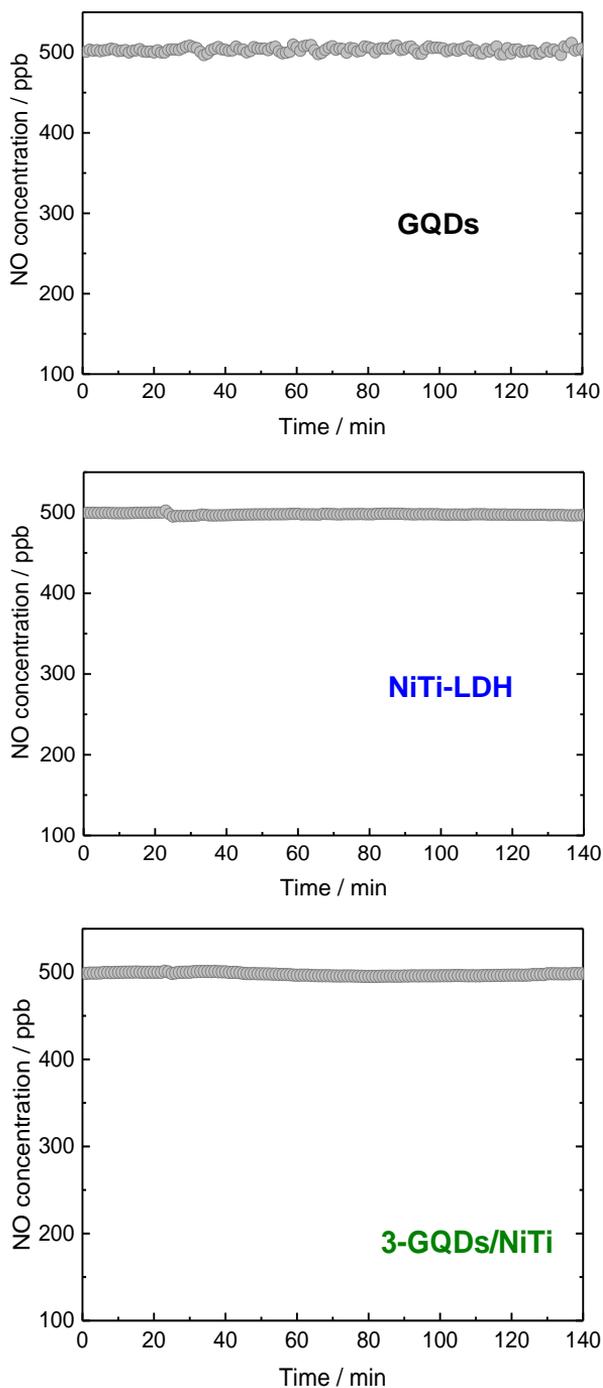
Figure S10. *NO gas concentration evolution on NiTi-LDH, GQDs and GQDs/NiTi samples in the absence of light irradiation.*
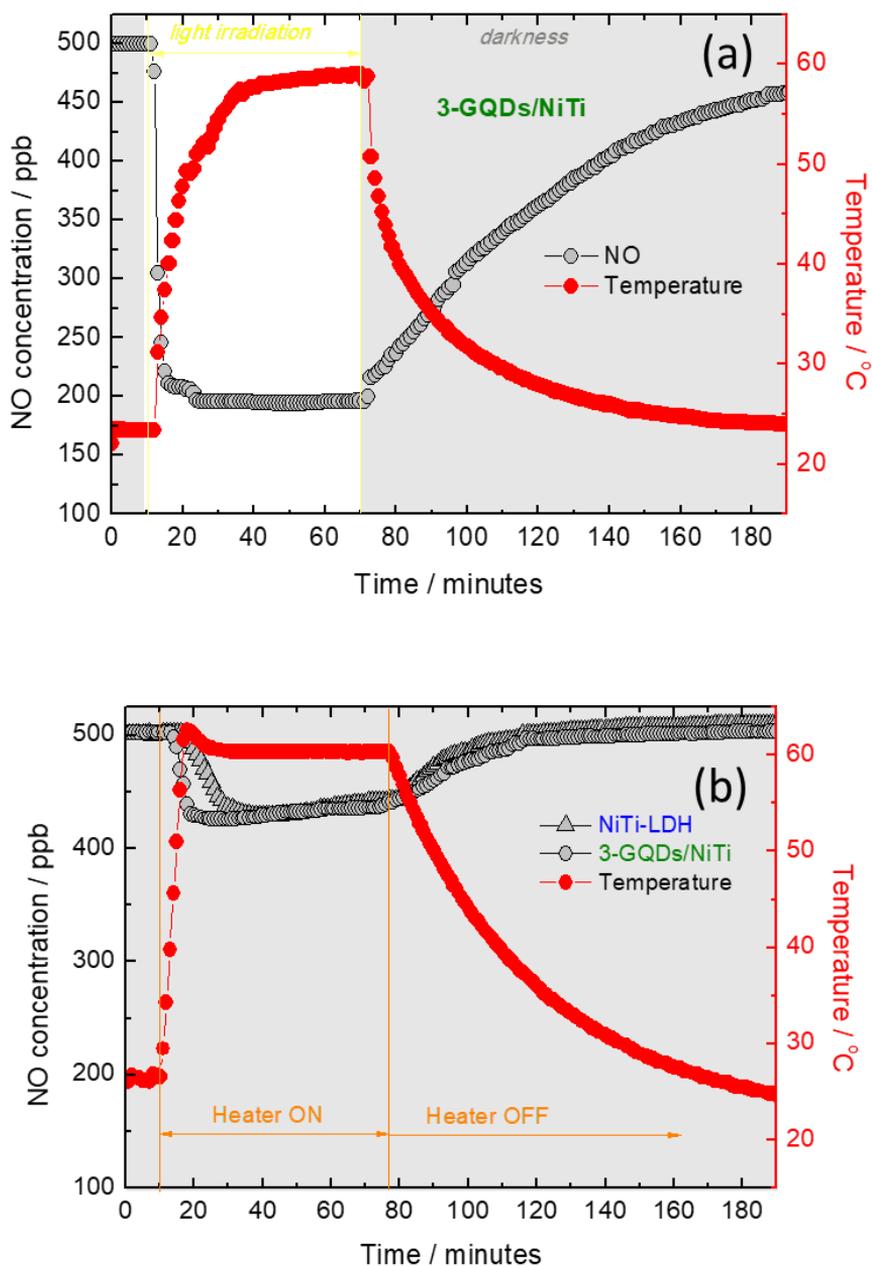
Figure S11. *(a) NO gas concentration and surface temperature evolution during the catalytic reaction of NO in light/dark periods on the 3-GQDs/NiTi sample. (b) NO gas concentration and reaction chamber temperature evolution during the catalytic reaction of NO in the dark on NiTi-LDH and 3-GQDs/NiTi samples, at controlled temperature (50 °C).*
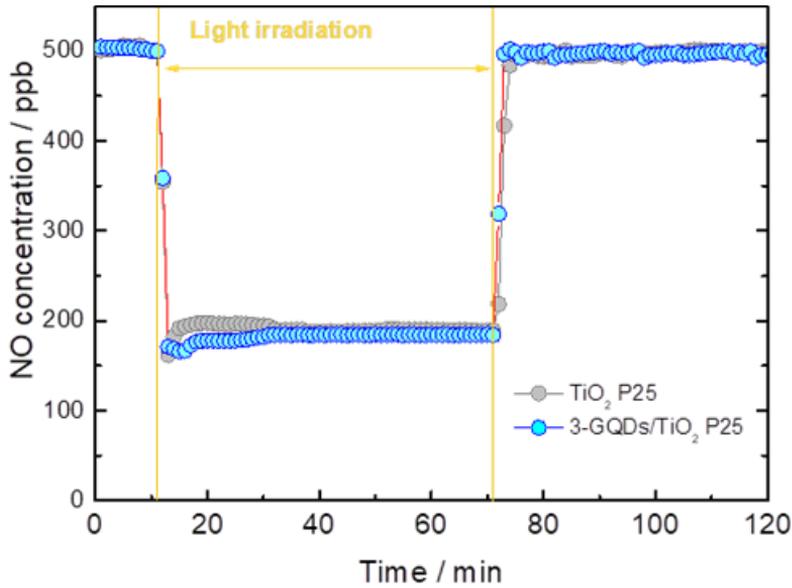
Figure S12. *Gas concentration evolution during the photodegradation of NO under UV-Vis light irradiation on TiO₂ and GQDs/TiO₂ samples.*
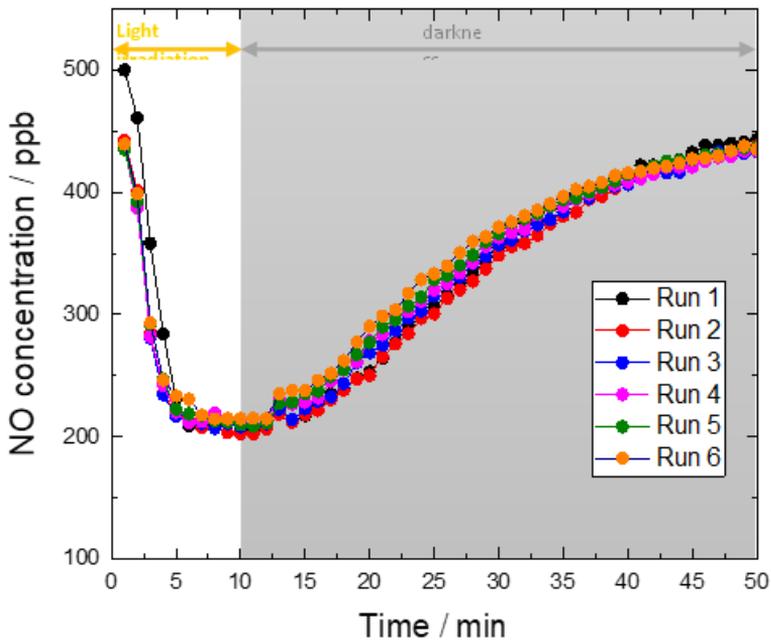
Figure S13. *Gas concentration evolution during running tests for the photodegradation of NO under light/dark conditions for the 3-GQDs/NiTi sample.*

Table S2. *Assignment of the in-situ DRIFTS bands observed during De-NOx tests over the present sample.*

Position (cm^{-1})	Assignment	Ref.
918-920	NO_2^-	[12]
944-1039	monodentate NO_3^-	[13]
1063-1066	bridge NO_3^-	[14]
1098-1100	linear NO_2^-	[15]
1116	NO^-	[15]
1143-1147	bridge NO_2^-	[14]
1162- 1175	NO^-	[15]
1188	Bidentate NO_3^-	[16]
1212-1225	bridge NO_3^-	[14]
1288, 1313	Bidentate NO_3^-	[15]
1243, 1263, 1327	bridge NO_3^-	[13-15]
1347 nitrito	bridge NO_2^-	[15]
1367 nitrito	NO_2^-	[17]
1392-1397	N_2O_4	[16]
1420-1432; 1461-1476	Chelated NO_2^-	[16]
1500-1507	NO_3^-	[17]
1525, 1534, 1559, 1584	Bidentate NO_3^-	[6,14,18,19]
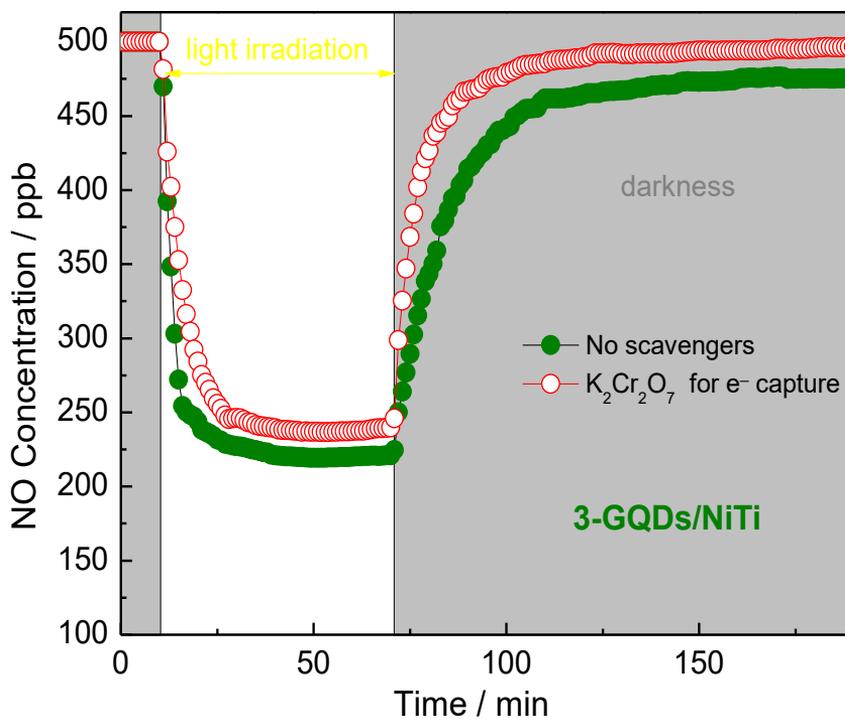
Figure S14. *Active species trapping experiments for the photocatalytic NO oxidation process over the 3-GQDs/NiTi sample.*
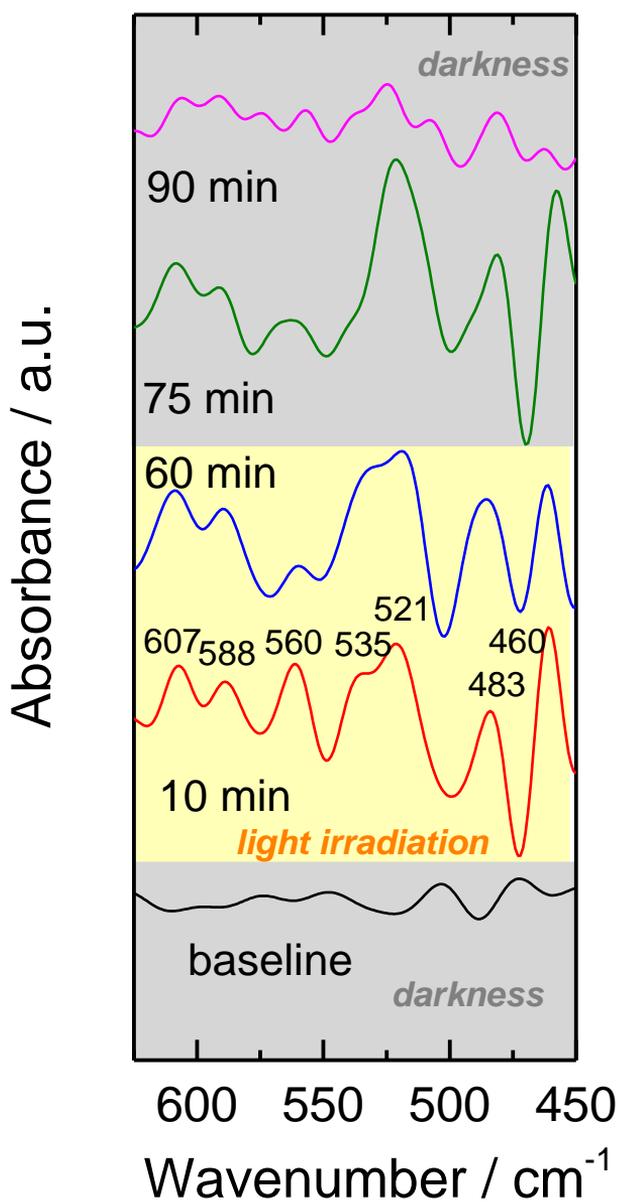
Figure S15. *Far-IR DRIFTS spectra for 3-GQDs/NiTi sample obtained during light irradiation and dark periods.*
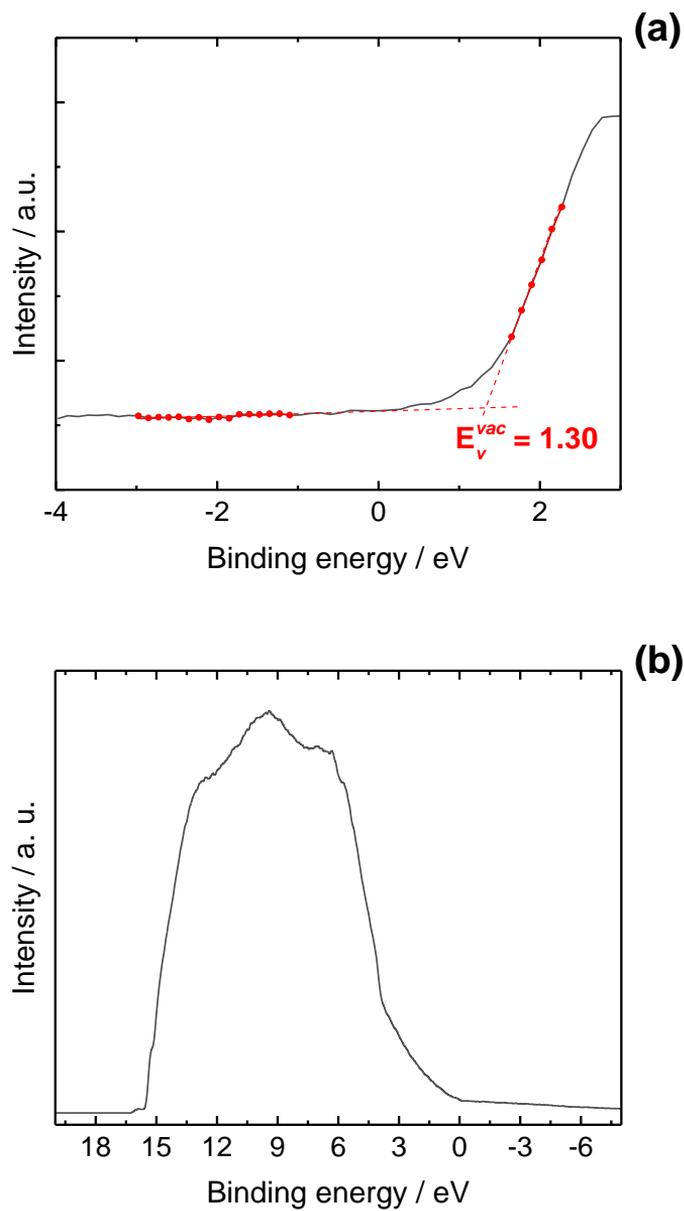
Figure S16. *(a) Valence band XPS spectrum of NiTi-LDH. E_V^{vac} refers to the valence band energy versus Fermi level. E_v = 3.14 V vs. NHE [20]. (b) UPS spectrum of NiTi-LDH.*
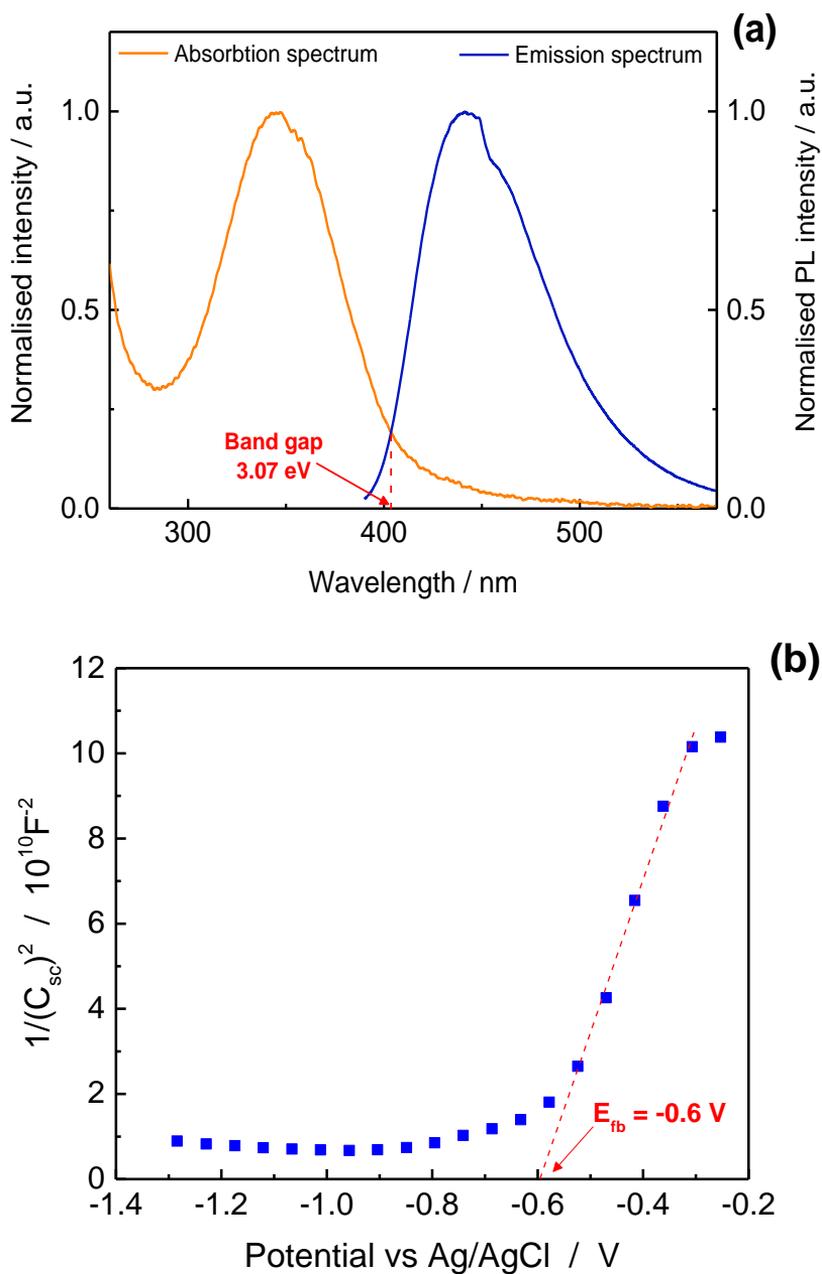
Figure S17. *(a) normalised UV-Vis absorption and emission spectra and (b) Mott-Schottky plot of GQDs. E_{fb} refers to the flat band potential.*
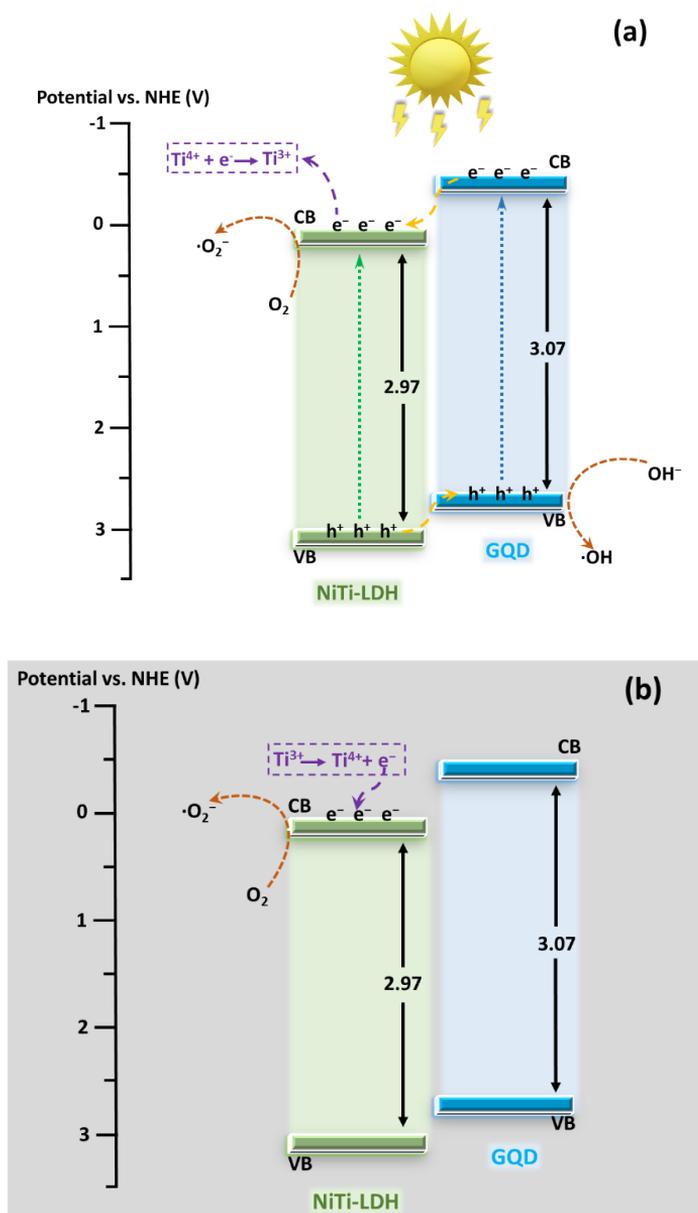
Figure S18. *(a) Schematic p-n heterojunction energy band diagrams for GQDs/NiTi samples with approximate energy levels with respect to the normal hydrogen electrode (NHE) scale. CB and VB: conduction and valence band edges, respectively. (b) Under dark conditions, the chemically stored electrons are released and the production of •O_2^- is maintained.*

Photocatalytic mechanism

Photogenerated electrons and holes (1) once having reached the material surface, in contact with oxygen and water molecules (2, 3), promote the formation of ·OH and ·O_2^- radicals initiating the progressive NO oxidation (4 - 10) [21]:

$$Semiconductor + hv \rightarrow e^- + h^+ \tag{1}$$
$$h^+ + H_2O \rightarrow H^+ + \bullet OH \tag{2}$$
$$e^- + O_2 \rightarrow \bullet O_2^- \tag{3}$$
$$2NO + \bullet O_2^- \rightarrow 2NO_2 + e^- \tag{4}$$
$$NO + \bullet OH \rightarrow HNO_2 \tag{5}$$
$$2NO + \bullet O_2^- + e^- \rightarrow 2NO_2^- \tag{6}$$
$$NO + \bullet O_2^- \rightarrow NO_3^- \tag{7}$$
$$NO_2 + \bullet OH \rightarrow HNO_3 \tag{8}$$
$$NO_2^- + 2(\bullet OH) \rightarrow NO_3^- + H_2O \tag{9}$$
$$2NO_2^- + \bullet O_2^- \rightarrow 2NO_3^- + e^- \tag{10}$$
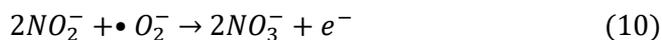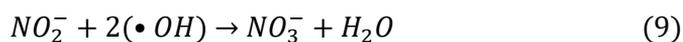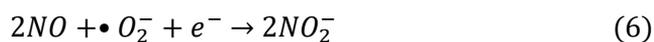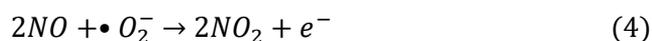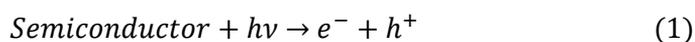
References

[1] B. de Foy, City-level variations in NO_x emissions derived from hourly monitoring data in Chicago, Atmos. Environ. 176 (2018) 128–139. https://doi.org/10.1016/j.atmosenv.2017.12.028.

[2] S. Tiwari, A. Dahiya, N. Kumar, Investigation into relationships among NO, NO_2, NO_x, O_3, and CO at an urban background site in Delhi, India, Atmos. Res. 157 (2015) 119–126. https://doi.org/10.1016/j.atmosres.2015.01.008.

[3] H. Li, H. Shang, X. Cao, Z. Yang, Z. Ai, L. Zhang, Oxygen Vacancies Mediated Complete Visible Light NO Oxidation via Side-On Bridging Superoxide Radicals, Environ. Sci. Technol. 52 (2018) 8659–8665. https://doi.org/10.1021/acs.est.8b01849.

[4] M. Wang, G. Tan, S. Feng, M. Dang, Y. Wang, B. Zhang, H. Ren, L. Lv, A. Xia, W. Liu, Y. Liu, Defects and internal electric fields synergistically optimized g-C_3N_{4-x}/BiOCl/$WO_{2.92}$ heterojunction for photocatalytic NO deep oxidation, J. Hazard. Mater. 408 (2021) 124897. https://doi.org/10.1016/j.jhazmat.2020.124897.

[5] Y. Cui, T. Wang, J. Liu, L. Hu, Q. Nie, Z. Tan, H. Yu, Enhanced solar photocatalytic degradation of nitric oxide using graphene quantum dots/bismuth tungstate composite catalysts, Chem. Eng. J. 420 (2021) 129595. https://doi.org/10.1016/j.cej.2021.129595.

[6] Y. Jing, A. Fan, J. Guo, T. Shen, S. Yuan, Y. Chu, Synthesis of an ultrathin MnO_2 nanosheet-coated Bi_2WO_6 nanosheet as a heterojunction photocatalyst with enhanced photocatalytic activity, Chem. Eng. J. 429 (2022) 132193. https://doi.org/10.1016/j.cej.2021.132193.

[7] J. Zhang, H. Tao, S. Wu, J. Yang, M. Zhu, Enhanced durability of nitric oxide removal on TiO_2 (P25) under visible light: Enabled by the direct Z-scheme mechanism and enhanced structure defects through coupling with C_3N_5, Appl. Catal. B. 296 (2021) 120372. https://doi.org/10.1016/j.apcatb.2021.120372.

[8] A. Pastor, J. Balbuena, M. Cruz-Yusta, I. Pavlovic, L. Sánchez, ZnO on rice husk: A sustainable photocatalyst for urban air purification, Chem. Eng. J. 368 (2019) 659–667. https://doi.org/10.1016/j.cej.2019.03.012.

[9] A. Pastor, F. Rodriguez-Rivas, G. de Miguel, M. Cruz-Yusta, F. Martin, I. Pavlovic, L. Sánchez, Effects of Fe^{3+} substitution on Zn-Al layered double hydroxides for enhanced NO photochemical abatement, Chem. Eng. J. 387 (2020). https://doi.org/10.1016/j.cej.2020.124110.

[10] Y. Ou, G. Zhu, F. Rao, J. Gao, J. Chang, X. Xie, W. Zhang, Y. Huang, M. Hojamberdiev, Coral-Shaped $TiO_{2-\delta}$ Decorated with Carbon Quantum Dots and Carbon Nanotubes for NO Removal, ACS Appl. Nano Mater. 4 (2021) 7330–7342. https://doi.org/10.1021/acsanm.1c01306.

[11] J. Balbuena, J. Miguel Calatayud, M. Cruz-Yusta, P. Pardo, F. Martin, J. Alarcon, L. Sánchez, Mesocrystalline anatase nanoparticles synthesized using a simple hydrothermal approach with enhanced light harvesting for gas-phase reaction, Dalton Transactions. 47 (2018) 6590–6597. https://doi.org/10.1039/c8dt00721g.

[12]   X. Lv, J. Zhang, X. Dong, J. Pan, W. Zhang, W. Wang, G. Jiang, F. Dong, Layered double hydroxide nanosheets as efficient photocatalysts for NO removal: Band structure engineering and surface hydroxyl ions activation, Appl. Catal. B. 277 (2020) 119200. https://doi.org/10.1016/j.apcatb.2020.119200.

[13]   W. Zhang, X. Dong, Y. Liang, Y. Sun, F. Dong, Ag/AgCl nanoparticles assembled on $BiOCl/Bi_{12}O_{17}Cl_2$ nanosheets: Enhanced plasmonic visible light photocatalysis and in situ DRIFTS investigation, Appl. Surf. Sci. 455 (2018) 236–243. https://doi.org/10.1016/j.apsusc.2018.05.171.

[14]   P. Chen, H. Liu, Y. Sun, J. Li, W. Cui, L. Wang, W. Zhang, X. Yuan, Z. Wang, Y. Zhang, F. Dong, Bi metal prevents the deactivation of oxygen vacancies in $Bi_2O_2CO_3$ for stable and efficient photocatalytic NO abatement, Appl Catal B. 264 (2020). https://doi.org/10.1016/j.apcatb.2019.118545.

[15]   W. Huo, W. Xu, T. Cao, X. Liu, Y. Zhang, F. Dong, Carbonate-intercalated defective bismuth tungstate for efficiently photocatalytic NO removal and promotion mechanism study, Appl. Catal. B. 254 (2019) 206–213. https://doi.org/10.1016/j.apcatb.2019.04.099.

[16]   X. Li, W. Zhang, W. Cui, J. Li, Y. Sun, G. Jiang, H. Huang, Y. Zhang, F. Dong, Reactant activation and photocatalysis mechanisms on Bi-metal@Bi_2GeO_5 with oxygen vacancies: A combined experimental and theoretical investigation, Chem. Eng. J. 370 (2019) 1366–1375. https://doi.org/10.1016/j.cej.2019.04.003.

[17]   W. Huo, W. Xu, T. Cao, Z. Guo, X. Liu, G. Ge, N. Li, T. Lan, H.-C. Yao, Y. Zhang, F. Dong, Carbonate doped Bi_2MoO_6 hierarchical nanostructure with enhanced transformation of active radicals for efficient photocatalytic removal of NO, J. Colloid. Interface Sci. 557 (2019) 820–828. https://doi.org/10.1016/j.jcis.2019.09.089.

[18]   W. Huo, T. Cao, W. Xu, Z. Guo, X. Liu, H.-C. Yao, Y. Zhang, F. Dong, Facile construction of $Bi_2Mo_3O_{12}$@$Bi_2O_2CO_3$ heterojunctions for enhanced photocatalytic efficiency toward NO removal and study of the conversion process, Chinese Journal of Catalysis. 41 (2020) 268–275. https://doi.org/10.1016/S1872-2067(19)63460-1.

[19]   H. Wang, Y. Sun, G. Jiang, Y. Zhang, H. Huang, Z. Wu, S.C. Lee, F. Dong, Unraveling the Mechanisms of Visible Light Photocatalytic NO Purification on Earth-Abundant Insulator-Based Core–Shell Heterojunctions, Environ. Sci. Technol. 52 (2018) 1479–1487. https://doi.org/10.1021/acs.est.7b05457.

[20]   M.A. Khan, S. Mutahir, F. Wang, W. Lei, M. Xia, S. Zhu, Facile one-step economical methodology of metal free g-C3N4 synthesis with remarkable photocatalytic performance under visible light to degrade trans-resveratrol, J. Hazard. Mater. 367 (2019) 293–303. https://doi.org/10.1016/j.jhazmat.2018.12.095.

[21]   M. Cruz-Yusta, M. Sánchez, L. Sánchez, Metal oxide nanomaterials for nitrogen oxides removal in urban environments, in: C. Maccato, D. Barreca (Eds.), Tailored Functional Oxide Nanomaterials: From Design to Multi-Purpose Applications, Wiley-VCH GmbH, 2022, pp.229-276. ISBN-13: 978-3527347599; https://doi.org/10.1002/9783527826940.ch7.

3.4. Implementing the use of layered double hydroxides as photocatalytic additive for DeNOx building mortars: ZnCr-CO₃ a case of study
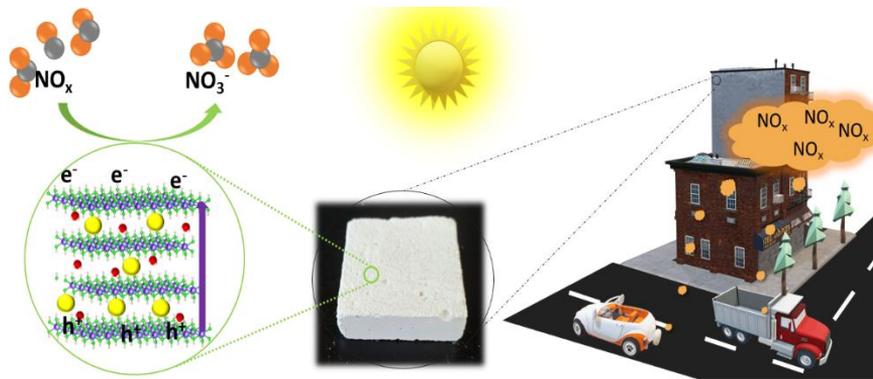
ABSTRACT

Layer double hydroxide, Zn_2Cr-CO_3, is implemented as photocatalytic additive for DeNOx building mortars. When this additive was prepared by the AMOST method (ZnCr-AMO), a high NO_x removal efficiency was achieved (E_{NO} = 67 %). ZnCr-AMO has been easily scaled and added to the cement-base mortars formulation in different percentages (0.5, 1 and 2 wt %) and submitted to the DeNOx photocatalytic test. The results showed that the DeNOx activities of mortars containing ZnCr-LDH and commercial TiO_2 were quite similar, around 50 %, which is a very promising data for this new application of LDH in building materials.

Javier Fragoso,*,[1] José Balbuena,[2] Manuel Cruz-Yusta,[1] Ivana Pavlovic,[1] Mercedes Sánchez[1] and Luis Sánchez*,[1]

[1] Departamento de Química Inorgánica, Instituto Químico para la Energía y Medioambiente (IQUEMA), Universidad de Córdoba, Campus de Rabanales, E-14014 Córdoba, España.

[2] Centro de Innovación Andaluz para la Construcción sostenible (CIAC), Parque Científico-Tecnológico Rabanales 21, E-14014, Córdoba, España.

HIGHLIGHT

- Zn_2Cr-CO_3 LDH is successfully prepared by AMOST procedure.
- ZnCr-AMO photocatalyst exhibits high DeNOx efficiency and outstanding selectivity.
- ZnCr-AMO photocatalyst can be used as additive for cement-based mortars.
- Photocatalytic ZnCr-mortar exhibits noticeable DeNOx efficiency.
- ZnCr-mortar can abate the NO concentration peak pollution typical of urban centers.

3.4.1. Introduction

Air pollution in urban environments is one of the major concerns of society, with special attention to the control of NO_x gas concentration ($NO_x = NO + NO_2$), since it is estimated that thousands of premature deaths worldwide are related to the presence of these gases in urban atmospheres [1,2]. In this sense, at present, the use of materials containing photocatalytic titania nanoparticles is considered as one of the most promising alternatives for the removal of NO_x gases in highly polluted urban atmospheres (DeNOx action) [3]. Since Italcementi S.P.A.'s invention of including photocatalytic TiO_2 nanoparticles in a hydraulic material [4], the use of photocatalytic treatments to building materials has been implemented.

A vast number of studies were reported on titania-based photocatalysts showing brilliant results concerning to the removal of NO_x gases when studied under the controlled conditions of laboratory [5]. However, even though the field studies are still limited [6-10], the efficiency of these materials for the photocatalytic NO_x abatement when applied in real urban environments is not conclusively confirmed in some cases [11-14].

Factors affecting photocatalytic performance include the weathering of photocatalytic construction materials and the drawbacks of titania as a photocatalyst. Regarding the latter, the poor ability of TiO_2 to absorb visible light is well known, which is a handicap for applications located in geographical areas with low incidence of ultraviolet light [15]. In addition, TiO_2 exhibits a low selectivity towards the NO photochemical oxidation, meaning that an important amount is released again to the

atmosphere as the highly toxic NO_2 gas [16]. From the above, apart from the various actions to improve the DeNOx capability of TiO_2 [5], researchers in the field have devoted their efforts in the last decade to study new DeNOx photocatalysts as an alternative to TiO_2. Thus, a considerable number of alternative compounds have been proposed (vg. α-Fe_2O_3, g-C_3N_4, $BaWO_4$/g-C_3N_4, $LaFeO_3$-$SrTiO_3$, FeOOH-Carbon quantum dots, WO_3/ZnO, ZnO@SiO_2, BiOCl-OV, $BiSbO_4$, Bi_2MoO_6, etc.) [5], in some cases with highlighted findings in that concerning to the photochemical NO_x removal efficiency and selectivity [17,18]. Nevertheless, the use of these new advanced DeNOx photocatalysts in building materials is very scarce and only a few recent studies tackle the use of these additives in cementitious materials. Thus, g-C_3N_4 was employed in mass (0.5 – 2 %) on cement pastes [19] or coated onto asphalt pavement aggregates [20] and mortars [21]. In both cases, the materials were tested under visible light irradiation, due to the adequate band gap of g-C_3N_4, showing good NO_x removal efficiency. Besides, the ability of g-C_3N_4 DeNOx photocatalytic additive in cement mortar was enhanced by the formation of composites with a CoAl layered double hydroxides [22]. In similar way, the DeNOx ability under UV-Vis light of cement pastes modified with polymeric carbon nitride (PCN) additions (0.1 – 2.0 %) were successfully reported [23]. BiOBr photocatalyst was also incorporated (1 %) in ceramic coatings materials of the type stucco and ceramic paint, the materials exhibiting a good NO conversion degree under visible light irradiation [24]. Finally, ZnO was studied to prepare photocatalytic DeNOx mortars exhibiting a reduced NO_x removal ability when compared to the use of TiO_2 as photocatalyst [25].

Conversely, layered double hydroxides (LDHs) have recently emerged as an important photocatalyst family of compounds [26] which use as highly efficient DeNOx photocatalyst was first reported a few years ago by our research group [27]. LDH has the general formula of $[M^{II}_{1-x}M^{III}_x(OH)_2]^{x+}A_{x/n}^{n-}\cdot mH_2O$, in which M includes a large variety of metal cations and A of inorganic or organic anions. A large number of different LDHs can be prepared by introducing changes in the metal ratio, metal valence or interlayer anions. Thus, modulating the LDH structure, photocatalysts with different electronic properties, like different band-gap values, exhibiting different photochemical ability [28] can be synthetized. In the field of DeNOx photocatalysis, our group has reported that enhanced photochemical NO conversion can be obtained by introducing changes in the crystallinity of the compound and substituting the metal cations of the layer or the interlayer anions, leading to higher NO removal rate, visible light harvesting and exceptional selectivity [27,29-33]. Therefore, LDHs seems a promising photocatalyst to be implemented as additive in building materials for DeNOx applications with improved performance.

In this work, for the first time, we have successfully used LDH as photocatalytic additive to prepare a DeNOx cement-based mortar. Based on the previous results of our research group and considering parameters such as the efficiency and the selectivity of the photochemical reaction along with the light absorption capacity, the Zn_2Cr-CO_3 formulation was chosen as the preferred LDH admixture. As a novelty, this LDH formulation was here prepared by the first time using the Aqueous Miscible Organic Solvent Treatment (AMOST), a simple method of synthesis which allows the preparation of two dimensional (2D) LDHs [34]. Thanks to their higher

specific surface area, 2D-LDHs enhance the performance of the catalytic process [33]. The physicochemical properties and the photocatalytic performance of the prepared Zn_2Cr-CO_3 LDHs were characterised for this study. The scalability of the synthesis procedure and the preparation of a photocatalytic cement-based mortar was also assessed. Finally, the photocatalytic NO abatement in experimental conditions near to real urban environments were conducted. We found that mortars containing AMOST LDH additive exhibit noticeable results as DeNOx building materials.

3.4.2. Experimental

3.4.2.1. Materials

$ZnCl_2$, $CrCl_3·6H_2O$ and 5,5-dimethyl-1-pyrroline-N-oxide (DMPO) were purchased from Sigma-Aldrich. $Na_2CO_3·10H_2O$, NaOH and ethanol (99.5%) were purchased from PanReac AppliChem. Demineralised water was used in all the experiments.

3.4.2.2. Preparation of LDH photocatalysts

ZnCr layered double hydroxide was synthesized by the conventional co-precipitation method. In order to increase its surface area, the post-treatment method AMOST was used [34]. For the conventional method, 100 mL of $ZnCl_2$ (66.7 mmol) and $CrCl_3·6H_2O$ (33.3 mmol) solution were slowly added dropwise into a bottom flask containing 100 mL of $Na_2CO_3·10H_2O$ (16.7 mmol) while stirring for 1h. During the reaction, the pH value was maintained at 10.0 ± 0.2, using a 4 M NaOH solution. The mixture was stirred overnight at room temperature, filtered, and washed

with water until pH = 7. Afterwards, the wet solid was resuspended in 400 mL of water. 200 mL of this solution was filtered and dried in a vacuum oven at 30 ˚C. Thus, 5 g of powder was obtained and was labelled as ZnCr-C. For the AMOST treatment, the other 200 mL of solution were used. The suspension was filtered, stirred in 300 mL of ethanol during 4 h, filtered and dried. Around 5 g of powder, labelled as ZnCr-AMO, was obtained.

To study the application of ZnCr LDH in building materials, the previously described synthesis was scaled with slight differences. 200 mL of $ZnCl_2$ (133.4 mmol) and $CrCl_3 \cdot 6H_2O$ (66.6 mmol) were added dropwise into 200 mL of $Na_2CO_3 \cdot 10H_2O$ (33.4 mmol) while stirring for 1h. During the reaction, the pH value was maintained at 10.0 ± 0.2, using a 4 M NaOH solution. The whole wet solid obtained was resuspended in 800 mL of water, filtered, and the wet solid is stirred in 600 mL of ethanol during 4h, filtered and dried. This procedure let obtaining around 25 g in each batch, and three different batches were prepared and properly mixed, conforming the sample ZnCr-AMO-S.

3.4.2.3. LDH characterization

Structural, morphological, chemical identity and physical properties of the compounds were characterised by using different techniques. X-ray diffraction (XRD) data were collected on a Bruker D8 Discover diffractometer using Cu K_α radiation (λ = 1.5405 Å). Fourier transform infrared spectrum (FT-IR) was recorded with PerkinElmer Frontier equipped with an ATR. Elemental chemical analyses were measured by induced coupled plasma mass spectroscopy (ICP-MS) on a PerkinElmer Nexion-X instrument. Thermogravimetric analysis (TGA) was performed on a TGA/DSC 1 Star System Mettler Toledo equipment in oxygen

atmosphere (flow: 100 mL min^{-1}; heating rate: 5 ˚C min^{-1}). Scanning electron microscopy (SEM) morphological images were performed on a Jeol JSM 7800 F microscope. High-Resolution Transmission Electron Microscopy images were obtained with a FEI Talos F200X. Pore microstructure and textural properties were studied by N_2 adsorption-desorption isotherms at 77.4 K on a Micromeritics ASAP 2020. UV-Vis diffuse reflectance spectroscopy (DRS) spectra were measured employing a Cary 5000 spectrophotometer. X-ray photoelectron spectroscopy (XPS) was carried out with a Versaprobe II equipment from PHI provided with a focused monochromatic X-ray source (Al-K$_\alpha$ 1486.6 eV). Electron paramagnetic resonance (EPR) spectra were recorded on a EMX micro spectrometer at room temperature. Water or methanol LDH dispersions (for •OH or •O_2^- detection, respectively) were irradiated for 30 min using 45 mM solution DMPO as spin-trap agent.

3.4.2.4. Preparation and characterization of photocatalytic mortars

Commercially available plastering cement-based mortar (Morcemsec® Capa Fina CR CSIV W2, Grupo Puma, Spain) [35] was used in this study. Dosages of 0.5, 1 and 2 wt % of ZnCr-AMO were added as the photocatalytic additive. The photocatalytic mortars were denoted MZnCr-0.5, MZnCr-1 and MZnCr-2, respectively. Mortar containing 0.5 wt % of Aeroxide® TiO$_2$ P25 (Evonik Industries) was used for comparative purposes. The mixing of the mortars was performed in accordance with UNE EN 196-1:2005 standard, maintaining a water/mass weight ratio of 0.16. Consistency and wet density were determined following the UNE-EN-1015-3 and UNE-EN-1015-6 standards, respectively. The mortar specimens were cast in 40 x 40 x 160 mm molds. After 48 h, the specimens

were demolded and cured at 20 °C at 65 ± 5% relative humidity (RH). The flexural and compressive strength of each sample were measured, in triplicate, at 28 days of curing. In order to simulate the performance of the mortars at long time, 28 days cured mortars were aged in a CO_2 chamber for a month (1 % CO_2; 21 ± 2 °C; 60 ± 10 % relative humidity) to carbonate the mortar surface.

3.4.2.5. Photocatalytic experiments

The activity of the ZnCr-LDH in powder and ZnCr-containing mortars towards photochemical oxidation of NO was studied by using a laminar flow reactor. The reactor was placed inside a light sealed irradiation box (Solarbox 3000e RH) equipped with a Xe lamp with controlled irradiance. 400 mg of powder, placed on a 50 × 50 mm quartz sample holder, was used in each photocatalytic test. In the case of ZnCr-containing mortars, 40 x 40 x 10 mm pieces (obtained from the 40 x 40 x 160 mm specimens cured for 28 days) were used to measure the photocatalytic activity. Artificial sunlight (25 and 500 $W \cdot m^{-2}$ for UV and visible irradiances, respectively) was used as irradiation. A mixture of air/NO was sent to the photoreactor. Air and NO streams were mixed to obtain the desired NO concentration: 500 ppb. Previously, air was conveyed by a gas-washing bottle, filled with demineralized water to keep the relative humidity of the supplied gas fixed at 40 ± 5 %. A flow rate of 0.75 $L \cdot min^{-1}$ was employed. The accurate measurement of the concentration of NO, NO_x and NO_2 was carried out using a chemiluminescence analyser (model Environnement AC32M). For each test, the air/NO gas stream ran over the sample in the dark for a period of 10 min without changes in the NO_x concentration profiles were observed, discarding the NO_x adsorption on the sample

surface. The average gas concentration values were calculated from triplicate experiments. The obtained standard deviations were ± 0.3 ppb for NO concentration and ± 1.0 ppb for NO_2 and NO_x concentrations. The following efficiency (E_{NO}, E_{NOx}) and selectivity (S) indexes were used to estimate the photocatalytic performance of the samples at the end of the light illumination period:

$$E_z = (C_i - C_o) \times 100 / C_i \qquad\qquad S = (E_{NOx}/E_{NO}) \times 100$$

where C_i and C_o represent the measured inlet and outlet concentrations and z the gas measured (NO or NO_x).

3.4.3. Results and Discussion

3.4.3.1. Composition and structural characterization of photocatalyst

The X-ray diffraction (XRD) patterns corresponding to Zn_2Cr-CO_3 LDH sample prepared by a simple coprecipitation and the AMOST procedure are shown in Fig. 1a. The reflections located at 2θ ~ 11.5° and 23.0° correspond to the (003) and (006) basal planes, respectively, while those appearing at a higher 2θ angle pertain to (012), (015), (018), (110) and (113) planes [36]. The basal spacing d_{003} 7.78 Å is typical for a ZnCr LDH with the carbonate anion in the interlayer space [29,31]. The basal XRD reflections are broad and of low intensity, corresponding to a decrease in layer stacking as a consequence of LDH delamination caused by the AMOST procedure. The use of ethanol solvent (see experimental section) favours the replacement of the co-intercalated water molecules present in the LDH interlayer gallery, reducing the hydrogen bonding between layers, thus promoting the delamination process [34,37]. For

comparison, the same sample was prepared following the conventional co-precipitation method. As previously observed for LDHs with Cr^{3+} cations in the hydroxyl layers [29,31], this sample also results very poorly crystallized. However, the basal planes are narrower because delamination of the LDH does not occur (Table 1), as will be confirmed later by electron microscopy.

The characteristics bands for LDH were registered on the corresponding FT-IR spectra, Fig. 1b [36]. Identical signals appeared in the spectra of both samples indicating the same chemical identity. The bands at 3370 cm^{-1} and 1634 cm^{-1} correspond to the O-H bonds stretching vibration and bending modes of water molecules, respectively. The presence of interlayer carbonate anions is identified by the vibration mode v_3 of the CO_3^{2-} molecule, which appears asymmetrically split in the 1469 and 1345 cm^{-1} bands. Additionally, intense bands appear at lower frequencies corresponding to the HO-M-OH (742 cm^{-1}) and M-O (560 and 502 cm^{-1}) vibrational bending modes in the basal layer.
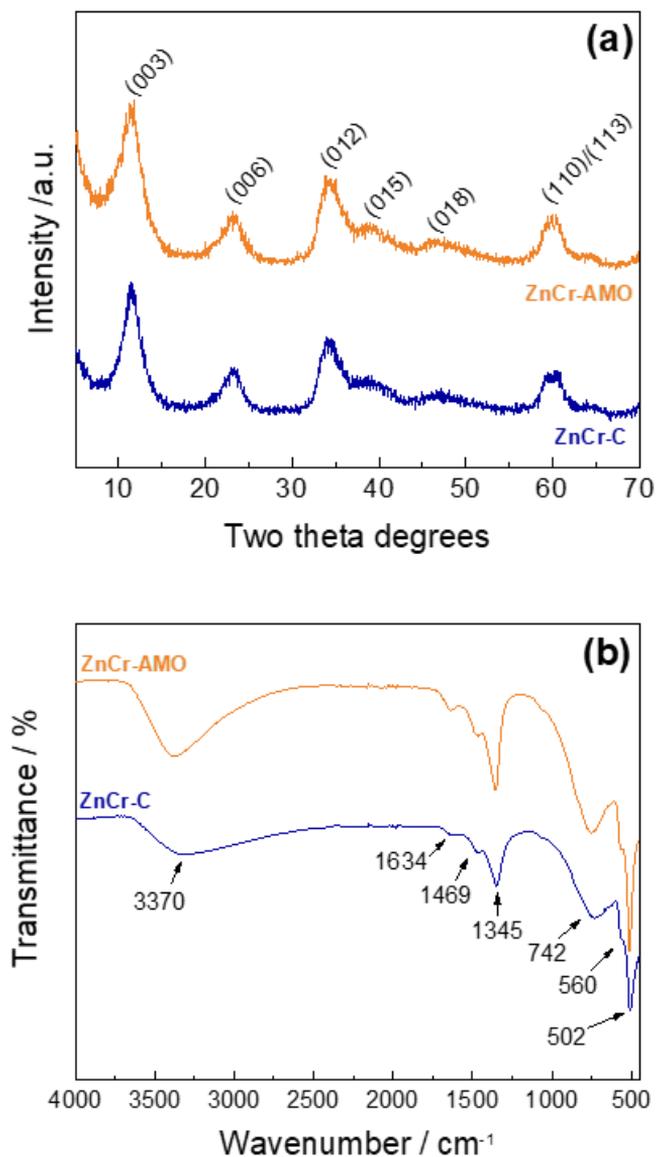
Figure 1. *(a) XRD patterns and (b) FT-IR spectra obtained for the ZnCr-C and ZnCr-AMO samples.*

X-ray photoelectron spectroscopy was used to assess the oxidation states of the metallic elements. Fig. S1 (Supplementary Material) shows the Zn 2p, Cr 2p, C 1s and O 1s normalized XPS spectra of Zn_2Cr-CO_3

sample. The Zn 2p signal appears centred at 1022.5 eV (Fig S1a), the binding energy value expected for $Zn(OH)_2$ [38]. Fig. S1b shows the Cr 2p signal, containing two peaks at 577.3 and 586.6 eV due to the characteristic spin-orbit splitting in the 2p level ($2p_{3/2}$ and $2p_{1/2}$, respectively), which are correlated to the presence of the Cr^{3+} [39]. Of importance, the Cr(VI) species expected at binding energies of 579 eV were no detected. Two peaks were observed for the C 1s signal (Fig S1c): the main peak at 284.8 eV corresponds to adventitious carbon (being used to correct the spectra because charge effects), while that at 289 eV is the characteristic peak from carbonate. Finally, the O 1s peak at around 531 eV is the expected for Zn^{2+} and Cr^{3+} hydroxides (Fig. S1d) [40]. The proposed chemical formulae of samples prepared by the AMOST and conventional synthetic procedures are shown in Table 1. From ICP-MS analysis, in both cases the Zn/Cr ratio results around 2.0, that of the starting solution used to prepare the LDH material. The amount of carbonate anions was assumed that necessary to compensate all positive charge caused by the presence of Cr^{3+} ions in the metallic layer. On the other hand, the TG curves (Fig. S2) were used to calculate the number of water molecules.

Table 1. *X-ray diffraction data and chemical composition for the ZnCr-LDH samples.*

Sample	XRD FWHM / 2θ		% w/w		Zn^{2+}/Cr^{3+} atomic ratio	Formula
	(003)	(006)	Zn^{2+}	Cr^{3+}		
ZnCr-C	2.26	2.51	36.20	13.10	2.12	$[Zn_{0.68}Cr_{0.32}(OH)_2](CO_3)_{0.16}$ $\cdot 0.76H_2O$
ZnCr-AMO	2.56	2.77	33.33	13.35	2.03	$[Zn_{0.67}Cr_{0.33}(OH)_2](CO_3)_{0.165}$ $\cdot 0.9\ H_2O$

3.4.3.2. Morphology, textural and optical properties

Zn_2Cr-CO_3 LDH sample crystallizes in particulate aggregates larger than 40 microns (Fig. S3) and exhibiting different particle morphology according to the synthetic procedure used. SEM microscopy shows how the sample crystallizes as aggregates of micronic/sub-micronic unshaped particles (Fig. 2a) when prepared by the conventional synthesis. Conversely, the aggregates observed for the ZnCr-AMO sample are constituted by rounded nanoparticles lower than 25 nm in size (Fig. 2b). In both cases the particles are poorly crystallized as observed in the corresponding XRD patterns (Fig. 1). HRTEM study assisted to gain knowledge of the precise morphology of the particles for each sample. Fig. 2c shows how ZnCr-C particles are highly aggregated whereas, because the delamination process, widespread thinnest nano-sheets are observed in Fig. 2d for ZnCr-AMO sample.
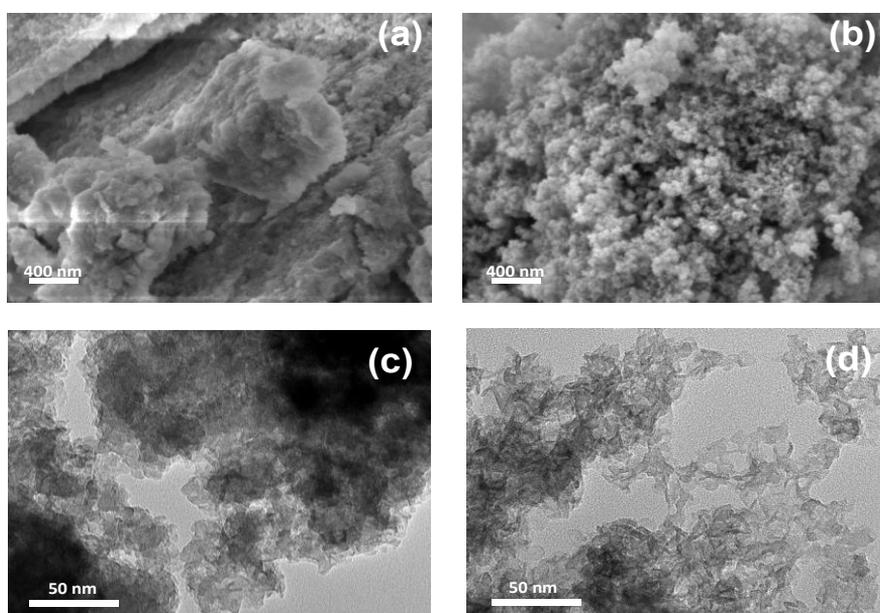

Figure 2. *SEM images of (a) ZnCr-C and (b) ZnCr-AMO samples. HRTEM images of (c) ZnCr-C and (d) ZnCr-AMO samples.*

Consequently, the light activation capacity and the specific surface area of the samples were determined to know their potential activity as photocatalysts. According to their chemical identity, the UV-Vis spectra were similar for both samples (Fig. 3a). As expected for Zn containing LDHs, a main intense absorption peak appears at $\lambda \approx 250$ nm in the UV light range. Due to their characteristic d-d transition in octahedral coordination, the presence of Cr^{3+} ions in LDH gives rise to absorption peaks at 414 and 578 nm [41]. Interestingly, this set of three absorption bands from 250 to 800 nm suggests the potential utilization of these samples as UV and visible light active photocatalysts. To increase the activity of the photocatalyst, in addition to an adequate light absorption capacity, it is very important that it also has a large surface area. In this way, more active centres will be exposed to close contact with reactive molecules. Thus, the N_2 adsorption-desorption isotherm of the samples were recorded, being the specific surface area values measured by the BET method. Because of their different particle morphology, the isotherm shape differs for ZnCr-C and ZnCr-AMO samples, Figs. 3b and 3c. Both samples develop a type II isotherm but have a different hysteresis loop [42].
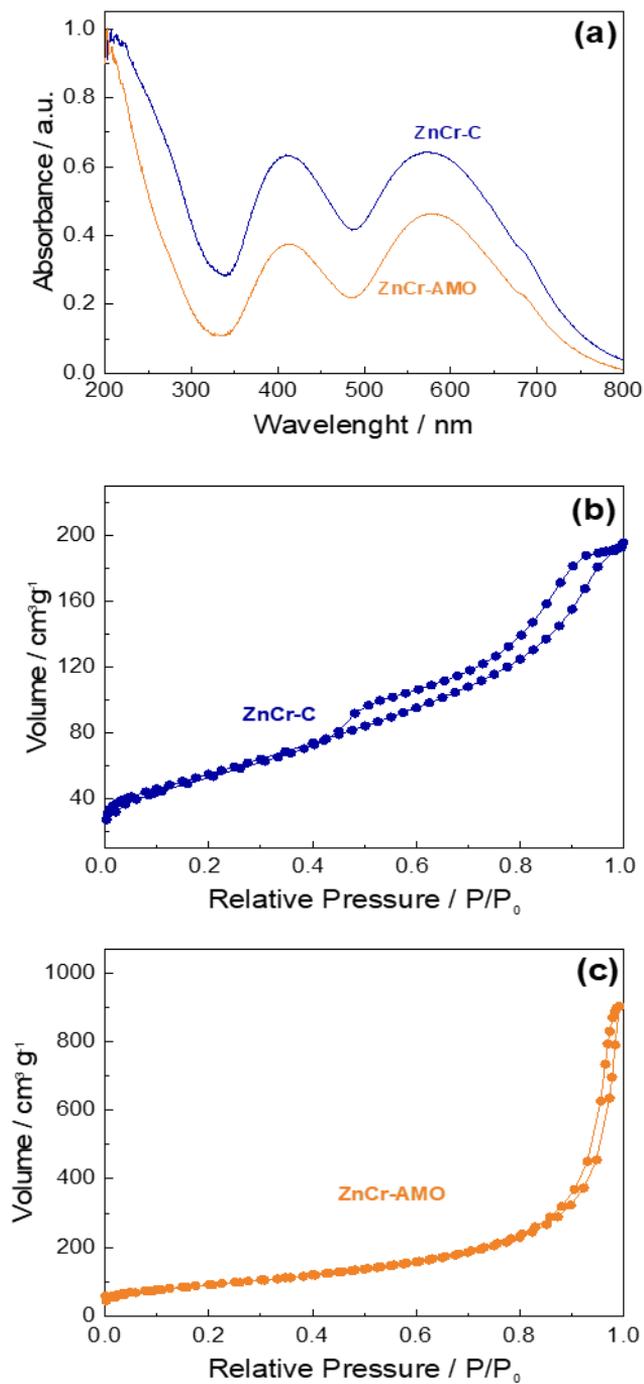
Figure 3. *(a) UV-Vis absorption spectra and (b-c) N$_2$ adsorption-desorption isotherms for ZnCr-C and ZnCr-AMO samples.*

In the case of the ZnCr-C sample, an H5-type hysteresis is observed (Fig. 3b), typical of pore structures containing open and partially blocked mesopores. However, the ZnCr-AMO sample exhibits an H3-type hysteresis loop, generally associated with slit-like pores arising from the layered morphology, as observed in the HRTEM images. The specific surface area values measured were 200 and 330 $m^2 \cdot g^{-1}$ for ZnCr-C and ZnCr-AMO samples, respectively. As intended, the use of the AMOST preparation method has allowed us to significantly increase the exposed surface area of the photocatalyst and, therefore, an increase in photocatalytic performance is expected.

3.4.3.3. Photocatalytic DeNOx activity

The ability of Zn_2Cr-CO_3 LDH samples to eliminate nitrogen oxides from air through a photochemical oxidation process (PCO) was evaluated. Figure 4 shows the variation on the NO, NO_2 and NO_x concentration measured during a standard DeNOx test. In the absence of light irradiation, the first ten minutes, gas concentration remains constant, indicating that the incoming NO gas does not interact with the sample or the chamber. The UV-Vis lamp is then switched on and a sudden decay of the NO concentration values is observed, due to the transformation of NO by a light-activated chemical process. As previously reported, the photochemical NO_x abatement is a complex process activated by reactive oxygen species (ROS), which can be summarized in the following sequential steps [5]: $NO \rightarrow HNO_2 \rightarrow NO_2 \rightarrow NO_3^-$. As a semiconductor, under the appropriate light, the incidence of photons at the surface of the particles of Zn_2Cr-CO_3 LDH generates electrons (e^-) and holes (h^+) pairs. These mobile charges react with the water and oxygen molecules

adsorbed on the surface of the photocatalyst to produce •OH and •O_2^- radicals (ROS species) initiating the oxidation of NO gases, which are thus removed from the air as they are transformed into nitrite and nitrate species [5]. In fact, EPR measurements demonstrated the ability of ZnCr-AMO LDH to produce ROS species validating its role as photocatalyst, Fig. S4. Once the steady state is reached in this photochemical process, it is observed that the efficiency for NO gas removal is enhanced when the ZnCr-AMO sample is used Fig. 4a. Thus, this sample exhibits an E_{NO} value of 67 % while it is only 32 % in the case of the ZnCr-C sample. This difference in efficiency is associated to the high specific surface area of AMOST sample [33], which favours contact between the reactant molecules and the active photocatalyst´s sites. Interestingly, as expected for LDH photocatalysts [27,29-33], NO_2 release is negligible for the two ZnCr-LDH photocatalysts used, being reduced to about ten ppb. This is of importance since NO_2 has been declared to be much more toxic than NO [43]. Consequently, the estimated selectivity of DeNOx is S = 97 %, an exceptional value rarely reported for advanced DeNOx photocatalysts [33]. The mentioned results were compared with those obtained for the photocatalyst TiO_2 P25 (Fig. 4b), which is used as a standard in this field of photocatalysis and as a photocatalytic additive in many DeNOx building materials. TiO_2 photocatalyst exhibits a similar E_{NO} value of 65 % but a significant NO_2 release (77 ppb; S = 75 %), which reduces the efficiency to abate the NO_x to E_{NOx} = 47 %. However, due to its high DeNOx selectivity values, the E_{NOx} efficiency for ZnCr-AMO is 65% indicating that this is a very suitable photocatalyst for preparing DeNOx building materials.
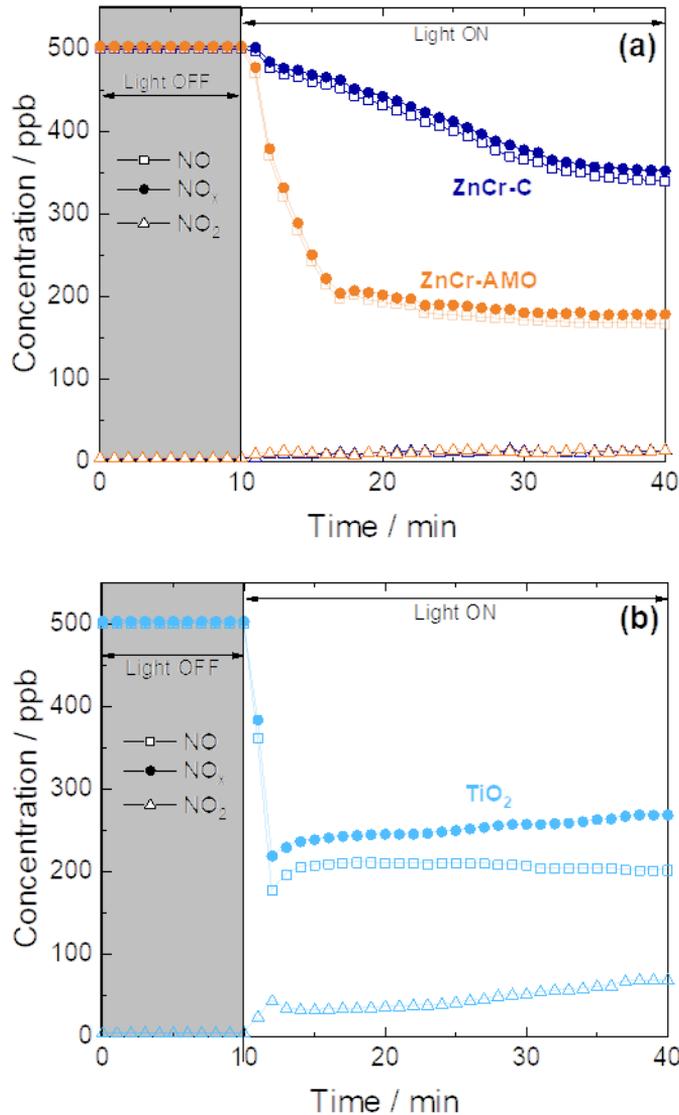
Figure 4. *NO, NOx and NO2 concentration evolution during photocatalytic process under UV-Vis irradiation for (a) ZnCr-C and ZnCr-AMO and (b) TiO2 – P25 samples.*

On the other hand, in order to propose the potential use of ZnCr-AMO in the construction field, it is interesting to evaluate the scalability of its production. In a typical standard procedure of synthesis, 5 g of ZnCr-AMO are obtained. As commented in the experimental section, new

reaction batches were prepared to produce about 25 g per batch, and the products of three batches were mixed to obtain a final amount of about 75 g, which means that the final product has been scaled up by 15. This scaled sample (ZnCr-AMO-S) was fully characterized by XRD, IR, SEM and UV-Vis techniques and the chemical formula and specific surface area calculated (Fig. S5, Table S1), remaining all the recorded properties identical to those above mentioned for the ZnCr-AMO sample. More important, the DeNOx yields for both samples ZnCr-AMO and ZnCr-AMO-S were similar (Fig. S6) validating the use of AMOST method to produce large amounts of photocatalytic additives.

3.4.3.4. Photocatalytic DeNOx mortars

The photocatalytic NO_x removal of cement-based mortars containing different dosages of ZnCr-AMO-S was studied. Figure 5 shows the efficiency values for the NO_x removal obtained for samples MZnCr-0.5, MZnCr-1 and MZnCr-2, after 28 days of curing, under different experimental conditions: NO gas inlet concentration and light illumination time (Figs 5a to 5c). For comparison, a mortar with TiO_2 P25 was also tested. In this case, to compare the same number of photocatalytic active atoms (Zn or Ti) per mass, the molecular weights of of ZnCr-AMO-S and TiO_2 P25 are considered for comparable dosage estimation. Because of the molecular weight of TiO_2 is 2.3 lowest, a dosage of 0.5 % of TiO_2 P25 (MTiO_2-0.5 mortar) was estimated the composition with similar number of active centers between to that of samples MZnCr-1 and MZnCr-2. In all the different DeNOx tests performed, the efficiency for NO_x removal follows the sequence: MZnCr-0.5 < MZnCr-1 > MZnCr-2. Thus, the measured activity increases with the amount of photocatalyst, but an excess of ZnCr

could lead to a decrease in the number of active sites [44,45], and thus reducing the photocatalytic efficiency in the case of MZnCr-2 mortar. At high concentrations of inlet NO gas (500 ppb; Fig. 5a), the MZnCr-1 mortar exhibits a NO_x removal efficiency of 46%, being 22% lower than that exhibited by $MTiO_2$-0.5. However, it can be found in different reports that the concentration of NO_x measured in different highly polluted urban centers is lower and follows the same trend [46-48], with a main peak of NO_x pollution lasting about six hours in the morning due to intense road traffic, with measured concentration values reaching 150 ppb [48]. With the aim to know the potential use of these LDH-based mortars for practical cases of air decontamination, the experimental conditions of the DeNOx tests were modified to simulate the commented real urban scenario, and the NO_x removal was measured under a 150 ppb NO inlet flow, Fig. 5b. Now, the MZnCr-1 mortar reaches a E_{NOx} value of 56%. Under similar NO inlet concentration but extending the experiment for 6 hours (a period similar to the real urban pollution daily episode), Fig. 5c, the efficiency of LDH containing mortars is maintained. Thus, for the best case (MZnCr-1 mortar), the activity of mortars containing LDH and TiO_2 is quite similar, above 50 % of NO_x removal efficiency when realistic urban pollution conditions are considered. Conversely, it should be noted that the progress of the curing and processes over time should modify the surface properties of the mortars and, therefore, their photocatalytic activity. Therefore, it is of interest to know how the air decontamination activity of these mortars might change when aged for a prolonged time. In this sense, the mortars were aged in a CO_2 chamber for one month to carbonate the mortar surface. Subsequently, the carbonated mortars were subjected to DeNOx test, Fig. 5d. Although small differences were found in the E_{NOx} values measured in the mortars before and after aging, these were not

significant, indicating the viability of the mortars to act as DeNOx construction materials.
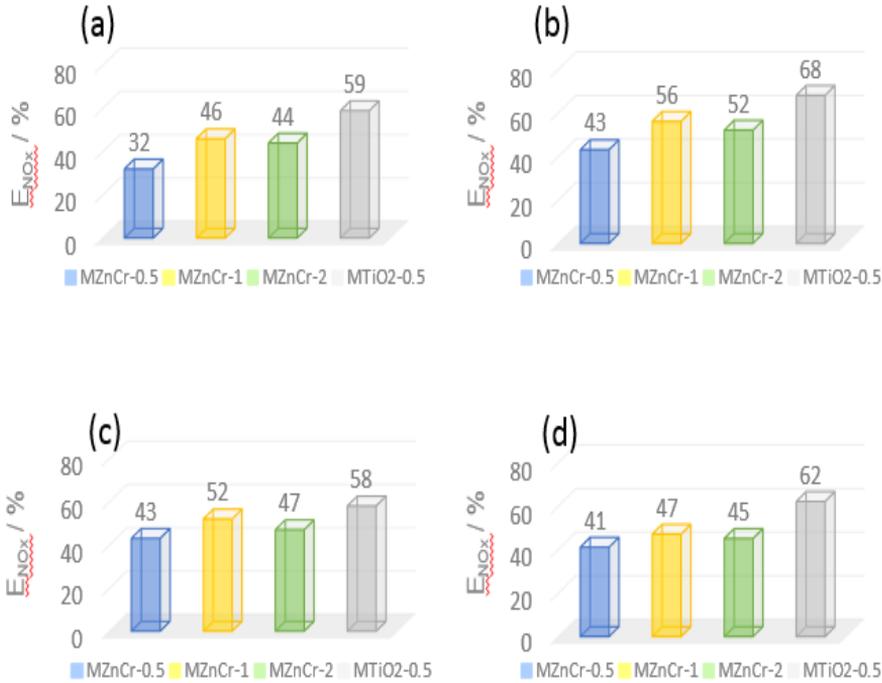
Figure 5. NO$_x$ removal efficiency of the mortars under different experimental conditions: NO gas inlet concentration ([NO]$_{in}$) and light illumination time (t). (a) [NO]$_{in}$ = 500 ppb, t = 30 min; (b) [NO]$_{in}$ = 150 ppb , t = 30 min, (c) [NO]$_{in}$ = 150 ppb , t = 6 h ; (d) carbonated samples , [NO]$_{in}$ = 150 ppb, t = 6 h.

On the same manner, for practical applications, it is important to evaluate the influence of the additive on the properties of the mortar, both in the fresh and hardened state. The slump and the density were measured in the fresh mortar and the flexural and compressive strengths were obtained after 28 days of curing. In Table 2 comparative values of the different parameters for a reference mortar and a mortar containing 1% LDH additive, the one with the best photocatalytic performance, are shown. As can be deduced from the Table 2, no significant influence is

observed in any of the measured properties when the LDH addition is considered. According to the standard UNE-EN 1015-2 the value of the wet density of the mortar, higher than 1.2 kg/m^3, are in good agreement with the slump of 170 mm measured for both types of mortar. The compressive strength of the mortar containing the photocatalytic additives also correspond to that required for a plastering mortar type CS IV, such as the reference one used in this study, with higher values than 6 N/mm^2.

Table 2. *Physical and mechanical properties of mortars with (MZnCr-1) and without (Reference) ZnCr-AMO photocatalytic additive, after 28 days of curing.*

Mortar	Consistency / mm	Wet density / g·cm^{-3}	Flexural strength / N·mm^{-2}	Compressive strength / N·mm^{-2}
Reference	170	1.86	1.68	6.77
MZnCr-1	170	1.74	1.05	6.28

On the other hand, due to the potential toxicity of Cr(VI) species, it is worth mentioning that they are not detected in the XPS analysis performed on the cured mortars, Fig. S7. Again, the peaks observed for the Cr 2p signal appear at the characteristic binding energy values corresponding to Cr(III).

Finally, considering the possible practical application of LDH photocatalytic mortars, some issues such as the extended NO removal efficiency, the visible light activity and the market price of photocatalytic additive materials are worth commenting on. Figure 6a shows the diurnal profiles of NO concentration in urban centers, as an example the one measured at the edge of an urban road in Seoul, Korea [48]. Superimposed, the NO abatement performed by the aged MZnCr-1 mortar

is drawn, concluding that this sample would be able to eliminate an important part of this peak. In addition, the DeNOx activity in visible light (cut-off filter ≥ 410 nm) of the MZnCr-1 sample was measured, Fig. 6b. Under visible light, about 10% DeNOx efficiency can be maintained, which is useful when UV light is scarce, as mentioned in the introduction section. In dark areas of cities, the shadows of buildings or narrow streets where there is no direct sunlight, UV light irradiation decreases drastically. In addition, due to geography and gloomy weather conditions, UV radiation levels reaching the surface in central/northern European or North American cities are low [15]. Therefore, it is interesting to develop DeNOx materials with visible light response.
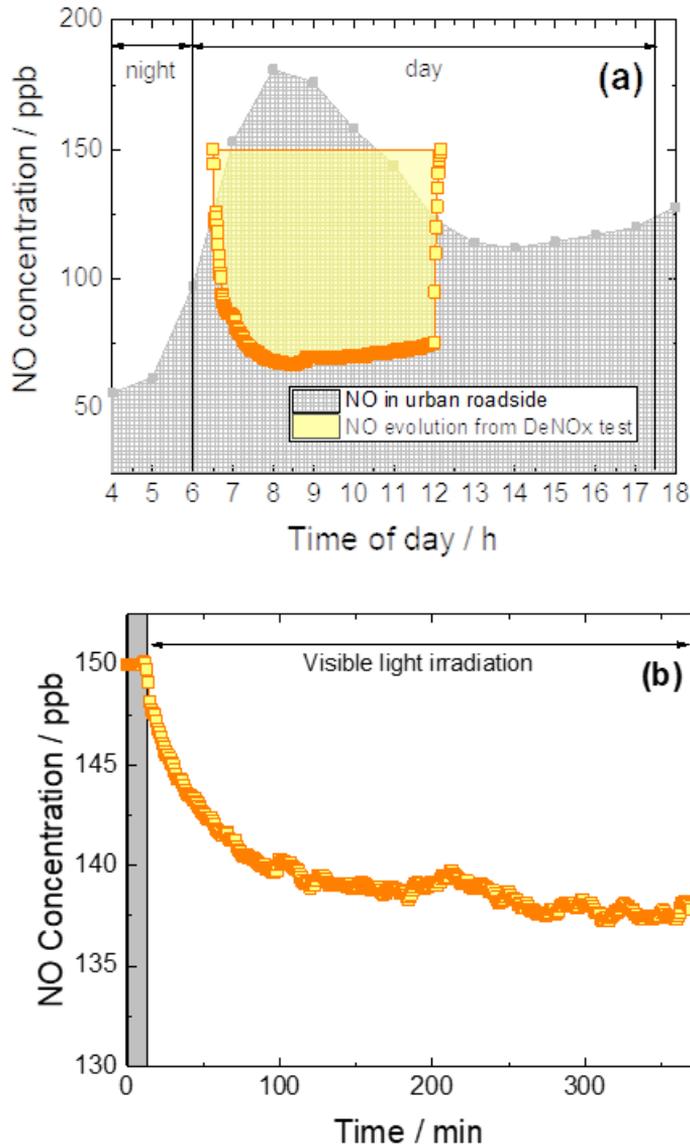
Figure 6. *(a) Diurnal profile of NO gas concentration at urban roadsides and the NO concentration profile obtained for the MZnCr-1 mortar. (b) NO concentration evolution during photocatalytic process under visible irradiation for the MZnCr-1 mortar.*

As far as market prices are concerned, the LDH product is 25 times less expensive than TiO_2 (Merck products, CAS numbers 11097-59-9 and 13463-67-7, respectively [49]), being this a unique advantage considering a future large-scale implementation in urban architecture. From the above, LDH results in a low-cost photocatalytic additive that once added to mortar allows the preparation of construction materials with successful DeNOx response.

3.4.4. Conclusions

ZnCr-LDH has been used for the first time as an active agent in building materials for the removal of NO_x gases in urban environments. Compared with the Zn_2Cr-CO_3 prepared by the conventional coprecipitation method, that prepared by the AMOST method has more specific surface area, which significantly improves the photocatalytic activity.

The ZnCr-AMO photocatalyst has a similar NO_x removal efficiency to the standard TiO_2-P25 (E_{NOx} 65%), but a higher selectivity (97% vs. 75%). The preparation of this product is easily scalable, and the material obtained maintains its physicochemical, structural and photochemical properties unaltered.

The ZnCr-AMO photocatalyst was successfully incorporated in different proportions (0.5, 1.0 and 2.0 %) into a commercial mortar without essentially affecting the physico-mechanical properties of the reference mortar. The DeNOx tests of the mortar with the ZnCr-AMO photocatalyst showed acceptable performance for the different

proportions tested and revealed that the best performance was presented by the sample in which the photocatalyst was added at 1 % (MZnCr-1).

The NO_x removal efficiency of mortars containing ZnCr-AMO or TiO_2-P25 photocatalysts was quite similar ($[NO]_{in}$ = 150 ppb; light irradiation time = 6 h). The price of LDH as a photocatalytic additive is lower than TiO_2, being LDH-mortars able to abate an important part of the NO concentration peak typical of polluted urban centers, showing also activity under visible light irradiation.

These findings open the door to the use of the large family of LDH compounds in building materials with the aim of finding new environmental solutions using photocatalysis.

3.4.5. Acknowledgements

3.4.6. References

[1]   International Institute for Applied Systems Analysis , J. Borken-Kleefeld, 5.000 deaths annually from dieselgate in Europe. https://iiasa.ac.at/web/home/about/news/170918-diesel-nox.html, 2017 (accessed 16 December 2022).

[2]   United Nations, Sustainable Development Actions, 11- Sustainable cities and communities. https://www.un.org/sustainabledevelopment/cities/, 2015 (accessed 17 December 2022).

[3]   The Environmental Industries Commision, A clear choice for the UK: Technology options for tackling air pollution. https://eic-uk.co.uk/media/fy0noosl/technology-options-for-tackling-air-pollution.pdf, 2015 (accessed 17 December 2022).

[4]   C. Luigi, C. Pepe (1997). Paving Tile Comprising an Hydraulic Binder and Photocatalyst Particles.   EP   1 600 430   A1,   21. https://patentimages.storage.googleapis.com/a0/76/35/41ae4be6d197b0/EP1600430A1 .pdf (accessed 12 December 2022).

[5]   M. Cruz-Yusta, M. Sánchez, L. Sánchez, Metal oxide nanomaterials for nitrogen oxides removal in urban environments, in: Tailored Functional Oxide Nanomaterials: From Design to Multi-Purpose Applications, Wiley-VCH, 2022: pp. 229–276. ISBN-13: 978-3527347599. https://doi.org/10.1002/9783527826940.ch7.

[6]   Th. Maggos, J.G. Bartzis, M. Liakou, C. Gobin, Photocatalytic degradation of NO_x gases using TiO_2-containing paint: A real scale study, J. Hazard. Mater. 146 (2007) 668–673. https://doi.org/10.1016/j.jhazmat.2007.04.079.

[7]   R. Nevshupa, E. Jimenez-Relinque, M. Grande, E. Martinez, M. Castellote, Assessment of urban air pollution related to potential nanoparticle emission from photocatalytic pavements, J. Environ. Manage. 272 (2020) 111059. https://doi.org/10.1016/j.jenvman.2020.111059.

[8]   G.L. Guerrini, Photocatalytic performances in a city tunnel in Rome: NO_x monitoring results, Constr. Build. Mater. 27 (2012) 165–175. https://doi.org/10.1016/j.conbuildmat.2011.07.065.

[9]   Th. Maggos, A. Plassais, J.G. Bartzis, Ch. Vasilakos, N. Moussiopoulos, L. Bonafous, Photocatalytic degradation of NOx in a pilot street canyon configuration using TiO_2-mortar panels, Environ. Monit. Assess. 136 (2008) 35–44. https://doi.org/10.1007/s10661-007-9722-2.

[10]   E. Boonen, A. Beeldens, Recent Photocatalytic Applications for Air Purification in Belgium, Coatings. 4 (2014) 553–573. https://doi.org/10.3390/coatings4030553.

[11]   A. Folli, M. Strøm, T.P. Madsen, T. Henriksen, J. Lang, J. Emenius, T. Klevebrant, Å. Nilsson, Field study of air purifying paving elements containing TiO_2, Atmos. Environ. 107 (2015) 44–51. https://doi.org/10.1016/j.atmosenv.2015.02.025.

[12]   M. Gallus, V. Akylas, F. Barmpas, A. Beeldens, E. Boonen, A. Boréave, M. Cazaunau, H. Chen, V. Daële, J.F. Doussin, Y. Dupart, C. Gaimoz, C. George, B. Grosselin, H. Herrmann, S. Ifang, R. Kurtenbach, M. Maille, A. Mellouki, K. Miet, F. Mothes, N. Moussiopoulos, L. Poulain, R. Rabe, P. Zapf, J. Kleffmann, Photocatalytic de-pollution in the Leopold II tunnel in Brussels: NO_x abatement results, Build. Environ. 84 (2015) 125–133. https://doi.org/10.1016/j.buildenv.2014.10.032.

[13]   King's College London, B. Barratt, Environmental Research Group, Statistical analysis of monitoring results from the City of London's NO_x-reducing paint study, https://www.londonair.org.uk/london/reports/CoL_de-nox_paint_statistical_report.pdf ,2007 (accessed 5 December 2022).

[14]   King's College London, A. Tremper and D. Green, Artworks D-NO$_x$ Paint Trial Report   .
https://www.southwark.gov.uk/assets/attach/2407/Artworks_PainTrial_Report_final.pdf , 2016 (accessed 5 December 2022).

[15]   A. Folli, J.Z. Bloh, M. Strøm, T.P. Madsen, T. Henriksen, D.E. Macphee, Efficiency of Solar-Light-Driven TiO$_2$ Photocatalysis at Different Latitudes and Seasons. Where and When Does TiO$_2$ Really Work?, J. Phys. Chem. Lett. 5 (2014) 830–832. https://doi.org/10.1021/jz402704n.

[16]   R.S. Wade, C.E. Castro, Reactions of oxymyoglobin with NO, NO$_2$, and NO$_2^-$ under Argon and in Air, Chem. Res. Toxicol. 9 (1996) 1382–1390. https://doi.org/10.1021/tx9600457.

[17]   H. Li, H. Shang, X. Cao, Z. Yang, Z. Ai, L. Zhang, Oxygen Vacancies Mediated Complete Visible Light NO Oxidation via Side-On Bridging Superoxide Radicals, Environ. Sci. Technol. 52 (2018) 8659–8665. https://doi.org/10.1021/acs.est.8b01849.

[18]   A. Pastor, J. Balbuena, M. Cruz-Yusta, I. Pavlovic, L. Sanchez, ZnO on rice husk: A sustainable photocatalyst for urban air purification, Chem. Eng. J. 368 (2019) 659–667. https://doi.org/10.1016/j.cej.2019.03.012.

[19]   Y. Yang, T. Ji, W. Su, B. Yang, Y. Zhang, Z. Yang, Photocatalytic NO$_x$ abatement and self-cleaning performance of cementitious composites with g-C$_3$N$_4$ nanosheets under visible light, Constr. Build. Mater. 225 (2019) 120–131. https://doi.org/10.1016/j.conbuildmat.2019.07.189.

[20]   Y. Yang, T. Ji, W. Su, Y. Kang, Y. Wu, Y. Zhang, Enhanced washing resistance of photocatalytic exposed aggregate cementitious materials based on g-C$_3$N$_4$ nanosheets-recycled asphalt pavement aggregate composites, Constr. Build. Mater. 228 (2019) 116748. https://doi.org/10.1016/j.conbuildmat.2019.116748.

[21]   Y. Yang, T. Ji, Z. Yang, Y. Zhang, W. Su, R. Wu, Z. Wu, Efficiency and durability of g-C$_3$N$_4$-based coatings applied on mortar under peeling and washing trials, Constr. Build. Mater. 234 (2020) 117438. https://doi.org/10.1016/j.conbuildmat.2019.117438.

[22]   M. Huang, Z. Yang, L. Lu, J. Xu, W. Wang, C. Yang, The Preparation of g-C$_3$N$_4$/CoAl-LDH Nanocomposites and Their Depollution Performances in Cement Mortars under UV-Visible Light, Catalysts. 12 (2022) 443. https://doi.org/10.3390/catal12040443.

[23]   Y. Yang, Z. Yan, L. Zheng, S. Yang, W. Su, B. Li, T. Ji, Interaction between composition and microstructure of cement paste and polymeric carbon nitride, Constr. Build. Mater. 335 (2022) 127464. https://doi.org/10.1016/j.conbuildmat.2022.127464.

[24]   J.M. Montoya-Zamora, A. Martínez-de la Cruz, E. López-Cuéllar, F.A. Pérez González, BiOBr photocatalyst with high activity for NO$_x$ elimination, Adv. Powder Technol. 31 (2020) 3618–3627. https://doi.org/10.1016/j.apt.2020.07.009.

[25]   B.O. Bica, J.V.S. de Melo, Concrete blocks nano-modified with zinc oxide (ZnO) for photocatalytic paving: Performance comparison with titanium dioxide (TiO$_2$), Constr. Build. Mater. 252 (2020) 119120. https://doi.org/10.1016/j.conbuildmat.2020.119120.

[26]   L. Mohapatra, K. Parida, A review on the recent progress, challenges and perspective of layered double hydroxides as promising photocatalysts, J. Mater. Chem. A. 4 (2016) 10744–10766. https://doi.org/10.1039/C6TA01668E.

[27]   F. Rodriguez-Rivas, A. Pastor, C. Barriga, M. Cruz-Yusta, L. Sánchez, I. Pavlovic, Zn-Al layered double hydroxides as efficient photocatalysts for NOx abatement, Chem. Eng. J. 346 (2018) 151–158. https://doi.org/10.1016/j.cej.2018.04.022.

[28]   S.F. Ng, M.Y.L. Lau, W.J. Ong, Engineering Layered Double Hydroxide–Based Photocatalysts Toward Artificial Photosynthesis: State-of-the-Art Progress and Prospects, Solar RRL. 5 (2021) 2000535. https://doi.org/10.1002/solr.202000535.

[29]   F. Rodriguez-Rivas, A. Pastor, G. de Miguel, M. Cruz-Yusta, I. Pavlovic, L. Sánchez, Cr^{3+} substituted Zn-Al layered double hydroxides as UV-Vis light photocatalysts for NO gas removal from the urban environment, Sci. Total Environ. 706 (2020). https://doi.org/10.1016/j.scitotenv.2019.136009.

[30]   A. Pastor, F. Rodriguez-Rivas, G. de Miguel, M. Cruz-Yusta, F. Martin, I. Pavlovic, L. Sanchez, Effects of Fe^{3+} substitution on Zn-Al layered double hydroxides for enhanced NO photochemical abatement, Chem. Eng. J. 387 (2020). https://doi.org/10.1016/j.cej.2020.124110.

[31]   J. Fragoso, M.A. Oliva, L. Camacho, M. Cruz-Yusta, G. de Miguel, F. Martin, A. Pastor, I. Pavlovic, L. Sánchez, Insight into the role of copper in the promoted photocatalytic removal of NO using $Zn_{2-x}Cu_xCr-CO_3$ layered double hydroxide, Chemosphere. 275 (2021) 130030. https://doi.org/10.1016/j.chemosphere.2021.130030.

[32]   A. Nehdi, N. Frini-Srasra, G. de Miguel, I. Pavlovic, L. Sánchez, J.Fragoso, Use of LDH- chromate adsorption co-product as an air purification photocatalyst, Chemosphere. 286 (2022) 131812. https://doi.org/10.1016/j.chemosphere.2021.131812.

[33]   A. Pastor, C. Chen, G. de Miguel, F. Martin, M. Cruz-Yusta, J.C. Buffet, D. O'Hare, I. Pavlovic, L. Sánchez, Aqueous miscible organic solvent treated NiTi layered double hydroxide De-NOx photocatalysts, Chem. Eng. J. 429 (2022) 132361. https://doi.org/10.1016/j.cej.2021.132361.

[34]   Q. Wang, D. O'Hare, Large-scale synthesis of highly dispersed layered double hydroxide powders containing delaminated single layer nanosheets, Chem. Commun. 49 (2013) 6301–6303. https://doi.org/10.1039/C3CC42918K.

[35]   Grupo Puma, https://www.grupopuma.com/es-ES/productos/ver/morcemsec-capa-fina-cr-csiv-w2-es-es (accessed 5 December 2022).

[36]   V. Rives, Layered double hydroxides: Present and Future, Nova Science Publishers, New York, 2001.

[37]   C. Chen, M. Yang, Q. Wang, J.C. Buffet, D. O'Hare, Synthesis and characterisation of aqueous miscible organic-layered double hydroxides, J. Mater. Chem. A. 2 (2014) 15102–15110. https://doi.org/10.1039/C4TA02277G.

[38]   J.M. Wu, Y.R. Chen, Ultraviolet-Light-Assisted Formation of ZnO Nanowires in Ambient Air: Comparison of Photoresponsive and Photocatalytic Activities in Zinc Hydroxide, J. Phys. Chem. C. 115 (2011) 2235–2243. https://doi.org/10.1021/jp110320h.

[39]   P. Gupta, R. Bhargava, R. Das, P. Poddar, Static and dynamic magnetic properties and effect of surface chemistry on the morphology and crystallinity of $DyCrO_3$ nanoplatelets, RSC Adv. 3 (2013) 26427–26432. https://doi.org/10.1039/C3RA43088J.

[40]   M.C. Biesinger, L.W.M. Lau, A.R. Gerson, R.St.C. Smart, Resolving surface chemical states in XPS analysis of first row transition metals, oxides and hydroxides: Sc, Ti, V, Cu and Zn, Appl. Surf. Sci. 257 (2010) 887–898. https://doi.org/10.1016/j.apsusc.2010.07.086.

[41]   J.L. Gunjakar, T.W. Kim, H.N. Kim, I.Y. Kim, S.J. Hwang, Mesoporous Layer-by-Layer Ordered Nanohybrids of Layered Double Hydroxide and Layered Metal Oxide: Highly Active Visible Light Photocatalysts with Improved Chemical Stability, J. Am. Chem. Soc. 133 (2011) 14998–15007. https://doi.org/10.1021/ja203388r.

[42]   M. Thommes, K. Kaneko, A.V. Neimark, J.P. Olivier, F. Rodriguez-Reinoso, J. Rouquerol, K.S.W. Sing, Physisorption of gases, with special reference to the evaluation of surface area and pore size distribution (IUPAC Technical Report), 87 (2015) 1051–1069. https://doi.org/doi:10.1515/pac-2014-1117.

[43]   R.J. Lewis, Sax's Dangerous Properties of Industrial Materials, 5 Volume Set, 12th Edition, Twelth, Wiley & Sons, New Jersey, 2012.

[44]   S.S. Lucas, V.M. Ferreira, J.L.B. de Aguiar, Incorporation of titanium dioxide nanoparticles in mortars — Influence of microstructure in the hardened state properties and photocatalytic activity, Cem. Concr. Res. 43 (2013) 112–120. https://doi.org/10.1016/j.cemconres.2012.09.007.

[45]   O. Carp, C.L. Huisman, A. Reller, Photoinduced reactivity of titanium dioxide, Prog. Solid State Chem. 32 (2004) 33–177. https://doi.org/10.1016/j.progsolidstchem.2004.08.001.

[46]   B. de Foy, City-level variations in NO_x emissions derived from hourly monitoring data in Chicago, Atmos. Environ. 176 (2018) 128–139. https://doi.org/10.1016/j.atmosenv.2017.12.028.

[47]   S. Tiwari, A. Dahiya, N. Kumar, Investigation into relationships among NO, NO_2, NO_x, O_3, and CO at an urban background site in Delhi, India, Atmos. Res. 157 (2015) 119–126. https://doi.org/10.1016/j.atmosres.2015.01.008.

[48]   S.K. Pandey, K.H. Kim, S.Y. Chung, S.J. Cho, M.Y. Kim, Z.H. Shon, Long-term study of NO_x behavior at urban roadside and background locations in Seoul, Korea, Atmos. Environ. 42 (2008) 607–622. https://doi.org/10.1016/j.atmosenv.2007.10.015.

[49]   Merck, https://www.sigmaaldrich.com/ES/en, (accessed 6 December 2022.

Appendix IV: Supplementary Material
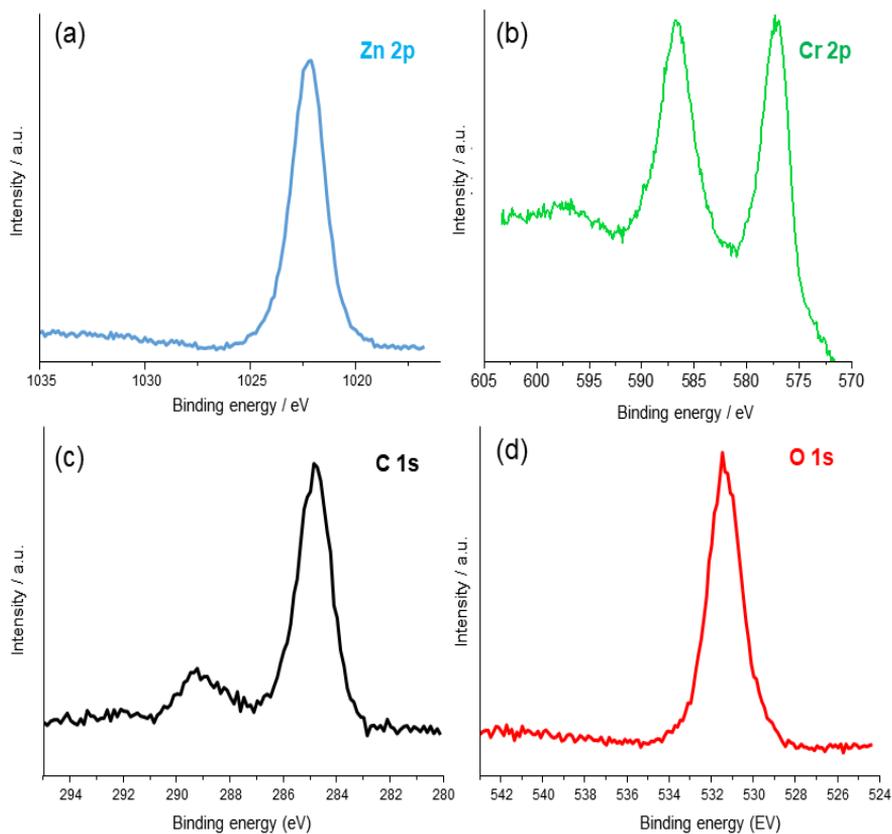
Figure S1. *XPS spectra obtained from ZnCr-AMO sample surface: (a) Zn 2p, (b) Cr 2p, (c) C 1s and (d) O 1s.*
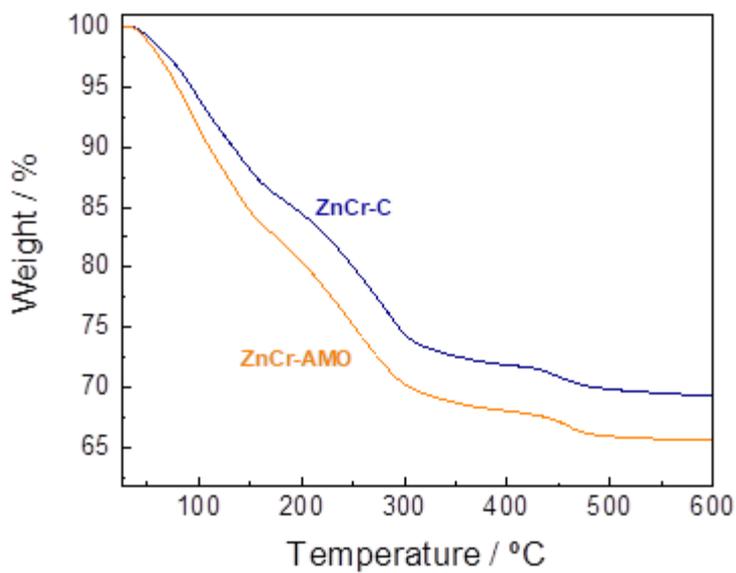
Figure S2. *TG curve for ZnCr-C and ZnCr-AMO samples.*
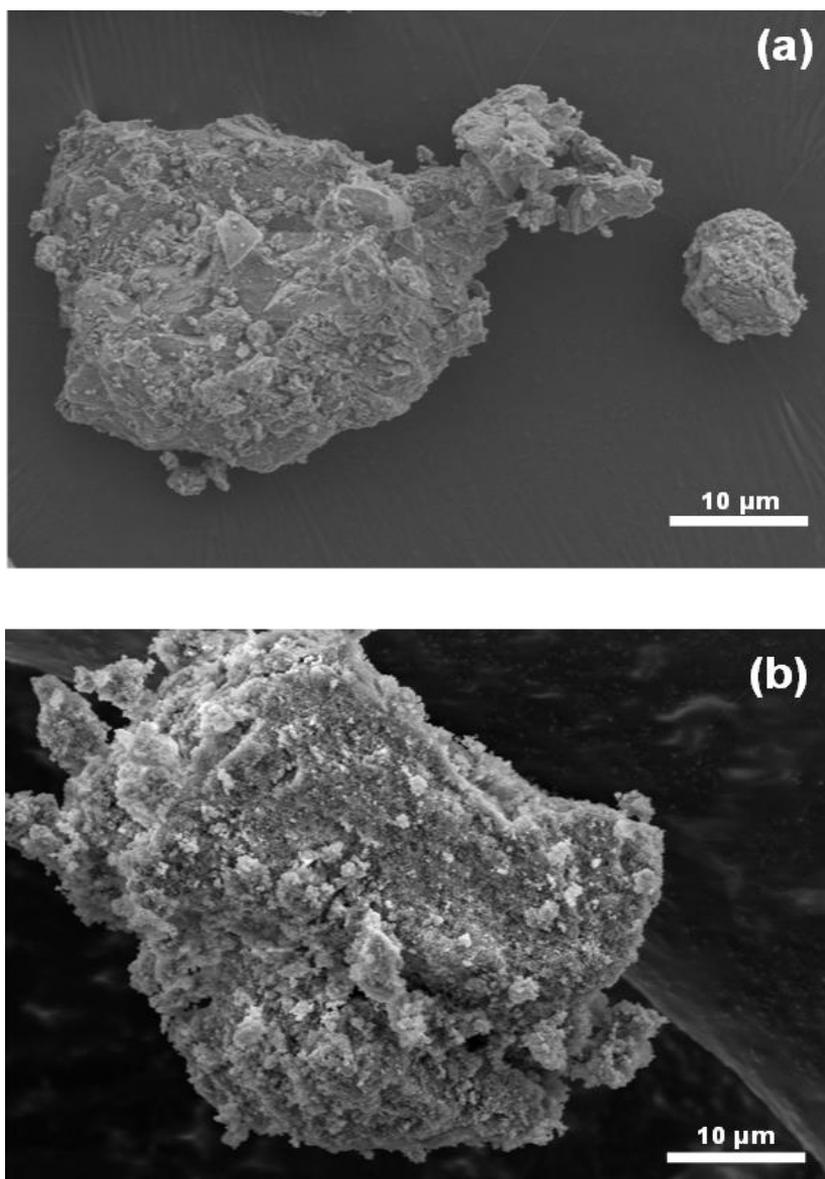
Figure S3. *SEM images of (a) ZnCr-C and (b) ZnCr-AMO samples.*
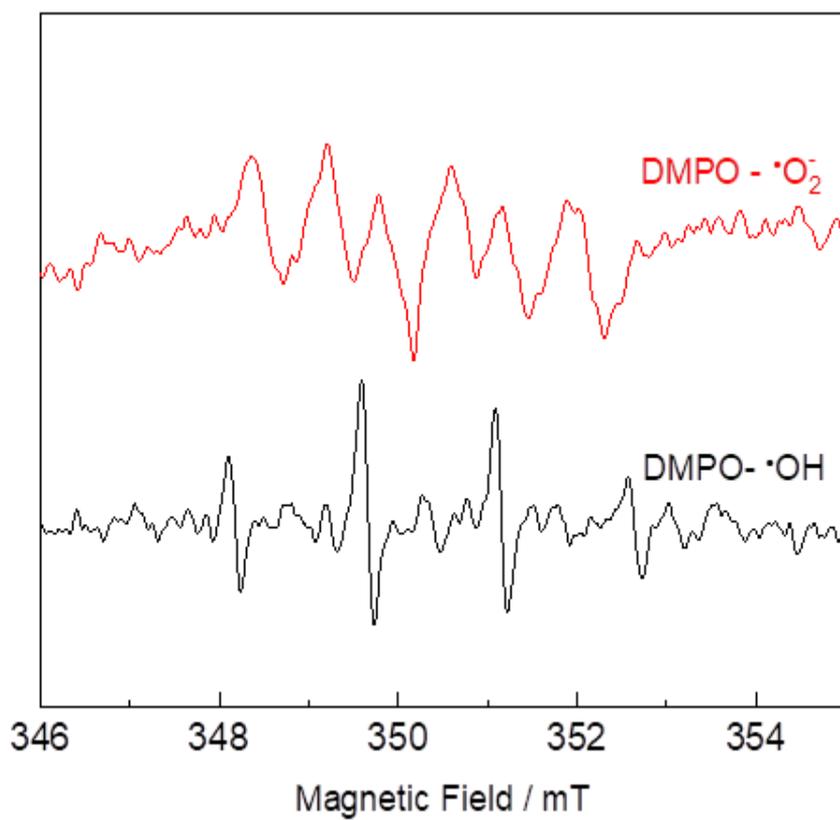
Figure S4. *DMPO spin trapping EPR obtained for the ZnCr-AMO sample.*
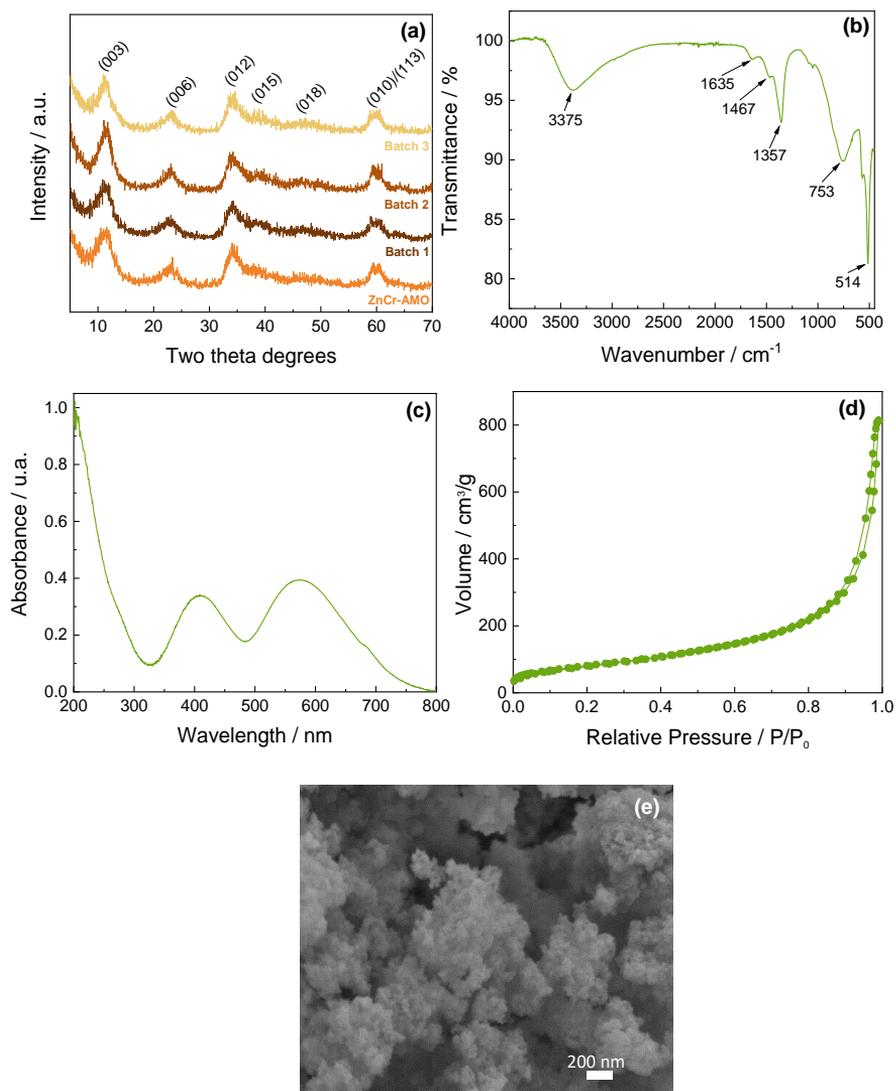
Figure S5. *(a) XRD patterns of sample ZnCr-AMO and the different batches constituing the sample ZnCr-AMO-S. (b) FT-IR spectra, (c) UV-Vis spectra, (d) N_2 adsorption-desorption isotherm and (e) SEM image of ZnCr-AMO-S sample.*

Table S1. *Chemical and physical properties for the ZnCr-AMO-S sample: metal content and ratio; proposed formulae and BET surface.*

Sample	% w/w		Zn^{2+}/Cr^{3+} ratio	Formula	S_{BET} / m^2g^{-1}
	Zn^{2+}	Cr^{3+}			
ZnCr-AMO-S	34.13	13.35	2.05	$[Zn_{0.67}Cr_{0.33}(OH)_2](CO_3)_{0.165} \cdot 0.82H_2O$	297
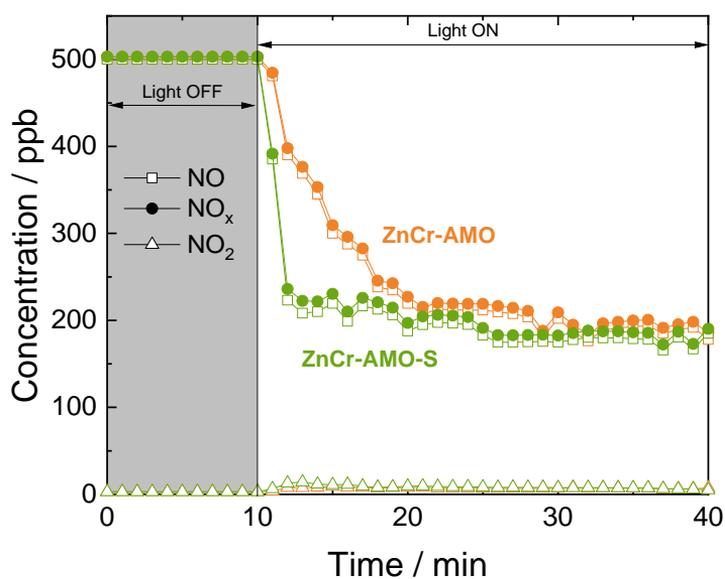
Figure S6. *NO, NO_x and NO_2 concentration evolution during photocatalytic process under UV-Vis irradiation for ZnCr-AMO (orange) and ZnCr-AMO-S (green) samples.*
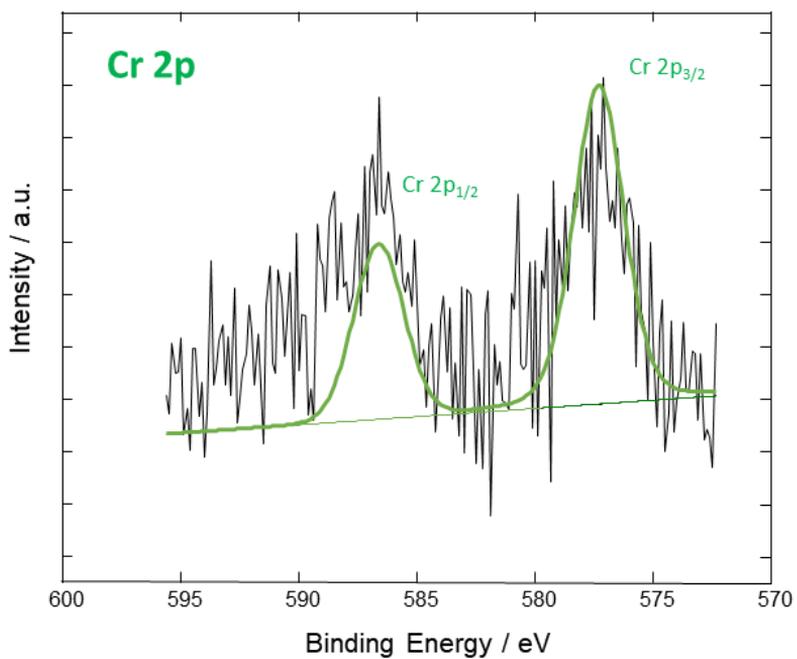
Figure S7. *XPS spectra (Cr 2p signal) obtained from MZnCr-1 mortar surface.*

Capítulo 4
Resumen

La fotocatálisis se presenta como una metodología prometedora para la remediación de la contaminación atmosférica de gases NO_x en las zonas urbanas. En la búsqueda de nuevos materiales fotocatalíticos DeNOx alternativos al TiO_2, los hidróxidos dobles laminares se muestran como una alternativa interesante. Dada la gran versatilidad que presenta su estructura, estos materiales pueden ser diseñados para obtener un mayor aprovechamiento de la radiación solar. En este contexto, la presente tesis doctoral se ha centrado en dos ámbitos: 1) el diseño de hidróxidos dobles laminares con propiedades fotocatalíticas DeNOx mejoradas y 2) La aplicación de estos compuestos, como aditivo fotocatalítico DeNOx, en materiales de construcción para su potencial uso en tareas de descontaminación atmosférica en zonas urbanas.

1) Diseño de HDL con propiedades fotocatalíticas DeNOx mejoradas

En primer lugar, se ha llevado a cabo el estudio de la influencia de diferentes modificaciones en los hidróxidos dobles laminares, concretamente la composición de la lámina de hidróxidos metálicos, la composición de la interlámina así como su heterounión con otro semiconductor. Cada una de estas modificaciones ha dado lugar a la publicación de un artículo científico.

❖ Modificación de la composición metálica

En este trabajo (ver **sección 3.1**), se ha llevado a cabo el dopado del HDL Zn_2Cr-CO_3 con diferentes cantidades del ion cobre(II) para formar compuestos $Zn_{2-x}Cu_xCr-CO_3$, con x = 0, 0.2 y 0.4. La preparación de estos compuestos se realizó empleando el método de coprecipitación.

Los resultados fotocatalíticos, empleando radiación ultravioleta-visible, mostraron un mayor rendimiento del proceso DeNOx al aumentar las cantidades de Cu(II) presente en la estructura, pasando de una eficiencia del 27 % en la muestra que no contenía cobre, a un 51 % en la muestra con mayor contenido. No obstante, todas las muestras presentaron una selectividad sobresaliente hacia la oxidación completa del gas NO con valores de selectividad superiores al 97 %. El aumento de la cantidad de iones de cobre en las láminas del HDL dio lugar a ligeros cambios en la estructura y morfología y a una importante variación de las propiedades ópticas de los HDL. Así, los cálculos de densidades de estados (DOS) sugirieron que la presencia de iones Cu(II) en la estructura del HDL introducen nuevos niveles en la banda de valencia, dificultando así la recombinación de los portadores de carga e^-/h^+, lo que favoreció una mayor producción de especies reactivas de oxígeno ($\bullet OH$ y $\bullet O_2^-$) y con ello, una mejora de la actividad fotocatalítica. La presencia de iones Cu(II) en la estructura del HDL incrementa el rango de luz solar que es capaz de adsorber el compuesto, viéndose con ello favorecida la actividad fotocatalítica bajo irradiación de luz visible.

❖ <u>Modificación del anión interlaminar</u>

Aprovechando la capacidad de reconstrucción de los HDL, se decidió llevar a cabo un estudio para una doble remediación medioambiental (ver *sección 3.2*). En primer lugar, se decidió eliminar un contaminante industrial del agua, como es el ion cromato, mediante su adsorción con un óxido mixto (resultante de la calcinación a 500 °C del HDL) y posteriormente probar la capacidad fotocatalítica de este producto de adsorción, HDL-cromato. Con este objetivo, se sintetizó el HDL de MgAl-CO$_3$ mediante el método de coprecipitación con una relación de

metales de 3:1. Después de su calcinación a 500 °C se obtuvo el óxido mixto y, posteriormente, se sintetizó el sistema MgAl-CrO$_4$ empleando el método de reconstrucción. Los resultados mostraron que después del uso del óxido mixto como adsorbente, el producto de adsorción recuperó la estructura del HDL ("efecto memoria"). Las pruebas fotocatalíticas mostraron una muy buena eficiencia de eliminación de gas NO, así como una alta selectividad. La incorporación del ion cromato a la estructura del HDL mejoró la absorción de luz en la región visible del espectro. El mejor aprovechamiento de la luz solar que incide sobre este compuesto permitió una mejora del 20 % en la eliminación fotoquímica de gas NO, respecto al HDL sin cromato. Los resultados de EPR y PL destacan el papel del ion cromato en el incremento de fotoactividad observada, facilitando la producción de electrones foto-excitados y retardando la recombinación de los portadores de carga (huecos y electrones).

❖ <u>Heterounión con otro semiconductor</u>

Para estudiar la influencia de la heterounión entre los HDL y otro semiconductor en las propiedades fotocatalíticas, se decidió emplear puntos cuánticos de grafeno luminiscentes azules (GQD) con nano-láminas de HDL de níquel y titanio (NiTi-LDH) sintetizadas mediante el método AMOST. Dicha heterounión se llevó a cabo mediante un simple método de impregnación. Las heterouniones GQDs/NiTi-LDH se prepararon con diferentes cantidades de GQD. La incorporación de GQD condujo a una mejor respuesta DeNOx de los fotocatalizadores GQD/NiTi en comparación con NiTi-LDH. Concretamente, el rendimiento mejorado de GQD/NiTi-LDH propició a una excelente actividad de foto-eliminación de gases NOx (61 %) y una liberación insignificante de NO$_2$ (< 0,6 %), superando al TiO$_2$ P25 estándar (48 % y 14,2 %, respectivamente). A

destacar, esta elevada eficiencia fotocatalítica DeNOx se mantiene aun cuando la muestra se irradia solo con luz visible. Además, tras finalizar el período de irradiación, las heterouniones GQD/NiTi-LDH mantuvieron una eficiencia fotocatalítica superior al 20 % durante 75 minutos. El mecanismo fotocatalítico luz/oscuridad se explicó por la capacidad de almacenamiento de electrones en el NiTi-LDH bajo excitación de luz, que es asistida por la migración de electrones desde los GQD hacia el HDL NiTi-LDH. Una vez que se apaga la luz, los electrones se liberan y participan en la generación de radicales superóxido. La fotocatálisis persistente es un proceso atractivo para ampliar el espectro de aplicaciones ambientales. Esta investigación se desarrolló en la ***sección 3.3***.

2) Aplicación de los HDL como aditivos fotocatalíticos DeNOx en materiales de construcción

En este estudio (***sección 3.4***) se ha utilizado por primera vez un hidróxido doble laminar (Zn_2Cr-CO_3) como aditivo fotocatalítico en materiales de construcción para la eliminación de gases NO_x en entornos urbanos. En comparación con el HDL preparado por el método de coprecipitación convencional, el HDL preparado mediante el método AMOST presentó una mayor área superficial, lo que mejoró significativamente su actividad fotocatalítica. El fotocatalizador ZnCr-AMO mostró una eficiencia fotocatalítica de eliminación de gases NO_x similar a la del TiO_2-P25 estándar (65%), pero con una selectividad superior (97 % frente a 75 %). La preparación de este producto fue fácilmente escalable, y el material obtenido mantuvo inalteradas sus propiedades físico-químicas, estructurales y fotoquímicas. El fotocatalizador ZnCr-AMO se incorporó con éxito en diferentes proporciones (0.5, 1.0 y 2.0 %) a un mortero de capa fina comercial, sin afectar esencialmente las propiedades

físico-mecánicas del mortero de referencia. Las pruebas fotocatalíticas del mortero con el aditivo HDL ZnCr-AMO mostraron un comportamiento aceptable para las diferentes proporciones ensayadas y revelaron que el mejor comportamiento lo presentó la muestra en la que se adicionó el fotocatalizador al 1 % (MZnCr-1).

Chapter 4
Summary

Photocatalysis is presented as a promising methodology for the remediation of NO_x air pollution in urban areas. In the search for new DeNOx photocatalytic materials as an alternative to TiO_2, layered double hydroxides (LDHs) are an interesting alternative. Given the great versatility of their structure, these materials can be designed for better harvesting of solar spectrum radiation. In this context, the present doctoral thesis has focused on two scopes: 1) the design of layered double hydroxides with improved DeNOx photocatalytic properties and 2) the application of these compounds, as a DeNOx photocatalytic additive, in construction materials for their potential use in atmospheric decontamination tasks in urban areas.

1) Design of LDH with improved photocatalytic DeNOx properties

Firstly, the study of the influence of different modifications on the layered double hydroxides has been carried out, namely the composition of the metal hydroxide layer, the composition of the interlayer as well as its heterojunction with another semiconductor. Each of these modifications has resulted in the publication of a scientific paper.

❖ Modification of the metallic composition

In this work (see **section 3.1**), doping of LDH Zn_2Cr-CO_3 with different amounts of copper(II) ion has been carried out to form $Zn_{2-x}Cu_xCr-CO_3$ compounds, with x = 0, 0.2 and 0.4. The preparation of these compounds was conducted using the coprecipitation method.

Photocatalytic results, using ultraviolet-visible radiation, showed a higher performance of the DeNOx process as the quantities of Cu(II) present in the structure increased, going from an efficiency of 27 % in the

sample that did not contain copper, to 51 % in the sample with its highest content. However, all samples showed outstanding selectivity towards complete oxidation of NO gas with selectivity values above 97 %. The increment in the amount of copper ions in the LDH layers resulted in slight changes in the structure and morphology and a significant variation in the optical properties of the LDHs. Thus, density of states (DOS) calculations suggested that the presence of Cu(II) ions in the LDH structure introduce new levels in the valence band, thus hindering the recombination of e^-/h^+ charge carriers, which favored a higher production of reactive oxygen species ($\bullet OH$ and $\bullet O_2^-$), and with it, an enhancement of the photocatalytic activity. The presence of Cu(II) ions in the LDH structure increases the range of sunlight that the compound is able to adsorb, thus favoring the photocatalytic activity under visible light irradiation.

❖ <u>Modification of the interlayer anion</u>

Taking advantage of the reconstruction capacity of LDH, a study was carried out for a double environmental remediation (see ***section 3.2***). Firstly, an industrial water pollutant, chromate ion, was removed by adsorption with a mixed oxide (resulting from calcination at 500 °C of LDH) and then the photocatalytic capacity of this adsorption product, LDH-chromate, was tested. For this purpose, MgAl-CO$_3$ LDH was synthesized by the coprecipitation method with a metal ratio of 3:1. After calcination at 500 °C, the mixed oxide was obtained and, subsequently, the MgAl-CrO$_4$ system was synthesized using the reconstruction method. The results showed that after the use of the mixed oxide as adsorbent, the adsorption product recovered the LDH structure ("memory effect"). Photocatalytic tests showed an excellent NO gas removal efficiency as well as a high selectivity. The incorporation of chromate ion into the LDH structure

improved light absorption in the visible region of the spectrum. The higher utilization of the sunlight incident on this compound allowed a 20 % improvement in the photochemical removal of NO gas, with respect to LDH without chromate. EPR and PL results highlight the role of the chromate ion in the observed increase in photoactivity, facilitating the production of photoexcited electrons and retarding the recombination of charge carriers (holes and electrons).

❖ Heterojunction with another semiconductor

To study the influence of heterojunction between LDHs and another semiconductor on the photocatalytic properties, it was decided to employ blue luminescent graphene quantum dots (GQDs) with nickel-titanium LDH nanosheets (NiTi-LDH) synthesized by AMOST method. Such heterojunction was carried out by a simple impregnation method. GQDs/NiTi-LDH heterojunctions were prepared with different amounts of GQDs. The incorporation of GQDs led to an improved DeNOx response of the GQD/NiTi photocatalysts compared to NiTi-LDH. Specifically, the improved performance of GQD/NiTi-LDH led to excellent NO_x gas photo-removal activity (61 %) and insignificant NO_2 release (< 0.6 %), outperforming standard TiO_2 P25 (48 % and 14.2 %, respectively). To highlight, this high DeNOx photocatalytic efficiency is maintained even when the sample is irradiated with visible light only. Moreover, after the end of the irradiation period, the GQD/NiTi-LDH heterojunctions maintained a photocatalytic efficiency higher than 20 % for 75 min. The light/dark photocatalytic mechanism was explained by the electron storage capacity in NiTi-LDH under light excitation, which is assisted by electron migration from GQDs to NiTi-LDH LDH. Once the light is turned off, the electrons are released and participate in the generation of

superoxide radicals. Persistent photocatalysis is an attractive process to broaden the spectrum of environmental applications. This research was developed in *section 3.3*.

2) Application of LDH as photocatalytic DeNOx additives in building materials

In this study (*section 3.4*), a layered double hydroxide (Zn_2Cr-CO_3) was used for the first time as a photocatalytic additive in building materials for the removal of NO_x gases in urban environments. Compared with the LDH prepared by the conventional coprecipitation method, the LDH prepared by the AMOST method exhibited a higher surface area, which significantly improved its photocatalytic activity. The ZnCr-AMO photocatalyst showed a photocatalytic NOx removal efficiency similar to that of standard TiO_2-P25 (65%), but with a higher selectivity (97 % vs. 75 %). The preparation of this product was easily scalable, and the material obtained maintains its physicochemical, structural and photochemical properties unchanged. The ZnCr-AMO photocatalyst was successfully incorporated in different proportions (0.5, 1.0 and 2.0 %) into a commercial thin layer mortar, without essentially affecting the physico-mechanical properties of the reference mortar. The photocatalytic tests of the mortar with the LDH ZnCr-AMO additive showed an acceptable behavior for the different proportions tested and revealed that the best behavior was presented by the sample in which the photocatalyst was added at 1 % (MZnCr-1).

Capítulo 5
Conclusiones

Los resultados obtenidos en la presente tesis doctoral permiten establecer las siguientes conclusiones generales:

En lo que respecta al diseño de sistemas HDL con propiedades fotocatalíticas mejoradas:

1. La incorporación de metales de transición en la estructura de los HDL ya sea tanto en la lámina como en el espacio interlaminar, originan principalmente: i) una mejora de la absorción lumínica de estos compuestos en la región visible del espectro, ii) una modificación de sus propiedades electrónicas que favorece la mitigación de la recombinación de los portadores de carga producidos durante el proceso fotoquímico. Los HDL modificados con metales de transición presentan una mayor actividad fotocatalítica.

2. Dada su aplicación como adsorbentes, los HDL pueden ser empleados en tareas de doble remediación medioambiental. En primer lugar, pueden eliminar los contaminantes metálicos del agua por adsorción y posteriormente, el producto de la adsorción HDL-contaminante puede ser empleado como fotocatalizador para tareas de descontaminación atmosférica.

3. La formación de una adecuada heterounión electrónica, en este caso entre el HDL de NiTi y el GQD, permite obtener fotocatalizadores con dos propiedades muy destacables: i) una gran actividad fotocatalítica DeNOx empleando solamente radiación visible, ii) desarrollar una actividad DeNOx post-fotocatalítica, actividad que perdura hasta 75 minutos en la oscuridad tras cesar la irradiación lumínica en la muestra.

4. Los HDL estudiados mostraron, en todos los casos, una excelente selectividad con respecto a la completa oxidación fotoquímica de los óxidos de nitrógeno, superando claramente al fotocatalizador de referencia TiO$_2$ P25.

Por otro lado, en relación con su empleo como aditivo fotocatalítico en materiales de construcción para aplicaciones de remediación medioambiental de atmósferas con gases NO$_x$:

1. El HDL de ZnCr preparado mediante el método AMOST presentó mejor eficiencia fotoquímica que el mismo preparado por el método convencional. La síntesis de HDL mediante el método AMOST es fácilmente escalable y el material obtenido mantiene inalteradas sus propiedades fisicoquímicas, estructurales y fotoquímicas.

2. El HDL de ZnCr preparado mediante el método AMOST se incorporó con éxito en diferentes proporciones en un mortero comercial sin afectar esencialmente a las propiedades físico-mecánicas del mismo.

3. Los resultados fotocatalíticos del mortero funcionalizado mostraron un buen comportamiento para las diferentes proporciones ensayadas.

4. Estos resultados abren la puerta al uso de los HDL en materiales de construcción con el objetivo de encontrar nuevas soluciones ambientales mediante fotocatálisis.

A partir de lo anterior, se puede concluir de forma general que los hidróxidos dobles laminares son una opción muy interesante y novedosa de fotocatalizadores para llevar a cabo tareas de purificación del aire.

Chapter 5
Conclusions

The results obtained in this doctoral thesis allow to establish the following general conclusions:

Regarding the design of LDH systems with enhanced photocatalytic properties:

1. The incorporation of transition metals in the LDH structure, either in the layer or in the interlayer space, lead mainly to: i) an improvement of the light absorption of these compounds in the visible region of the spectrum, ii) a modification of their electronic properties that promotes the mitigation of the recombination of the charge carriers produced during the photochemical process. LDH modified with transition metals present a higher photocatalytic activity.

2. Given their application as adsorbents, LDHs can be employed in dual environmental remediation tasks. First, they can remove metal pollutants from water by adsorption and subsequently, the LDH-pollutant adsorption byproduct can be employed as a photocatalyst for atmospheric decontamination tasks.

3. The formation of a suitable electronic heterojunction, in this case between the NiTi HDL and the GQD, allows to obtain photocatalysts with two very remarkable properties: i) a high DeNOx photocatalytic activity using only visible radiation, ii) to develop a post-photocatalytic DeNOx activity, that lasts up to 75 minutes in the dark after the cessation of light irradiation on the sample.

4. The LDHs studied showed, in all cases, excellent selectivity with respect to the complete photochemical oxidation of nitrogen oxides, clearly beating the reference photocatalyst TiO_2 P25.

On the other hand, concerning its use as a photocatalytic additive in building materials for environmental remediation applications in NO_x gas atmospheres:

1. ZnCr LDH prepared by AMOST method presented an improved photochemical efficiency than the same prepared by the conventional method. The synthesis of LDH by the AMOST method is easily scalable and the material obtained maintains its physicochemical, structural and photochemical properties unaltered.

2. ZnCr LDH prepared by the AMOST method was successfully incorporated in different proportions in a commercial mortar without essentially affecting the physico-mechanical properties of the mortar.

3. Photocatalytic results of the functionalized mortar showed an excellent performance for the different proportions tested.

4. These results open the door to the use of LDHs in building materials with the aim of finding new environmental solutions through photocatalysis.

From the above, it can be generally concluded that layered double hydroxides are a highly interesting and novel choice of photocatalysts for air purification tasks.

Capítulo 6
Producción y
Difusión Científica

6.1. Publicaciones en revistas científicas. Indicios de calidad

a) Publicaciones derivadas de la Tesis Doctoral

1- **Título:** Graphene quantum dots/NiTi layered double hydroxide heterojunction as a highly efficient De-NOx photocatalyst with long persistent post-illumination action

Autores: Javier Fragoso, Adrián Pastor, Manuel Cruz-Yusta, Francisco Martín, Gustavo de Miguel, Ivana Pavlovic, Mercedes Sánchez y Luis Sánchez.

Revista: Applied Catalysis B: Environmental

Código ISSN: 0926-3373

Año: 2023 ; **Volumen:** 322 ; **Número de referencia:** 122115

Editorial: Elsevier

DOI: 10.10106/j.apcatb.2022.122115

Base de datos en la que está indexada: Journal Citation Reports

Índice de impacto de la revista: 24.319

Lugar que ocupa/ Nº revistas del área temática

Chemistry, Physical: 6/165 Q1

Engineering, Chemical: 3/143 Q1

Engineering, Environmental: 1/54 Q1

2- Título: Use of LDH-chromate adsorption co-product as an air purification photocatalyst

Autores: Amina Nehdi, Najoua Frini-Srasra, Gustavo de Miguel, Ivana Pavlovic, Luis Sánchez and Javier Fragoso

Revista: Chemosphere

Código ISSN: 0045-6535

Año: 2022 ; **Volumen:** 286 ; **Número de referencia:** 131812

Editorial: Elsevier

DOI: 10.1016/j.chemosphere.2021.131812

Base de datos en la que está indexada: Journal Citation Reports

Índice de impacto de la revista: 8.943

Lugar que ocupa/ Nº revistas del área temática:

Environmental Sciences: 33/279 Q1

3- Título: Insight into the role of copper in the promoted photocatalytic removal of NO using $Zn_{2-x}Cu_xCr-CO_3$ layered double hydroxide

Autores: Javier Fragoso, María de los Ángeles Oliva, Luis Camacho, Manuel Cruz-Yusta, Gustavo de Miguel, Francisco Martin, Adrián Pastor, Ivana Pavlovic and Luis Sánchez.

Revista: Chemosphere

Código ISSN: 0045-6535

Año: 2021 ; **Volumen:** 275 ; **Número de referencia:** 130030

Editorial: Elsevier

Base de datos en la que está indexada: Journal Citation Reports

Índice de impacto de la revista (2021): 8.943

Lugar que ocupa/ Nº revistas del área temática

Environmental Sciences: 33/279 Q1

b) Otras publicaciones derivadas de la formación investigadora

1-   Título: Enhanced photocatalytic removal of NO_x gases by β-Fe_2O_3/CuO and β-Fe_2O_3/WO_3 nanoheterostructures.

Autores: Javier Fragoso, Davide Barreca, Lorenzo Bigiani, Alberto Gasparotto, Cinzia Sada, Oleg I. Lebedev, Evgeny Modin, Ivana Pavlovic, Luis Sánchez and Chiara Maccato

Revista: Chemical Engineering Journal

Código ISSN: 1385-8947

Año: 2022   ; **Volumen**: 430   ; **número de referencia:** 132757

Editorial: Elsevier

Base de datos en la que está indexada: Journal Citation Reports

Índice de impacto de la revista (2021): 16.744

Lugar que ocupa/ Nº revistas del área temática:

Engineering, Chemical: 4/143 Q1

Engineering, Environmental: 2/54 Q1

2- Título: Tailored Co_3O_4-Based Nanosystems: Toward Photocatalysts for Air Purification

Autores: Javier Fragoso, Davide Barreca, Lorenzo Bigiani, Cinzia Sada, Oleg I. Lebedev, Evgeny Modin, Ivana Pavlovic, Luis Sánchez and Chiara Maccato

Revista: ACS Applied Materials & Interfaces

Código ISSN: 1944-8244

Año: 2021   ; **Volumen**: 13   ; **Páginas:** 44520-44530

Editorial: American Chemical Society

DOI: 10.1021/acsami.1c0992

Base de datos en la que está indexada: Journal Citation Reports

Índice de impacto de la revista (2021): 10.383

Lugar que ocupa/ Nº revistas del área temática:

Materials Science, Multidisciplinary: 49/345 Q1

Nanoscience & Nanotechnology: 23/109 Q1

6.2. Comunicaciones en Congresos Científicos

1- Congreso: 11th European Conference on Solar Chemistry and Photocatalysis: Environmental Applications.

Tipo de participación: póster

Título: Graphene quantum dots/NiTi-LDH as a highly efficient day-night air purification photocatalyst

Autores: Javier Fragoso, Manuel Cruz-Yusta, Francisco Martín, Adrián Pastor, Ivana Pavlovic and Luis Sánchez

Fecha de celebración: 6 al 10 de junio de 2022

Ámbito: Internacional

Entidad organizadora: Dipartimento di Chimica - Università degli Studi di Torino

Lugar de celebración: Turín (Italia)

2- Congreso: 11th European Conference on Solar Chemistry and Photocatalysis: Environmental Applications.

Tipo de participación: póster

Título: ZnCr layered double hydroxide as a photocatalytic additive for NOx gases remediation in building materials

Autores: Javier Fragoso, José Balbuena, Manuel Cruz, Manuel Lloris, Ivana Pavlovic y Luis Sánchez

Fecha de celebración: 6 al 10 de junio de 2022

Ámbito: Internacional

Entidad organizadora: Dipartimento di Chimica - Università degli Studi di Torino

Lugar de celebración: Turín (Italia)

3- Congreso: XIX Reunión del Grupo Especializado de Química Inorgánica y XIII Reunión del Grupo Especializado de Química de Estado Sólido – QIES 22

Tipo de participación: presentación flash y póster

Título: Estudio del rol del catión Cu^{2+} en la mejora de la oxidación fotocatalítica de NO promovida por el hidróxido doble laminar $Zn_{2-x}Cu_xCr$-CO_3

Autores: Javier Fragoso, María de los Ángeles Oliva, Luis Camacho, Manuel Cruz, Gustavo de Miguel, Francisco Martín, Adrián Pastor, Ivana Pavlovic y Luis Sánchez

Fecha de celebración: 30 de enero al 2 de febrero de 2022

Ámbito: Nacional

Entidad organizadora: Grupo Especializado de Química Inorgánica y Grupo Especializado de Química de Estado Sólido (Real Sociedad Española de Química).

Lugar de celebración: Sevilla (España)

4-   Congreso: XIX Reunión del Grupo Especializado de Química Inorgánica y XIII Reunión del Grupo Especializado de Química de Estado Sólido – QIES 22

Tipo de participación: póster

Título: GQDs/NiTi-LDH como fotocatalizador día-noche altamente eficiente para la purificación de aire

Autores: Adrián Pastor, Javier Fragoso, Manuel Cruz-Yusta, Ivana Pavlovic y Luis Sánchez

Fecha de celebración: 30 de enero al 2 de febrero de 2022

Ámbito: Nacional

Entidad organizadora: Grupo Especializado de Química Inorgánica y Grupo Especializado de Química de Estado Sólido (Real Sociedad Española de Química).

Lugar de celebración: Sevilla (España)

5- **Congreso:** 2nd International Conference on Sustainable, Environmental Friendly Construction Materials

Tipo de participación: Póster

Título: Layered Double Hydroxides as photocatalytic additive for De-NO$_x$ building materials

Autores: Javier Fragoso, Adrián Pastor, Jean-Charles Buffet, Chunping Chen, Manuel Cruz, Dermot O'Hare, Ivana Pavlovic y Luis Sánchez

Fecha de celebración: 31 de agosto al 2 de septiembre de 2021

Ámbito: Internacional

Entidad organizadora: West Pomeranian University of Technology in Szczecin

Lugar de celebración: Szczecin (Polonia)

6- **Congreso:** 6th Edition of the International Conference Nanotech France

Tipo de participación: Póster

Título: Hydrotalcite-like material for a double environmental remediation

Autores: Javier Fragoso, Amine Nehdi, Manuel Cruz, Ivana Pavlovic y Luis Sánchez

Fecha de celebración: 23 al 25 de junio de 2021

Ámbito: Internacional

Entidad organizadora: SECTOR Conferences and Exhibitions

Lugar de celebración: París (Francia) /online

7- Congreso: IX Congreso Científico de Investigadores en Formación de la Universidad de Córdoba.

Tipo de participación: Poster

Título: Hidróxidos Dobles Laminares como aditivos para materiales de construcción DeNO$_x$

Autores: Javier Fragoso, Ivana Pavlovic y Luis Sánchez

Fecha de celebración: 3 al 6 de mayo de 2021

Ámbito: Nacional

Entidad organizadora: Escuela de Doctorado de la Universidad de Córdoba y Escuela Internacional de Doctorado en Agroalimentación

Lugar de celebración: online

8- Congreso: 1st International Electronic Conference on Catalysis Sciences

Tipo de participación: Póster

Título: Effect of chromate anion on the photocatalytic activity of Mg-Al layered double hydroxide

Autores: Amine Nehdi, Javier Fragoso, Najoua Frini-Srasra, Ivana Pavlovic y Luis Sánchez

Fecha de celebración: 10 al 30 de noviembre de 2020

Ámbito: Internacional

Entidad organizadora: Catalysts, MDPI

Lugar de celebración: online

9- **Congreso:** VIII Congreso Científico de Investigadores en ForMACIÓN DE LA Universidad de Córdoba

Tipo de participación: comunicación oral

Título: Estudio del sistema $Zn_{2-x}Cu_xCr$ como fotocatalizador para la eliminación de gases NO_x

Autores: Javier Fragoso, María de los Ángeles Oliva, Manuel Cruz, Ivana Pavlovic y Luis Sánchez

Fecha de celebración: 18 y 19 de febrero de 2020

Ámbito: Nacional

Entidad organizadora: Escuela de Doctorado de la Universidad de Córdoba y Escuela Internacional de Doctorado en Agroalimentación.

Lugar de celebración: Córdoba (España)

6.3. Contribuciones a capítulos de libro

1- **Título del capítulo:** Graphene quantum dots/NiTi-LDH as a highly efficient day-night air purification photocatalyst

Autores: Luis Sánchez, Javier Fragoso, Adrián Pastor, Manuel Cruz, Francisco Martín, Ivana Pavlovic

Título del libro: 11th European Conference on Solar Chemistry and Photocatalysis: Environmental Applications (SPEA11)

Páginas: 358-359

Editoria: Organizing Committee SPEA11

Año de publicación: 2022

ISBN: 979-12-210-0970-5

2- **Título del capítulo:** ZnCr layered double hydroxide as a photocatalytic additive for NO_x gases remediation in building materials

Autores: Javier Fragoso, José Balbuena, Manuel Cruz-Yusta, Manuel Lloris, Ivana Pavlovic y Luis Sánchez

Título del libro: 11th European Conference on Solar Chemistry and Photocatalysis: Environmental Applications (SPEA11)

Páginas: 624-625

Editoria: Organizing Committee SPEA11

Año de publicación: 2022

ISBN: 979-12-210-0970-5

3- Título del capítulo: Layered Double Hydroxides as photocatalytic additive for De-NO$_x$ building materials.

Autores: Javier Fragoso, Adrián Pastor, Jean-Charles Buffet, Chunping Chen, Manuel Cruz-Yusta, Dermot O'Hare, Ivana Pavlovic, Luis Sánchez.

Título del libro: 2nd International COnference on Sustainable, ENvironmental Friendly Construction Materials (ICSEFCM 2021).

Páginas: 129-130

Editorial: West Pomeranian University of Technology, Szczecin Publishing House al. Piastów 48, 70-311 Szczecin, Poland

Año de publicación: 2021

ISBN: 978-83-7663-324-4

4- Título del capítulo: Hidróxidos Dobles Laminares como aditivos para materiales de construcción DeNO$_x$

Autores: Javier Fragoso, Ivana Pavlovic, Luis Sánchez

Título del libro: IX Congreso Científico de Investigadores en Formación de la Universidad de Córdoba: Nuevos desafíos, nuevas oportunidades

Páginas: 303-306

Editorial: UCOPress. Ediciones Universidad de Córdoba. Campus Universitario de Rabanales. Carretera nacional IV, km. 396. 14.71, Córdoba, España

Año de publicación: 2021

ISBN: 978-84-9927-640-3

5- **Título del capítulo:** Estudio del sistema $Zn_{2-x}Cu_xCr$ como fotocatalizador para eliminación de gases NO_x

Autores: Javier Fragoso Núñez, María de los Ángeles Oliva Lamarca, Manuel Cruz Yusta, Ivana Pavlovic Milicevic y Luis Sánchez Granados.

Título del libro: Creando redes doctorales Vol. VIII. "La investigación del futuro"

Páginas: 333-336

Editorial: UCOPress. Ediciones Universidad de Córdoba. Campus Universitario de Rabanales. Carretera Nacional IV, km. 396. 14071, Córdoba, España

Año de publicación: 2020

ISBN: 978-84-9927-508-6

6.4. Estancias de investigación

1- **Institución de destino:** Dipartimento di Chimica, Università degli Studi di Torino, Turín (Italia).

Fecha: del 14 de marzo hasta el 30 de julio de 2022.

Objetivos de la estancia:

- Estudiar del fundamento teórico, así como el manejo instrumental, de la resonancia paramagnética del electrón.

- Estudiar de los defectos estructurales en hidróxidos dobles laminares.

- Estudiar la influencia de la composición metálica en la actividad fotocatalítica.

Supervisora: Prof.ª Maria Cristina Paganini

6.5. Participación en proyectos de investigación

1- **Título del proyecto:** Sistemas 2D y 3D basados en hidrotalcitas como fotocatalizadores para la eliminación de gases NO_x.

Investigador responsable: Luis Sánchez Granados (Universidad de Córdoba, España).

Entidad financiadora: Ministerio de Economía, Industria y Competitividad; Convocatoria 2017

Duración del proyecto: del 01/01/2018 al 30/09/2021

2- **Título del proyecto:** proyecto PID2020-117516GB-l00

Investigador responsable:

Entidad financiadora: Ministerio de Ciencia e Innovación

Duración del proyecto:

6.6.   Participación en eventos de difusión científica

1-   Título: XV Jornadas de Introducción al Laboratorio Experimental de Química

Lugar de celebración: Universidad de Córdoba, España

Fecha de participación: 25/01/2023

Entidad organizadora: Facultad de Ciencias (Universidad de Córdoba)

T**ipo de participación:** Preparación y desarrollo experimental de sesiones prácticas de laboratorio para el alumnado de institutos.

2-   Título: XI edición de la Noche Europea de los Investigadores

Lugar de celebración: Universidad de Córdoba, España

Fecha de participación: 30/09/2022

Entidad organizadora: Fundación Descubre – Universidad de Córdoba

Tipo de participación: Realización y explicación de la línea de investigación del grupo a los viandantes.

3-   Título: XIII Jornadas de Introducción al Laboratorio Experimental de Química

Lugar de celebración: Universidad de Córdoba, España

Fecha de participación: 16/01/2020

Entidad organizadora: Facultad de Ciencias (Universidad de Córdoba)

Tipo de participación: Preparación y desarrollo experimental de sesiones prácticas de laboratorio para el alumnado de institutos.

4- **Título:** XII Jornadas de Introducción al Laboratorio Experimental de Química

Lugar de celebración: Universidad de Córdoba

Fecha de participación: 01/02/2019

Entidad organizadora: Facultad de Ciencias (Universidad de Córdoba)

Tipo de participación: Preparación y desarrollo experimental de sesiones prácticas de laboratorio para el alumnado de institutos

6.7. Referencias de los diferentes actos de difusión realizados en prensa y otros medios de comunicación

1- **Referencia:** Noticia en prensa

Titular: Investigadores de la UCO desarrollan un compuesto que descontamina el aire durante la noche.

CÓRDOBA

MEDIO AMBIENTE

Investigadores de la UCO desarrollan un compuesto que descontamina el aire durante la noche

El grupo de trabajo está liderado por la profesora Ivana Pavlovic y el profesor Luis Sánchez

Europa Press

Córdoba | 22·11·22 | 13:18

Fachada del Rectorado de la Universidad de Córdoba. / A.J. GONZÁLEZ

Medio de comunicación donde se ha publicado la noticia: Diario Córdoba

Fecha de publicación: 22/11/2022

Enlace web: https://www.diariocordoba.com/cordoba-ciudad/2022/11/22/investigadores-uco-desarrollan-compuesto-descontamina-78916709.html

2- **Referencia:** Noticia en prensa

Titular: Investigadores desarrollan en Córdoba un compuesto que descontamina aire de las ciudades.

CORDOPOLIS / IQ

Integrantes del grupo de investigación de la UCO que ha participado en el estudio.

Redacción Cordópolis 22 de noviembre de 2022 - 12:10h 💬 0
🐦 @cordopolis_es
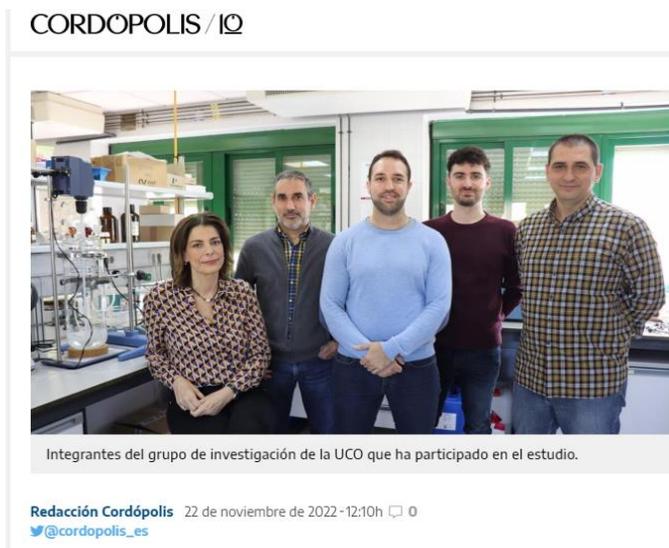
Medio de comunicación donde se ha publicado la noticia: Cordopolis

Fecha de publicación: 22/11/2022

Enlace web: https://cordopolis.eldiario.es/cordoba-hoy/sociedad/investigadores-desarrollan-cordoba-compuesto-descontamina-aire-ciudades_1_9732823.html

3- **Referencia:** Noticia en prensa

Titular: Investigadores de la Universidad de Córdoba desarrollan un compuesto que descontamina el aire de las ciudades de noche.

Medio de comunicación donde se ha publicado la noticia: Europa Press

Fecha de publicación: 22/11/2022

Enlace web: https://www.europapress.es/andalucia/noticia-investigadores-universidad-cordoba-desarrollan-compuesto-descontamina-aire-ciudades-noche-20221122105140.html

4- **Referencia:** Noticia en prensa

Titular: Un compuesto químico descontamina el aire de las ciudades durante la noche.

Medio de comunicación donde se ha publicado la noticia: Vivasevilla

Fecha de publicación: 22/11/2022

Enlace web: https://vivasevilla.es/cordoba/1126105/un-compuesto-quimico-descontamina-el-aire-de-las-ciudades-durante-la-noche/#

5-   **Referencia:** Noticia en prensa

Título: Investigadores desarrollan un compuesto que descontamina aire de las ciudades durante la noche.

Estación de medición de la calidad del aire en Córdoba

Medio de comunicación donde se ha publicado la notica: Córdobahoy

Fecha de publicación: 22/11/2022

Enlace web: https://www.cordobahoy.es/articulo/la-ciudad/investigadores-desarrollan-compuesto-que-descontamina-aire-ciudades-noche/20221122130946126895.amp.html

6- **Referencia:** Notica en prensa

Título: El invento español que logra limpiar el aire de las ciudades por la noche

El Confidencial   Iniciar

FOTOCATÁLISIS SIN LUZ SOLAR

El invento español que logra limpiar el aire de las ciudades por la noche

Investigadores de la Universidad de Córdoba desarrollan un nuevo compuesto que, incluido en los materiales de las fachadas, elimina los gases tóxicos procedentes del tráfico

Capa de contaminación sobre la ciudad de Madrid. (EFE/Juan Carlos Hidalgo)

Medio de comunicación donde se ha publicado la noticia: El confidencial

Fecha de publicación: 29/11/2022

Enlace web: https://www.elconfidencial.com/tecnologia/ciencia/2022-11-29/invento-espanol-descontaminar-aire-noche_3529910/

7- **Referencia:** Entrevista en la radio al IP, Luis Sánchez Granados

Título: El proyecto español que reduce la contaminación usando pintura y materiales de construcción: "Es instantáneo"

Medio de comunicación donde se ha publicado la noticia: Cope

Fecha de publicación: 30/11/2022

Enlace web:
https://www.cope.es/actualidad/sociedad/noticias/proyecto-espanol-que-reduce-contaminacion-usando-pintura-materiales-construccion-instantaneo-20221130_2428212

8-   Referencia: Noticia Actualidad Universitaria UCO

Título: Un nuevo compuesto descontamina el aire de las ciudades durante la noche
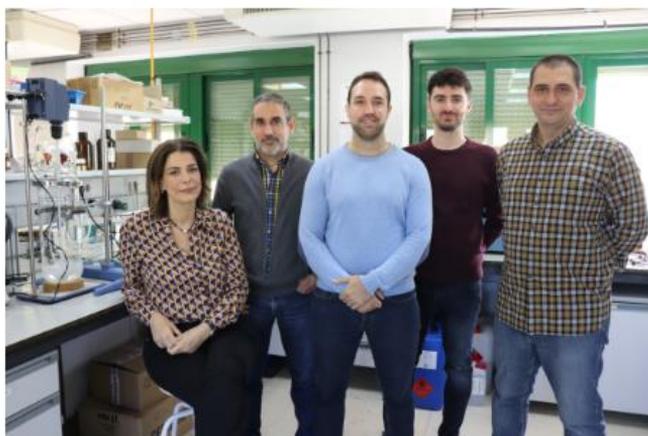
Imagen del grupo de investigación que ha participado en el estudio.

Medio de comunicación donde se ha publicado la noticia: Actualidad universitaria – Universidad de Córdoba

Fecha de publicación: 22/11/2022

Enlace web:
https://www.uco.es/servicios/actualidad/ciencia/item/147563-un-nuevo-compuesto-descontamina-el-aire-de-las-ciudades-durante-la-noche?lang=es

9- **Referencia:** Artículo de divulgación.

Título: Cuando la luz se aprovecha incluso en su ausencia:

descontaminación nocturna de la atmósfera mediante fotocatálisis.

Medio de comunicación donde se ha publicado la noticia: Nova Ciencia

Fecha de publicación: 23/01/2023

Enlace web: https://novaciencia.es/cuando-la-luz-se-aprovecha-incluso-en-su-ausencia-descontaminacion-nocturna-de-la-atmosfera-mediante-fotocatalisis/